To the Graduate Council:
I am submitting herewith a thesis written by Xiyou Peng entitled "Structural and Electronic Properties of Epitaxial FeSe and FeTe Thin Films on $SrTiO_3$." I have examined the final paper copy of this thesis for form and content and recommend that it be accepted in partial fulfillment of the requirements for the degree of Doctor of Philosophy, with a major in Physics.

Hanno Weitering, Major Professor

We have read this thesis
and recommend its acceptance:

Hanno Weitering

Norman Mannella

Steve Johnston

Adolfo G Eguiluz

Dustin A. Gilbert

Accepted for the Council:

Dixie L. Thompson

Vice Provost and Dean of the Graduate School

To the Graduate Council:
I am submitting herewith a thesis written by Xiyou Peng entitled "Structural and Electronic Properties of Epitaxial FeSe and FeTe Thin Films on $SrTiO_3$." I have examined the final electronic copy of this thesis for form and content and recommend that it be accepted in partial fulfillment of the requirements for the degree of Doctor of Philosophy, with a major in Physics.

Hanno Weitering, Major Professor

We have read this thesis
and recommend its acceptance:

Hanno Weitering

Norman Mannella

Steve Johnston

Adolfo G Eguiluz

Dustin A. Gilbert

Accepted for the Council:

Dixie L. Thompson

Vice Provost and Dean of the Graduate School

(Original signatures are on file with official student records.)

Structural and Electronic Properties of Epitaxial FeSe and FeTe Thin Films on $SrTiO_3$

A Dissertation Presented for the

Doctor of Philosophy

Degree

The University of Tennessee, Knoxville

Xiyou Peng

December 2024

© by Xiyou Peng, 2024
All Rights Reserved.

Acknowledgements

I would like to thank all the people who helped me throughout my Ph.D. journey.

Firstly, I want to sincerely thank Prof. Hanno Weitering. His broad understanding of physics greatly assisted me in addressing the key challenges I faced. He has always been patient in answering all my questions. Without his guidance, I would not have achieved what I have.

I would also like to thank all the members of my committee: Profs. Norman Mannella, Steve Johnston, Adolfo Eguiluz, and Dustin Gilbert, for their fruitful discussions and insightful questions.

I would like to thank the members of the groups led by Profs. Weitering and Mannella. Prof. Norman Mannella consistently challenged my understanding of physics, reminding me of the importance of not overlooking any details. Dr. Paolo Vilmercati was not just a problem solver; he shared his experimental knowledge and was always willing to enlighten us through discussions. I am grateful to my peers for their collaboration and discussions: Dr. Tyler Smith, Dr. Dongwon Shin, Kaleb McClure, Shiva Dahal, and Michael McConnell. I would also like to thank Randal McMillan; without his contributions to the machine work, we could not have modified and repaired the equipment we needed.

I would like to thank Prof. Wonhee Ko for his guidance on scanning tunneling microscopy (STM) and for allowing us to use his low-temperature STM system.

Finally, I want to express my gratitude to my parents, Yiyuan Peng and Tianping Tu, for their unwavering support and encouragement, which helped me persevere during the toughest times.

Abstract

The discovery of high-temperature superconductivity in an epitaxial monolayer of FeSe grown on the $SrTiO_3(001)$ substrate suggests the possibility of realizing high superconducting critical temperatures via heterostructure engineering. The mechanism behind this remarkable phenomenon remains unclear, however, although it is evident that the $SrTiO_3$ substrate plays a crucial role. Possible contributing factors include enhanced electron-phonon coupling involving the Fuchs-Kliewer phonon modes of the substrate, and carrier donation by the substrate. In this dissertation, I focus on the possible origins of charge donation. Specifically, I explore the possible role of oxygen vacancies and niobium dopants in the $SrTiO_3$ substrate and the role of Fe vacancies in the FeSe films. The experiments involved detailed studies of the substrate preparation and thin film growth protocols, using molecular beam epitaxy, scanning tunneling microscopy, (angle-resolved) photoemission, and *ex-situ* X-ray diffraction and magnetic measurements. We show that the use of selenium etched $SrTiO_3$ substrates minimizes charge transfer across the interface and that the T_c enhancement via postannealing is primarily due to the reduction of Fe vacancies in the film. The latter has a profound effect on the Fermi level location and screening dynamics of the films. We finally investigated FeTe monolayers on $SrTiO_3$. While the structure and composition of these films are nearly identical to those of FeSe on $SrTiO_3$, they are not superconducting. Possible reasons for this dissimilar behavior will be discussed.

Table of Contents

1 Introduction **1**

1.1 Conventional Superconductivity 1

1.2 Unconventional Superconductors: Cuprates 4

1.3 Iron-Based Superconductors 6

1.4 Single Layer of Iron Selenide on $SrTiO_3(001)$ 9

1.4.1 Interface phonon 12

1.4.2 The role of magnetism 15

1.4.3 Electron correlation 17

1.5 Scope of the Thesis 18

2 Experimental Methods **21**

2.1 Ultra High Vacuum and Molecular Beam Epitaxy 21

2.2 Scanning Tunneling Microscopy 28

2.3 Reflection High Energy Electron Diffraction 33

2.4 X-ray Photoelectron Spectroscopy 38

2.4.1 General description 38

2.4.2 Stoichiometry of thin films 38

2.4.3 Understanding the XPS spectrum 39

2.4.4 Core level binding energy 44

2.4.5 Auger spectrum and electron correlation 46

2.5 Low Energy Electron Diffraction 48

2.6 Angle-Resolved Photoemission Spectroscopy 50
2.7 X-ray Diffraction 52
2.7.1 2θ-ω scan 54
2.7.2 X-ray reflectivity measurement 54
2.7.3 Reciprocal space mapping 55
2.8 Magnetic Property Measurement System 56

3 $SrTiO_3$(001) Substrate Preparation 60
3.1 Introduction 60
3.2 Oxygen Vacancies and Surface Reconstructions 61
3.2.1 The $(\sqrt{5} \times \sqrt{5})$, (2×2) and (2×1) surface reconstructions of STO 62
3.2.2 Oxygen annealing: $c(6 \times 2)$, (2×2) and (2×1) reconstructions 62
3.2.3 Acid etching: (1×1) and (2×1) surface reconstructions . . . 67
3.2.4 Selenium and tellurium etching: $(\sqrt{13} \times \sqrt{13})$ reconstruction . 71
3.3 Electro-migration 74
3.4 Oxygen Vacancy Concentration of Se-etched STO 76
3.5 SrO versus TiO_x Surface Termination 84
3.6 Conclusions 90

4 Bulk FeSe 91
4.1 Crystal Structure and Phase Diagram of FeSe 91
4.2 Epitaxial Growth of FeSe Films on STO(001) 95
4.2.1 Substrate temperature: 2D step-flow growth vs. 3D growth . . 95
4.2.2 Fe/Se flux ratio 96
4.3 Domain Wall and Dislocation Defects 99
4.4 Strain Relaxation 104
4.5 Magnetic Properties 110
4.6 Conclusions 114

5 Ultrathin FeSe Films on $SrTiO_3$ **115**

5.1 Morphology of Monolayer and Multilayer FeSe on STO. 115

5.2 Electron Doping 123

5.3 Superconducting Gap 124

5.4 Conclusions 127

6 Core Level and Auger Spectroscopy of FeSe on STO **130**

6.1 Survey Spectrum of FeSe on $SrTiO_3$ 130

6.2 Fe $2p$ Core Level and CVV Auger Spectrum 133

6.3 Valence Band Spectra and Core Level Shifts 136

6.4 Conclusions 140

7 FeTe on $SrTiO_3$ **142**

7.1 MBE synthesis, STM and XRD characterization 142

7.2 STS of Monolayer and Second-layer FeTe film 157

7.3 XPS Survey Scan 161

7.4 Stoichiometry 164

7.5 Fe $2p$ Core Level and CVV Auger Spectrum 167

7.6 Valence Band Spectrum 168

7.7 Magnetic Property Measurement 171

7.8 Conclusions 172

8 Summary and Outlook **174**

Bibliography **177**

Vita **195**

List of Tables

3.1 The details of the UHV annealing on the STO 62
3.2 Details of the oxygen annealing parameters for the STO surface in Figure 3.3 67
3.3 Etching protocols for STO 69
3.4 Fitting parameters for Ti 2p in normal emission 81
3.5 Fitting parameters for Ti 2p in grazing emission 81
3.6 Fitting parameters for O 1s in normal emission 84
3.7 Fitting parameters for Sr 3d in normal emission 87
3.8 Fitting parameters for Sr 3d in grazing emission 87

4.1 Growth condition of the FeSe thick films on Se-etched STO 99
4.2 Out-of-plane lattice parameter c of the 177 ML thick FeSe films with and without post annealing 109
4.3 Lattice parameters of thick FeSe films obtained from RSM 111

5.1 Post annealing condition of the monolayer and double FeSe films on Se-etched STO 121

7.1 Growth conditions of FeTe films on a 1 UC-thick FeSe layer on Se-etched STO 151
7.2 Growth condition of the FeTe films on Te-etched STO 152
7.3 Out-of-plane lattice parameter of the 146 ML thick FeTe films (#245) on Te-etched STO 156

List of Figures

1.1 Zero DC resisitivty and Meissner effect of a superconductor 2
1.2 Timeline of the discovery of superconductors versus T_c 3
1.3 Generic properties of cuprates 5
1.4 Schematic of magnetic frustration when hole-doping the cuprates . . 6
1.5 Generic properties of FeSCs 8
1.6 Differences between the pnictide (chalcogenide) and cuprate superconductors. 8
1.7 Scanning tunneling spectrum of the monolayer and double layer FeSe film on STO 10
1.8 Fermi surface and bandstructure of FeSe 11
1.9 Doing and interface effect of FeSe systems 12
1.10 Dome-like behavior of FeSe monolayers on different reconstructed STO(001) surfaces 13
1.11 Interface phonon mechanism of superconductivity 14
1.12 Phase diagram of $FeTe_{1-x}Se_x$ 16
1.13 Magnetic moment and re normalization of mass in FeSCs 17

2.1 Schematic of UHV chambers 23
2.1 Schematic of UHV chambers continued 24
2.2 The vapor pressure of Se 26
2.3 Molecular Beam Epitaxy 27

2.4 Main contributions to the tunneling current with different tip/surface configurations. 30
2.5 Schematic of STM 31
2.6 Edwald Construction 34
2.7 Schematic of various real surfaces with its real space, reciprocal space and RHEED pattern 36
2.8 Mechanism of Kikuchi line formation 37
2.9 Energy conservation in X-ray photoelectron spectroscopy 39
2.10 Schematic of $KL_{23}L_{23}$ Auger process 41
2.11 An example of chemical shift in Fe $2p_{3/2}$ 42
2.12 Schematic of how tail feature in metal forms due to conduction electrons scattered by the core-hole potential 43
2.13 Determination of correlation energy U in iron pnictide superconductors from Auger spectra 47
2.14 Low Energy Electron Diffraction 49
2.15 Schematic geometry of an ARPES measurement 51
2.16 Schematic of XRD 53
2.17 Schematic of XRD alignment 54
2.18 Information obtained from an XRR measurement 55
2.19 Magnetic susceptibility for different types of magnetic materials . . . 57
2.20 Magnetization loops for different magnetic materials 57
2.21 Sketch of a DC SQUID magnetometer 59

3.1 STM images of UHV annealed STO 63
3.2 RHEED patterns of UHV annealed STO 64
3.3 Effects of oxygen annealing of the STO substrates 65
3.4 Over annealed STO 66
3.5 Relation between oxygen pressure and surface reconstruction of STO 68
3.6 STM images of acid etched STO surfaces 70

3.7 RHEED patterns of acid treated STO 71
3.8 STM and RHEED imageS of Se/Te-etched STO 73
3.9 Summary of the oxygen vacancy concentration on the STO prepared with different methods 74
3.10 Temperature effects on the quality of the STO ($\sqrt{13} \times \sqrt{13}$) surface reconstruction 75
3.11 RHEED images of Se-etched STO under AC current heating 77
3.12 RHEED patterns with annealing history of the STO surface 78
3.13 XPS study of selenium-etched STO 80
3.14 XPS study of the O 1s core level for various STO substrates 83
3.15 XPS study on SrO/TiO_x termination 85
3.16 Fitting on Sr 3d spectra 86
3.17 Schematic of partially SrO terminated STO surface 88
3.18 Structure of the surface ($\sqrt{13} \times \sqrt{13}$) reconstruction 89

4.1 β-FeSe in real space and reciprocal space 92
4.2 Crystal structures of tetragonal and hexagonal FeSe 92
4.3 Bulk FeSe phase diagram 93
4.4 Phase diagram near the β-phase region 94
4.5 Effect of substrate temperature on the growth of FeSe films 96
4.6 RHEED patterns of FeSe films grown under Fe rich conditions 97
4.7 RHEED and LEED patterns of thick FeSe films with different Fe/Se ratios 98
4.8 STM images of the two types domain boundaries on monolayer FeSe film 100
4.9 Domain wall orientation proposed by Ge 101
4.10 Observation of a (2×1) reconstruction on monolayer FeSe 102
4.11 Effects of temperature on domain boundaries in monolayer FeSe . . . 103
4.12 Strain relaxation of FeSe films on STO 105

4.13 Defects on Se-etched STO and on a 90 ML FeSe film 106
4.14 RHEED patterns of 177 ML thick FeSe films 107
4.15 2θ-ω scan of 177 ML thick FeSe films with and without post annealing 108
4.16 XRR data of the annealed 177 ML thick FeSe film 109
4.17 Reciprocal space map of FeSe bulk sample 111
4.18 Magnetic properties measurement on bulk FeSe 112

5.1 2D step-flow growth of an FeSe monolayer on STO (Sample #155), resulting in a uniform step morphology 115
5.2 Effects of high-temperature annealing on monolayer FeSe (#132) . . . 117
5.3 STM images showing some bright particles on top of the FeSe film . . 118
5.4 Growth rate inconsistency between the first and second FeSe layer (#157) on STO 119
5.5 Extra Fe deposition on monolayer FeSe film without post annealing . 122
5.6 ARPES measurement on monolayer FeSe 124
5.7 Comparison of the band structure of monolayer FeSe after one or two annealing cycles 125
5.8 Comparison of the momentum distribution curve along cut #1 and #2 126
5.9 Scanning tunneling spectroscopy of monolayer FeSe 128
5.10 Scanning tunneling spectroscopy of the second layer FeSe 129

6.1 XPS survey spectrum of a 2ML-thick FeSe film on STO 131
6.2 Fe $2p$ core level and CVV spectra 134
6.3 Valence band of various FeSe films and STO substrates 137
6.4 Core level shift and band bending 139

7.1 RHEED patterns of FeTe films grown on Se-etched STO for different flux ratios. 143
7.2 Influence of post annealing temperature on the quality of the FeTe thin film, according to RHEED 145

7.3 Evolution of the FeTe film morphology for different post annealing temperatures, monitored with STM. 146
7.4 Influence of growth temperature and post annealing time on FeTe monolayers on STO, monitored with STM 147
7.5 High quality tetragonal FeTe monolayer, grown on Te-etched STO . . 148
7.6 Thick FeTe film (#158) grown on a 1 UC thick FeSe film under Te rich growth condition. 150
7.7 Thick FeTe film (#159) grown on a 1 UC thick FeSe film on STO, grown at 333−341 °C 151
7.8 Thick 146 ML FeTe film (#245) grown on the $(\sqrt{13} \times \sqrt{13})$ reconstructed STO surface under Te rich growth condition 153
7.9 146 ML thick FeTe film (#245) grown on the Te ecthed $(\sqrt{13} \times \sqrt{13})$ reconstructed STO surface under optimal Fe:Te flux ratio 154
7.10 XRD 2θ-ω scan of a 146 ML thick FeTe film (#245) on Te-etched STO 155
7.11 XRR data of the 146 ML thick FeTe film (#245) on Te-etched STO . 156
7.12 RSM data of the 146 ML thick FeTe film (#245) on Te-etched STO . 157
7.13 Scanning Tunneling Spectroscopy of an FeTe monolayer film on Te-etched STO 158
7.14 Comparison of the monolayer and second layer FeTe film on STO . . 159
7.15 Atomically-resolved contrast variations in a 1 UC thick FeTe layer on STO 160
7.16 Bias-dependent atomically-resolved contrast variations. 162
7.17 XPS survey spectrum of a 1 UC thick FeTe film on STO 163
7.18 Stoichiometry determination of the FeTe films on STO from the XPS 165
7.19 Fe $2p$ core level and CVV spectra 169
7.20 Valence band of various FeTe films and STO substrates 170
7.21 Magnetic property measurement of the 146 ML thick FeTe film (#245) and of the Nb doped STO substrate 172

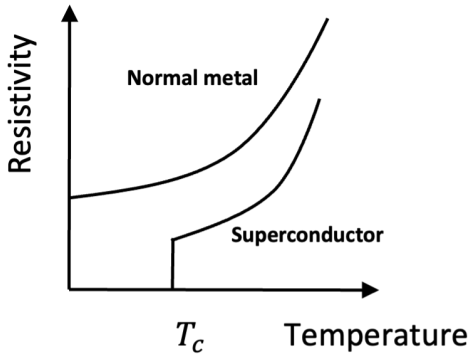
Chapter 1

Introduction

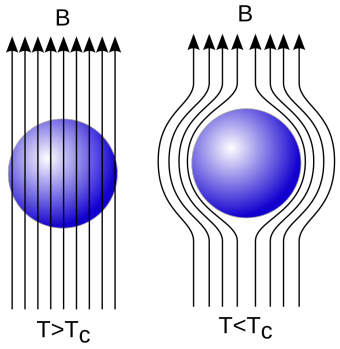
1.1 Conventional Superconductivity

Quite a few materials exhibit zero DC electrical resistance and perfect diamagnetism below a certain critical temperature T_c; this phenomenon is called superconductivity (Figure 1.1a and Figure 1.1b). Diamagnetism arises from the fact that in the presence of a magnetic field, a superconductors spontaneously generates a supercurrent or screening current at its surface to prevent the field from entering its interior. This is the so-called Meissner effect. Due to the superconductors' ability to carry electrical current without dissipation, superconducting coils have been commercialized very successfully to generate large magnetic fields. However, superconductors lose their superconducting property above a certain critical magnetic field (H_c).

Bulk elemental superconductors, originally discovered by Kamerlingh Onnes (1911), are classified as Type I superconductors. Type II superconductors were discovered in later years. These are characterized by an upper and a lower critical magnetic field. Superconductivity ceases to exist above the upper critical magnetic field (H_{c2}), where the superconductor becomes a normal metal. Below the lower critical magnetic field (H_{c1}), type II superconductors have zero DC resistance and are perfectly diamagnetic, just like the Type I superconductors. However, in-between



(a) Resistivity as a function of temperature of a normal metal and a superconductor.



(b) Type I superconductors become perfect diamagnets in the superconducting state (Jaworski, 2005).

Figure 1.1: Zero DC resisitivty and Meissner effect of a superconductor.

the lower and upper critical fields, Type II superconductors still have zero resistance but they are no longer perfectly diamagnetic. Here, magnetic fields penetrate the superconductor in the form of vortices, each of which carries a single flux quantum.

Over the last century, physicists have spent much effort to identify new superconductors, ideally those with a higher T_c and/or H_{c2}. The discovery of superconductivity in elemental metals such as mercury and lead (Onnes, 1911b,a) was soon followed by the discovery of superconducting alloys and compounds, such as NbN, Nb_3Sn, and Nb_3Ge, but T_c never exceeded 30 K until 1986. These compounds are indicated by the green circles in the discovery timeline plot in Figure 1.2.

Theories of superconductivity were developed during that same time. The London brothers, Fritz and Heinz London, derived their famous 'London' equation in 1935. Even though it had been derived from classic physics, it was able to explain the Meissner effect (London and London, 1935; Ashcroft and Mermin, 1976). In the 1950's, Ginzburg and Landau developed a phenomenological theory of superconductivity where they expanded the expression for the free energy of a superconductor in terms of an order parameter and its derivatives, and then minimized the free energy with respect to that same order parameter (Ginzburg,

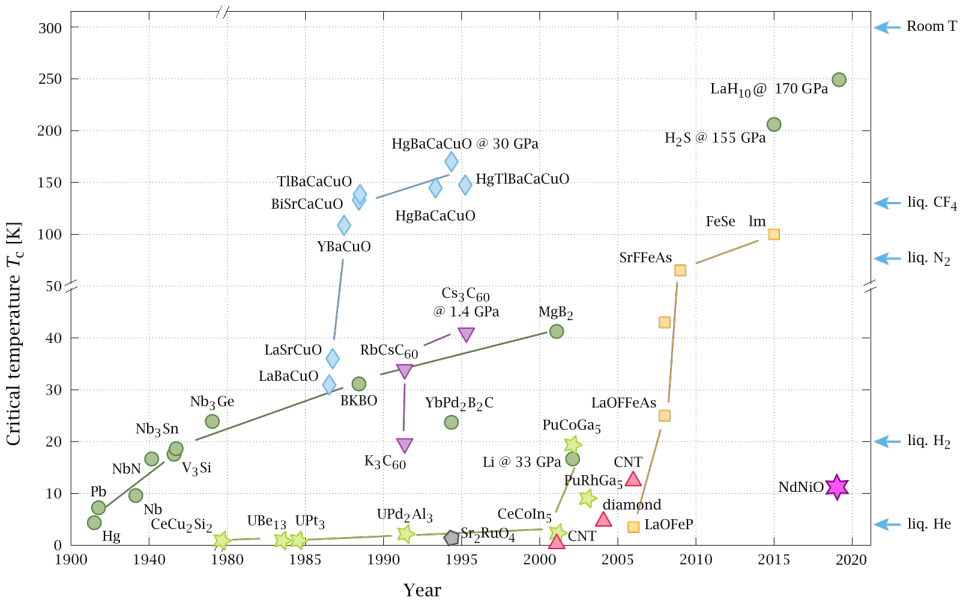


Figure 1.2: Timeline of the discovery of superconductors versus T_c: High-temperature superconductors typically refer to materials that have a critical temperature exceeding the boiling point of liquid nitrogen (77 K). Most of these materials are classified as unconventional superconductors, with the exception of some high-pressure materials, such as H_2S and LaH_{10} (PJRay, 2015).

1950; Ashcroft and Mermin, 1976; Tinkham, 2004). The theory allows for the spatial variation of properties within the superconductor and naturally introduces the concept of a superconducting coherence length. The order parameter was later identified as the superfluid density $n_s(\vec{r})=|\Psi(\vec{r})|^2$, where $\Psi(\vec{r}) = |\Psi(\vec{r})|e^{i\phi}$ is a complex wavefunction that allows for the existence of a supercurrent. By connecting the supercurrent density from Ginzburg-Landau theory with the London expression $\vec{J} = -(n_s e^2/m)\vec{A}$ ($\vec{A}$ is the vector potential), it was possible to firmly establish the connection between the order parameter $|\Psi(\vec{r})|^2$ and the superfluid density. It also indicated that the superconducting current is carried by electron pairs.

Bardeen, Cooper and Schrieffer developed the microscopic theory (BCS theory) of superconductivity in 1957 (Cooper et al., 1957). The theory demonstrated that no matter how weak the attractive interaction between the electrons around the Fermi level is, it will always lead to the formation of a two-electron singlet bound state. The total angular momentum of this 'Cooper pair' is zero, which is usually referred to as

isotropic s-wave pairing. The attractive interaction is made possible by the coupling to the phonon system, and only involves electrons within a very narrow energy shell of $\hbar\omega_{\mathrm{D}}$ (ω_{D} is the Debye frequency) around Fermi level. The pairing interaction opens up a finite energy gap Δ in the energy spectrum, which prevents electrons from scattering elastically as there are no single-particle states available to scatter into. The superconducting state can be viewed as a Bose-Einstein condensate of the individual Cooper pairs. The Cooper pair wavefunction $\Psi(\vec{r})$ acquires rigidity in the sense that it is macoscopically coherent with a globally rigid phase. The latter explains many superconducting phenomena such as Meissner screening, flux quantization, and the Josephson effect.

Key (mean-field theory) predictions of the BSC theory are:

$$\Delta(T=0) = 1.764 k_{\mathrm{B}} T_{\mathrm{c}} \tag{1.1}$$

$$k_{\mathrm{B}} T_{\mathrm{c}} = 1.134 \hbar\omega_{\mathrm{D}} e^{-1/(N(0)V)} \tag{1.2}$$

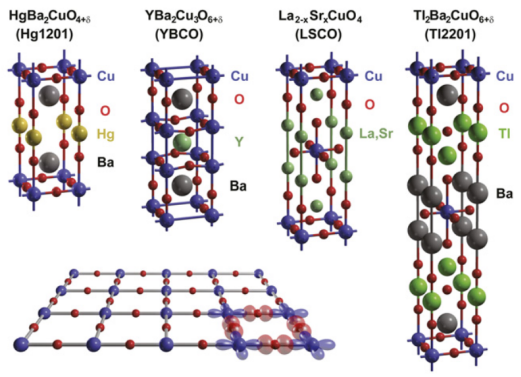
$N(0)$ is the density of states at the Fermi level and V is the electron-phonon coupling constant. A large number of metal elements satisfy the BCS gap equation quite well. These are usually called conventional superconductors. Physicists tried to enhance T_{c} by fabricating material with higher ω_{D} and $N(0)$, but the T_{c} of most conventional superconductors remains 30 K with only a few notable exceptions. Physicists later noticed the remarkable connection between Ginzburg-Landau theory and the BCS theory (Ashcroft and Mermin, 1976). In particular, when the temperature is very close to T_{c}, the BSC theory can be reduced to the Ginzburg-Landau theory (Gor'kov, 1959).

1.2 Unconventional Superconductors: Cuprates

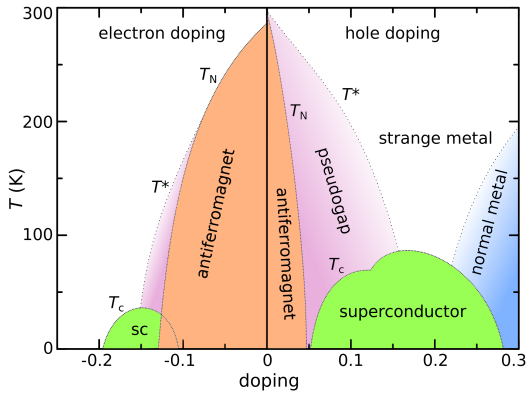
Following the predictions of BCS theory, physicists started to investigate materials with strong electron-phonon coupling. This could potentially be realized in doped

perovskite materials with narrow metallic bands and strong Jahn-Teller deformations. Following this strategy, Johannes Georg Bednorz and Karl Alex Müller discovered that lanthanum barium copper oxide was a superconductor with $T_c = 35$ K, higher than all the other superconductors found previously (Bednorz, J George and Müller, K Alex, 1986). This success was recreated in many other cuprates including $La_{2-x}M_xCuO_4$ (LMCO, with M = Ba, Sr, Ca), $YBa_2Cu_3O_{7-y}$ (YBCO) and others that are indicated by the blue diamond symbols in Figure 1.2. The T_c of YBCO was even higher than the boiling point of liquid nitrogen (77 K), which was a major breakthrough as it would no longer be necessary to use expensive liquid He refrigerant to enter the superconducting phase.

The cuprates all have similar crystal structures (Figure 1.3a): the superconductivity takes place in 2D CuO_2 layers, which are separated by insulating layers that provide the dopant charges. The undoped cuprates are antiferromagnetic (AFM) insulators and only become superconducting with a certain doping range. A generic phase diagram of the cuprates is shown in Figure 1.3b. Soon after the discovery of the high T_c cuprates, it became clear that the physics of these systems in dominated by strong electron correlation and spin fluctuations. Carrier doping introduces magnetic frustration as illustrated in Figure 1.4 and suppresses AFM order. In light of



(a) Sandwich-like structure of the cuprate superconductors (Barišić et al., 2013)



(b) Phase diagram of a typical cuprate compound (Motzkau, 2013)

Figure 1.3: Generic properties of cuprates.

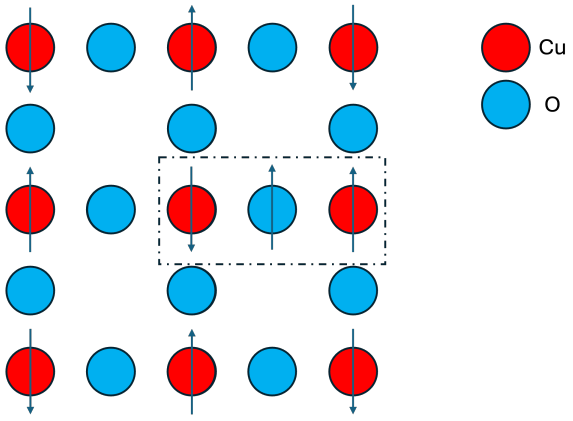


Figure 1.4: Schematic of magnetic frustration when doping the cuprates

the close proximity of the AFM and superconducting phases, researchers began to explore the possibility that the pairing interaction is mediated by spin fluctuations or paramagnons, as opposed to the conventional phonon picture (Scalapino, 2012). Due to the strong electron-electron repulsion in these compounds, electrons can only pair up if they can avoid double occupancy, which can only be realized in a non-zero angular momentum state. This situation is fundamentally different from that in conventional superconductors where the (time-retarded) interaction is on-site. It is now generally accepted that the Cooper pairs in cuprates pair up in the $l = 2$ angular momentum channel, thus implying d-wave pairing (Tsuei and Kirtley, 2000). Still, the mechanism of high temperature superconductivity in the cuprates is not fully understood. For further discussion, see Ref. (Plakida, 2012).

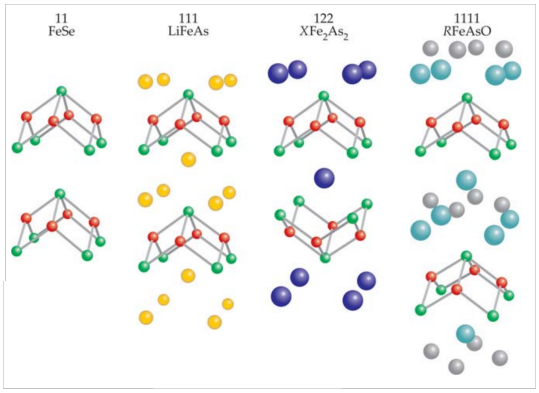
1.3 Iron-Based Superconductors

Magnetism is supposed to kill superconductivity, as it may flip the spin and break the singlet Cooper pairs. It therefore was a great surprise to discover superconductivity in iron-based compounds. In 2006, Kamihara and collaegues discovered superconductivity in LaFePO with a T_c about 5 K (Kamihara et al., 2006). Two years later they found that fluorine-doped LaFeAs reaches a T_c of about 25 K

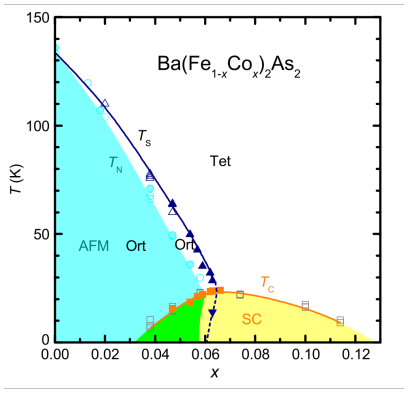
(Kamihara et al., 2008). This led to the discovery of a new class of doped high-temperature superconductors, as indicated by the orange square symbols in Figure 1.2.

Based on their chemical composition, Fe-based superconductors can be grouped into the pnictide family (FePn, Pn: As/P) and chalcogenide family (FeCh, Ch:S/Se/Te). Based on the element ratio, they can be classified as: LaFeAsO(1111), $M\mathrm{Fe_2As_2}$(122), MFeAs(111), FeSe(11), $\mathrm{Sr_2}M\mathrm{O_3FePn}$(21311), and the defect structure $\mathrm{A_{0.8}Fe_{1.6}Se_2}$ (122^*) (Stewart, 2011). Similar to the cuprates, these materials have a quasi 2D crystal structure, where superconductivity takes place in layers made of Fe-Pn (Fe-Ch) tetrahedrons. Figure 1.5a shows the crystal structure of the pnictide and chalcogenide families. Their superconducting properties are dominated by multiple Fe $3d$ bands crossing the Fermi level. This situation is far more complex than that of the cuprates, which are single-band ($3d_{x^2-y^2}$-$2p$ hybridized) systems. Interestingly, the phase diagram of the Fe-based superconductors is quite similar to that of the cuprates in the sense that the undoped parent compounds are generally antiferromagnetic while superconductivity is established via chemical doping. An important difference is that the parent compounds are metallic, as opposed to the Mott insulating behavior of the cuprates, while some of the undoped compounds are already superconducting. In some cases, (spin density wave) magnetism may even co-exist with SC (Chen et al., 2009). These Fe-based superconductors generally exhibit a structural transition from a tetragonal high-temperature phase to a low-temperature distorted orthorhombic structure, as illustrated for $\mathrm{Ba(Fe_{1-x}Co_x)_2As_2}$ in Figure 1.5b.

Considering the remarkable similarity of the cuprate and pnictide (chalcogenide) phase diagrams, as well as their high T_c, it seems natural to attribute Cooper pair formation to spin fluctuations. However, there are essential differences that make the Fe-based superconductors special. First, the electron-correlation strength is much weaker than in the cuprates, as was shown by Yang et al. and Vilmercati et al., see Figure 1.6a (Yang et al., 2009; Vilmercati et al., 2012). As a result, the order parameter might still have the s-wave symmetry. In fact, the order parameter

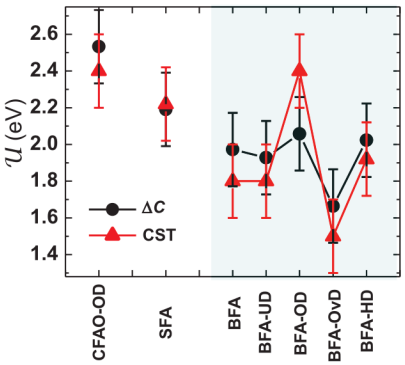


(a) Crystal structure of the FeSCs families (Chubukov and Hirschfeld, 2015)

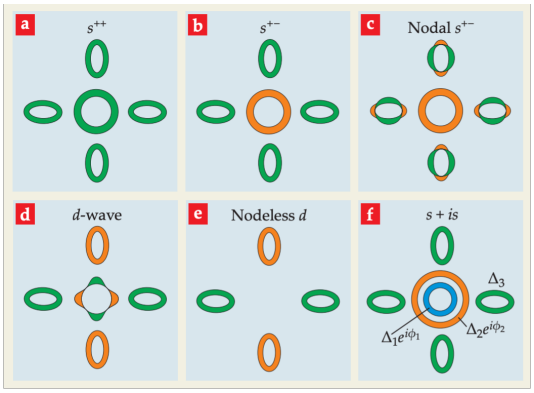


(b) Phase diagram of $Ba(Fe_{1-x}Co_x)_2As_2$ (Nandi et al., 2010)

Figure 1.5: Generic properties of FeSCs.



(a) The effective two-hole repulsion energy U for different Fe pnictides: Δc and CST labels are data from a rough estimation based on the location of the centroids of the Auger spectrum, and the fitting of the Auger spectrum using the Cini-Sawatzky theory (CST), respectively. With bandwidth $W = 6$ eV, $U/W = 0.3$, indicating weak correlations (Vilmercati et al., 2012).



(b) Schematics of different gap symmetries: The color indicates the phase of $\Delta(\vec{k})$. (a) isotropic s^{++} as in BCS theory. (b) s^{+-} gap on the hole and electron pockets of the Fermi surface are same in magnitude but opposite in phase (with π phase difference). Due to the presence of multiple orbitals, the gap may have angular dependence, such as (c) nodal s^{+-}, (d) d-wave, (e) nodeless d-wave, and (f) even more complicated cases with arbitrary phase differences (Chubukov and Hirschfeld, 2015).

Figure 1.6: Differences between the pnictide (chalcogenide) and cuprate superconductors.

symmetry of the pnictides is likely of the s^{+-} type, which is due to the presence of multiple Fermi surface pockets inside the Brillouin zone (Onari et al., 2010). Figure 1.6b illustrates the possible order parameter symmetries in such multi-pocket systems.

1.4 Single Layer of Iron Selenide on $SrTiO_3(001)$

Among the FeSCs, Iron Selenide (FeSe) has the simplest crystal structure, which makes it a good template to study the mechanism of superconductivity. Bulk FeSe has a T_c about 8 K (Hsu et al., 2008), which can be enhanced by applying high pressure (Medvedev et al., 2009; Sun et al., 2016), intercalating chemical dopants into the van der Waals gap, see, *e.g.*, $(Li_{1-x}Fe_x)OHFeSe$ and $K_xFe_{2-y}Se_2$) (Chen et al., 2016; Lu et al., 2015), or by applying an electric field (Shiogai et al., 2016). The resulting T_c is typically in the 30−40 K range. Surprisingly, a one-unit-cell thick FeSe layer or 'monolayer' FeSe grown epitaxially on a $SrTiO_3(001)$ or 'STO' substrate revealed a spectacular increase of T_c to about 65 to 80 K, according to *in-situ* ARPES (Lee et al., 2014; He et al., 2013) and STM (Wang et al., 2012; Li et al., 2014) experiments. T_c determined from *ex-situ* transport (Wang et al., 2012; Zhang et al., 2014; Pedersen et al., 2020; Sun et al., 2014) and magnetic measurements (Zhang et al., 2014; Sun et al., 2014; Deng et al., 2014) is usually lower, presumably because the protective capping layer weakens the superconductivity. This one order of magnitude enhancement over the bulk T_c is puzzling, because T_c is expected to decrease with decreasing film thickness. For instance, when monolayer FeSe was grown on graphene, $T_c = T_{c0}(1 - d_c/d)$, where T_{c0} is the bulk T_c and $d_c = 7$ Å is the critical thickness below which superconductivity disappears (Song et al., 2011).

With the help of scanning tunneling spectroscopy (STS), Wang *et al.* found that only the first monolayer exhibits enhanced superconductivity, while a second layer of FeSe is semiconducting. STS of both monolayer and second layer FeSe on STO are shown in Figure 1.7. The first monolayer reveals a superconducting gap with coherence peaks at ±9 and ±20.1 meV while the second layer exhibits a gap

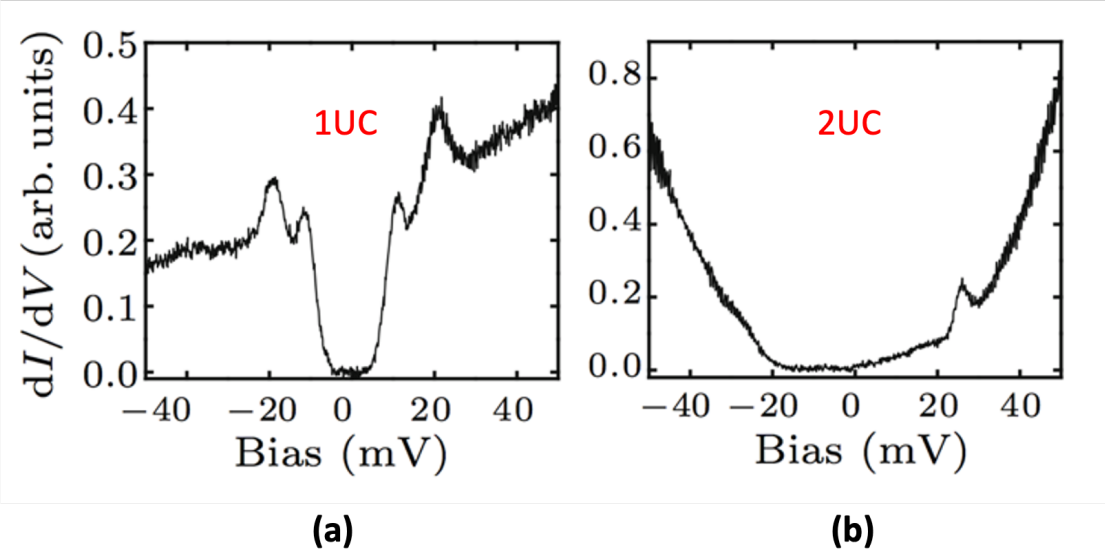


Figure 1.7: Scanning tunneling spectrum of the monolayer and double layer FeSe film on STO: (a) Monolayer FeSe displays a superconducting gap with coherent peaks at ±9 and ±20.1 meV; (b) The second layer FeSe reveals an asymmetric semiconducting gap (Wang et al., 2012).

that is no longer centered at the Fermi energy. The latter is reminiscent of an n-type semiconductor gap. This result suggests that the FeSe/ STO interface plays a crucial role in the enhancement of T_c. The next step is to understand what is so special about STO and what would be the crucial step towards achieving high T_c. A particularly exciting prospect is to control the superconducting transition temperatures via interface engineering.

The lattice parameters of bulk STO and FeSe are 3.90 and 3.77 Å, respectively, thus the FeSe monolayer is likely under a 3% tensile strain. However, similar T_c values were obtained when monolayer FeSe was grown on $KTaO_3$ (Peng et al., 2014a), $BaTiO_3$ (Peng et al., 2014b), STO(110) (Zhang et al., 2016a), $LaAlO_3$ (Huang et al., 2016), Anatase TiO_2 (001) (Ding et al., 2016), Rutile TiO_2 (100) (Rebec et al., 2017), $LaFeO_3$ (Song et al., 2021), even though the substrate lattice parameters are all different, especially in the case of STO (110), where the lattice constant b is enlarged by a factor of $\sqrt{2}$. Therefore, in-plane strain hardly seems to be an essential factor for achieving high T_c.

Doping is an another important factor to discuss as it plays an important role in the cuprates and other FeSCs. The Fermi surface of bulk FeSe exhibits a hole pocket centered at Γ and an electron pocket centered at M. Monolayer FeSe on STO, on the other hand, only exhibits an electron pocket at M while the hole pocket at Γ dropped below the Fermi level, as shown in Figure 1.8. This suggest a significant amount of carrier doping, presumably due to charge transfer from the STO substrate (Lee et al., 2014; Rebec et al., 2017).

Other STS and ARPES experiments on monolayer FeSe/STO revealed that the films have to be post annealed in order to obtain the superconducting phase. Post annealing further populates the electron pocket at Γ, which appears to be essential for obtaining high T_c (Li et al., 2014; He et al., 2013). Doping alone, however, cannot explain the high T_c of the monolayer films. Deposition of potassium atoms onto the FeSe/STO monolayer did not produce conclusive corroborative results and it is increasingly likely that these oxide substrates contribute to the T_c enhancement in a

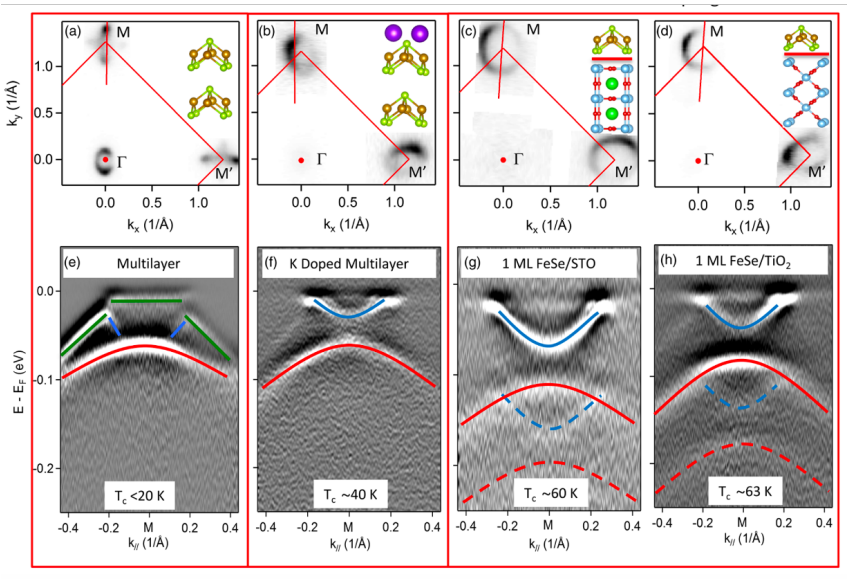


Figure 1.8: Fermi surface of (a) 60ML-FeSe, (b) K doped 3ML-FeSe/STO (001), (c) 1ML-FeSe/STO (001), (d) 1ML-FeSe TiO_2, (e)−(h) The respective bandstructures around M, measured along the red line cuts through the Fermi surface (Rebec et al., 2017).

rather special way (Yao et al., 2019; Shi et al., 2017; Miyata et al., 2015; Tang et al., 2016; Song et al., 2016). A summary of T_c and superconducting gap values for a variety of FeSe systems is given in Figure 1.9.

It is not fully understood in which way the STO substrate dopes the FeSe thin film, but it is quite likely that oxygen vacancies produced during the high-temperature annealing of the STO substrate in vacuum and selenium depletion during the post annealing of the FeSe films both play an important role. Tanaka and his colleagues grew FeSe monolayers on different STO(001) surface reconstructions and claimed a dome-like T_c behavior as function of the valence band location for each of these surface reconstructions, see Figure 1.10 (Tanaka et al., 2018, 2020b). In this study, the location of the valence band feature in STS is considered a measure of the doping level. It is generally believed that the reconstructions of the STO(001) surface are related to the different ordering patterns of the oxygen vacancies.

1.4.1 Interface phonon

Another important clue was provided by Lee *et al.* In their ARPES experiments, they found that the monolayer exhibited replica bands at 100 meV below the main band

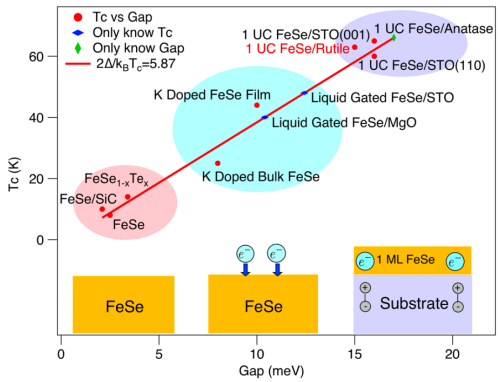


Figure 1.9: Linear fit of T_c and superconducting gap for a variety of FeSe systems. These systems are dived into three groups: Without doping and interface effect (red), chemical doping (light blue), substrate doping and interface effect (purple) (Rebec et al., 2017).

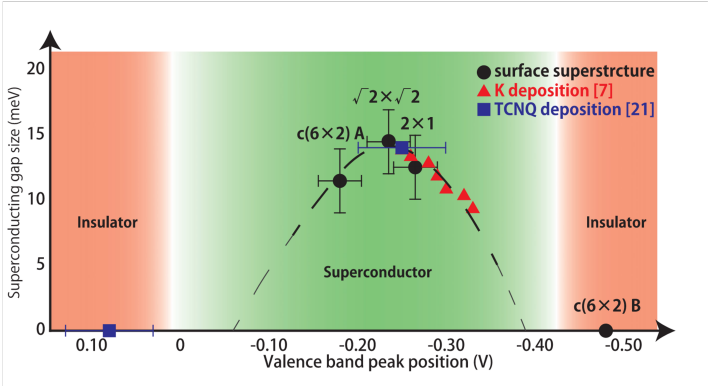
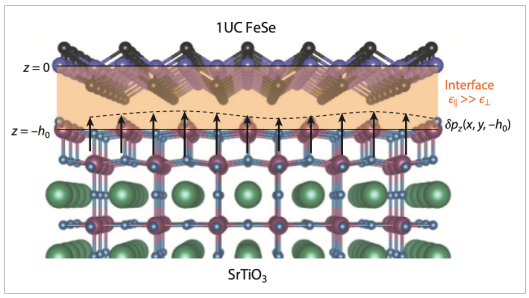


Figure 1.10: Dome-like behavior of FeSe monolayers on different reconstructed STO (Tanaka et al., 2020b).

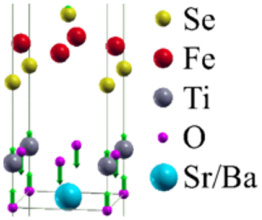
feature at the M-point (Figure 1.8 (g)). No such replica bands were seen on thicker FeSe layers (Lee et al., 2014). The prevailing interpretation of this replica band is that it is caused by a bosonic excitation from electron-phonon coupling intrinsically. Because the dispersion of the main band and replica band are identical, there is no significant momentum transfer in this process (Lee et al., 2014). One of the most promising models is that Cooper pairing in the FeSe layer is mediated by the Fuchs-Kliewer (FK) optical phonon of the STO substrate. In Lee *et al.*'s model, it is assumed that there is a single-layer of FeSe located at $z = 0$ and that there is a 2D array of oscillating dipole moments at the STO surface at $z = -h_0$; see Figure 1.11a. The dipole moments $\delta p_z(x,y,-h_0)$ are associated with the phonon excitation associated with the perpendicular vibrations of the Ti and oxygen atoms, and induce an electrostatic potential in the FeSe layer. The electron-phonon coupling in the FeSe layer would be proportional to the Fourier component of the potential, resulting in:

$$g(\vec{q}) = g_0 e^{-|\vec{q}|/q_0} \tag{1.3}$$

where $q_0^{-1} = h_0\sqrt{\frac{\varepsilon_\parallel}{\varepsilon_\perp}}$, $\varepsilon_\parallel$ and $\varepsilon_\perp$ are the in-plane and perpendicular dielectric constant in the interface region, respectively. If q_0^{-1} is large, the induced potential will be exponentially peaked at $q = 0$, or in other words, in the forward scattering direction. It can also be shown that the forward-focused interaction can enhance the



(a) Electrostatic model of the interface electron-phonon coupling model (Huang and Hoffman, 2017).



(b) Relevant STO phonon mode from *ab initio* calculations (Wang et al., 2016)

Figure 1.11: Interface phonon mechanism of superconductivity.

Cooper pairing for any pairing symmetry (Lee et al., 2014; Bulut and Scalapino, 1996; Johnston et al., 2014; Sandvik et al., 2004; Johnston et al., 2010; Varelogiannis et al., 1996; Aperis et al., 2011; Santi et al., 1996). When $T_c \ll \Omega$, which is true for FeSe, T_c can be evaluated from (Rademaker et al., 2016):

$$T_c = \frac{\lambda_m}{2 + 3\lambda_m}\Omega \propto \frac{g_0^2}{\Omega} \tag{1.4}$$

where $\lambda_m = g_0^2/\Omega^2$, Ω is the FK phonon frequency. Based on this electrostatic model of the interface electron-phonon coupling, T_c will be enhanced significantly when the interface has a large anisotropy $\varepsilon_\parallel \gg \varepsilon_\perp$ and a large distance between the superconducting layer and the dipole plane h_0.

The FK mode of the STO substrate involves the titanium (Ti) and oxygen (O) atoms oscillating vertically relatively to the plane of the film, This is illustrated in Figure 1.11b. The energy of this mode is about 92 meV from *ab initio* calculations (Wang et al., 2016), which agrees with the energy shift of the replica band in APRES (Lee et al., 2014). The relevant FK phonon mode spectra have also been obtained experimentally via high-resolution-electron-energy-loss-spectroscopy (HREELS) (Zhang et al., 2016b, 2018). The intensity of the relevant FK phonon mode in HREELS decays as the thickness of the FeSe film increases, which may explain why T_c can only be enhanced for FeSe films thinner than several unit-cells. Transmission

electron microscopy (TEM) and synchrotron X-ray diffraction experiments indicated that the STO surface is terminated by a double TiO_x layer. which is directly relevant for understanding the surface phonon spectra (Li et al., 2016a; Sims et al., 2019; Peng et al., 2020; Zou et al., 2016).

Similar replica band in ARPES were found for high T_c monolayer FeSe grown on $BaTiO_3$ (Peng et al., 2014b), TiO_2 (Figure 1.8 (d)) and $FeLaO_3$ (Song et al., 2021). A double FeO_x termination of $FeLaO_3$ was also found in TEM (Song et al., 2021). However, an exception was noted: monolayer FeS grown on $SrTiO_3$ exhibited a replica band and sufficient electron doping, but it did not show superconductivity (Shigekawa et al., 2019). Alternatively, the replica band observed in ARPES can also be explained by the interaction between photoelectrons and the substrate extrinsically, within the framework of semiclassical dielectric theory. The appearance of these replicas depends on the free electron density, particularly in two-dimensional confinement. Moreover, the intensity of the replicas in HREELS and ARPES is consistent with this model. Although this model does not diminish the importance of electron-phonon coupling. (Li and Sawatzky, 2018). Despite all these results, more experiments are needed to firmly elucidate the role of the surface phonons in enhancing T_c. In particular, there still is no consensus on the role of oxygen vacancy and non-ideal stoichiometry of the FeSe monolayer films.

1.4.2 The role of magnetism

The dome-like feature in the phase diagram of FeSe monolayers on STO is reminiscent of the phase diagrams of bulk cuprates and pnictides. It is thus reasonable to assert that the pairing mechanism in the FeSe monolayer is mediated by spin fluctuations. Even so, the Fermi surface of an FeSe monolayer on STO is quite different from those of bulk FeSe and pnictide superconductors. Since there is no hole pocket around Γ, the s^{+-} pairing symmetry seems unlikely unless considering the incipient band pairing (Huang and Hoffman, 2017; Bang, 2019). While neutron scattering experiments

of bulk FeSe revealed strong spin fluctuations below the orthorhombic transition temperature, no such experiments can be performed on monolayer FeSe/STO. Neither is there any evidence of magnetic ordering in these films (Huang and Hoffman, 2017).

Interestingly, a monolayer FeTe on STO, which is structurally very similar to the FeSe/STO system, does not show any superconductivity at all. Neither does bulk FeTe. The monolayer film becomes superconducting, however, when forming a solid solution with Se as in $FeTe_{1-x}Se_x$; see (Figure 1.12) (Li et al., 2015; Han et al., 2017; Maheshwari et al., 2015). Actually, AFM ordering was found in bulk FeTe, which led to the idea that superconductivity in FeTe is preempted by antiferromagnetism. (Bao et al., 2009; Maheshwari et al., 2015; Fang et al., 2008; Yeh et al., 2008).

The pairing symmetry in monolayer FeSe on STO is also an open question. ARPES measurements found an almost isotropic energy gap (Zhang et al., 2016c). Quasiparticle interference imaging (QPI) revealed the existence of in-gap Bogoliubov bound states and absence thereof near magnetic and non-magnetic defects, respectively (Fan et al., 2015). These results suggest ordinary *s*-wave pairing, but more evidence is needed. It is also possible, and in fact quite likely, that several bosonic

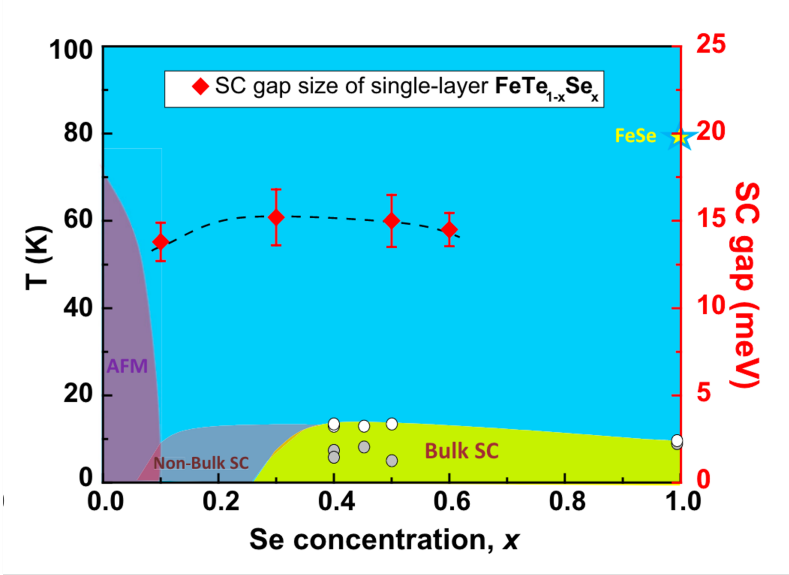
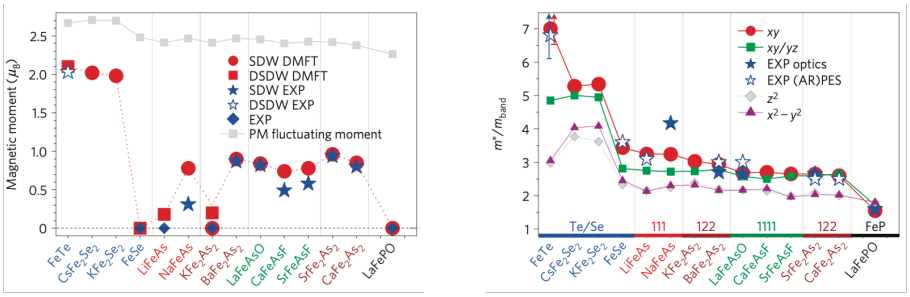


Figure 1.12: Phase diagram of $FeTe_{1-x}Se_x$ (Li et al., 2015).

channels conspire to boost T_c in the FeSe monolayer (Rademaker et al., 2021). For further discussion, see (Huang and Hoffman, 2017).

1.4.3 Electron correlation

Establishing the role of electron correlations in determining the pairing symmetry and mechanism of high temperature superconductivity is always important. The chalcogenides are generally believed to be more (less) correlated than the pnictides (cuprates). They also exhibit different magnetic properties, for instance, FeSe does not exhibit magnetic ordering, see Figure 1.13. Theoretically, the correlation strength seems related to the height difference between the pnictide/chalcogenide atoms and the Fe layer (Acharya et al., 2021; Choi and Choi, 2019; Fukaya et al., 2018), but there is no experimental evidence to support this claim. On the other hand, TEM measurements indicated an increase in the Ti-Se distance at the interface following post annealing, which is the necessary step to obtain high T_c (Li et al., 2016a). It is not clear yet how any of this relates to a change in correlation strength.



(a) Magnetic moment of FeSCs from theoretical calculation and experiment data

(b) Renormalization of effective mass in $3d$ orbitals of FeSCs from theoretical calculation and experiment data

Figure 1.13: Magnetic moment and renormalization of mass in FeSCs (Yin et al., 2011).

1.5 Scope of the Thesis

With so many unsettled questions, it first seems necessary to acquire full understanding of the normal state properties before delving into the mechanistic details of superconductivity. In this thesis, we focus our attention on the role of the substrate and precise stoichiometry of the optimally doped thin films, Recent studies indicated that prolonged post annealing may not be a necessary step as long as one supplies a small excess amount of Fe following the growth of the FeSe layer (Liu and Zou, 2020; Hu et al., 2018). This indicates that Fe vacancies may be detrimental for establishing superconductivity. We focus our attention on establishing well defined reproducible procedures for the preparation of the STO substrates. Our next goal is to grow high quality FeSe/STO and FeTe/STO interfaces with well controlled stoichiometry, as determined from STM and XPS. In particular, we show that as-grown and post annealed thick films are generally Fe deficient, which directly affects the efficacy of the non-local screening channels in XPS. This produces a useful XPS fingerprint signaling the presence of Fe vacancies. We use Auger electron spectroscopy to monitor the changes in electron correlation strength in the monolayer and bulk forms of FeSe and FeTe. Our results indicate that electron correlations in FeSe and FeTe are indeed stronger as compared to the pnictide superconductors, but we also found intriguing differences in the dynamics of core-hole screening between FeSe and FeTe. Finally, we measured the Fermi surface and band structure of the monolayer FeTe/STO and FeSe/STO interfaces with ARPES. While the FeTe/STO data need more analysis, we can state that the FeSe films are optimally doped.

The organization of this dissertation is as follows. Chapter 2 will first describe the Ultra High Vacuum system and Molecular Beam Epitaxy method for film growth, and all the apparatus and techniques that have been used in this research, including STM, XPS, RHHED, LEED, ARPES, XRD and magnetic measurements. Our main emphasis will be on STM and XPS. We will explain how one determines the

stoichiometry of the FeTe thin films via core level spectroscopy and how one can measure the electron correlation strength via Auger spectroscopy.

Chapter 3 focuses on the STO substrate preparation. Depending on the substrate treatment, *e.g.*, acid etching, vacuum annealing, oxygen annealing, and selenium etching, one can obtain a variety of surface reconstructions with different concentrations of oxygen vacancies. By comparing AC and DC current heated samples, as well as samples subject to thermal gradients, we found evidence for electromigration across the substrate. Se etched STO substrates were found to exhibit the least amount of oxygen vacancies and provided excellent terrace morphology for the growth of atomically flat FeSe monolayers.

Chapter 4 briefly discusses the bulk phase diagram of FeSe. We then provide details on how to control the growth mode of the FeSe thin films by via varying substrate temperature and Fe/Se flux ratio. Their stoichiometry will be determined by XPS. STM images indicate that the monolayer and bilayer films exhibit different domain-wall structures that are possibly related to the different strain misfit and composition within each layer. The lattice parameters of thick FeSe films on STO are studied with XRD, showing that these films are fully relaxed. As grown thick film contain a fairly large amount of Fe vacancies. Post annealing vastly improves the film morphology and reduces the number of vacancies via Se depletion, but it also produces magnetic precipitates, as measured via SQUID magnetometry. This is indicative of phase separation between (possibly) stoichiometric FeSe and Fe deficient precipitates.

Chapter 5 focuses on the characterization of monolayer FeSe films on STO. The surface morphology will be presented from STM images and a superconducting gap is found in STS. The stoichiometry of the monolayer film will be characterized by XPS. ARPES indicates the formation of the electron pocket at the M point of the Brillouin zone, consistent with previous studies. Interestingly, post annealing does not seem to increase the number of oxygen vacancies in the STO surface layer, suggesting that the FeSe films are self-doped by virtue of their increased Fe content.

Chapter 6 mainly discusses the core level and Auger spectra of single layer FeSe and bulk FeSe on STO. The survey scan will be shown first. We provide a detailed analysis of the Fe $2p$ core level spectrum and its correlation with the Fe-vacancy content. We will use the Auger spectrum to elucidate the strength of electron correlations in these materials.

Chapter 7 focuses entirely on the FeTe system, and especially monolayer FeTe on STO. Only very few studies on FeTe monolayers have been reported so far. We provide the optimum growth condition and STM characterization of both monolayer and bulk FeTe thin films on STO. The stoichiometry of the films will be provided from XPS. The two components of Fe $2p$ level will be compared to those of FeSe, and electron correlation will again be analyzed on the basis of the Auger spectra. Finally, we measured the Fermi surface of monolayer FeTe with ARPES.

The conclusions of our work will be summarized in Chapter 8, along with recommendations for future studies.

Chapter 2

Experimental Methods

2.1 Ultra High Vacuum and Molecular Beam Epitaxy

To study the properties of a surface or thin film using surface analytical techniques, one needs to make sure that the surface remains atomically clean for the duration of the experiment. Contaminants in a surface science experiment mainly originate from the residual gas molecules in the vacuum chamber. The flux I of particles impinging on the surface is given by (Oura et al., 2003):

$$I = \frac{p}{\sqrt{2\pi m k_{\mathrm{B}} T}} \tag{2.1}$$

where p is the pressure and m is the mass of the ambient molecules; k_{B} is Boltzmann's constant and T is the temperature. Then the time τ needed to form an adsorbate layer will be:

$$\tau = \frac{n_0}{I} = \frac{n_0 \sqrt{2\pi m k_{\mathrm{B}} T}}{p} \tag{2.2}$$

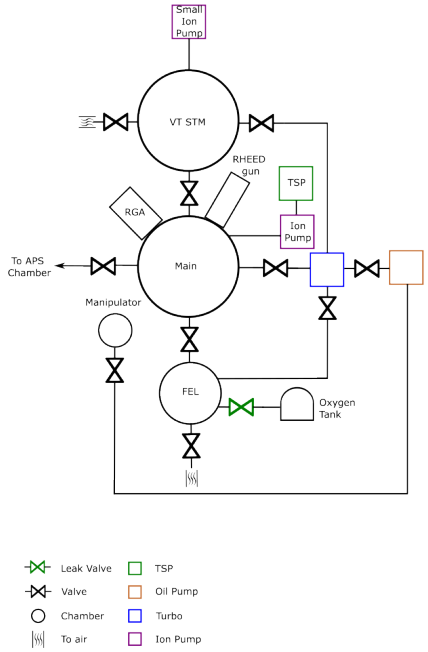
where n_0 is the number of atoms per unit area. For instance, assuming a sticking coefficient of one, it takes about one hour to form a monolayer of contaminants at 10^{-9} mbar. Thus, ultra high vacuum or UHV ($p < 10^{-9}$ mbar) is required to keep

samples as clean as possible. Our chamber typically operates in the low 10^{-10} to 10^{-11} mbar range. UHV is maintained by a combination of vacuum pumps. The system is initially pumped down with a mechanical pump until a pressure of 10^{-3} mbar is reached. Then, the turbo-molecular pump is turned on to pump the system to about 10^{-8} mbar while the mechanical pump keeps running to maintain a 10^{-2} to 10^{-3} mbar fore-line pressure for the turbo pump. Ultrahigh vacuum is achieved after thoroughly baking the system for 24 to 48 hours with the additional help of an ion pump and titanium sublimation pump. During normal operation, the turbo pump is valved off. Because a turbopump generates mechanical vibrations, it is shut down during STM experiments.

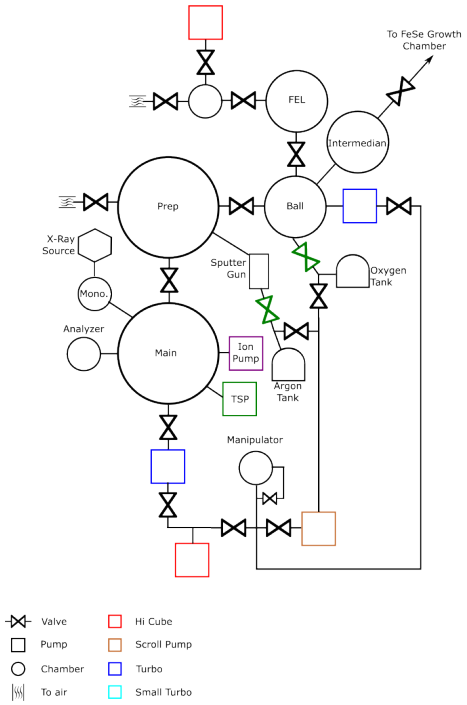
Ion pumps are always running during normal operations to capture residual gases that are constantly being released from the chamber walls and hot filaments. An ion pump ionizes residual gas molecules and accelerates them with electric field to sputter the electrodes inside the pump. The sputtered material (typically titanium) then reacts with and/or traps residual gas molecules so as to maintain 10^{-10} to 10^{-11} mbar pressure. Titanium sublimation pumps (TSP) are also used to reached the ultimate low pressure of about 10^{-11} mbar. Here, titanium is sublimated from the Ti filament onto a metal shield to create a fresh and very reactive thin Ti deposit that captures residual gases.

Schematic drawings of our UHV chambers are shown in Figure 2.1. FeSe and FeTe samples were grown in the 'FeSe Chamber', which was directly connected to the Advanced Photoelectron Spectroscopy (APS) core facility. In addition, we used a vacuum suitcase to transfer samples between the FeSe chamber and low-temperature Scanning Tunneling Microscopy (STM) chamber. The latter is also connected to an Angle-Resolved Photoemission Spectroscopy (ARPES) chamber.

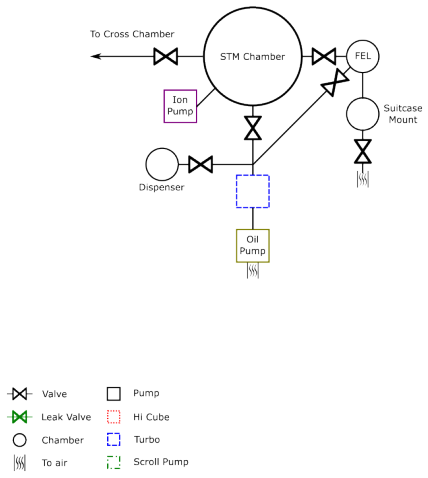
Effusion cells loaded with Fe, Se, and Te were used to grow epitaxial FeSe and FeTe thin films with Molecular Beam Epitaxy (MBE). The source material is contained within a ceramic crucible mounted inside a hot filament coil, and evaporated with an accurately controlled rate with the help of a thermocouple and PID temperature



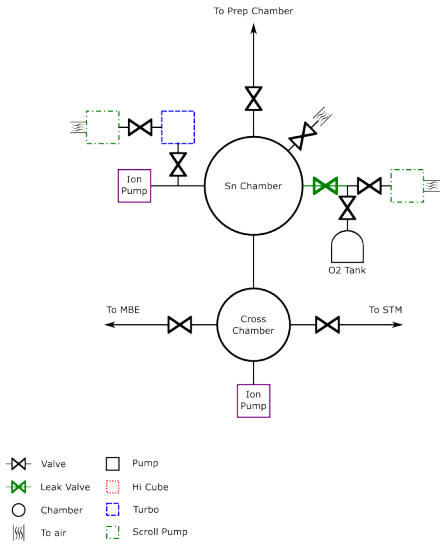
(a) FeSe Growth Chamber



(b) APS Chamber

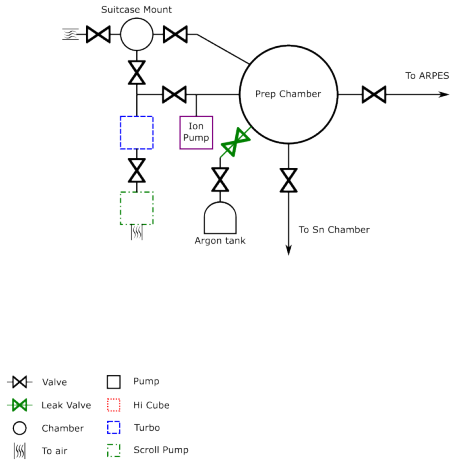


(c) STM Chamber

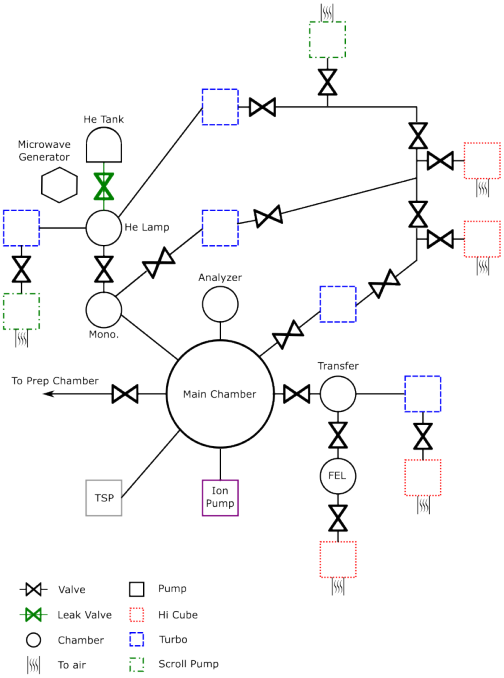


(d) Sn Chamber

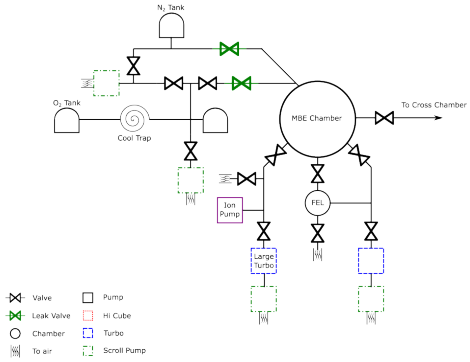
Figure 2.1: Schematic of UHV chambers



(e) Prep Chamber



(f) ARPES Chamber



(g) MBE Chamber

Figure 2.1: Schematic of UHV chambers continued

controller. The particle flux I is given by (Oura et al., 2003):

$$I = \frac{P(T)A}{\pi L^2 \sqrt{2\pi m k_{\mathrm{B}} T}} \tag{2.3}$$

where $P(T)$ is the equilibrium vapor pressure of the material, A is the evaporation/sublimation area, L is the distance from the source to the substrate, and m is the mass of the molecules. With the help of equilibrium vapor pressure tables, one can roughly estimate the required effusion cell temperature to obtain desired growth speed (typically 0.1−1 ML/min). The vapor pressure of Se is given in Figure 2.2: a 10^{-4} to 10^{-5} mbar Se flux requires an effusion cell temperature of about 400−440 K (127−167 °C). Because Se and Te easily condensate around the aperture of the effusion cell, a hot-lip effusion cell is designed such that the filament provides a higher temperature around the aperture. We modified a low-temperature effusion cell and mounted an extra filament around the aperture to mimic the operation of a commercial hot-lip cell. After prolonged usage, Se and Te would still clog the aperture, which in turn reduces the Se/Te flux, growth rate and composition of the film. The change in growth rate is readily noticed in STM and the aperture was cleaned as needed. The stoichiometry of the films is currently being determined with X-ray Photoelectron Spectroscopy (XPS). The source temperatures in our experiments were $\mathrm{T_{Fe}} = 1250$ °C, $\mathrm{T_{Se}} = 160{-}200$ °C, and $\mathrm{T_{Te}} = 330{-}370$ °C, which resulted in a growth rate about 5 minutes per monolayer. Here, a monolayer is defined as a single van der Waals slab of FeSe or FeTe. Details of the growth conditions will be discussed in Chapter 4−7.

Apart from MBE, there exist other methods for growing thin films in UHV. In Solid Phase Epitaxy (SPE), amorphous material is first deposited at low temperature and subsequently annealed at higher temperature to achieve crystallinity. In Chemical Vapor Deposition (CVD), gas phase materials reach a hot substrate, decompose, and react to form the desired material. This is usually a high pressure process although it can be also be done under UHV conditions. Growth rates in CVD can be much

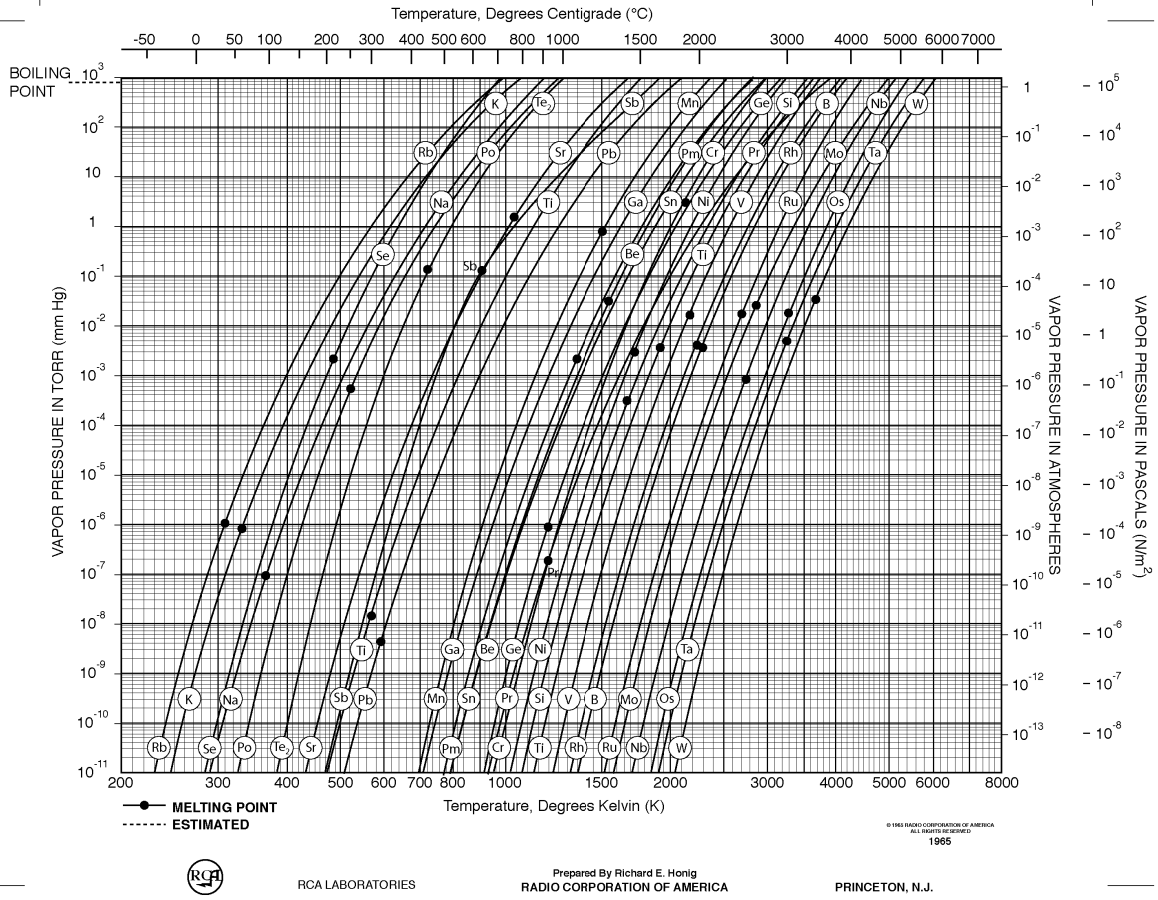
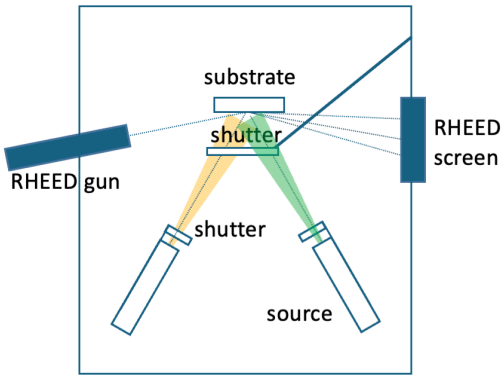


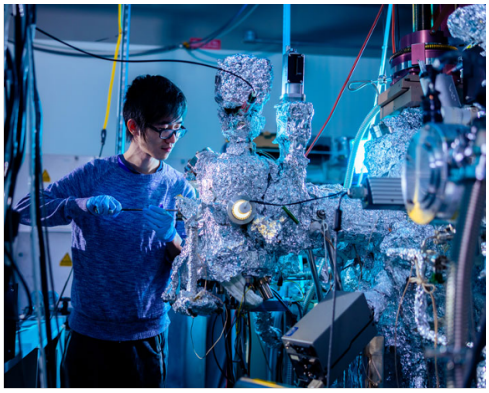
Figure 2.2: The vapor pressure of Se

higher than in MBE. Some materials may not suitable for MBE because their vapor pressures are extremely high or low and therefore difficult to control. Pulsed laser deposition (PLD) uses laser ablation of a target material which then condenses onto a crystalline substrate. PLD is the preferred growth method for epitaxial thin film materials with complex chemical compositions, such as ternary or quaternary oxide compounds, though its crystallinity may not be as good as that of MBE. Comparing with SPE, CVD, and PLD, MBE provides the utmost control of thickness, structure and composition, but it is also the most difficult process to master and control. Arguably, it is the least economic method in terms of time, money, and throughput.

Our MBE chambers are all equipped with Reflection High Energy Electron Diffraction (RHEED), which allows for real time monitoring of the thin film structure, morphology, and growth rate (if one can see RHEED intensity oscillations). A schematic of the experimental MBE setup and photo of our home built FeSe growth chamber is shown in Figure 2.3a and Figure 2.3b, respectively.



(a) Sketch of a typical MBE set up



(b) Photo of the home-built FeSe growth chamber

Figure 2.3: Molecular Beam Epitaxy

2.2 Scanning Tunneling Microscopy

Scanning Tunneling Microscopy (STM) is a well-developed analytical technique to investigate the morphology, atomic corrugation, and electronic structure of a surface. The operating principle of STM is based on quantum tunneling: when a sharp metal tip approaches the surface to within nanometer distances, a tunneling current will flow between the tip and the sample, depending on the applied voltage, even if there is no physical contact.

The simplest model to describe this phenomenon employs a simple one-dimensional rectangular tunneling barrier along the z-direction normal to the sample plane. The Schrödinger equation is given by

$$-\frac{\hbar^2}{2m_{\mathrm{e}}}\frac{\partial^2\Psi(z)}{\partial z^2} + U(z)\Psi(z) = E\Psi(z) \tag{2.4}$$

where $U(z)$ has a constant value within the gap region, *i.e.*, in-between the tip and the sample, $\Psi(z)$ is the wave function of the electron, m_{e} is the mass of the electron, and E is the energy of the electron. If the gap size is d, it can be shown that tunneling current density has the expression:

$$I \propto e^{-2\kappa d} \tag{2.5}$$

where $\kappa = \sqrt{2m_e(U-E)}/\hbar$. The derivation of this formula is given in introductory quantum mechanics textbooks. Importantly, the current density decays exponentially as the distance between the tip and the surface d increases. This makes the STM extremely sensitivity to height corrugations on the surface.

John Bardeen modeled the tunneling process using more realistic wavefunctions (Bardeen, 1961; Wiesendanger, 1994). He first assumed that the tip and the surface are far away so that they can be described by two independent tip(surface)-vacuum systems. Within each system, the wavefunction of the tip(sample) $\Psi^{\mathrm{T}}(\Psi^{\mathrm{S}})$ decays into vacuum as expected from the solution of the Schrödinger equation for a step-like

potential $U^{\mathrm{T}}(U^{\mathrm{S}})$. He then reduces the spacing between the two subsystems to the tunneling regime. Employing Fermi's golden rule, the transmitted current from the tip to the sample is given by:

$$I_{\mathrm{ST}} = \frac{2\pi}{\hbar}|M_{\mathrm{ST}}|^2 \frac{dN}{dE_{\mathrm{S}}} \tag{2.6}$$

where $\frac{dN}{dE_{\mathrm{S}}}$ is the local density of states of the sample. The tunneling matrix element M_{ST} is given by:

$$M_{\mathrm{ST}} = \int \Psi_{\mathrm{S}}^{*} H_{\mathrm{T}} \Psi_{\mathrm{T}} dz = M_{\mathrm{TS}} \equiv M \tag{2.7}$$

H_{T} is the transfer Hamiltonian. The net tunneling current I includes tunneling contributions in both directions:

$$I = I_{\mathrm{ST}} - I_{\mathrm{TS}} = \frac{4\pi e}{\hbar} \int |M|^2 n_{\mathrm{T}}(\epsilon) n_{\mathrm{S}}(\epsilon + eV)[f_{\mathrm{T}}(\epsilon) - f_{\mathrm{S}}(\epsilon + eV)] d\epsilon \tag{2.8}$$

where $n(\epsilon)$ is the density of states of the tip (T)/sample (S) with a continuous energy spectrum, and $f(\epsilon)$ is the Fermi-Dirac distribution. In general it is not an easy task to solve this equation. Tersoff and Hamann (1983, 1985) assumed that the wave function of the tip has S wave symmetry (Tersoff and Hamann, 1983, 1985; Wiesendanger, 1994). At low temperature and low bias, the tunneling current then simplifies to

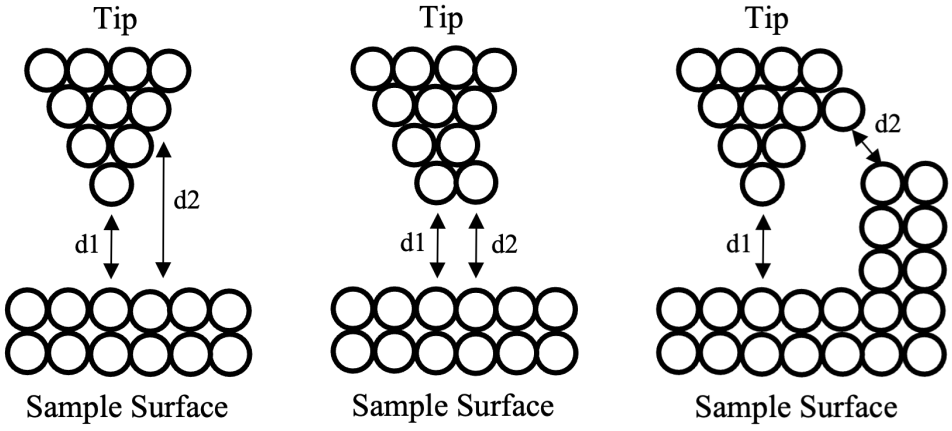
$$I \propto V n_{\mathrm{T}}(\epsilon_{\mathrm{F}}) e^{2\kappa R} n_{\mathrm{s}}(\epsilon_{\mathrm{F}}, \vec{r}_0) \propto e^{-2\kappa d} \tag{2.9}$$

Here V is the bias applied between the tip and the sample, $n_{\mathrm{T}}(\epsilon_{\mathrm{F}})$ is the density of states at the Fermi level of the tip, R is the effective tip radius, $\vec{r}_0$ is the center of curvature of the tip, $n_{\mathrm{s}}(\epsilon_{\mathrm{F}}, \vec{r}_0)$ is the sample local density of states (LDOS) at the Fermi level evaluated at $\vec{r}_0$. $\kappa = (2m_e\phi)/\hbar$ with ϕ defined as the effective local potential height. d is the distance between the front edge of the tip and the surface. Once again, the tunneling current decays exponentially as a function of distance d. It can be shown that this exponential dependence also holds for non-s-wave tips.

The STM is based on this decay behavior of the tunneling current: typically κ is of order about 1 Å^{-1}, if d is increased by 1 Å, the tunneling current will be reduced by a factor e^{-2}, almost one order of magnitude smaller. The size of an atom is also about 1 Å. Therefore, the main contribution to the tunneling current originates from the few atoms at the apex of the tip and the atoms on the surface. If the tip end is sharp and the sample surface is flat, see Figure 2.4a, the tunneling current will mainly be determined by channel d1 while the contribution from d2 will be minimum.

Let's define the surface of the sample as the x-y plane and move the tip across the sample surface. In the constant current mode, we measure the vertical deflection of tip as a function of its location in the x-y plane, while keeping the tunneling current constant through an electronic feedback loop. Such a measurement represents an atomic scale topographic image of the surface or, strictly speaking, an atomically-resolved real-space map of the surface local density of states (LDOS).

A schematic of the STM is shown in Figure 2.5. The fine motion of the tip can be controlled along the x, y, and z directions by applying a voltage V_{piezo} to the three piezoelectric elements that control the (x, y, z) motion of the tip. The bias voltage



(a) Sharp STM tip above a flat surface

(b) A 'double' tip above a flat surface

(c) Blunt STM tip above a rough surface or step edge on the surface

Figure 2.4: Main contributions to the tunneling current with different tip/surface configurations.

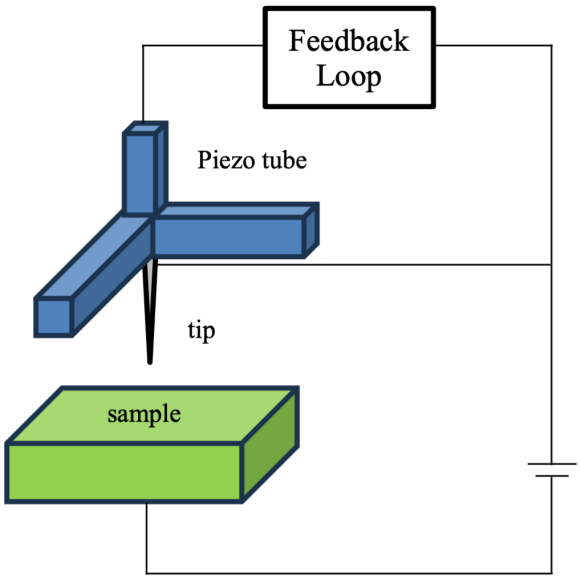


Figure 2.5: Schematic of STM: The motion of the tip will be controlled by the piezoelectric material, the feedback loop tunes the voltage applied to piezoelectric material while tracking the tunneling current when STM works in constant current mode.

V_{bias} is applied between the tip and the sample. Usually the sample is grounded via the sample stage. The feedback loop controls V_{piezo} while measuring the value of tunneling current. In addition, there is also constant height mode, which keeps the tip position in z direction unchanged while measuring tunneling current $I(x, y)$. This mode is faster than the constant current mode but if the surface is not flat enough, the tip may crash easily. Also, the interpretation of such images is less straightforward.

The tip condition is very important for acquiring atomic resolution images. If there are two atoms at the apex of the tip, see Figure 2.4b, the STM image will be a superposition of images originating from the d1 and d2 tunneling channel. This is usually referred to as a 'double' tip effect. In the worst scenario, a blunt tip provides several tunneling channels as shown in Figure 2.4c, which would, *e.g.*, underestimate step heights on the surface and/or wash out most atomic details.

The information about the LDOS is contained in the expression for the tunneling current as shown in Eq. (2.8). At low temperatures and low bias, only electrons within an eV_{bias} energy interval will take part in the tunneling process. In addition,

we may assume that the tunneling matrix elements varies slowly within this narrow energy window. Then, assuming a constant density of states for the metal tip, we can write:

$$\frac{dI}{dV} \propto n_{\mathrm{s}}(\epsilon + eV) \tag{2.10}$$

Thus the LDOS of the surface can be obtained by sweeping the bias voltage at a fixed tip position (x, y) with feedback loop off (otherwise the tip would retract or approach during the bias sweep). This is called scanning tunneling spectroscopy (STS). By taking the derivative of the measured current, we obtain the $\frac{dI}{dV}$ spectrum which is proportional to the LDOS. There is an another way to measure $\frac{dI}{dV}$ directly by applying a bias voltage of the form $V(t) = V_{\mathrm{DC}}(t) + V_{\mathrm{AC}} \sin \omega t$, where V_{AC} is small high-frequency alternating current (AC) ripple riding on top of a direct current (DC) bias. This AC modulation produces a sinusoidal modulation in the tunneling current that can be detected with a lock-in amplifier. The first harmonic response of the current signal measured with the lock-in amplifier is then (via Taylor series expansion) directly proportional to $\frac{dI}{dV}$.

The tip condition is very important for both microscopy and spectroscopy. A sharp tip is required to obtained atomic resolution. However, such a tip configuration is often unstable as atoms may hop back and forth between tip and sample, which makes it hard to conduct reliable STS. On the other hand, a blunt tip may make it difficult to acquire a good microscopy image, but it may be still good to perform STS. The tip condition is easily degraded when scanning on a rough surface or on an oxide material as the tip may easily 'grab' atoms from the surface, making it poorly conducting. One can apply a pulse (large bias, short time) between the tip and the sample to sharpen the tip, or crash the tip into a gold or platinum foil to make sure the apex has a metallic density of states.

In contrast to angle-resolved photoemission, which probes the electronic structure over mesoscopic or macroscopic distances, STM/STS truly is a local probe that probes the local electronic structure with atomic resolution. On the other hand, it is much

more difficult (though not impossible) to acquire momentum resolution with STS, for which ARPES is superior. As such, STS and ARPES are truly complementary tools. The combination of these two techniques is very powerful in the study of surfaces and thin film materials.

2.3 Reflection High Energy Electron Diffraction

Reflection High Energy Electron Diffraction (RHEED) was mentioned in section 2.1 and is widely used during MBE growth. Electrons are emitted and accelerated inside the electron gun with a beam energy of 10−100 keV, and are focused using electrostatic lenses. The collimated electron beam impinges onto the substrate at grazing angle. Forward scattered electron beams then form a diffraction pattern on a florescent screen on the opposite side of the chamber. Due to the grazing geometry (typically 1−5°), the RHEED gun and screen won't be in the path of the effusion cell beams. Therefore it is possible to monitor the diffraction pattern real time during growth.

For the 15 keV electron beam used in our studies, the electron mean free path inside the film, obtained using Eq. (2.11), is about 66 Å.

$$\lambda(\text{nm}) = \frac{143}{(E/\text{eV})^2} + 0.054\sqrt{E/\text{eV}} \tag{2.11}$$

For a grazing angle about 5°, the effective mean free path is about 66 Å × sin(5°) = 6 Å. The escape depth of the elastically scattered electron is about three times that number or 18 Å. Hence, RHEED only probes the the outer atomic layers of the crystal or thin film. The diffraction geometry can be determined by Ewald construction, as shown in Figure 2.6. We only consider elastic scattering. Energy conservation requires that

$$|\vec{k}_{\text{out}}| = |\vec{k}_{\text{in}}| \tag{2.12}$$

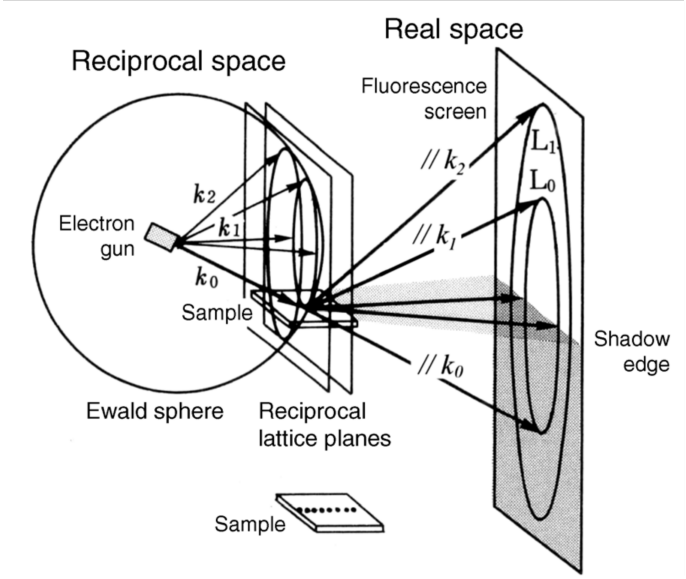


Figure 2.6: Direct space and reciprocal space of RHEED (Hasegawa, 2012).

In the Ewald sphere construction, the incident wavevector points at the origin of reciprocal space and defines a sphere of radius $|\vec{k}|$. The diffraction condition is fulfilled when

$$\vec{k}_{\text{out}} - \vec{k}_{\text{in}} = \vec{G} \tag{2.13}$$

where $\vec{G}$ is the reciprocal lattice vector the of the crystal. For a strictly 2D film, the reciprocal lattice constitutes an ordered array of reciprocal lattice rods as the Bragg condition perpendicular to the film plane is fully relaxed (there is no discrete lattice spacing along the perpendicular direction). Accordingly, the diffraction condition becomes

$$\vec{k}_{\text{out}} - \vec{k}_{\text{in}} = \vec{G}_{\parallel} \tag{2.14}$$

where $\vec{G}_{\parallel}$ is a reciprocal lattice vector in the plane of the film. The intersection of a reciprocal lattice plane and the Ewald sphere will always be circle. Therefore, the diffraction spots follow circular patterns, which are the 'Laue zones' L_0 and L_1 in Figure 2.6. In other words, the RHEED pattern represents a cut through reciprocal space. By collecting RHEED patters at different azimuthal angles, one can in principle reconstruct the reciprocal lattice.

Notice that half the RHEED screen will be dark because the electron beam can not pass through the sample. The shadow edge indicates the vertical height of the sample which is helpful for aligning the electron beam. The schematic in Figure 2.6 should be flipped since the effusion cells in our systems are pointing from the bottom of the chamber with the substrate facing down.

The coherence length of the beam is given as (Hasegawa, 2012):

$$l = \frac{\lambda}{\sqrt{2(\Delta\theta)^2 \sin^2\alpha + (\Delta E/E)^2 \cos^2\alpha}} \tag{2.15}$$

where Δ E and $\Delta\theta$ are the divergence of the beam energy and beam angle, λ is the wavelength of electron beam, α is the angle between the incident beam and direction for measuring the coherence length. For a typical 10 keV beam, l_{L} ($\alpha = 0°$) = 100−200 nm, l_{T} ($\alpha = 90°$) = 30−80 nm, which is about one order larger than that of Low Energy Electron Diffraction (LEED). This means that structural coherence over length scales larger than the coherence length will not sharpen the diffraction pattern. In other words, the width of the diffraction spots is instrument limited. Likewise, structural coherence on length scales shorter than the coherence length will result in a broadening of the diffraction spots.

No perfect 2D surface exists in the real world. Finite-size domains broaden the reciprocal lattice rods, which in turn broadens the RHEED spots. Instrumental factors can lead to a broadening of the Ewald sphere producing elongated streaks instead of sharp diffraction spots. Surface roughness produces all sorts of features in reciprocal space that affect the diffraction pattern, see Figure 2.7. Finally, as the RHEED beam penetrates several atomic layers, the intensity along the reciprocal lattice rods will be modulated by broadened Bragg diffraction along the vertical direction. If the thin films has a 3D island morphology, RHEED beams could completely penetrate the islands from the side and be subject to 3D Bragg condition. In that case, the diffraction pattern will be a 3D transmission pattern, similar to

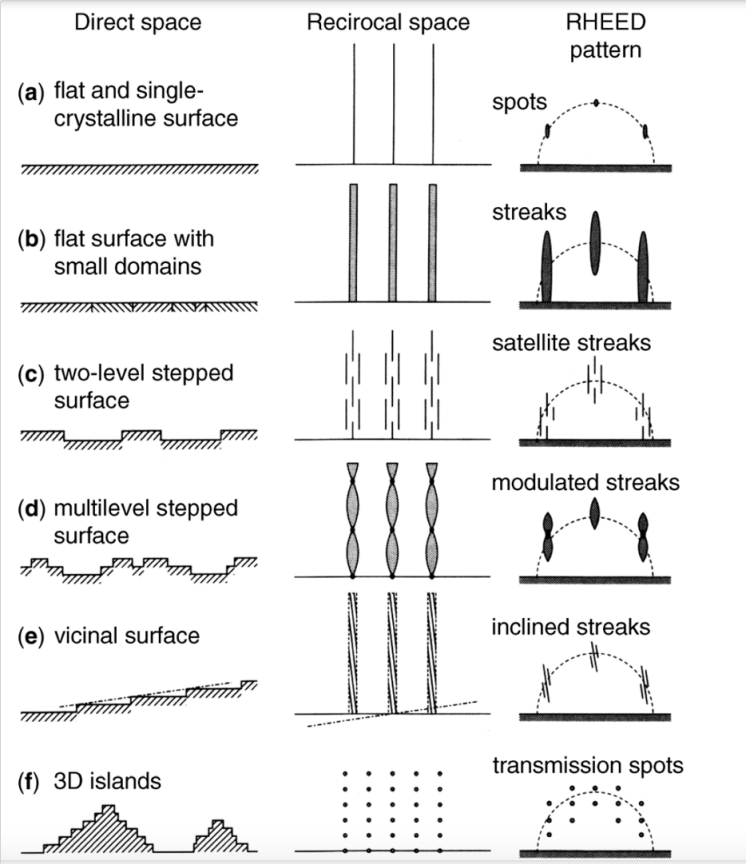
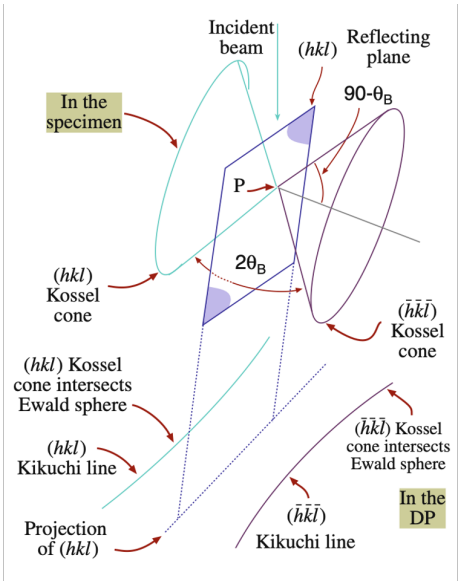


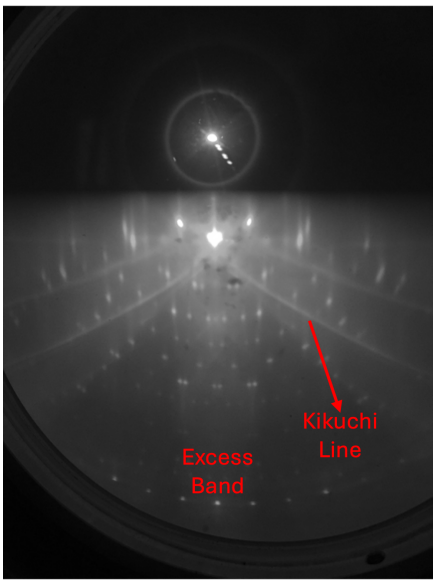
Figure 2.7: Schematic of various real surfaces with its real space, reciprocal space and RHEED pattern (Hasegawa, 2012).

that of X-ray diffraction, which allows for the determination of the lattice periodicity normal to the thin film plane.

Due to its high beam energy, inelastic scattering can give rise to so-called Kikuchi patterns. After numerous inelastic scattering evens, the penetrating electrons are no longer coherent with the incident beam and become a 'point source' of incoherent electrons inside the crystal, emitting electron waves in all directions. Some of these scatter off a set of parallel hkl lattice planes before exiting the crystal. The scattered intensity is strongly peaked in the forward direction, mostly parallel to the incident electron beam, and the intersection of the corresponding diffraction cones with the RHEED screen produces the Kikuchi lines. Kikuchi lines always come in pairs labeled hkl and $\bar{h}\bar{k}\bar{l}$ (Figure 2.8a). In addition, one observes Kikuchi bands and Kikuchi envelopes. Figure 2.8b shows an example of a Kikuchi line and a Kikuchi band in the RHEED pattern of a Se-etched STO crystal. The analysis of Kikuchi patterns produces structural information of the 3D bulk.



(a) A Sketch of Kossel cone (Carter, 2009)



(b) RHEED images of Se-etched STO(001)

Figure 2.8: Mechanism of Kikuchi line formation

2.4 X-ray Photoelectron Spectroscopy

2.4.1 General description

When a beam of photons impinges on a surface, it will interact with electrons inside the sample and, provided the incident beam energy exceeds the work function of the material, eject electrons into the vacuum with a certain distribution of kinetic energies. This is the well known photoelectric effect. The kinetic energy of the photoelectrons E_{k} is given by (Figure 2.9):

$$E_{\mathrm{k}} = \hbar\omega - E_{\mathrm{B}} - \phi \tag{2.16}$$

which follows from energy conservation. Here, $\hbar\omega$ is the energy of the incident photons. E_{B} is binding energy defined as the minimum energy required to excite an electron from initial state energy E_{i} to the Fermi level E_{F}. ϕ is the work function, which is defined as the energy difference between the Fermi level of the sample and the vacuum level. When photoelectrons are detected by a photoelectron spectrometer, one should use the work function of the spectrometer instead. With X-ray photons, one can access both the valence levels and the core levels of the constituent atoms (Figure 2.9). Since the core level binding energies are element specific, one often uses X-ray Photoelectron Spectroscopy (XPS) as a fingerprint tool to determine the chemical composition of the sample.

2.4.2 Stoichiometry of thin films

For a homogeneous surface of the sample, the core level intensity associated with a specific element is given by:

$$I = nf\sigma\theta y\lambda AT \tag{2.17}$$

Where $n = N/V$ is the volume density of the atoms, f is the X-ray flux intensity, namely the number of incident photons per area per unit time, σ is the photoelectric cross section, θ is the angular efficiency factor that depends on the geometry of

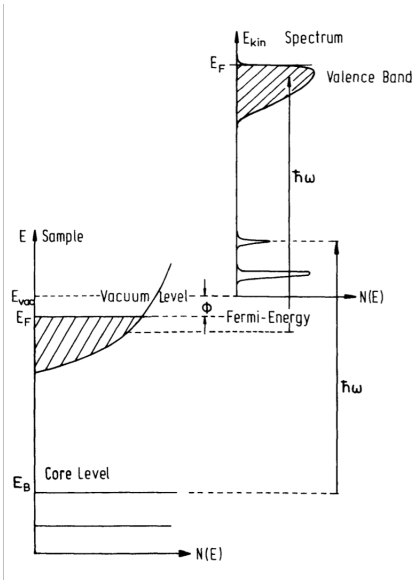


Figure 2.9: Energy conservation in X-ray photoelectron spectroscopy (Hüfner, Stephan, 2013).

the X-ray source, sample and the detector, λ is the inelastic mean free path of the photoelectrons in the sample, A is the area of the detected surface, and T is the detection efficiency (Chastain and King Jr, 1992). When determining the stoichiometry of a sample, one typically tries to eliminate instrumental factors, for instance by taking intensity ratios, so that the determination of the stoichiometry mostly comes down to knowing the photoemission cross sections and inelastic mean free paths. For thin films, one also needs to know the growth morphology of the film.

2.4.3 Understanding the XPS spectrum

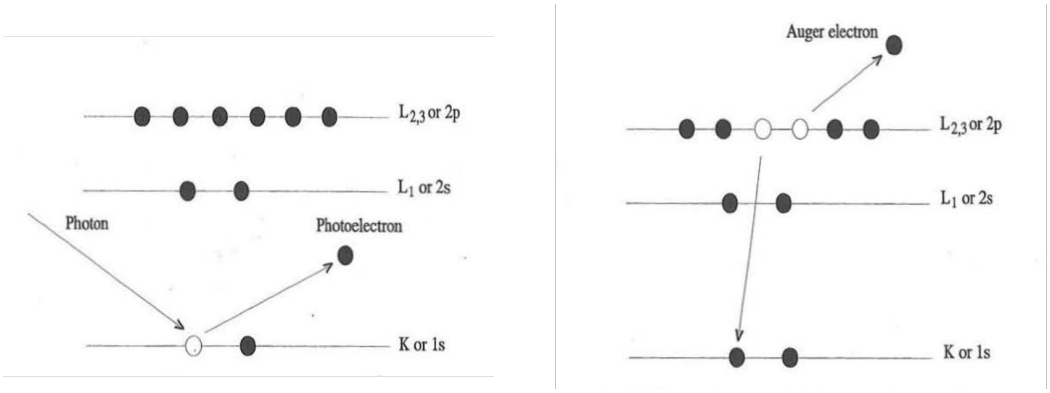
The photoemission process is often described within the three step model (Hüfner, Stephan, 2013): (a) the core electron is excited by the photon. (b) the excited electron travels from interior of the solid towards the surface. (c) Emission of the electron from the surface into the vacuum.

During step (b), electrons originating from deeper layers will scatter in-elastically on their way out. The photon energy in our experiment is 1486.7 eV (Al K_α radiation coming from the Al anode of our X-ray source). With ϕ being of the order of 4 eV,

the photoelectron energy varies between 0 and roughly 1480 eV. From the universal formula for the inelastic mean free path, Eq. (2.11), the photoelectron mean free path ranges from about 3 to 20 Å. As a rule of thumb, only electrons originating from a depth less than three times the inelastic mean free path can satisfy Eq. (2.16) and contribute to the peaks in the photoelectron spectrum. Consequently, XPS is quite surface sensitive. The surface sensitivity of an XPS measurement can be controlled to some extent by varying the angle between the cone of the photoelectron energy analyzer and the surface plane. For instance, in grazing emission, the escape depth of the photoelectrons is reduced by a factor $\cos\theta$, where θ is the angle between the analyzer cone and the surface normal. By comparing spectra recorded in both normal and grazing emission, one can obtain a depth profile of the chemical species near the surface.

The XPS spectrum contains many photoemission lines and various other features that provide fruitful information about the chemical and electronic properties of the sample. These include:

(1) Auger lines: Following the creation of a core hole by the incident photon, the hole decays when an electron from a higher energy level drops down to fill the hole. The energy released in that process may ionize another energy level. This process is illustrated in Figure 2.10. The photon ionizes the $1s$ level (K-shell). A $2p$ electron subsequently drops down to fill the core hole, leaving a hole in the $2p$ level (or L_{23} shell). The energy released in this decay process ionizes the $2p$ level once again, leaving two $2p$ holes in the final state. This is the so-called $KL_{23}L_{23}$ Auger transition. The emitted Auger electron's kinetic energy is solely determined by the spacing between the energy levels, orbital relaxations, and the hole-hole interaction in the final state of the Auger process. It is independent of the initial photon energy. As such it can easily be distinguished from ordinary photoemission lines, which shift as a function of the photon energy. In our work, we explore the use of Auger electron spectroscopy to probe the hole-hole repulsion in the valence bands of FeSe and FeTe, which should provide a good measure regarding the strength of the electron-electron



(a) Photoemission process leaving a core hole behind

(b) Auger transitions

Figure 2.10: Schematic of $KL_{23}L_{23}$ Auger process (Chastain and King Jr, 1992)

correlation in these compounds in comparison to other Fe-based superconductors, such as the pnictides.

(2) Surface core level shifts. The core level binding energies in a solid differ from those in free atoms. The chemical environment and nature of the chemical bonding has a profound effect on the core level binding energies, for instance through the Madelung potential in ionic solids. Figure 2.11 illustrates how the Fe $2p_{3/2}$ core level binding energy depends on the structure and chemistry of Fe containing bulk compounds. Generally speaking, the Madelung potential reduces the core level binding energies of the cation and increases those of the anions. Since the structural coordination of the atoms at the surface is reduced (there are fewer neighbors), they experience a smaller Madelung potential. In principle, the binding energies of the surface cations should increase, while those of the surface anions should decrease as compared to those originating from the bulk ions (Bagus et al., 2019). One may thus observe complex core level lineshapes due to partially overlapping core levels originating from atoms (ions) at the surface and those inside the bulk. Moreover, since core hole screening at the surface is less effective than in the bulk, surface core levels may experience additional shifts.

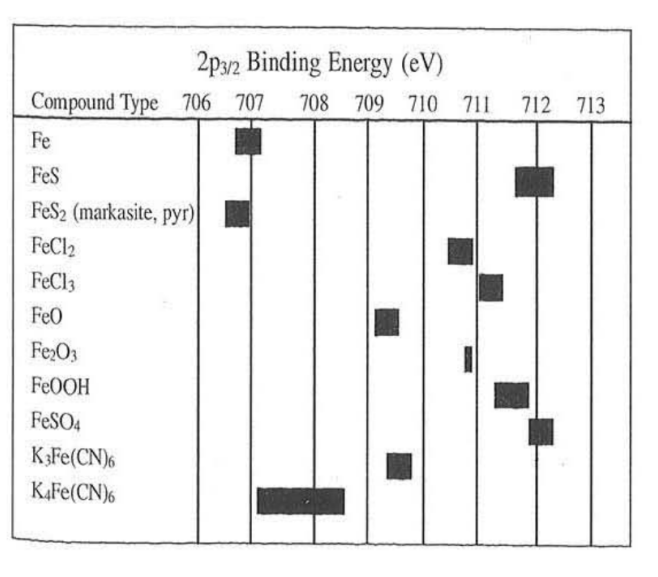


Figure 2.11: Binding energies of the Fe $2p_{3/2}$ core level in various compounds (Chastain and King Jr, 1992)

.

(3) Core level shake up spectra. During the photoemission process, there is finite possibility that a valence band electron will be excited to an unfilled conduction band state which is usually a few eV higher in energy. Due to energy conservation, this excitation reduces the kinetic energy of the photoelectron, and in principle produces a satellite peak. Metals allow for a continuum of single-particle excitations across the Fermi level that produce a tail on the high-binding energy side of the core level spectrum (Figure 2.12). Doniach and Sunjic derived the following expression for the photoemission line shapes in metals (Doniach and Sunjic, 1970; Hüfner, Stephan, 2013):

$$f(\omega) = \frac{\Gamma(1-\alpha)\cos[\pi\alpha/2 + (1-\alpha)\arctan(\omega/\gamma)]}{(\omega^2+\gamma^2)^{(1-\alpha)/2}} \tag{2.18}$$

Γ is the Γ-function, α the so-called asymmetry or skewness parameter, and 2γ the full width at half maximum of the Lorentzian line shape. The parameter α tends to increase with the density of states at the Fermi level and angular momentum of the conduction band states. As will be discussed in this thesis, we found that it

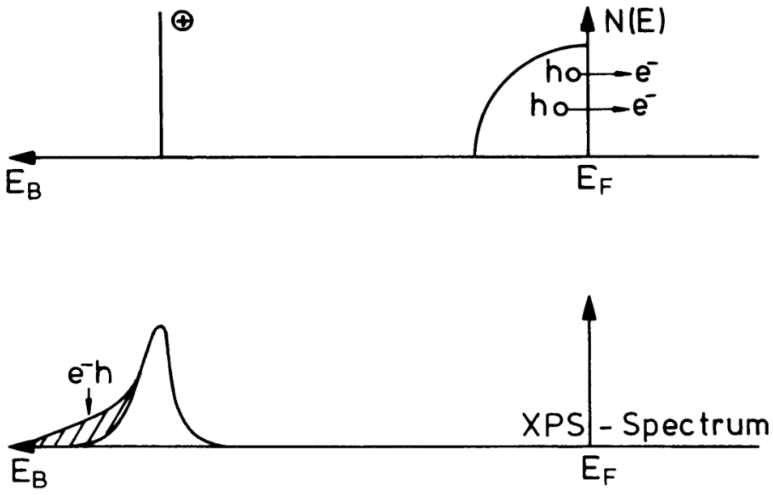


Figure 2.12: Schematic of how the tail feature in a metal arises from the scattering of the conduction band electrons scattered by the core-hole potential (Hüfner, Stephan, 2013).

is more practical to use the Mahan lineshape (Mahan, 1975) in order to determine the stoichiometry of a metal. The reason is that the integral of the Doniach-Sunjic lineshape does not converge.

The Mahan function used in the fitting of our XPS data is given by

$$I(\omega) = \Theta(-\omega)(\frac{\xi_0}{-\omega})^{\alpha-1} \tag{2.19}$$

where $\omega = \epsilon - \epsilon_0$, is the energy distance from the core level binding energy. The measured spectrum $P(w)$ includes the convolution of $I(w)$ with a Lorentzian line shape $L(w)$ plus the inelastic background:

$$P(\omega) = A_1 I(\omega) \circ L(\omega) + A_2 \int_{\omega}^{\infty} I(\omega) \circ L(\omega) d\omega \tag{2.20}$$

A_1 and A_2 will be referred as peak intensity and background intensity when listed in the results in the later chapters, and the convolved spectra is normalized to 1.

There are many contributions to the photoemission line shape. The Lorentzian lineshape mentioned above arises from the finite lifetime of the core hole. Gaussian broadening arises from vibrational excitations upon core ionization, structural or chemical inhomogeneity of the sample, as well as instrumental factors such as the finite spread in photon energy and the finite resolution of the electron kinetic energy analyzer.

Photoionization can also produce plasmon excitations that appear a distinct satellite peaks on the high binding energy side of the spectrum. The satellite energies correspond to the plasmon energy. In insulators, one might observe additional exciton and/or interband plasmon satellites. Importantly, these excitations are caused by the sudden creation of a core hole potential and are intrinsic to the photoionization process. In contrast, extrinsic energy losses arise from inelastic scattering of the photoelectron on its way to the surface. It is quite difficult, if not impossible, to separate intrinsic and extrinsic loss contributions to the photoelectron spectrum.

(4) Spin-orbit coupling and multiplet splitting. In the final state of the photoemission process, the core hole carries a spin angular momentum that couples to the orbital angular momentum of the core level. For instance, the photoionization of a $2p$ core level produces two peaks corresponding to $j = l + s = 3/2$ and $j = l - s = 1/2$. The peak splitting is determined by the spin-orbit coupling strength while their intensity ratio scales with the multiplicity of the angular momentum quantum number $(2j + 1)$, resulting in a peak intensity ratio of 2:1, respectively. In magnetic systems, the core hole angular momentum also couples with the unpaired spins in the valence levels, thus producing complex multiplet lineshapes.

2.4.4 Core level binding energy

The core level binding energy E_{B} in Eq. (2.16) is defined as the energy difference between initial ground state of the N electron system $E_{\mathrm{i}}(N)$ and the final (excited)

state of $N-1$ electron system $E_{\mathrm{f}}(N-1)$:

$$E_{\mathrm{B}} = E_{\mathrm{f}}(N-1) - E_{\mathrm{i}}(N) \tag{2.21}$$

The calculation of the binding energy is a complex many-body issue. In the Hartree-Fock approximation, many-body interactions are treated at the mean field level and by definition, the correlation energy $E^{\mathrm{c}} = E^{\mathrm{exact}} - E^{\mathrm{HF}}$. Eq. (2.21) can then be rewritten as:

$$E_{\mathrm{B}} = E_{\mathrm{f}}^{\mathrm{HF}}(N-1) - E_{\mathrm{i}}^{\mathrm{HF}}(N) + \Delta E^{\mathrm{c}} \tag{2.22}$$

where ΔE^{c} is a correction term due to the presence of correlations in both the initial and final state. Koopman attempted to solve it in a non-interaction picture, defining the orbital energy ϵ_{n} (by convention a negative value) of the initial N electron state as the difference between $E_{\mathrm{f}}^{\mathrm{HF}}(N-1)$ and $E_{\mathrm{i}}^{\mathrm{HF}}(N)$. This, of course, neglects the fact that the final $N-1$ electron state is an excited state that is not fully relaxed. The discrepancy to the exact solution (or measured binding energy) is defined as relaxation energy E_{R} (Egelhoff Jr, 1987; Hüfner, Stephan, 2013), and one finally arrives at the following equation:

$$E_B = -\epsilon_{\mathrm{n}} + \Delta E^{\mathrm{c}} - E^{\mathrm{R}} \tag{2.23}$$

-ϵ_{n} can be viewed as a first order approximation, especially when ΔE^{c} and E^{R} are close and approximately cancel. The core level binding energy shift ΔE_{B} then can be evaluated from -$\Delta\epsilon_{\mathrm{n}}$, $\Delta(\Delta E^{\mathrm{c}})$ and ΔE^{R}.

As discussed before, photoelectron spectra often contain shake up satellites. The main peak usually has the lowest binding energy and can approximately be viewed as the fully screened final state, which in turn corresponds to the lowest energy state of the $N-1$ electron system. Satellite peaks at higher binding energy may arise from other (poorer) screening channels and/or other excitations of the systems, *i.e.* particle-hole excitations in metals, exciton or plasmon satellites. The Lundqvist sum rule states that the centroid of the entire spectrum or first moment

of the photoelectron distribution corresponds to Koopman's eigenvalue $-\epsilon_{\mathrm{n}}$. The energy difference between the fully screened final state and the centroid of the spectrum equals the total screening energy associated with the ionization of the core hole (Lundqvist, 1969; Egelhoff Jr, 1987). This theorem only holds in the sudden approximation (high photon energy) and if the excitations are intrinsic to the core ionization. As mentioned, in practice it is often difficult to separate intrinsic from extrinsic excitations.

2.4.5 Auger spectrum and electron correlation

Auger spectrum can be useful to study electron correlations in many body system. In case of a core-valence-valence (CVV) auger process, the kinetic energy of the auger electron is given by (Vilmercati et al., 2012):

$$E_{\mathrm{k}}(C, V_1, V_2; X) = E_{\mathrm{B}}(C) - E_{\mathrm{B}}(V_1) - E_B(V_2) - U(V_1, V_2; X) \tag{2.24}$$

where $E_B(C)$ is the binding energy of the core level, $E_{\mathrm{B}}(V_1)$ and $E_{\mathrm{B}}(V_2)$ are the binding energy in valence band without considering electron correlation, $U(V_1, V_2; X)$ is the correlation energy of the final two holes in the state X. $U(V_1, V_2; X)$ can be rewritten as $U(V_1, V_2; X) = U^0(V_1, V_2; X) - R(V_1, V_2; X)$ which explicitly separates the Coulomb interaction term U^0 and relaxation or screen term R. In Cini-Sawatzky theory, the distribution of auger electron $D(E)$ can be written as (Sawatzky, 1977; Cini, 1978; Vilmercati et al., 2012):

$$D(E) = \frac{D^0(E)}{[1 - UF(E)]^2 + U^2 D^0(E)^2} \tag{2.25}$$

where $D^0(E) = \int_{VB} n(E - \epsilon) n(E + \epsilon) d\epsilon$ is the the self-convolution of the occupied density of state $n(E)$ (SCDOS). $F(E) = P \int_{-\infty}^{\infty} \frac{D^0(\epsilon) d\epsilon}{E - \epsilon}$ is the Hilbert transform of $D^0(E)$. In case of no correlation $U = 0$, $D(E)$ regresses to $D^0(E)$, which is easy to understand: hole pairs inside the valence band with total energy $2E = (E - \epsilon) + (E + \epsilon)$

all produce the same kinetic energy for the Auger electron, regardless of ϵ. If the bandwidth is W, one can easily see that the Auger spectrum becomes twice as wide. In experiment, one can roughly estimate the average correlation energy U from the difference between the $\langle D(E)\rangle$ and $\langle D^0(E)\rangle$, where $D(E)$ is the experimental Auger spectrum. There is another way to treat U more carefully, viewing U as a fitting parameter in the Eq. (2.25). Figure 2.13 shows how U was determined for several Fe-based pnictides, following the procedure outlined above (Vilmercati et al., 2012).

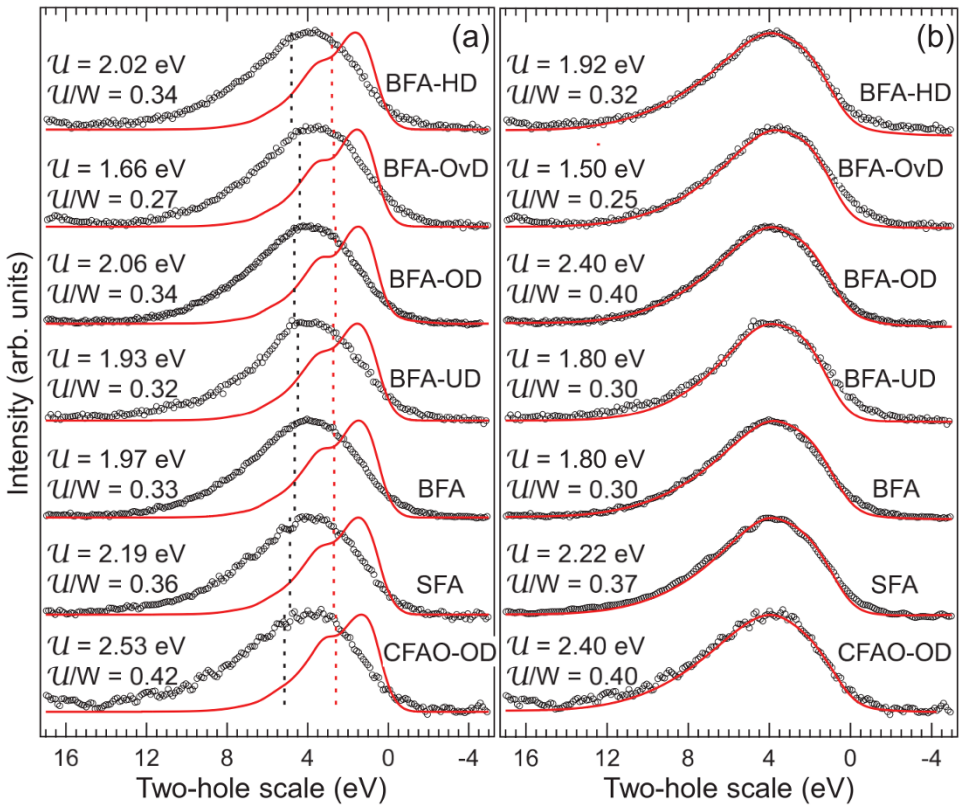


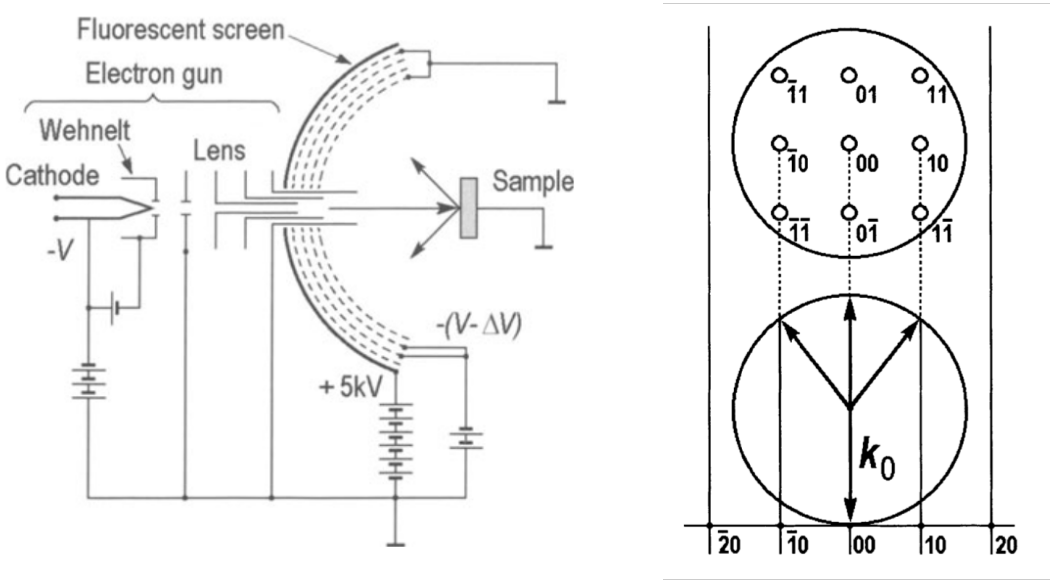
Figure 2.13: Determination of correlation energy U iron pnictide superconductors from Auger spectra. (a) The red lines and gray circled curves are the calculated SCDOS D^0 and the measured Auger spectra, the dashed lines indicates the position the average, U is obtained from the average difference. (b) The gray circled curve is the measured Auger spectra and the red curve is from fitting U as a parameter in D(E) (Vilmercati et al., 2012).

2.5 Low Energy Electron Diffraction

Low Energy Electron Diffraction (LEED) is a powerful tool to characterize the structure of the surface. Electrons with 30−200 eV energy are used in LEED, which corresponds to a wave length of about 1 to 2 Å. This is comparable to the atomic lattice spacing and so we can expect a diffraction pattern to form. From Eq. (2.11), the mean free path of electrons in LEED is about 5−8 Å, so only a few surface layers will be detected. A sketch of LEED setup is shown in Figure 2.14a: Electrons are emitted from a cathode, accelerated to an energy of typically 100 eV, and subsequently focused by a lens. The sample is located at the center of hemispherical fluorescent screen with four concentric grids. While the first, fourth gird and the sample are at ground potential, the potential of the second and third girds is slightly smaller than that of cathode, which is used to suppress in-elastically scattered electrons from reaching the fluorescent LEED screen. The LEED screen is at high positive bias to accelerate the mostly elastically back scattered electrons towards the screen where the diffraction pattern is visualized. The pattern represents the reciprocal lattice of the surface.

The diffraction pattern can be obtained once again via the Ewald sphere construction, see Eq. (2.12) and (2.13). The difference with RHEED is that the incident electron beam with momentum vector $\vec{k}_0$ impinges on the surface at normal incidence while the diffracted beams are back scattered towards the LEED screen. This is illustrated in Fig. 2.14b. Again, due to the finite escape depth of the LEED beams, the diffraction condition along the z-direction is mostly relaxed and thus the reciprocal lattice consists of a periodic array of diffuse rods. In that case, the Bragg condition (Eq. (2.13)) reduces to:

$$\vec{k}_{\text{out}\parallel} = \vec{G}_{\parallel} \tag{2.26}$$



(a) Experimental LEED setup **(b)** LEED indices

Figure 2.14: Low Energy Electron Diffraction

($\vec{k}_{\text{in}\parallel} = 0$). Graphically, the diffraction condition is satisfied when the reciprocal lattice rods intersect the Ewald sphere. The resulting pattern on the LEED screen represents a 2D map of $\vec{G}_{\parallel}$ vectors, which is the surface reciprocal lattice. This is further illustrated in Fig. 2.14b.

The coherence length of LEED typically is 10 to 20 nm. For domain sizes larger than this, the LEED pattern represents an incoherent superposition of scattered intensities originating from the different domains. For instance, if a (1×2) and (2×1) surface reconstruction coexist as a result of *e.g.*, the fourfold symmetry of the substrate, then the LEED pattern will be a superposition of two LEED patterns. One would see the extra $(0, 1/2)$ and $(1/2, 0)$ superlattice spots. On the other hand, if small anti-phase domains coexist on an area smaller than the LEED coherence length, additional phase relations exist that can alter the intensity and location of the superlattice reflections.

In this discussion it is important to recall that the diffraction pattern arises from the self-interference of the electron as in the famous double-slit experiment. This

should be thought of as a coherent process which is truly quantum mechanical in nature. Electrons originating from the LEED gun are completely incoherent, however. Interference between multiple electrons with random phases are washed out during the time it takes to collect the data. The diffraction pattern formed by a beam of electrons thus originates from the incoherent superposition of the probability distribution of each individual electron. Incoherent means that we are summing intensities, not amplitudes. Due to instrumental limitations such as the divergence and energy spread of the electron beam, the diffraction pattern is resolution limited as if the surface structure or 'grating' is of limited size. This is artificial. Self interfering electrons may be phase correlated over distances much greater than the coherence length, but there is no way to extract such information, other than through a deconvolution of the instrument response function.

2.6 Angle-Resolved Photoemission Spectroscopy

The electronic properties of a crystalline material are encoded in the band structure, and particularly the bands closest to the Fermi level. Angle-Resolved Photoemission Spectroscopy (ARPES) is able to measure the band structure, or more precisely, the single particle spectral function $A(\vec{k}, \omega)$, which makes it such a powerful tool (Damascelli et al., 2003). Like XPS, ARPES is based on the photoelectric effect and surface sensitive due to the limited escape depth of the photoelectrons. ARPES spectrometers are designed to measure both the energy and momentum of the photoelectron which, through the appropriate use of conservation laws, can be related to the energy and momentum of the electron inside the solid. Momentum resolution is achieved by measuring the angular distribution of the photoelectrons. (XPS spectra are usually measured in an angle-integrated mode). Figure 2.15 shows a schematic of an ARPES spectrometer. Eq. (2.16), $E_{\mathrm{k}} = \hbar\omega - E_{\mathrm{B}} - \phi$, should still be fulfilled. Translational symmetry parallel to the surface ensures the conservation of parallel

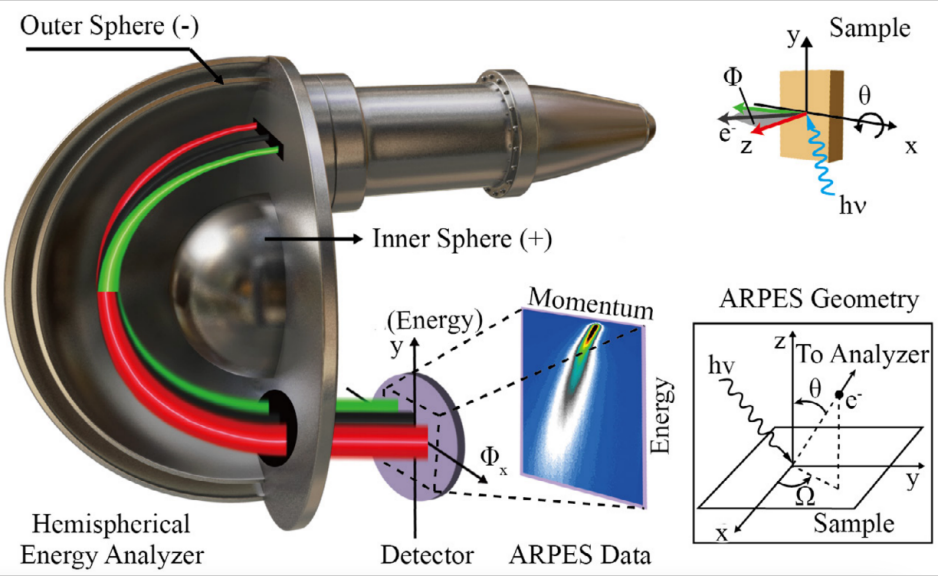


Figure 2.15: Schematic geometry of an ARPES measurement (Zhou et al., 2018).

momentum:

$$\hbar\vec{\mathrm{k}}_{\mathrm{f}\parallel} = \hbar(\vec{\mathrm{k}}_{\mathrm{i}\parallel} + \vec{G}) + \vec{p}_{\mathrm{photon}} \tag{2.27}$$

$$\hbar k_{\mathrm{f}\parallel} = \sqrt{2m_{\mathrm{e}}E_{\mathrm{k}}}\sin\theta \tag{2.28}$$

Where i, f stand for initial and final electron states, $\vec{p}_{\mathrm{photon}}$ is the momentum of the photon, and $\vec{G}$ is the reciprocal lattice vector parallel to the surface. The latter can be absorbed into $\vec{k}_{\mathrm{i}\parallel}$ when presented in the reduced Brillouin Zone. The perpendicular component of the momentum is not conserved as the photoelectron must traverse the potential barrier at the surface, *i.e.*, the work function. This is only of minor concern when studying quasi 2D materials such as tetragonal FeSe and FeTe. For materials with substantial band dispersion along the normal direction, one often approximates the perpendicular momentum by assuming a free-electron like final state with parabolic dispersion along the $\vec{k_z}$ direction with the bottom of the band located at $-V_0$, where the 'inner potential' V_0 is an empirical parameter of the order of 10 to 15 eV. In that case, one finds that $\hbar k_{\mathrm{f}\perp} = \sqrt{2m_{\mathrm{e}}(E_{\mathrm{k}}\cos^2\theta + V_0)}$ (Damascelli,

2004). In order to map the dispersion in the perpendicular direction, one typically resorts to ARPES measurements as a function of photon energy at the synchrotron.

In our experiments, we employ a UV light source with $He_{1\alpha}$ and $He_{2\alpha}$ radiation and photon energies of 21.22 eV and 40.81 eV, respectively. $k_{\text{photon}} = E/(\hbar c) \sim 10^{-2}$ Å, which is negligible compared to the size of the Brillouin zone and can be ignored. Experimentally, the orientation of the sample is selected using the manipulator controls which is guided by instant LEED observation. By measuring E_{k} at angle (Ω, θ), and using Eq. (2.16) and (2.28), the band structure $E_{\text{B}}(\vec{k})$ with $\vec{k} = (k_{\parallel}\cos\Omega,\ k_{\parallel}\sin\Omega)$ will be obtained. The ARPES data in this thesis were acquired by Mr. Kaleb McClure, in collaboration with the group of Prof. Norman Mannella.

2.7 X-ray Diffraction

X-ray photons are scattered relatively weakly in comparison to charged particles such as electrons and protons and, accordingly, they have a penetration depth of the order of microns. Hence, they are ideally suited for structural investigations of bulk materials. The wavelength used in X-ray diffraction (XRD) is also comparable to the atomic distances inside a material. We used XRD to determine the crystallographic structure of our FeSe and FeTe thin films. This is possible as long as the films are reasonably thick. The Bragg condition for constructive interference is

$$2d_{hkl}\sin\theta_{\text{B}} = n\lambda \tag{2.29}$$

where (hkl) are the Miller indices of the relevant crystal planes, d_{hkl} is the corresponding plane spacing, n is the integer number that defines the order of the diffraction maximum, and θ_{B} is the Bragg angle between the incident X-rays and the crystal plane.

Figure 2.16 illustrates a typical XRD experiment. Our FeSe or FeTe samples are grown on STO substrates with dimensions of $3\times8\times0.5$ mm. They were mounted onto

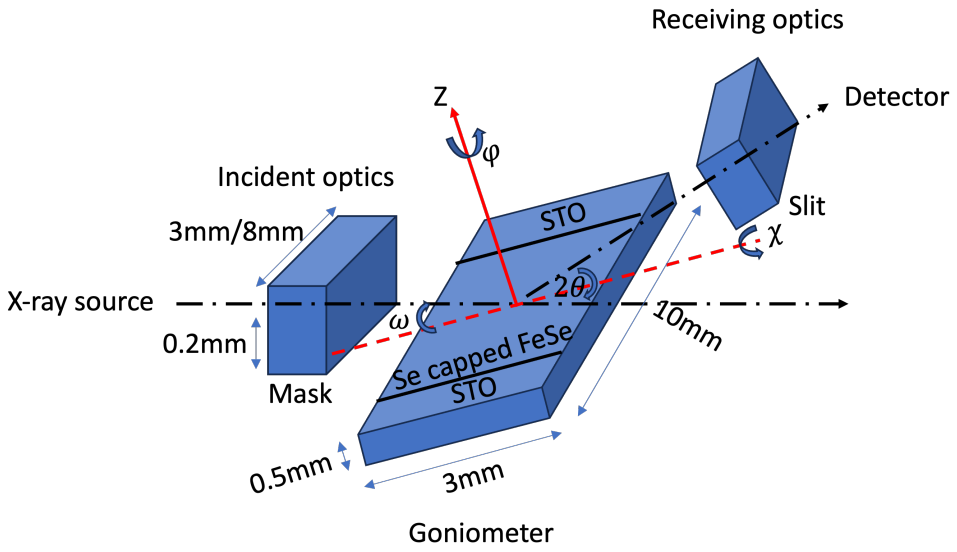


Figure 2.16: Schematic of XRD

a goniometer head with double sided tape. The goniometer controls the orientation of the samples by varying Z (parallel motion) and $\omega/\varphi/\chi$ (rotation). ω is the angle between the fixed X-ray source and sample. 2θ is the angle between the incident X-rays and detector and φ/χ are the tilt and azimuthal angles as illustrated in Figure 2.16. X-rays are generated when accelerated electrons emitted from a hot filament collide with the anode. Here we used Cu anode, producing Cu-$K_{\alpha 1}$ radiation with (λ = 1.5405980 Å). The X-rays were then focused and passed through the 'incident optics' before they hit the sample. The scattered X-rays pass through the receiving optics before they reach the detector. The incident optics and receiving optics can be changed depending on the precise purpose of the measurement. The incident optics contains an X-ray monochromator and a 0.2 mm × 3 (or 8) mm 'divergence slit' (or 'Mask'), which produces a narrow monochromatic X-ray beam. The receiving optics contains a receiving slit and a beam attenuator to control the angular resolution and count rate. Too high count rates could result in non-linearity of the detector and may even damage the detector. The coarse alignment of the sample was obtained from the incident X-ray beam by setting $2\theta = 0$, and alternate scanning of the translation parameter Z and angle ω, as shown in Figure 2.17.

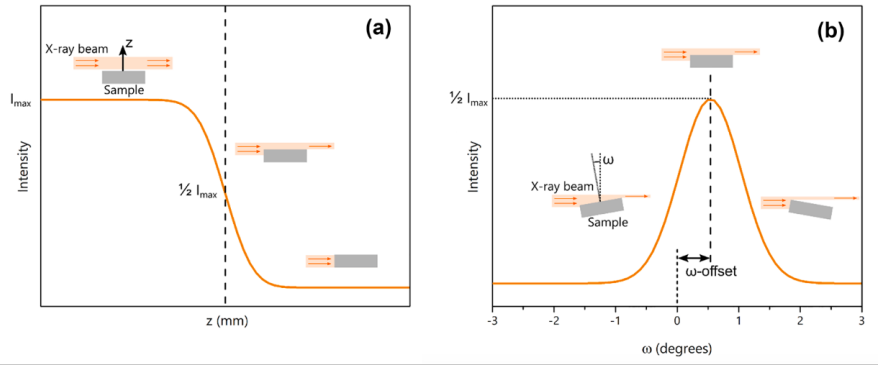


Figure 2.17: Schematic of XRD alignment: 2θ is set to 0, so that the incident X-ray is directly detected for the alignment of Z and ω. The dashed lines indicate the correct position (Harrington and Santiso, 2021).

2.7.1 2θ-ω scan

For a symmetric 2θ-ω scan, ω is first set to be half the scattering angle 2θ. In that case, peaks at $\theta = \theta_B$ will be found while scanning the angle 2θ. After the coarse alignment, precise alignment with respect to a well defined Bragg plane is needed before conducting the 2θ-ω scan. In our case, the (001) plane of the STO substrate (with $n = 2$ being most intense peak) is used for alignment. 2θ and ω are then set to 46.48° and 23.24°, respectively. An ω-scan (or Rocking Curve) is obtained when scanning ω while keeping 2θ fixed. By alternatively performing ω-scans and χ-scans, and assuming epitaxial growth of FeSe or FeTe on STO(001), we align the diffraction plane perpendicular to the FeSe(001) plane. The distance d_{001} and out of plane lattice parameter c of the film thus can be obtained from the peak position in the 2θ-ω scan.

2.7.2 X-ray reflectivity measurement

When an electromagnetic wave travels through medium 1 and enters medium 2, the incident angle θ_1 and refraction angle θ_2 obey Snell's law:

$$\frac{\sin\theta_1}{\sin\theta_2} = n_{21} \tag{2.30}$$

where n_{21} is the ratio of the refractive indices of medium 2 and 1, respectively. The angles θ are defined with respect to the direction normal to the dielectric interface. The critical angle for total reflection demands that $\theta_2 = 90°$. For X-rays incident from air, n_{21} is slightly less than one, which means that θ_1 should be slightly less than 90°. Total reflection for X-rays thus happens at very small incident angle relative to the interface. The X-ray reflectivity (XRR) measurement is a 2θ-ω scan around the critical angle. The grazing angle is typically of the order of a few tenths of a degree. XRR provides information about the mass density of the substrate ρ, the film thickness d, and surface roughness σ, see Figure 2.18:

2.7.3 Reciprocal space mapping

The symmetric 2θ-ω scan in the previous section only provides the out of plane lattice constant of the film. Other diffraction geometries are required to obtain the in-plane lattice constants. After aligning the sample along the (00l) direction, the sample can be further rotated to a specific orientation by varying the angles χ, φ and ω. We use the Bragg peak of the STO(103) plane to precisely align the sample, and perform

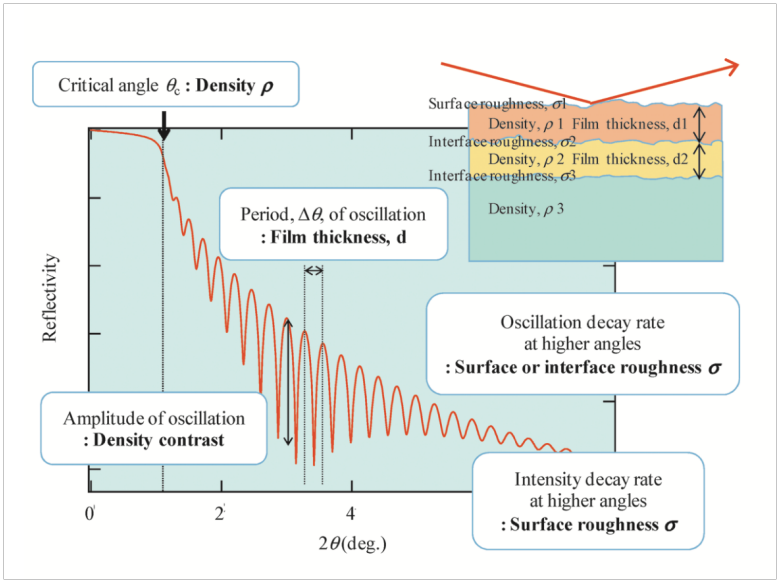


Figure 2.18: Information obtained from an XRR measurement (Yasaka et al., 2010).

a (2θ, ω) scan in a 'Reciprocal space mapping' (RSM) experiment. The FeSe(104) and FeTe(105) reflections are in close proximity to the (103) of the STO substrate, so by comparing the momentum transfers q_x and q_z of the substrate and the film, we can obtain the lattice parameters of the film. The measurement result is plotted in reciprocal space, using the formulae below:

$$q_x = \frac{1}{\lambda}\cos(\omega) - \cos(2\theta - \omega) \tag{2.31}$$

$$q_z = \frac{1}{\lambda}\sin(\omega) + \sin(2\theta - \omega) \tag{2.32}$$

2.8 Magnetic Property Measurement System

Magnetism and superconductivity were originally believed to be mutually exclusive, though now it is understood that magnetic fluctuations can provide the glue to bind electrons into Cooper pairs, as is generally believed to be the case in high-temperature cuprate superconductors. In the cuprate and possibly the Fe-based superconductors, antiferromagnetism and superconductivity appear to have an intricate connection that can be controlled via carrier doping. It is therefore important to explore the phase diagram of FeSe and FeTe for the existence of magnetic phases.

The magnetic properties of a material are characterized by magnetic susceptibility χ, which is defined as:

$$M = \chi H \tag{2.33}$$

M is the magnetization of the materiel and H is the strength of the applied magnetic field. One can measure χ as a function of temperature at fixed magnetic field, or measure a magnetization loop, *i.e.*, M as function of H at fixed temperature. In the former case, we distinguish field-cooled (FC) measurements from zero-field cooled (ZFC) measurement. Figure 2.19 illustrates the temperature dependence of the magnetic susceptibility for different types of magnets. Figure 2.20 shows the corresponding magnetization loops.

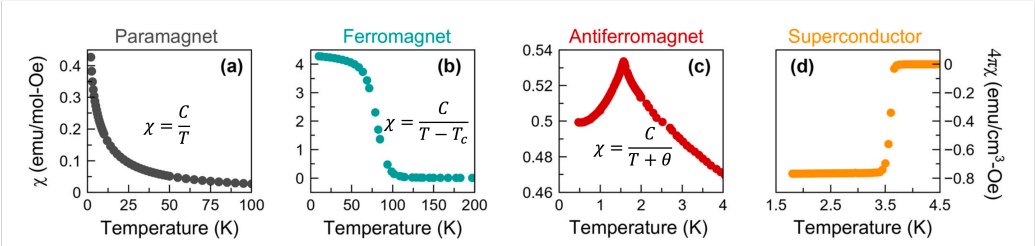


Figure 2.19: Magnetic susceptibility for different types of magnetic materials. The images are modified from (Mugiraneza and Hallas, 2022).

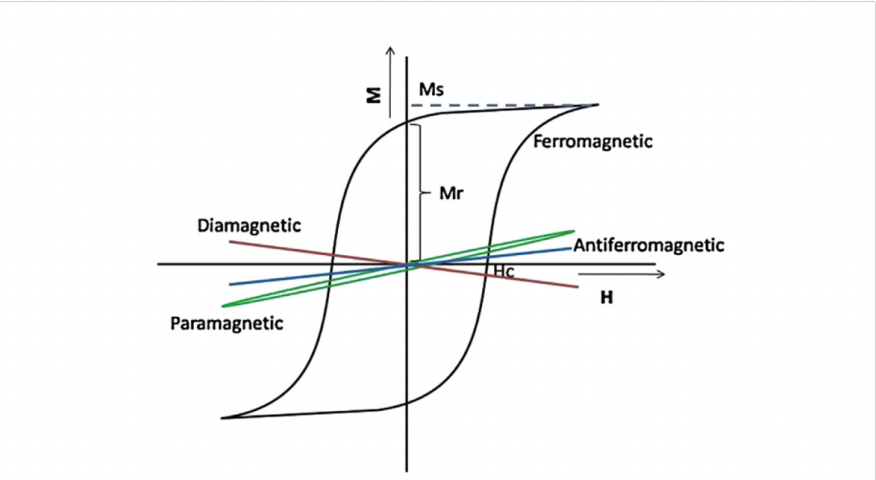


Figure 2.20: Magnetization loops for different magnetic materials: M_{r}, M_{s}, H_{c} are the remanent magnetization, saturation magnetization and coercivity, respectively (Kotnala and Shah, 2015).

Measuring the magnetic moment of a thin film is not an easy task as the absolute magnitude of the magnetic signal is very tiny, especially in the monolayer regime. A Superconducting Quantum Interference Device (SQUID) is a powerful tool to measure the magnetic property with ultrahigh sensitivity and precision. The operating principle of the SQUID magnetometer is based on the physics of the Josephson junction. When two superconductors are put together with a very thin insulating material in between, then the tunneling current $I(t)$ and voltage $V(t)$ are governed by (Tinkham, 2004; Kraft et al., 2017):

$$I(t) = I_c \sin(\phi(t)) \tag{2.34}$$

$$\frac{\partial \phi}{\partial t} = \frac{2eV(t)}{\hbar} \tag{2.35}$$

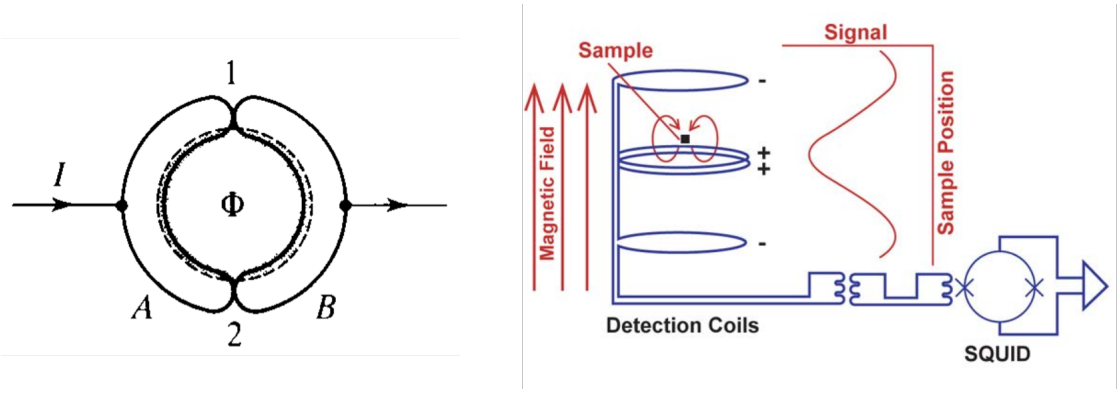
where I_c is the critical current and $\phi(t) = \phi_2 - \phi_1$ the phase difference between the superconducting order parameters on both sides of the junction. The wavefunction of the Cooper pair is written as $\Psi_j = \sqrt{n_j} e^{i\phi_j}$ (n is the Cooper pair density, $j = 1, 2$ labels the two superconductors). Note that in the absence of an applied bias ($V(t) = 0$), there will still be a tunneling current.

When two Josephson junctions are connected in parallel, it forms a DC SQUID, see Figure 2.21a. The current of the DC SQUID is given by (Kraft et al., 2017):

$$I = 2I_c \sin(\delta_0) \cos(\frac{q_e}{\hbar}\Phi) = I_m \cos(2\pi \frac{\Phi}{\Phi_0}) \tag{2.36}$$

where $I_m = 2I_c \sin(\delta_0)$, δ_0 is the mean value of the phase difference of the two Josephson junctions, $\Phi_0 = 2\pi\hbar/q_e$ is the flux quantum, and Φ is the magnetic flux. Φ can be measured directly once I_m is calibrated with a known field. Notice that because Φ_0 is so small, even a tiny change of Φ introduces a noticeable change in I.

In our experiment we used the Quantum Design Magnetic Property Measurement System (MPMS) 3. The schematics of this machine is shown in Figure 2.21b. The pickup coils are inductively coupled to the sample located at their center. With two



(a) DC SQUID **(b)** Magnetic property measurement system

Figure 2.21: Sketch of DC SQUID magnetometer: (a) is taken from (Tinkham, 2004), (b) is taken from the Quantum Design MPMS 3 user's manual.

counter-winding loops, the pickup coils work as a second order gradiometer, thus the generated current only responds to a magnetic disturbance. The sample size is typically much smaller than the pickup coil, and the measured signal depends on the sample position. The pickup coils are inductively coupled to the DC SQUID via an input transformer, and finally the SQUID voltage is amplified and digitized by the instrument electronics. In this sense the DC SQUID works as a highly sensitive current-to-voltage converter.

Chapter 3

$SrTiO_3$(001) Substrate Preparation

3.1 Introduction

As discussed in Chapter 1, the STO substrate plays an important role towards enhancing the superconducting T_c. The FK phonon mode and charge donation are the two key attributes of the STO substrate. High T_c FeSe monolayers can be grown epitaxially on different STO(001) surface reconstructions, including the $c(6 \times 2), (\sqrt{13} \times \sqrt{13}), (\sqrt{5} \times \sqrt{5}), (\sqrt{2} \times \sqrt{2}), (2 \times 1), (1 \times 1)$ reconstructions, which produce a range of doping levels in the FeSe thin film (Lee et al., 2014; Tanaka et al., 2020a; Zou et al., 2016). The different surface reconstructions are related to the varying oxygen content of the outermost surface layers, which in turn depend sensitively on the STO substrate preparation. Despite these differences, all of them appear to be terminated with a TiO_x double layer, according to TEM, XRD and XPS, and provide an excelent template for the growth of FeSe and FeTe thin films (Li et al., 2016a; Sims et al., 2019; Peng et al., 2020; Zou et al., 2016; Ohsawa et al., 2016). There is one notable exception, however. FeSe films grown on STO surfaces with a mixed SrO/TiO_x termination exhibit 3D clusters and a discontinuous morphology (Wang et al., 2014). In order to systematically study the mechanism of high temperature superconductivity in these films, we aim to establish a reliable

and reproducible procedure to fabricate the 'optimal' STO template for our FeSe and FeTe thin films. This will allow us to focus on the intrinsic properties of the films, such as stoichiometry and correlation strength.

3.2 Oxygen Vacancies and Surface Reconstructions

In order to obtain an atomically flat STO surface, it is essential to anneal the substrate at high temperature. During this process, oxygen vacancies are inevitably created. This can in principle be alleviated by annealing the STO substrate under an O_2 atmosphere.

Our STO(001) substrates were ordered from Shinkosha. They are doped with Nb (0.7% in weight percentage), which is essential to prevent charging in low-temperature STM measurements. They were cut into small rectangular pieces of $3 \times 10 \times 0.5$ mm^3, and cleaned in an ultrasonic bath of de-ionized water, acetone, and ethanol (5 mins per bath). Following this standard cleaning protocol, the substrates were mounted onto a molybdenum sample plate, equipped with electrical contacts for direct current heating in vacuum. The samples are then loaded into a fast-entry chamber which was separated from the main MBE growth chamber by a gate valve. The samples are degassed overnight in the fast entry lock or in the main MBE chamber before any further treatment, the degassing temperature was below 500 °C so as to minimize vacancy formation. The temperature of the sample was measured using an optical pyrometer with an emissivity setting of 0.7. Unless stated otherwise, the STO samples where heated by passing an AC or DC current through them.

3.2.1 The $(\sqrt{5}\times\sqrt{5})$, (2×2) and (2×1) surface reconstructions of STO

Atomically smooth STO terraces can be obtained via UHV annealing. After the samples were thoroughly degassed, they were heated inside UHV to about 950−1000 °C. The annealing parameters are indicated in Table 3.1. This procedure produces atomically flat terraces with single unit-cell-high steps and mostly straight step edges. The measured step height in STM is about 0.4 nm, which is close to the c-axis of STO. Atomic smoothness indicates that there are no SrO or TiO_x clusters on the surface. The terrace width increases at even higher temperature. However, this also produces double-height steps and meandering step edges, see Figure 3.1. Meanwhile, the RHEED pattern changes from a (2×1) diffraction pattern to a (2×2) and finally a $(\sqrt{5} \times \sqrt{5})$ pattern (Figure 3.2). The concentration of oxygen vacancies should also increase as a function of annealing temperature and annealing time, following the same sequence, *i.e.*, $(2 \times 1) < (2 \times 2) < (\sqrt{5} \times \sqrt{5})$.

3.2.2 Oxygen annealing: $c(6 \times 2)$, (2×2) and (2×1) reconstructions

Following standard cleaning procedures, STO substrates were loaded into the fast entry lock, which was pumped down to approximately 10^{-7} mbar. They were

Table 3.1: The details of the UHV annealing on the STO

Sample	T/°C	t/mins	RHEED	STM
#91	980−995	45	(2×1)	Single height steps Straight step edges
#86	1100−1313 1170−1220	13 several	(2×2)	Mixed
#76	1250−1350	90	$(\sqrt{5} \times \sqrt{5})$	Double height steps Meandering step edges

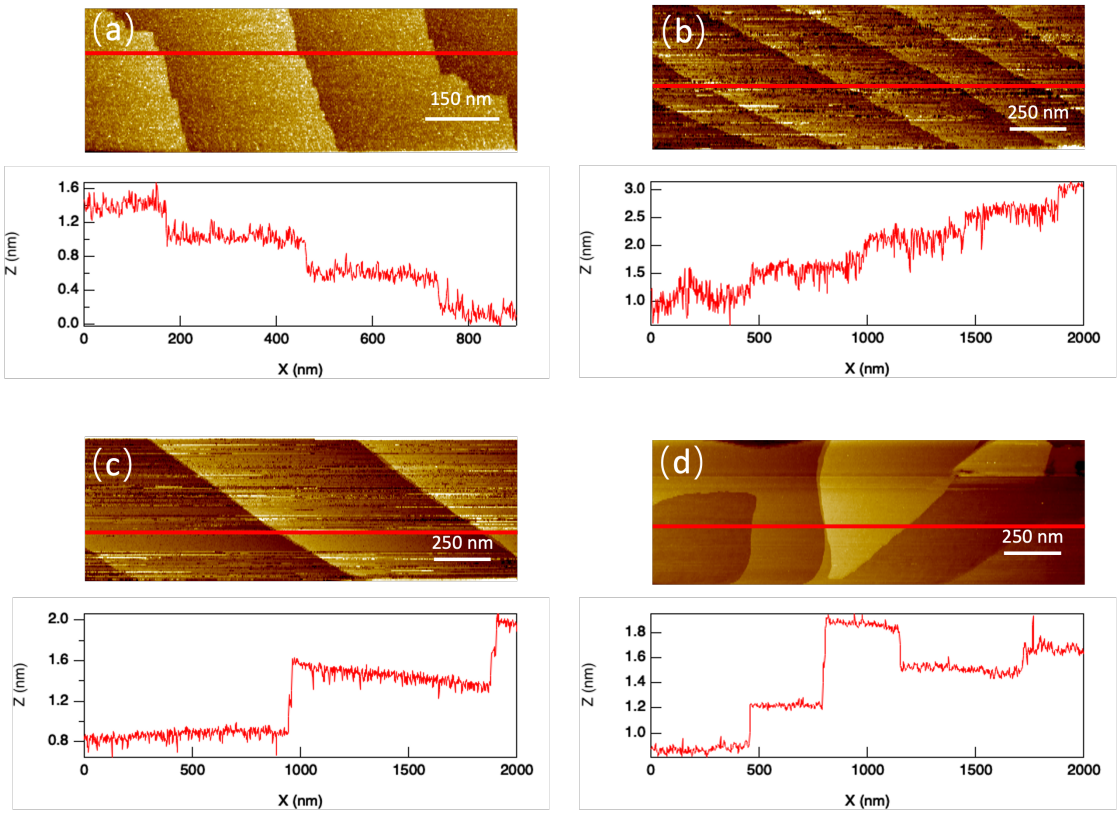


Figure 3.1: STM images of UHV annealed STO: the top images are STM images of sample (a) #91, (b) #86 colder part, (c) #86 hotter part, (d) #76, annealed at 980−995 °C, 1100−1170 °C, 1220−1313 °C,1250−1350 °C, respectively. See also Table 3.1. The bottom panels show the corresponding line profiles along the red lines in the topographic images.

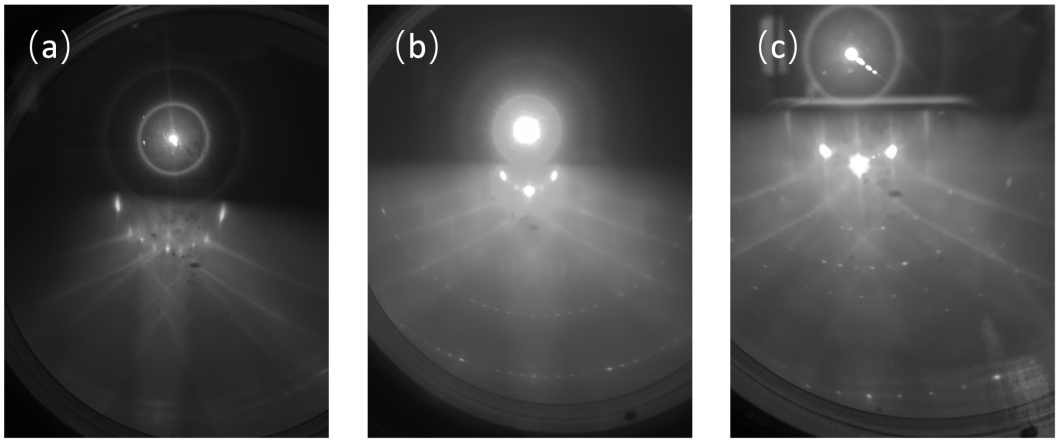


Figure 3.2: RHEED patterns of UHV annealed STO: as the annealing temperature increases, the STO surface displays a (a) (2×1), (b) (2×2), (c) $(\sqrt{5} \times \sqrt{5})$ reconstruction. All RHEED patterns were acquired with the incident electron beam pointing along the STO [100] direction.

subsequently degassed at about 500 °C under a steady flow of 10^{-4} to 10^{-6} mbar of molecular oxygen for up to two hours. Next, the samples were annealed under 10^{-5} to 10^{-1} mbar of oxygen at 800 to 1100 °C for several hours (0.75 to 9 hrs). The oxygen vapor pressure was controlled with a UHV leak valve.

The evolution of the surface morphology with temperature was similar to that of the vacuum annealed substrates, see Figure 3.3. The surface morphology changes from irregular disconnected patches to atomically flat terraces with straight single unit-cell-high steps. The surface morphology appeared optimal with a 1000 °C anneal. Higher temperature produces multi-step terraces with meandering step edges, as shown in Figure 3.4. Nano structures with several nanometer tall patches begin to form after the fourth oxygen annealing cycle of the the sample listed in Table 3.2. RHEED images display a streaky pattern, which indicates the existence of flat 2D patches with somewhat limited domain sizes, which is consistent with the STM observations.

The oxygen vacancy concentration is expected to depend on the oxygen pressure. At low oxygen pressure, typically 10^{-5} to 10^{-4} mbar range, STO surfaces exhibit a $c(6 \times 2)$ reconstruction. As the pressure of oxygen increases to the 10^{-4} to 10^{-1}

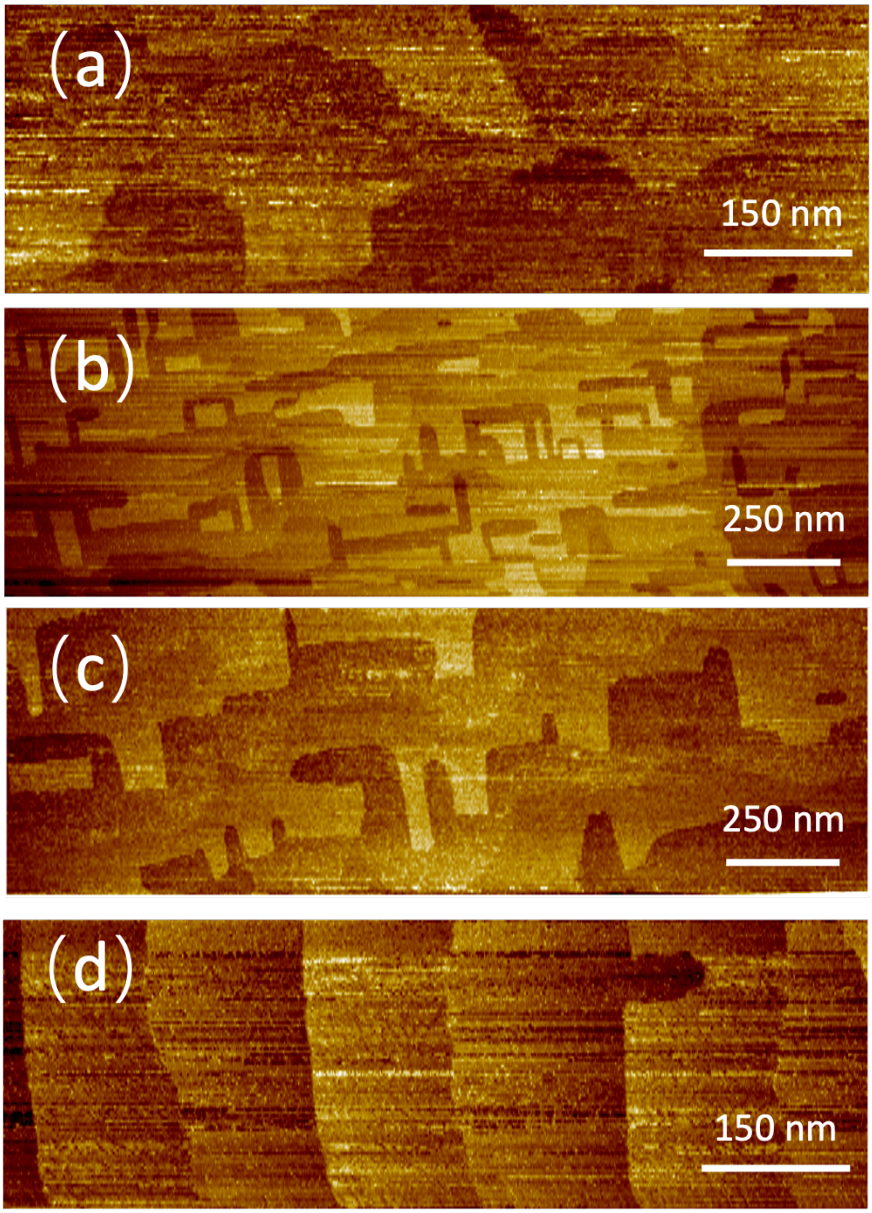


Figure 3.3: Effects of oxygen annealing of the STO substrates: (a) STM topographic image on the colder part of the STO sample, following the first oxygen annealing cycle. Same after the third oxygen annealing cycle with (b) the colder part, (c) the median part, and (d) the hotter part, respectively. The treatment parameters of this sample are listed in Table 3.2.

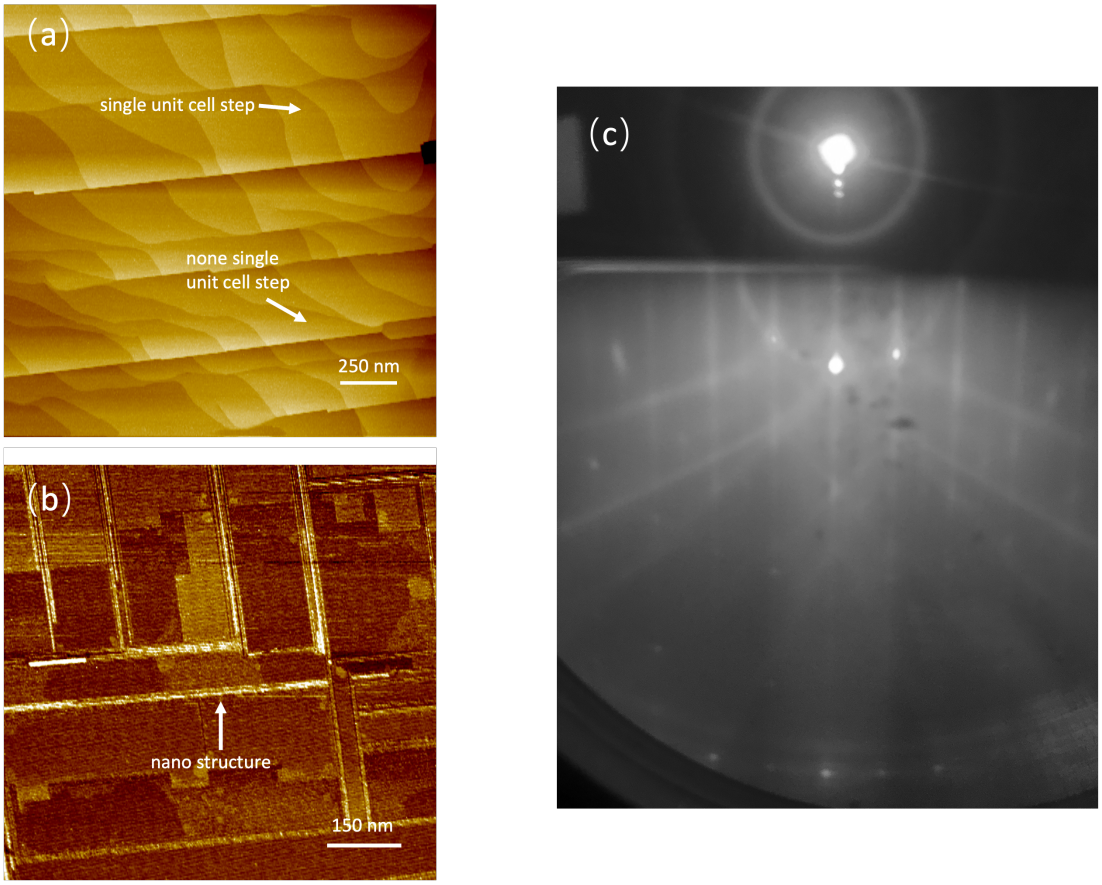


Figure 3.4: Over annealed STO: (a) Absence of single unit-cell-height steps and meandering step edges. (b) Nano-structures begin to form. (c) RHEED pattern with the incident electron beam along the STO [100] direction, displaying a streaky pattern.

Table 3.2: Details of the oxygen annealing parameters for the STO surface in Figure 3.3

Treatment	Temperature/°C	Time/mins	O_2 Pressure/mbar	RHEED
Degas	480−530	120	10^{-6}	/
Annealing 1	800−890/930−1040	40/5	10^{-5}	Spotty, $c(6 \times 2)$
Annealing 2	900−1000	240	10^{-5}	Spotty, $c(6 \times 2)$
Annealing 3	950−1050	120	10^{-4}	Spotty, $c(6 \times 2)$
Annealing 4	1000−1100	120	10^{-4}	Streaky, $c(6 \times 2)$

range, with STO being kept at 960−1000 °C, RHEED patterns reveal other higher order reflections including 1/6 order reflections not seen before, see Figure 3.5.

Samples with a large temperature gradient, annealed under an O_2 pressure of 10^{-3} mbar, revealed several reconstructions with the $c(6 \times 2)$ on the colder (900 °C) side and $(2 \times 2)/(2 \times 1)$ on the hotter (1100 °C) side. This suggests that the oxygen vacancy concentration follows the same sequence $c(6 \times 2) < (2 \times 1) < (2 \times 2)$.

3.2.3 Acid etching: (1×1) and (2×1) surface reconstructions

It was reported that acid etching using *e.g.*, hydrochloric acid or a buffered HF solution, produces a TiO_x terminated STO surfaces. SrO terminated surfaces would form a strontium hydroxide layer after cleaning the surface with de-ionized water. Subsequent acid etching would remove the strontium hydroxide layer, so that the STO substrate is solely terminated by a TiO_x layer (Kawasaki et al., 1994; Tan et al., 2013; Zhang et al., 2014).

Details of our etching protocols are listed in Table 3.3. The STO substrates were first cleaned in an ultrasonic bath with de-ionized water and then dipped into either diluted HF(10:1) for 10 mins or a buffered HF solution (6:1) for 1 min. The samples were subsequently rinsed with de-ionized water and loaded into the fast entry lock. After degassing and oxygen annealing, uniform and atomically flat terraces with single unit-cell-high steps were routinely obtained, as shown in Figure 3.6. However, one

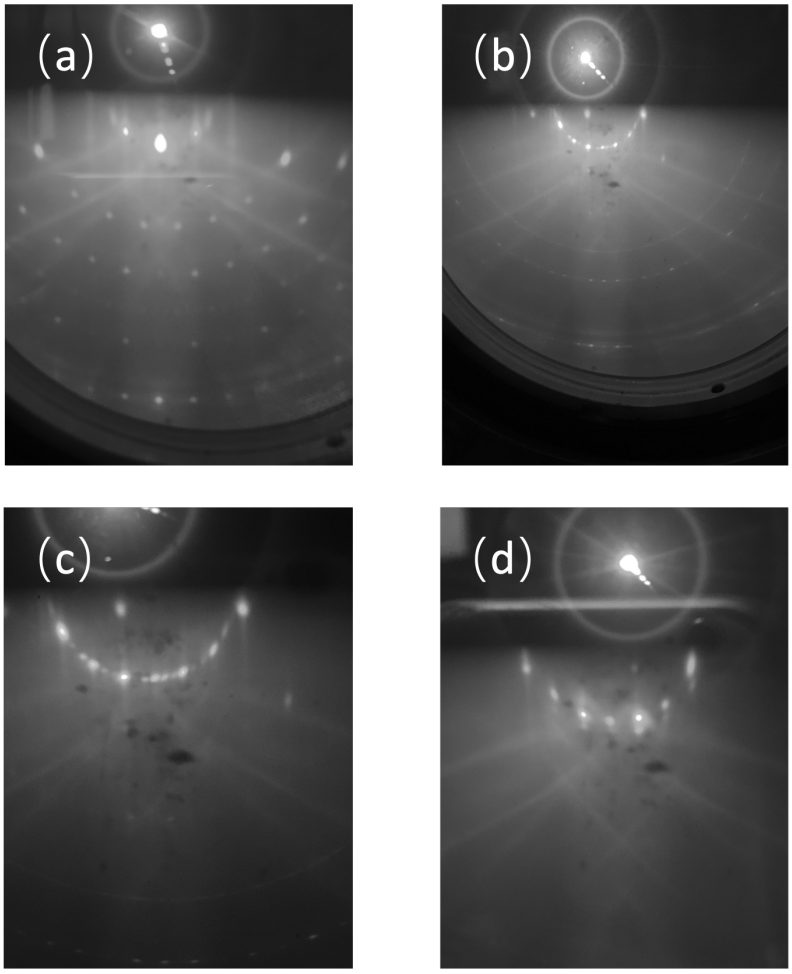


Figure 3.5: Relation between oxygen pressure and surface reconstruction of STO: (a) Median vacancy concentration. The RHEED pattern displays a $c(6 \times 2)$ reconstruction. (b) and (c) Low vacancy concentration. The RHEED pattern displays 1/2 and 1/6 order spots, different from those of the $c(6 \times 2)$ reconstruction in (a). (d) High vacancy concentration. The RHEED pattern displays a $(2 \times 2)/(2 \times 1)$ reconstruction. All RHEED images were taken with the incident beam along the STO [100] direction.

Table 3.3: Etching protocols for STO

Sample label	HF etching	Degas with O_2	Anneal with O_2	RHEED
#82	Diluted (10:1) 10 mins	500 °C 5×10^{-6} mbar 2.5 h	820-865 °C 5×10^{-5} mbar 40 mins, 1000 °C 5×10^{-5} mbar 5 mins	(2×1)
#83	Diluted (10:1) 10 mins	500 °C 5×10^{-5} mbar 2 h	820-865 °C 5×10^{-4} mbar 40 mins, 1000 C 5×10^{-5} mbar 5 mins	(2×1)
#87	Buffered (6:1) 1 min	500 °C 5×10^{-5} mbar 2 h	815-870 °C 5×10^{-4} mbar 40 mins, 1000 C 5×10^{-5} mbar 3 mins	(1×1)
#88	Buffered (6:1) 1 min	500 °C 1×10^{-6} mbar 2 h	850-990 °C 1×10^{-5} mbar 40 mins, 1000 °C 1×10^{-5} mbar 3 mins	(1×1)

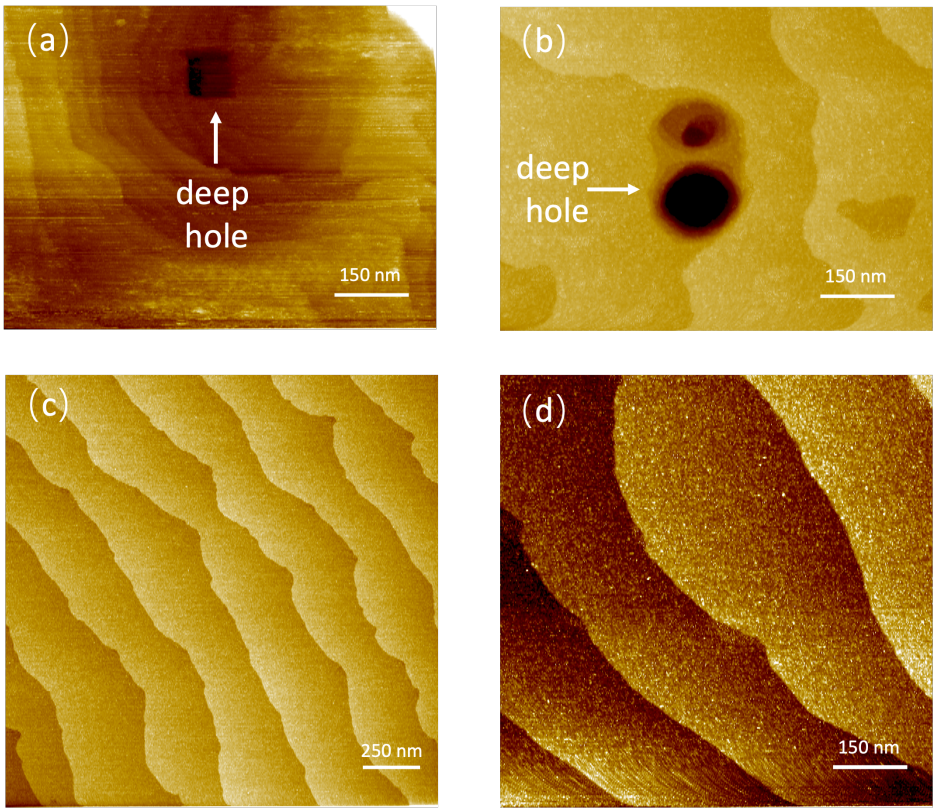


Figure 3.6: STM images of acid etched STO surfaces: (a), (b) STM images of samples #83 and #87, respectively, showing several nanometer deep etch pits. (c), (d) STM images from sample #88, showing atomically flat terraces after HF treatment and *in-situ* oxygen anneal, respectively.

also observes holes with depths of several nanometers, indicating that the etching speed may have been too high. This could possibly be remedied by diluting the acid and/or reducing the etching time. After oxygen annealing, RHEED patterns revealed the existence of a (2×1) reconstruction for substrates treated with diluted HF and unreconstructed (1×1) surface for substrates treated with buffered HF, see Figure 3.7.

3.2.4 Selenium and tellurium etching: $(\sqrt{13} \times \sqrt{13})$ reconstruction

In-situ selenium etching was reported to produce atomically flat defect-free STO terraces. It was also used to successfully grow high-T_c FeSe/STO interfaces (Wang et al., 2012). Since Se appears below oxygen in the Periodic Table, their chemical properties are expected to be quite similar. Se etching could thus have the same effect as oxygen annealing, *i.e.*, it would suppress the formation of oxygen vacancies during

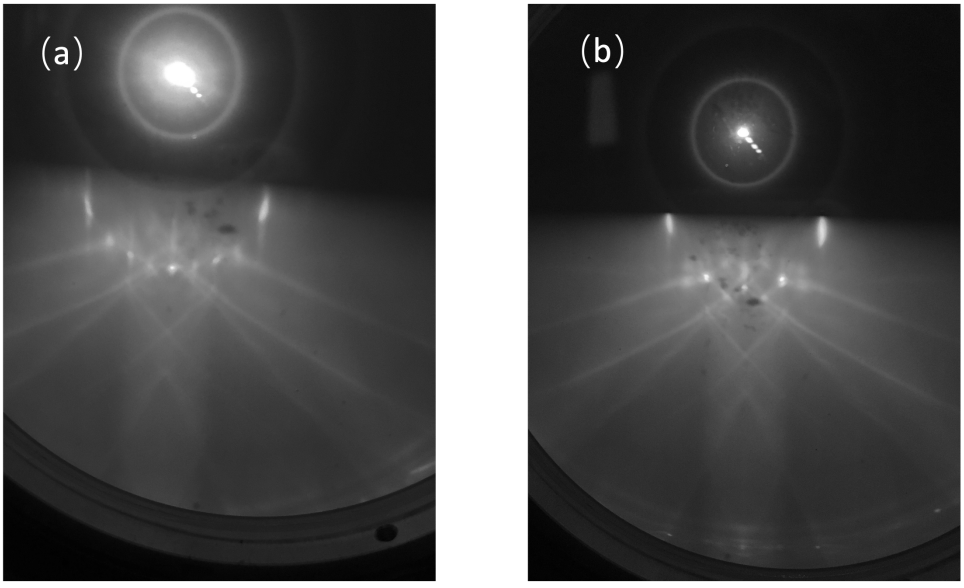
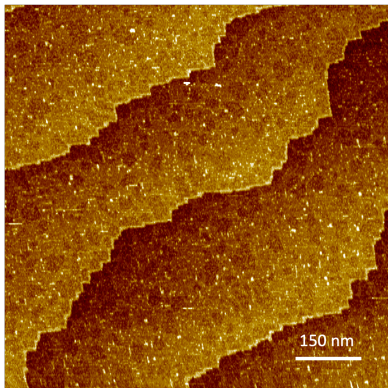


Figure 3.7: RHEED patterns of acid treated STO: (a), (b) are the RHEED patterns of samples #82 and #88, treated with diluted HF and buffered HF, and showing a (2×1) and unreconstructed (1×1) surface, respectively. All RHEED images were acquired with the incident beam along the STO [100] direction.

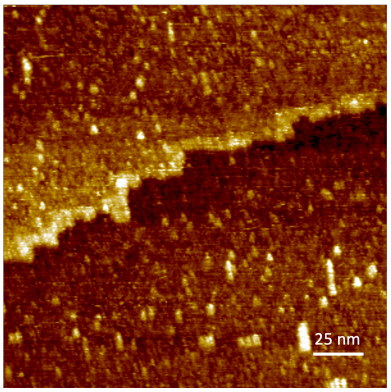
high-temperature annealing. Following Wang *et al.*'s recipe, we annealed the STO substrate around 980−1000 °C under a Se flux for about 45 mins, The Se source was kept at 160−180 °C, which corresponds to a chamber pressure of about 8×10^{-5} to 4×10^{-4} mbar. STM images once again displayed atomically flat surfaces with single unit-cell-high steps, although one occasionally finds small nanoparticles accumulated near the step edges. Since their height is less than 0.4 nm, these are possibly Se atom clusters' see Figure 3.8a and Figure 3.8b. The RHEED pattern displayed a $(\sqrt{13} \times \sqrt{13})$ reconstruction as shown in Figure 3.8c. The presence of sharp spots on perfect Laue circles indicates the presence of large domain sizes. As will be shown later, Se etching does not lead to an appreciable amount of Se incorporation into the STO.

We attempted a similar procedure using Te instead. This would enable us to grow FeTe on Te-etched STO without the risk of incorporating unwanted Se. Here, we kept the Tellurium source at about 330−370 °C, corresponding to a chamber pressure of 1×10^{-3} to 9×10^{-3} mbar, while heating the STO substrate to 950−1000 °C for about 45 minutes, as before. Once again, the STO surface exhibits a $(\sqrt{13} \times \sqrt{13})$ reconstruction as shown in Figure 3.8d. However, the RHEED pattern is much more streaky and somewhat blurred, which is indicative of smaller domain size and increased disorder. It may be possible to fine tune the Te etching protocol, but we opted to stick to the Se etching protocol. Here, it should be noted that practically speaking, *in-situ* Se etching is a straightforward protocol while high-pressure oxygen annealing represents an assault on the vacuum system as it can lead to deterioration of pumps and filaments.

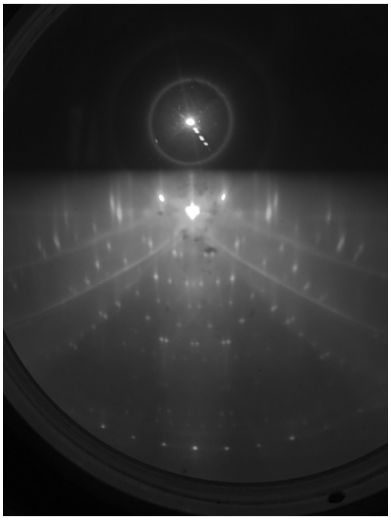
Combining the results from vacuum annealing, acid etching, oxygen annealing and Se/Te etching, we assert that the oxygen vacancy concentration increases following the sequence $c(6 \times 2)/(\sqrt{13} \times \sqrt{13}) < (2 \times 1) < (2 \times 2) < (\sqrt{5} \times \sqrt{5})$ (Figure 3.9).



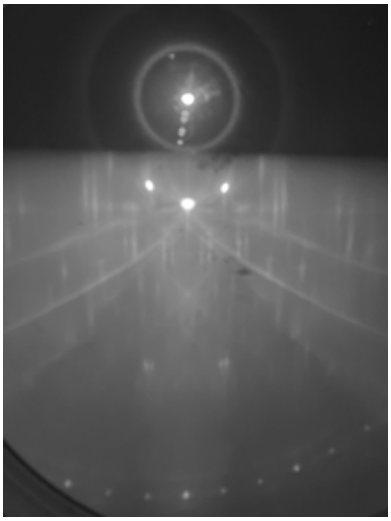
(a) STM image of Se-etched STO: large scale



(b) STM image of Se-etched STO: small scale



(c) RHEED image of Se-etched STO



(d) RHEED image of Te-etched STO

Figure 3.8: STM and RHEED images of Se/Te-etched STO, all the RHEED images were taken with the incident electron beam along the STO [100] direction.

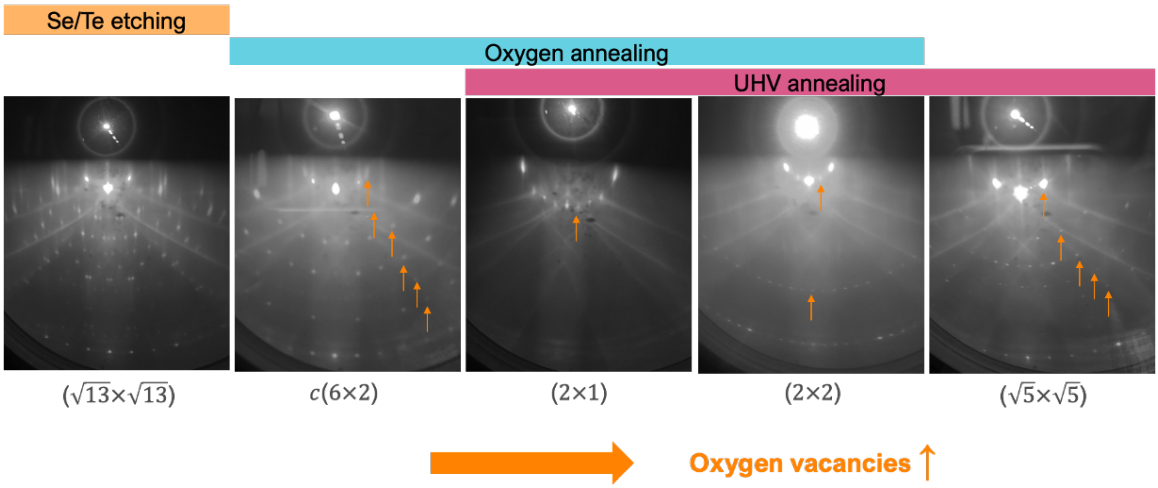
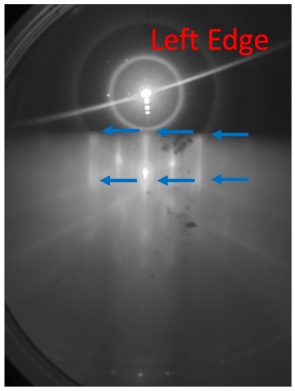


Figure 3.9: Summary of the oxygen vacancy concentration on the STO prepared with different methods: all the RHEED images were taken with the incident electron beam along the STO [100] direction.

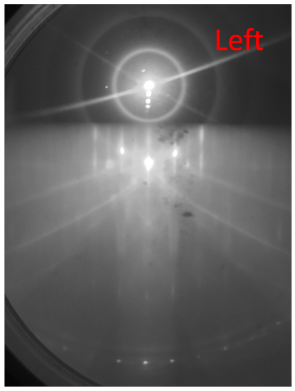
3.3 Electro-migration

By applying DC current through the STO substrate, one can find different surface reconstructions along the direction of the current flow. When the DC current direction is reversed, their order of appearance also reverses. This suggests that the polarity of the electrodes affects the distribution of oxygen vacancies across the surface (Shimizu et al., 2012). By applying an AC current, one would expect this effect to cancel which could lead to a more homogeneous distribution of oxygen vacancies.

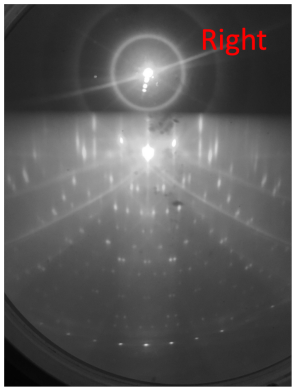
We found that the quality of the STO $(\sqrt{13}\times\sqrt{13})$ reconstruction is very sensitive to the temperature gradient under DC heating. Uniform sharp and spotty RHEED pattern are easily achieved when the temperature difference across the sample is less than 50 °C. On the other hand, RHEED patterns of a Se-etched STO sample with a 60 °C difference (960−996−1020 °C) reveal a dramatic effect, as shown in Figure 3.10. Here, one can clearly see that 3D islands are formed on the cold side of the STO (Left edge), while high-quality $(\sqrt{13}\times\sqrt{13})$ patterns can be found on the hot side. RHEED patterns across the large middle section of the sample are streaky, indicating



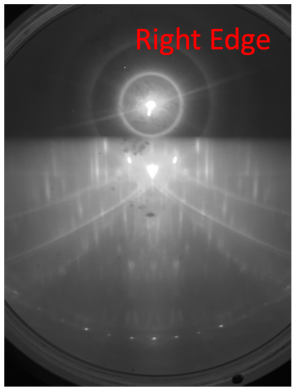
(a) Left edge: island spots



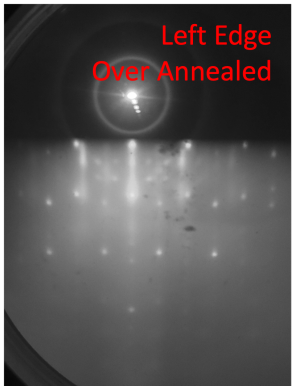
(b) Left: Streaky pattern



(c) Right: Spot pattern



(d) Right edge: Streaky pattern



(e) Left edge: Over annealed

Figure 3.10: Temperature effects on the quality of the STO $(\sqrt{13} \times \sqrt{13})$ surface reconstruction: (a)−(d) larger temperature gradients cause island formation (indicated by the blue arrows) on the cold side of the STO; (e) etching at higher temperature reduces the surface quality on the colder side. All RHEED images were taken with the incident electron beam along the STO [100] direction.

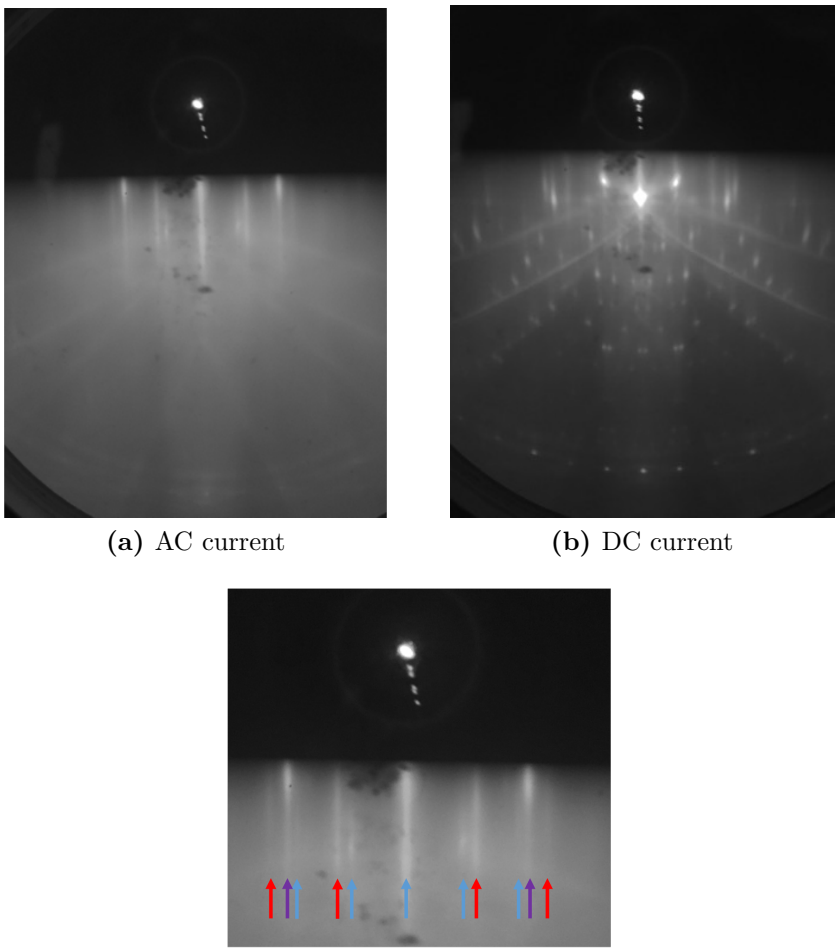
smaller domain sizes. Island formation seems irreversible. Once 3D islands are formed near the cold edge, increasing the temperature on the cold side to 970−1000 °C only makes the island spots only more intense. This irreversible process may be related to local variations in resistivity, heat dissipation, and stress. In such a case, the surface preparation is no longer reversible, nor controllable.

We repeated the same procedure, this time with AC current. The RHEED pattern showed modulated streaks and a blurred contrast, see Figure 3.11a. This indicates that the surface has become rough. The arrows in Figure 3.11c indicate the presence of extra streaks, in addition to the original original (1×1) streaks (blue arrows). Prolonged annealing with DC current under a Se flux will restore the $(\sqrt{13} \times \sqrt{13})$ surface reconstruction.

Importantly, the $(\sqrt{13} \times \sqrt{13})$ surface reconstruction can always be recovered via Se etching under DC current heating to about 980 °C, irrespective of the sample history. Subsequent UHV annealing once again produces the (2×1) reconstruction. This is not possible with AC heating (Figure 3.12). This suggests that uni-directional current flow helps smoothen the terraces via surface electro-migration. AC current heating suppresses electro-migration over large distances, thus resulting in a rougher surface.

3.4 Oxygen Vacancy Concentration of Se-etched STO

We attempted to quantify the oxygen vacancy concentration of Se-etched STO by studying the Ti $2p$ core level spectrum. The presence of oxygen vacancies reduces the oxidation state of the Ti^{4+} ion to Ti^{3+}, which should be detectable in XPS. The Ti^{3+}/Ti^{4+} intensity ratio in the Ti $2p$ core level spectrum provides a means to estimate the oxygen vacancy concentration within the escape depth of the XPS measurement (Ohsawa et al., 2016; Kim et al., 2023; Baek et al., 2020).



(a) AC current

(b) DC current

(c) AC current zoom in

Figure 3.11: RHEED images of Se-etched STO under AC current heating. AC current heating was followed by DC current heating while keeping the temperature and Se flux the same. The blue arrows in (c) indicate the original (1×1) RHEED streaks. All RHEED images were taken with the incident beam along the STO [100] direction.

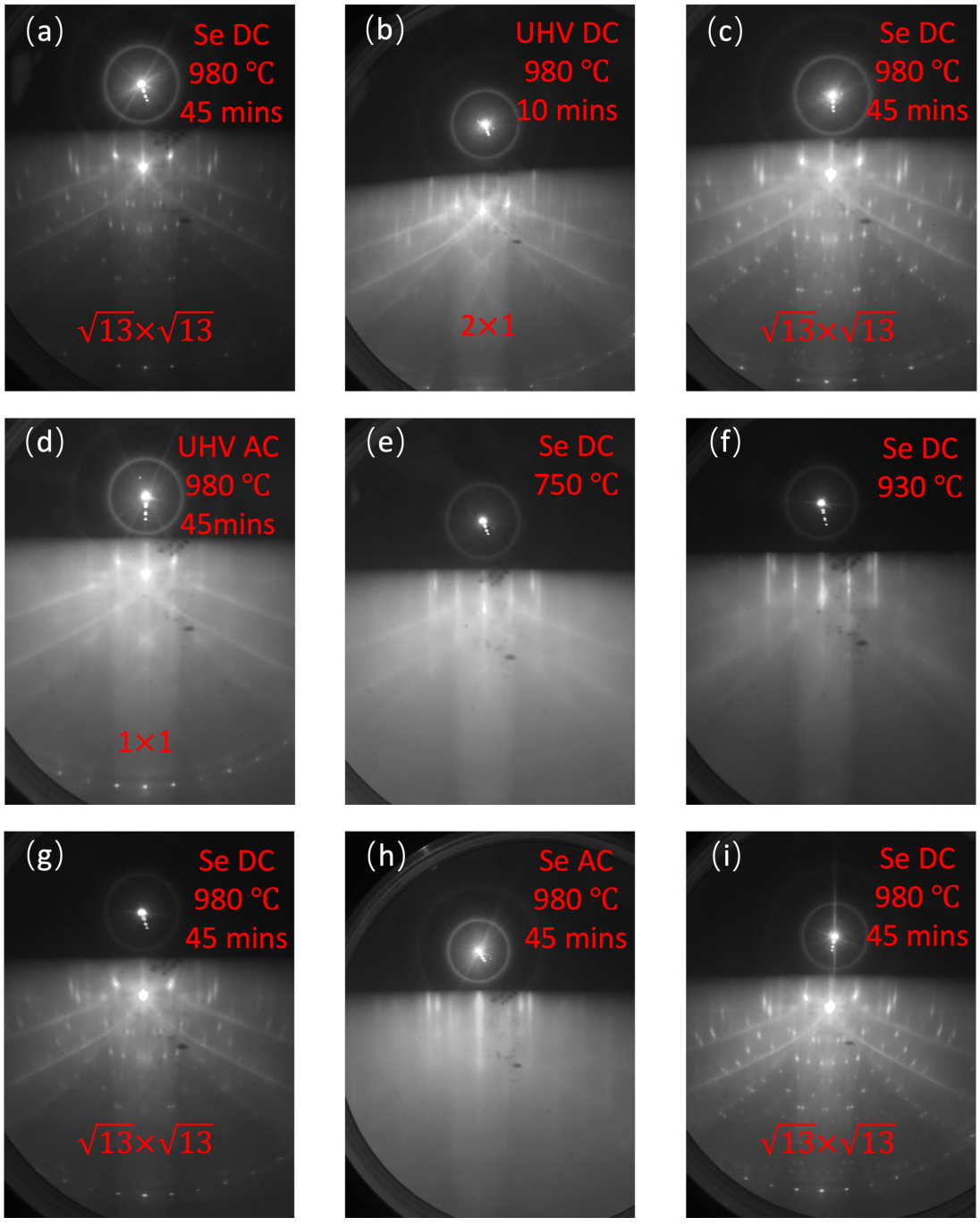
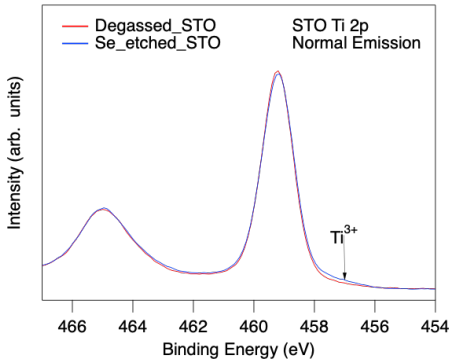


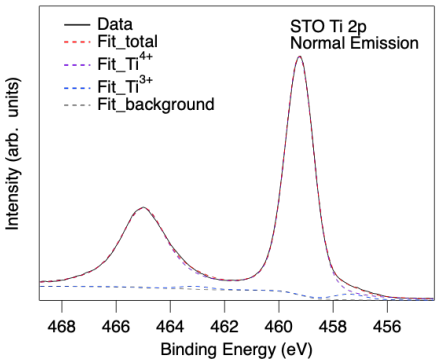
Figure 3.12: RHEED patterns with annealing history of the STO surface, including a switch between DC and AC current heating. All RHEED patterns were taken with the incident beam along the along STO [100] direction.

We first compare the Ti $2p$ normal emission spectrum of degassed (500 °C) STO to that of Se-etched STO and look for a shoulder on the low-binding energy side of the main $2p_{3/2}$ peak, see Figure 3.13a. It is evident that the intensity of this shoulder is very small, suggesting that the number of oxygen vacancies is also small, We fitted the Ti $2p$ spectrum with four Voigt line-shapes, representing the $2p_{3/2}$ and $2p_{1/2}$ peaks of the Ti^{3+} and Ti^{4+} ions. We assume a Shirley background. The spin-orbit splitting of the $2p_{3/2}$ and $2p_{1/2}$ core levels were constrained to their atomic value of 5.7 eV. The branching ratio of the $2p_{1/2}$ and $2p_{1/2}$ core levels is supposed to be 0.5, but an energy loss feature at $\sim$ 6.5 eV from the main $2p_{3/2}$ line coincides almost perfectly with the $2p_{1/2}$ spectrum. Rigorously speaking, one should fit the spectrum with the knowledge of the lineshape of the energy-loss peak, which is quite complicated. Instead, we no longer restrain the branching ratio of the Ti^{4+} core level to its theoretical value of 0.5. This is a pragmatic way to account for the presence of the loss peak under the $2p_{1/2}$ spectrum. Meanwhile, the branching ratio of the Ti^{3+} core level remains restricted to 0.5 as those peaks do not overlap the energy-loss feature.

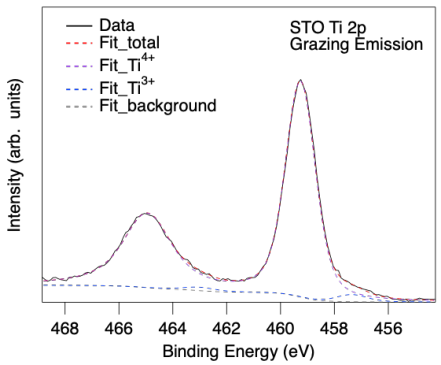
From the fitting (Figure 3.13b), the energy shift between the Ti^{3+} and Ti^{4+} core levels was 1.8 eV, consistent with published data. The ratio of Ti^{3+}/Ti^{4+} core level intensities is 2.7% $\pm$ 2.3%. The large error is due to the very low intensity of the Ti^{3+} core level. Grazing emission (grazing angle 60°) spectra displayed a similar result (Figure 3.13c). Here, the intensity ratio of Ti^{3+}/Ti^{4+} core levels was 3.4% $\pm$ 3.3%. Considering the large error, we believe that the difference between normal and grazing emission data are within the margin of error. Moreover, these spectra are hardly distinguishable from those obtained from samples that were degassed at 500 °C and never subjected to high temperature treatment. Specifically, we find that the core levels of degassed sample #208 almost perfectly overlap with those of Se-etched sample #220. In other words, the vacancy content of the Se-etched STO sample is insignificant as other STO samples exhibit similar vacancy levels, see Figure 3.13d. The Te-etched sample even contained fewer vacancies, as compared to Se-etched sample #220. The fitting parameters are summarized in Table 3.4 and 3.5.



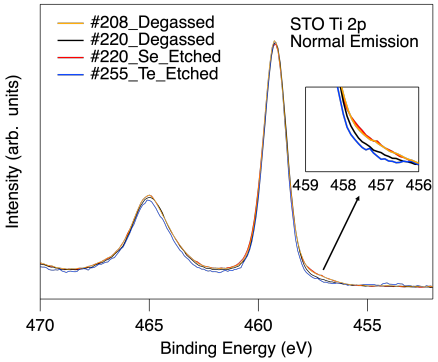
(a) Ti $2p$ core level spectrum: degassed STO versus Se-etched STO, recorded at normal emission



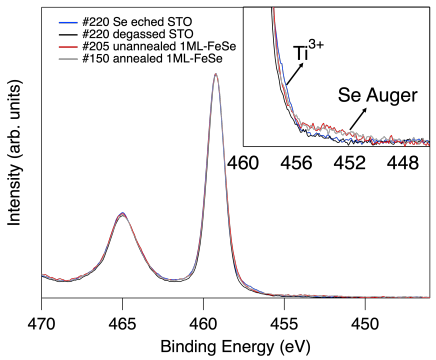
(b) Fitting of the Ti $2p$ core level spectrum at normal emission



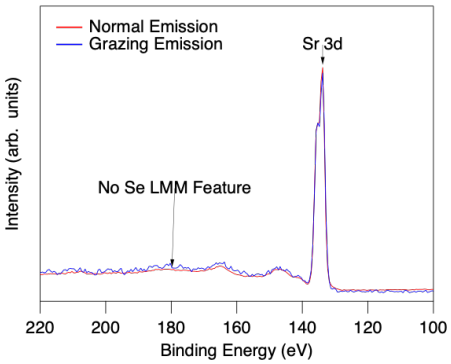
(c) Fitting of the Ti $2p$ core level spectrum at grazing emission



(d) Comparison of Ti $2p$ core level spectra for different STO substrates



(e) Comparison of Ti $2p$ core level spectra for different STO substrates with as-grown and post annealed FeSe monolayers.



(f) Se LMM Auger spectrum of Se-etched STO

Figure 3.13: XPS study of selenium etched STO

Table 3.4: Fitting parameters for Ti $2p$ in normal emission

Parameters	Ti^{4+}	Ti^{3+}
Gaussian width/eV	0.6177 ± 0.0115	Same as Ti^{4+}
Doublet ratio	0.6395 ± 0.0259	0.5 ± 0
$E_{2p_{3/2}}$/eV	459.0911 ± 0.00327	457.2532 ± 0.159
Peak intensity $A_{2p_{3/2}}$	96436 ± 722	2359 ± 793
Spin orbit split/eV	5.7459 ± 0.0151	5.7 ± 0
Lorentz width $2p_{3/2}$/eV	0.1966 ± 0.0147	0.274 ± 0.219
Lorentz width $2p_{1/2}$/eV	0.7685 ± 0.0287	0.264 ± 0.281
Background intensity $2p_{3/2}$	0.0286 ± 0.0104	-0.023 ± 0.813
Background intensity $2p_{1/2}$	0.012 ± 0.019	0.225 ± 0.934

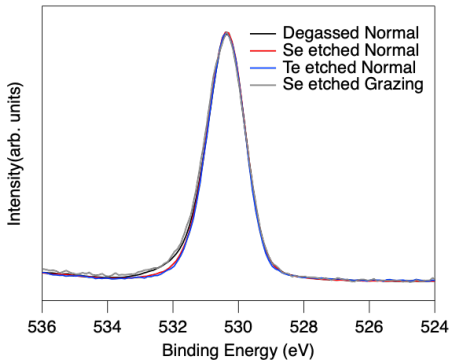
Table 3.5: Fitting parameters for Ti $2p$ in grazing emission

Parameters	Ti^{4+}	Ti^{3+}
Gaussian width/eV	0.617 ± 0	Same as Ti^{4+}
Doublet ratio	0.6383 ± 0.0385	0.5 ± 0
$E_{2p_{3/2}}$/eV	459.0437 ± 0.00526	457.121 ± 0.166
Peak intensity $A_{2p_{3/2}}$	7272.7 ± 91.6	242.2 ± 79.5
Spin orbit split/eV	5.7324 ± 0.0235	5.7 ± 0
Lorentz width $2p_{3/2}$/eV	0.25606 ± 0.00782	0.27 ± 0.25
Lorentz width $2p_{1/2}$/eV	0.8266 ± 0.0415	0.296 ± 0.315
Background intensity $2p_{3/2}$	0.0283 ± 0.0141	-0.003 ± 0.512
Background intensity $2p_{1/2}$	0.0226 ± 0.0252	0.39 ± 1.05

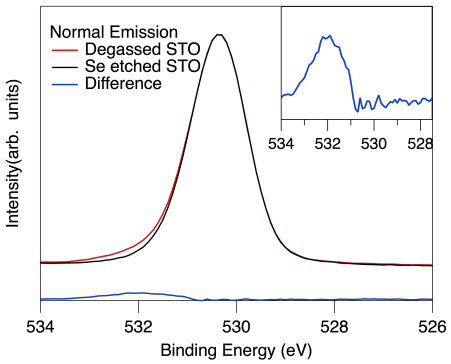
Post annealing is considered a crucial step towards achieving high T_c in monolayer FeSe films. Our ARPES data of post annealed FeSe monolayers, to be discussed in Chapter 5, indicate that the filling of the electron pocket at M is sufficient for high temperature superconductivity. In principle, the chemical interaction between the deposited Fe atoms and the outer TiO_x layer of the STO substrate could alter the concentration of oxygen vacancies at the interface, and thereby provide dopant charges for the FeSe layer. However, our Ti $2p$ core level data of post annealed FeSe monolayers on STO show no significant increase of the Ti^{3+}/Ti^{4+} intensity ratio. (Figure 3.13e). Again, the Ti^{3+}/Ti^{4+} intensity ratio seems less than 2%. Note that the presence of a nearby Se LMM Auger peak may even contribute to the Ti^{3+} core level intensity. Our results thus indicate that the increase in carrier concentration in the FeSe film with post annealing can not be attributed to vacancy formation in the substrate.

Finally, Figure 3.13f shows that the most intense Se feature in the XPS spectrum, namely the LMM Auger peak, is barely detectable for the Se-etched STO surface, indicating that little or no Se is incorporated into the substrate during etching.

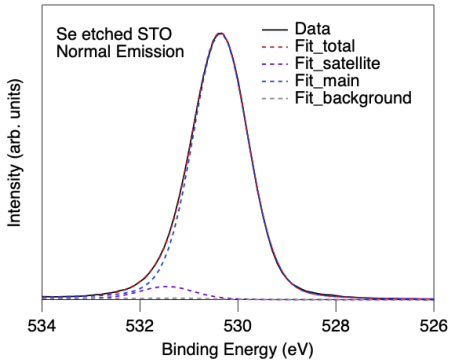
Oxygen $1s$ core level spectra were acquired to investigate the various oxygen species at the STO surface, including oxygen bonded to Ti or Sr or oxygen present as a surface contaminant such as OH^-. After Se etching and Te etching, the O $1s$ spectra look exactly alike (Figure 3.14a), suggesting that there are no significant differences in surface termination and/or cleanliness. The normal emission spectrum of the degassed sample reveals a shoulder on the high-binding energy side, which is almost eliminated upon Se etching. There are no noticeable changes on the low binding energy side. The differences before and after Se etching are plotted in Figure 3.14b. Evidently, the spectrum of the degassed sample contains a chemically shifted component at about 1.6 ± 0.1 eV from the main line. This agrees with the chemical shift of chemisorbed OH^- (Kim et al., 2023). Its intensity ratio with respect to the main O $1s$ is about 3.3%. Unfortunately, we do not have the corresponding data at grazing emission.



(a) Comparison of STO substrates before and after etching from the same sample (except for Te etching)



(b) Comparison between degassed STO and Se-etched STO from the same sample



(c) Fitting of the normal emission O 1*s* core level spectrum of Se-etched STO

Figure 3.14: XPS study of the O 1*s* core level for various STO substrates

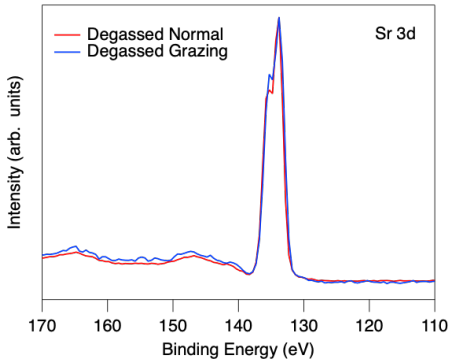
The grazing emission spectrum of the Se-etched STO overlaps almost perfectly with the normal emission spectrum of degassed STO. Both exhibit a clear shoulder. The spectrum can be fitted with two Voigt line shapes with an energy split of 1.1 ± 0.1 eV between the two lines (Figure 3.14c). The fitting parameters are listed in Table 3.6 . The high binding energy component has been attributed to the O $1s$ core level of SrO (Kim et al., 2023). The main peak is attributed to bulk STO, assuming there is no discernible distinction between oxygen bonded to Ti or Sr in bulk STO. The presence of the shifted O $1s$ core level might indicate the presence of small SrO patches on the surface, perhaps because Se etching may not produce uniform results all across the rather large viewing area of XPS. We will discuss this issue in section 3.5.

3.5 SrO versus TiO_x Surface Termination

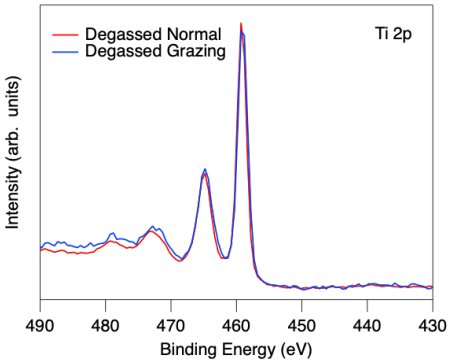
We return to the discussion of the surface termination of Se-etched STO, *i.e.*, whether the surface is terminated by a single TiO_x layer, a double TiO_x layer, a SrO layer, or a mixture thereof. Figure 3.15 (a)−(d) shows a series of spectra obtained from a survey scan. They are all normalized with respect to the Sr $3d_{5/2}$ spectrum. At first sight, there are no significant differences between the spectra acquired at normal emission

Table 3.6: Fitting parameters for O $1s$ in normal emission

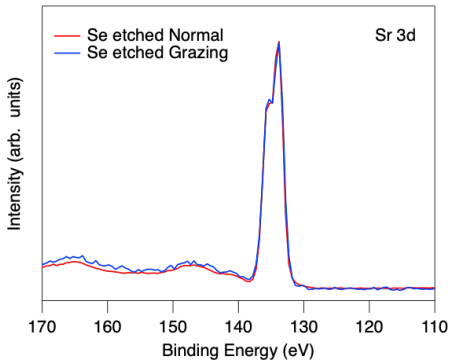
Gaussian width/eV	0.72684 ± 0.00892
Ratio	0.0410 ± 0.0054
E/eV	530.26 ± 0.004
Peak intensity A	16179 ± 1860
Energy shift/eV	1.1 ± 0.1
Lorentz width main/eV	0.1111 ± 0.0098
Lorentz width shoulder/eV	-0.036 ± 0.312
Background intensity main	0.0033 ± 0.0162
Background intensity shoulder	0.003 ± 0.392



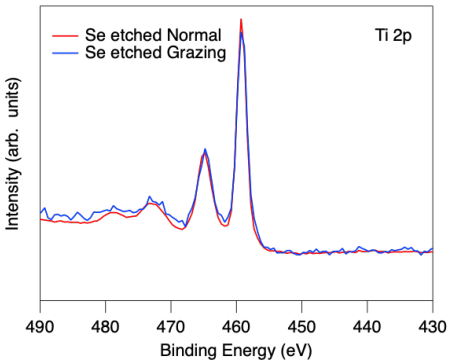
(a) Sr 3*d* of the degassed STO



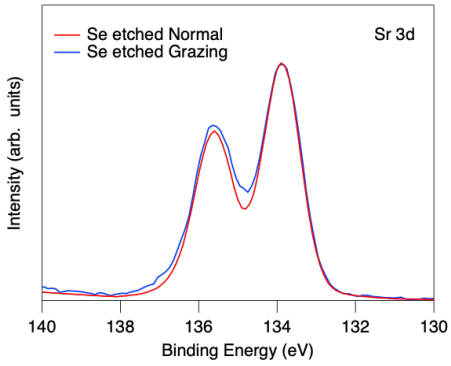
(b) Ti 2*p* of the degassed STO



(c) Sr 3*d* of the Se-etched STO



(d) Ti 2*p* of the Se-etched STO

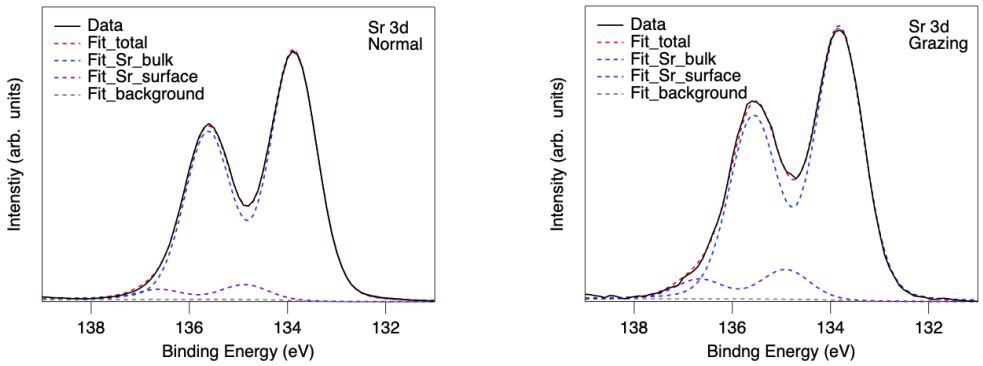


(e) Comparison of Se-etched STO at different emission geometry

Figure 3.15: XPS study on SrO/TiO_x termination

and 60° grazing emission, no matter whether the surface has only been degassed or whether the surface was subsequently etched with Se.

A close look at the Sr 3*d* core level spectrum reveals an excess intensity under the $3d_{3/2}$ spectrum in grazing emission. Spectral fitting with a single spin-orbit split doublet produces a branching ratio far greater than the expected 2/3 value for the 3*d* core level spectrum, indicating that there is a hidden peak underneath (Ohsawa et al., 2016; Kim et al., 2024; Bachelet et al., 2009). We therefore fitted the Sr 3*d* spectrum with two spin-orbit split doublets, using the theoretical branching ratio of 2/3 and documented spin-orbit splitting of 1.7(5) eV, and obtained an excellent fit by shifting the additional core level spectrum to 1.00 ± 0.05 eV higher binding energy (Figure 3.16). The fitting parameters are listed in Table 3.7 and 3.8. An interpretation for the appearance of the shifted component was provided by Bagus *et al.* who attributed this to a surface core level shift associated with the reduction of the Madelung potential at the surface of SrO (Bagus et al., 2019). A similar interpretation was proposed by Vanacore *et al.* for the case of STO (Vanacore et al., 2010). No such shift would be expected on the O 1*s* core level as the initial-state valence charge distribution on the surface oxygen is more diffuse, which offsets the Madelung contribution to the ionic potential (Bagus et al., 2019). The main line intensity of the Sr 3*d* core level spectrum would then be associated with the deeper



(a) Se-etched STO at normal emission **(b)** Se-etched STO at grazing emission

Figure 3.16: Fitting on Sr 3*d* spectra

Table 3.7: Fitting parameters for Sr $3d$ in normal emission

Parameters	Bulk SrO	Surface SrO
Gaussian width/eV	0.61987 ± 0.00415	Same as bulk Sr
Doublet ratio	0.6667 ± 0	Same as bulk Sr
$E_{3d_{5/2}}$/eV	133.7696 ± 0.0029	134.7724 ± 0.0518
Peak intensity $A_{3d_{5/2}}$	46269 ± 104	2784 ± 274
Spin orbit split/eV	1.756 ± 0	Same as bulk Sr
Lorentz width $3d_{5/2}$/eV	0.08 ± 0	Same as bulk Sr
Lorentz width $3d_{3/2}$/eV	0.08 ± 0	Same as bulk Sr
Background intensity $3d_{5/2}$	0.00672 ± 0	Same as bulk Sr
Background intensity $3d_{3/2}$	0.000458 ± 0	Same as bulk Sr

Table 3.8: Fitting parameters for Sr $3d$ in grazing emission

Parameters	Bulk SrO	Surface SrO
Gaussian width/eV	0.63573 ± 0.00628	Same as bulk Sr
Doublet ratio	0.6667 ± 0	Same as bulk Sr
$E_{3d_{5/2}}$/eV	133.7180 ± 0.0037	134.8208 ± 0.0427
Peak intensity $A_{3d_{5/2}}$	45777 ± 158	4983 ± 347
Spin orbit split/eV	1.755 ± 0	Same as bulk Sr
Lorentz width $3d_{5/2}$/eV	0.08 ± 0	Same as bulk Sr
Lorentz width $3d_{3/2}$/eV	0.08 ± 0	Same as bulk Sr
Background intensity $3d_{5/2}$	0.00672 ± 0	Same as bulk Sr
Background intensity $3d_{3/2}$	0.000458 ± 0	Same as bulk Sr

SrO layers. The intensity ratio of the surface and bulk components is $6.0\% \pm 0.6\%$ in normal and $10.9\% \pm 0.8\%$ in grazing emission. This allows us to estimate the area fraction of the SrO terminated surface using a simple layer-by-layer attenuation model.

Let us assume that the SrO area fraction in the outermost surface layer is m (Figure 3.17). The photoelectron intensity of the exposed SrO layer is then written as mI_0, where I_0 would be the photoelectron intensity for a full SrO layer, *i.e.*, $m = 1$. The attenuation factor of the Sr $3d$ photoelectrons originating from deeper layers is $z = e^{-d/(cos\theta\lambda)}$, where $d = 3.905$ Å is the lattice constant of STO; $\lambda = 2.6$ nm is the inelastic mean free path (Baeumer et al., 2015). Accordingly, we have:

$$I_{\mathrm{Sr}}^{\mathrm{surface}} = mI_0 \tag{3.1}$$

$$I_{\mathrm{Sr}}^{\mathrm{bulk}} = mI_0 \sum_{n=1}^{\infty} z^n + (1-m)I_0 \sum_{n=0}^{\infty} z^{n+1/2} \tag{3.2}$$

From Eq. (3.1) and (3.2) we evaluate $I_{\mathrm{Sr}}^{\mathrm{surface}}/I_{\mathrm{Sr}}^{\mathrm{bulk}}$ as a function of z and m. Using the experimental intensity ratio and the known value of z, we solve it for m with the fitting results (10.9% for grazing and 6.0% for normal emission). Using the normal emission data, we find that the SrO area fraction is 0.39 ± 0.04. In other words, about

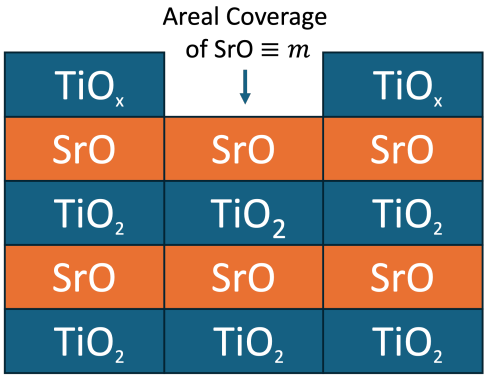


Figure 3.17: Schematic of partially SrO terminated STO surface.

$39\% \pm 4\%$ of the surface would be terminated by STO and $61\% \pm 4\%$ by TiO_x. A similar analysis at grazing emission yields $34\% \pm 3\%$ and $66\% \pm 3\%$, respectively.

Alternatively the high-binding energy component could be explained when we consider the structural model of the $(\sqrt{13} \times \sqrt{13})$ surface reconstruction. This reconstruction is derived from a TiO_2 double layer with both TiO_6 and TiO_5 polyhedral units in the outermost surface layers. The $(\sqrt{13} \times \sqrt{13})$ unit cell contains 13 Sr atoms, eight of which are fully coordinated, similar to their bulk environment, while five other atoms are undercoordinated and fully exposed to the vacuum (Figure 3.18). In this case, it would be reasonable to associate the shifted core level with the exposed Sr atoms. This would amount to a fractional coverage of $5/13 = 0.385$. This level of agreement the experimentally derived area fraction above is no doubt somewhat fortuitous for such a simple toy model, but it suggests that this interpretation of the Sr $3d$ core level spectrum is probably correct, especially because the surface is uniformly covered by the $(\sqrt{13} \times \sqrt{13})$ structure, as shown by RHEED, while

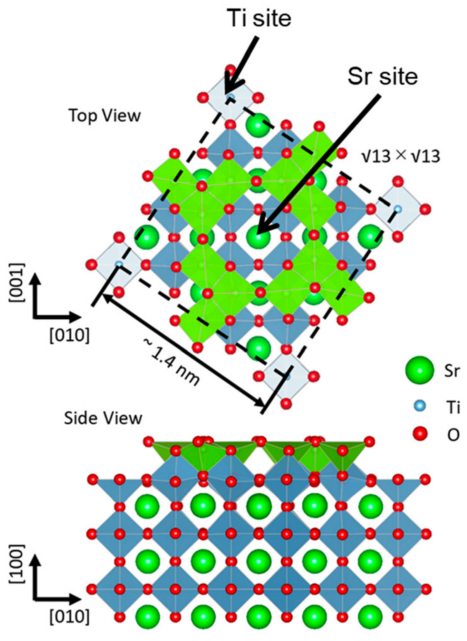


Figure 3.18: Structure of the surface $(\sqrt{13} \times \sqrt{13})$ reconstruction (Kienzle et al., 2011; Katsube et al., 2023).

STM measurements always reveal single unit-cell-high steps. A mixed SrO and TiO_x termination thus seems unlikely.

3.6 Conclusions

The synthesis of high quality FeSe thin films on the STO(001) surface demands a surface preparation procedure that produces atomically-flat TiO_x terminated terraces. This requirement can be met via high-temperature annealing at about 980 °C in UHV. This procedure, however, unavoidably leads to the formation of oxygen vacancies, a process that is difficult to control. Depending on the vacancy content, the surface exhibits a variety of ordered superstructures or surface reconstructions that often coexist. We obtained excellent and highly reproducible results by annealing the STO(001) substrate under a selenium flux inside the MBE chamber, which is often referred to as UHV selenium etching. This procedure results in wide, atomically-flat TiO_x terminated terraces with straight step edges. The Se-etched surface exhibits the $(\sqrt{13} \times \sqrt{13})$ reconstruction with only very few vacancy defects and no traceable amount of Se. This method is preferred over oxygen annealing because it produces atomically clean STO surfaces under MBE conditions without the need for backfilling the UHV chamber with 'dirty' oxygen gas. Sr $3d$ core level spectroscopy indicates the presence of Sr atoms at the surface, producing a surface core level on the high binding-energy side of the bulk spectrum. The relative intensity of the surface and bulk core levels is consistent with the structural model of the $(\sqrt{13} \times \sqrt{13})$ reconstruction. We will use this substrate termination for the growth of high-quality FeSe and FeTe thin films, as described in the following chapters. As we will see, the films are all electron-doped even though there are very few oxygen vacancies to provide the needed charge for establishing superconductivity. This suggest that the doping of the films does not require an oxygen deficient STO substrate.

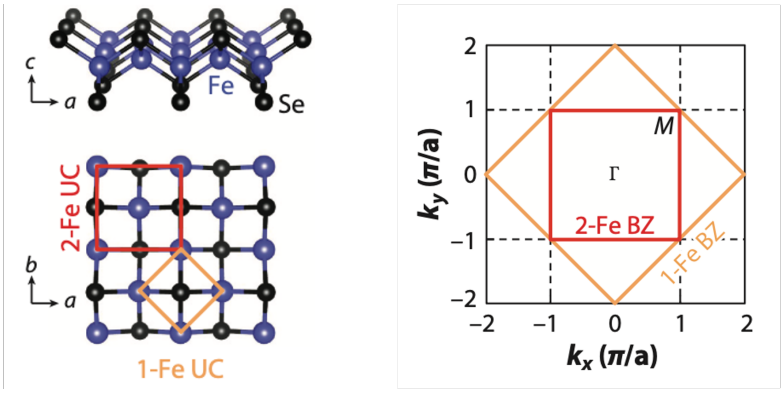
Chapter 4

Bulk FeSe

4.1 Crystal Structure and Phase Diagram of FeSe

The superconducting iron selenide phase (or β-phase) has the tetragonal PbO type structure (space group $P4/nmm$). The compound tends to be slightly off-stoichiometric, i.e., $Fe_{1+\varepsilon}Se_1$, meaning it is often Fe rich. We simply write FeSe (Hsu et al., 2008). The lattice parameters are $a = b = 3.77{-}3.82$ Å and $c = 5.52{-}5.58$ Å. In the conventional unit cell, there are two Fe and two Se atoms with Fe at the (0, 0, 0) and (1/2, 1/2, 0) positions and Se at the (1/2, 0, 0.26) and (0, 1/2, 0.74) positions. The β-phase is a layered (slab) structure with a van der Waals gap in between the Se layers (Figure 4.1a Top). Each FeSe slab consists of a two dimensional Fe layer with Se atoms above and below. For theory calculations, one often uses the primitive unit cell with only one FeSe unit. In that case, the size of the first Brillouin zone would be doubled (Figure 4.1b).

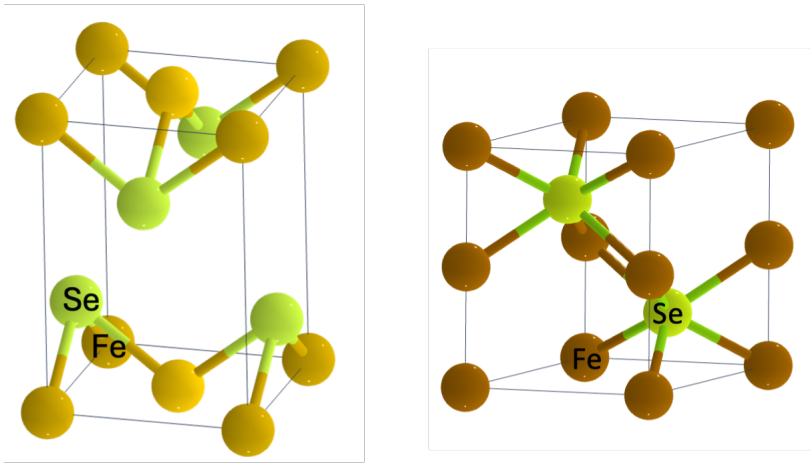
Another stable FeSe phase crystallizes in the hexagonal NiAs structure (space group $P6_3/mmc$), which is conventionally called the δ-phase (Figure 4.2b). The lattice parameters are $a = 5.82{-}5.91$ Å, $c = 5.52{-}5.58$ Å. Similarly there are two Fe and two Se atoms in the unit cell. However, it is usually Se rich, *i.e.*, one should write $Fe_1Se_{1+\varepsilon}$.



(a) Layered structure of β-FeSe

(b) Brillouin zone of β-FeSe

Figure 4.1: β-FeSe in real space and reciprocal space (Huang and Hoffman, 2017).



(a) Tetragonal FeSe

(b) Hexagonal FeSe

Figure 4.2: Crystal structures of tetragonal and hexagonal FeSe. The images are taken from The Material Project.

Apart from tetragonal and hexagonal FeSe, there is the γ-phase (monoclinic deformed δ-phase), Fe_7Se_8 (orthorhombic), $FeSe_2$ (marcasite) and some other metastable phases. Figure 4.3 shows the complete phase diagram. Details can be found in the reference (Okamoto, 1991).

The structure and properties of FeSe are very sensitive to the precise stoichiometry (Figure 4.4) (McQueen et al., 2009; Chen et al., 2014). This gives rise to confusion and sometimes contradictory results in the literature, as it is usually very difficult to determine the stoichiometry precisely, especially in ultra-thin film materials. Studies of superconductivity in ultra-thin FeSe films require very precise control of the growth conditions, and very accurate measurements of the stoichiometry. This will be discussed in the following sections.

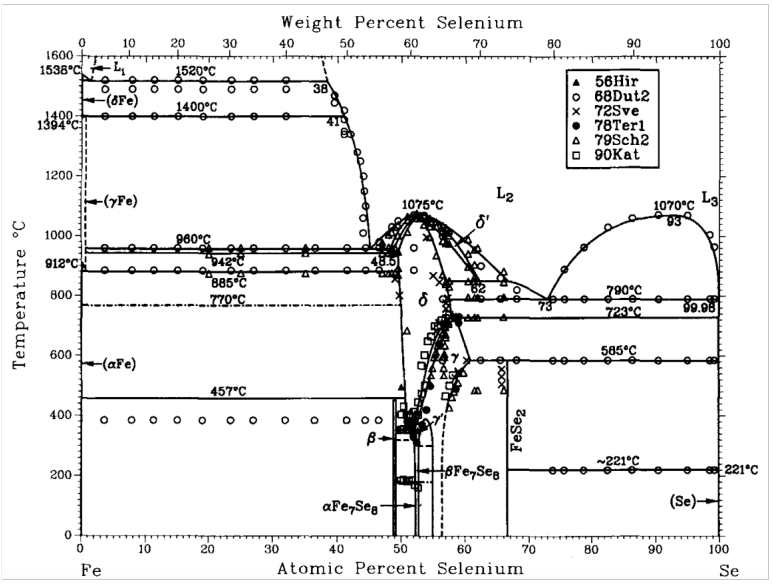


Figure 4.3: Bulk FeSe phase diagram (Okamoto, 1991).

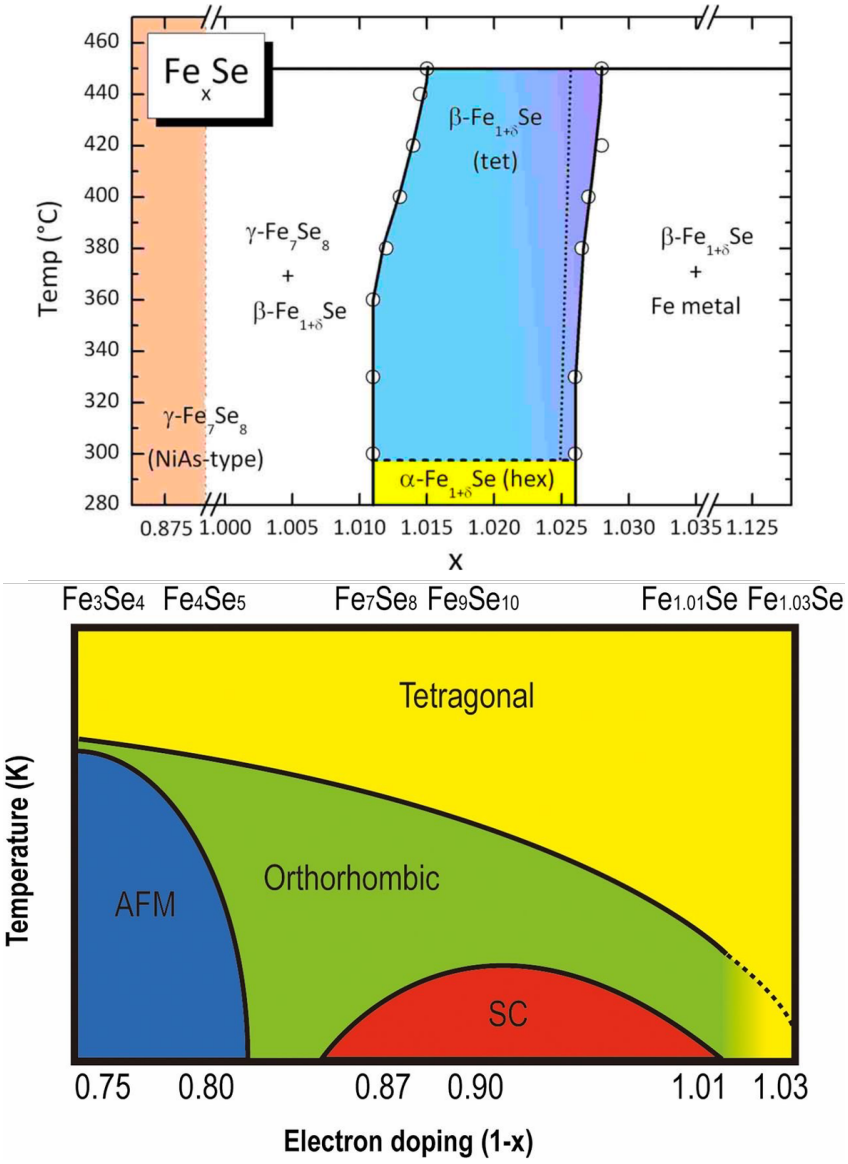


Figure 4.4: Phase diagram near the β-phase region, showing the extreme sensitivity of superconductivity to stoichiometry (McQueen et al., 2009; Chen et al., 2014).

4.2 Epitaxial Growth of FeSe Films on STO(001)

4.2.1 Substrate temperature: 2D step-flow growth vs. 3D growth

The growth mode of an epitaxial thin film depends on the substrate temperature. When the temperature is too low, the crystallinity would be poor and the film morphology would be rough. Since the mobility of the adatoms is low, small nuclei are dispersed across the substrate terraces, producing a 'patchy' appearance. As those patches merge at higher coverage, grain boundaries are formed. At higher temperature, growth defects would be fewer. Ideally, one would like to achieve step-flow growth where adatoms nucleate at the step edges and the growth front gradually spreads across the terrace. In our situation, FeSe starts to decompose at 500−600 °C, meaning that the growth temperature should be kept below 500°C. In order to grow β-FeSe, the stoichiometry should be close to 1:1. Here, we kept the temperature of the substrate T_{sub} well below the temperature of Fe source T_{Fe} but well above that of the Se source, T_{Se}. Figure 4.5 represents two different growth modes of FeSe on STO(001). The two films were prepared exactly the same way, except that we chose a different growth temperature for the second FeSe layer. Prior to FeSe deposition, STO substrates were etched *in-situ* with Se flux in order to obtain the $(\sqrt{13}\times\sqrt{13})$ surface reconstruction. The Fe and Se sources were kept at 1250 °C and 180 °C, respectively. The first FeSe layer was grown at a substrate temperature of around 450−460 °C for both samples. (The small temperature variation is due to the existence of a small thermal gradient across the sample). The second FeSe layer was grown at 370 °C and at 460 °C. In the first case, we achieved step-flow growth where the incoming adatoms remain confined to their landing terrace and diffuse to the step edge or growth front. Growth at 460 °C resulted in multilayer growth, where single, double, and triple layer thicknesses coexist on the same STO terrace. While on the one hand, the adatom mobility is clearly high enough to diffuse across the entire terrace, the temperature

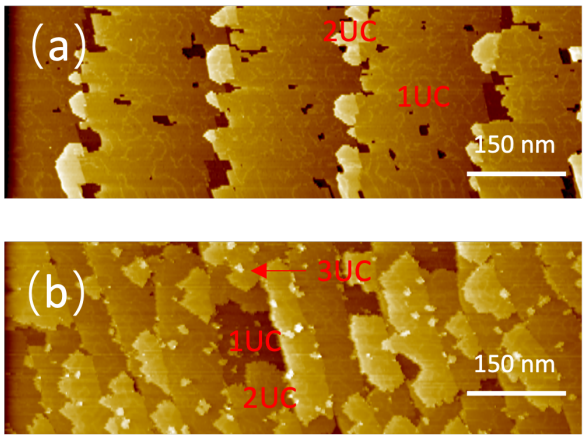
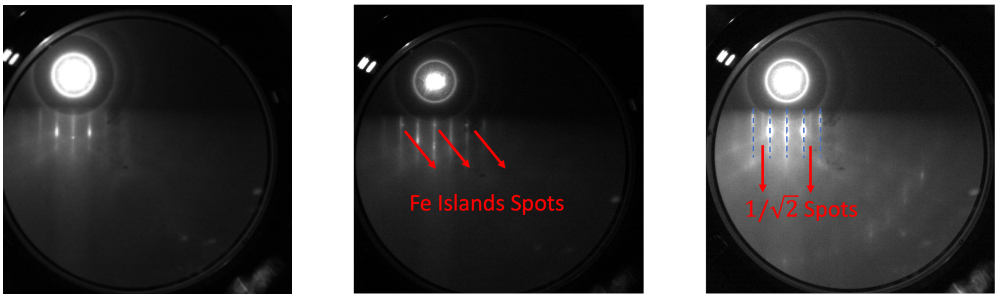


Figure 4.5: Effect of substrate temperature on the growth of FeSe films: (a) 2D step-flow growth mode, $T_{\text{sub}} = 370$ °C. (b) Multilayer growth, $T_{\text{sub}} = 460$ °C

is evidently high enough for those atoms to move across the step edges to start the next layer before the first one is completed. Another aspect to consider is that fewer Se atoms stick when the temperature is higher, which can lead to the formation of small Fe nuclei which in turn can lead to non-uniform growth.

4.2.2 Fe/Se flux ratio

As seen from bulk FeSe phase diagram, a slight change in stoichiometry could affect the physical properties or even produce a different phase. The Fe/Se ratio is determined by the Fe/Se source temperature, the substrate temperature, and the post annealing process. An added complication is that selenium easily condenses around the aperture of the effusion cell, so that the evaporation rate diminishes over time. In Figure 4.6, the substrate temperature during the growth of the first FeSe layer was 450 °C. Additional layers were grown at 370 °C. New transmission spots appear when the thickness of the film reaches three monolayers as indicated by the red arrows in Figure 4.6b. These spots are very close to the FeSe (02) streak and are attributed to the formation of small bcc Fe clusters. For the thicker 88 ML film, additional 45° rotated (1×1) pattern became visible as shown in Figure 4.6c. The transmission spots and extra RHEED streaks disappear when exposing the surface to

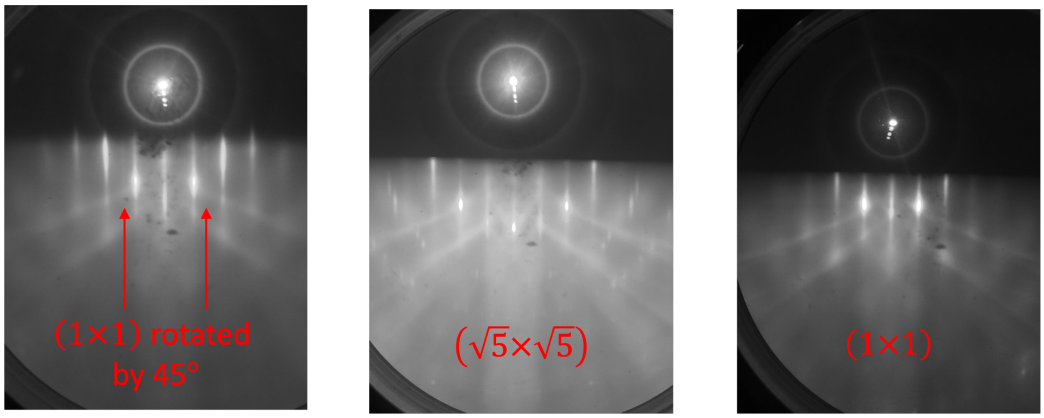


(a) 1ML FeSe **(b)** 3ML FeSe **(c)** 88ML FeSe (48 nm)

Figure 4.6: RHEED patterns of FeSe films grown under Fe rich conditions: (a) Monolayer FeSe reveals nice integer order RHEED streaks. (b) Additional transmission spots are formed when the thickness is about three monolayers. (c) Extra 45° rotated (1×1) pattern are formed for the 88 ML film. The blue dashed lines indicated the original FeSe (1×1) streaks. All the RHEED images were taken with the incident electron beam along the STO [100] direction.

a Se flux while keeping the Fe source closed. This suggest that the film was initially grown under Fe rich conditions, even though the substrate temperature was lowered and the Se flux exceeded that of Fe by almost one order of magnitude. The absence of bcc Fe clusters in the monolayer film, in spite the fact that its growth temperature was significantly higher, suggests that Se is more easily incorporated due to the interaction with the STO substrate. The 45° rotated (1×1) domain was also found in LEED (Figure 4.7d).

Further reduction of the substrate temperature to 350 °C resulted in Se rich conditions for the thick FeSe films. These films often display a $(\sqrt{5} \times \sqrt{5})$ superstructure, see Figure 4.7b and Figure 4.7e. This agrees with other studies that reported the formation of Fe_4Se_5 under Se rich conditions for bulk FeSe (Yeh et al., 2020), FeSe thin films (Liu and Zou, 2020), and monolayer FeSe on STO (Xue et al., 2023). The $(\sqrt{5} \times \sqrt{5})$ superstructure is due to vacancy ordering. The $(\sqrt{5} \times \sqrt{5})$ pattern disappears when the film is annealed at 350 °C for two hours. The most logical explanation is that excess Se is removed during prolonged annealing, so that the film becomes more stoichiometric. We should note that RHEED and LEED are



(a) RHEED: Fe rich **(b)** RHEED: Se rich **(c)** RHEED: Intermediate

(d) LEED: Fe rich **(e)** LEED: Se rich **(f)** LEED: Intermediate

Figure 4.7: RHEED and LEED patterns of thick FeSe films with different Fe/Se ratios: Fe rich (#155 sample), Se rich (#196 sample as-grown), intermediate (#196 sample after post annealing). The red arrows indicate the $(\sqrt{5} \times \sqrt{5})$ superlattice refelections. All the RHEED images were taken with the incident electron beam along the STO [100] direction. The growth condition is listed in Table 4.1.

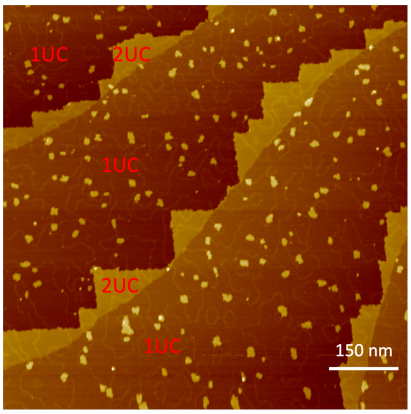
Table 4.1: Growth condition of the FeSe thick films on Se-etched STO: the substrate temperature and deposition time were listed in the monolayer/multilayer growth step and capping step, the annealing temperature and time was listed in the post annealing step.

Sample label	1st layer growth	Post anneal 1	Multilayer growth	Post anneal 2	Se capping
60 ML #155	371−377 °C 4.75 mins	372−377 °C 16 h	372−375 °C 5 h	367−375 °C 2 h	
90 ML #196	440−476 °C 4.75 mins		358−373 °C 7.5 h	351−393 °C 2 h	
90 ML #200	440−450 °C 4.75 mins		346−350 °C 7.5 h		
177 ML #246	430−453 °C 4.75 mins		350 °C 14 h		RT 0.5 h
177 ML #247	440−454 °C 4.75 mins		340−352 °C 14 h	337−350 °C 2 h	RT 0.5 h

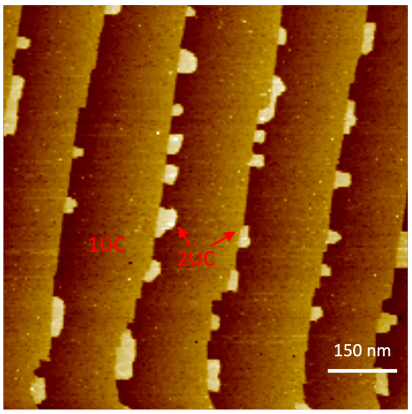
both surface sensitive so that the the $(\sqrt{5} \times \sqrt{5})$ superstructure may only be present near the surface.

4.3 Domain Wall and Dislocation Defects

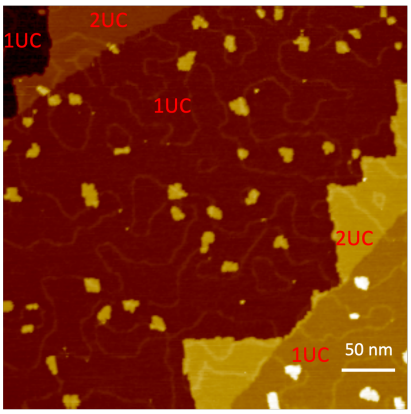
Two types of domain boundaries were found in monolayer FeSe grown on STO. The bright meandering lines in Figure 4.8a and 4.8c were found under Se rich conditions. After post annealing, the domain boundaries exhibit dark contrast. They are also straighter, as one would perhaps expect for a tetragonal structure; see Figure 4.8b and 4.8d. Our results agreed with Ge's observation (Ge, 2018). In addition, Ge proposed that the dark contrast domain boundaries are specular $[110]_{\mathrm{Fe}}$ edges; see the definition of the orientation in Figure 4.9. We lack the spatial resolution to determine the atomic structure of these domain boundaries, but we found that in the case of second layer FeSe, domain boundaries always appear to be bright and they



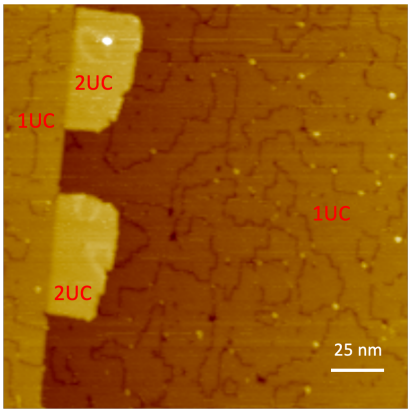
(a) Type 1: 900×900 nm^2



(b) Type 2: 900×900 nm^2



(c) Type 1: 400×400 nm^2



(d) Type 2: 200×200 nm^2

Figure 4.8: STM images of the two types domain boundaries on monolayer FeSe on STO.

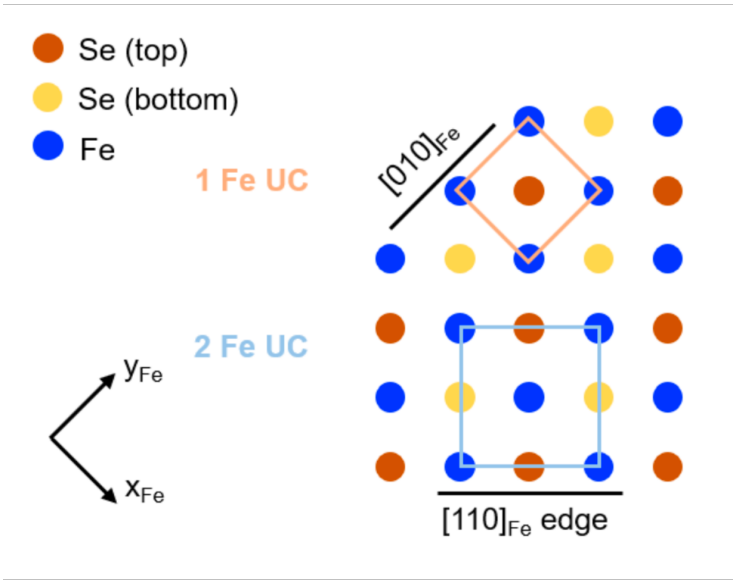
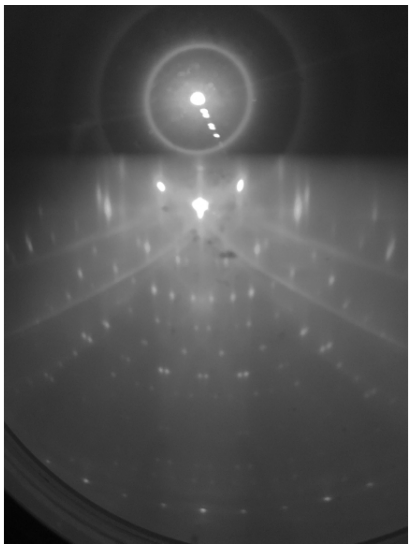


Figure 4.9: Domain wall orientation proposed by Ge (Ge, 2018).

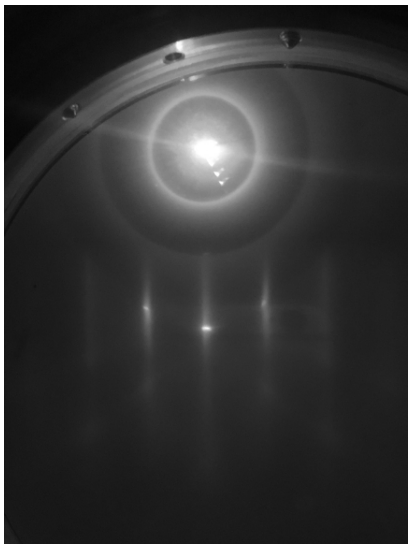
seamlessly connect to those present in the first layer. This suggests that they affect the nucleation and growth of the second layer.

Fan and Bang found that there was a 1/2-unit-cell phase slip between adjacent (2×1) FeSe domains no matter whether the domain walls appeared bright or dark. (Fan et al., 2015; Bang et al., 2013). They attributed the (2×1) reconstruction to the substrate (2×1) reconstruction, which in turn was attributed to oxygen vacancies in their STO. We occasionally found a (2×1) LEED pattern, even though our FeSe monolayer was grown on the STO $(\sqrt{13} \times \sqrt{13})$ substrate, see Figure 4.10. Moreover, we never observed the $(\sqrt{13} \times \sqrt{13})$ spots for the FeSe monolayer, even though the STO $(\sqrt{13} \times \sqrt{13})$ reconstruction is preserved below the monolayer (Si et al., 2022). It thus seems unlikely that the (2×1) reflections originate from the STO substrate. Instead, it is likely that they are a property of the FeSe film.

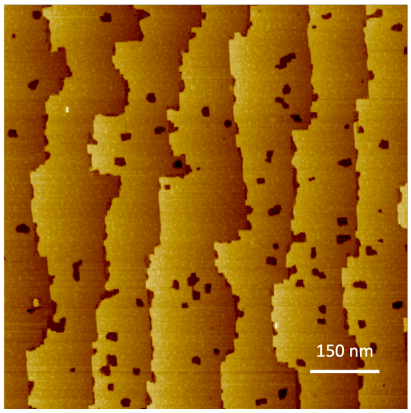
Since we heat our samples by driving a DC current through the sample, there is always a temperature gradient across the sample during thin film growth. This makes it possible to observe both bright and dark domain walls on the same sample. A monolayer FeSe sample was grown at 449−456 °C, annealed at 470−480 °C for 1 hour and at 373−378 °C for 17 hours. The bright and dark domain boundaries



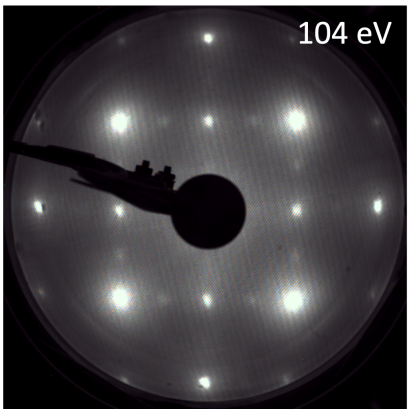
(a) RHEED: Se-etched STO



(b) RHEED: 1ML-FeSe//STO



(c) STM: 1ML-FeSe//STO

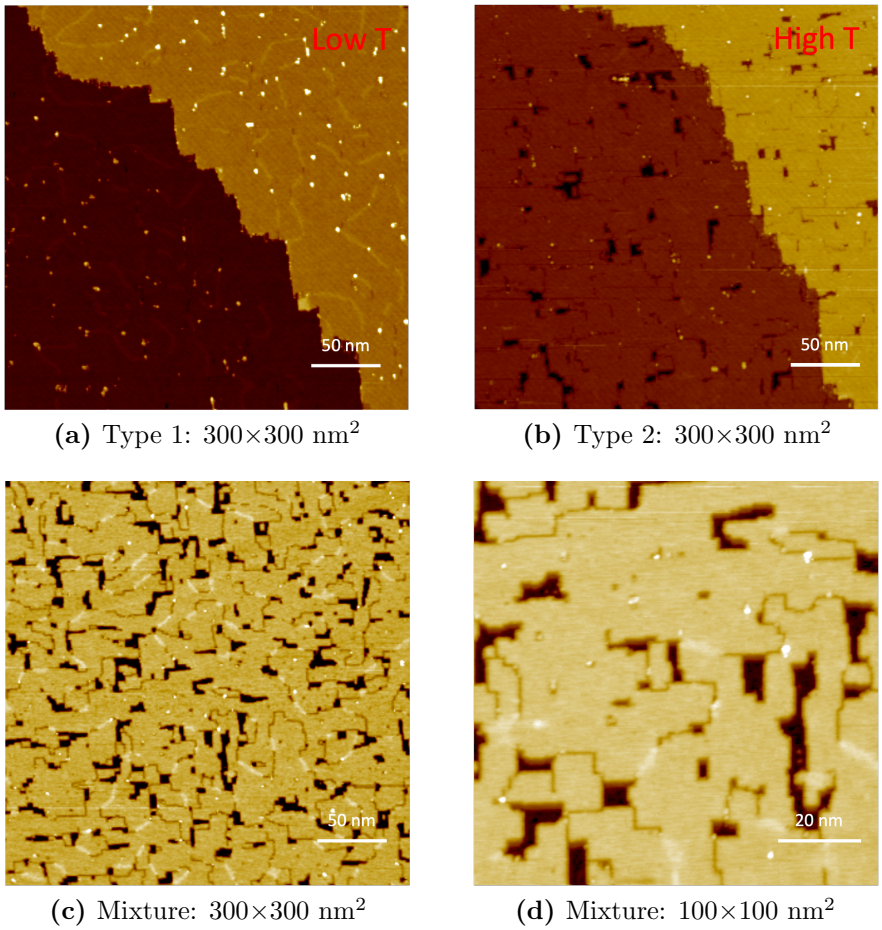


(d) LEED: 1ML-FeSe//STO

Figure 4.10: Observation of a (2×1) reconstruction on monolayer FeSe: Even though the STO substrate displayed a $(\sqrt{13} \times \sqrt{13})$ reconstruction, the FeSe (2×1) reconstruction could still be found in LEED. All the RHEED images were taken with the incident electron beam along the STO [100] direction.

were found at the low and high temperature side of the sample, respectively, as shown in Figure 4.11.

For the monolayer, it is possible to find both types of domain boundaries on the same area, depending on temperature. These results agree with the fact that post annealing converts Type 1 domain boundaries to Type 2, changing from bright contrast to a dark contrast. This contrast reversal could be due to the loss of Se atoms at the domain boundaries. However, second layer FeSe always exhibits bright domain walls, even after post annealing, This suggests that the STO/FeSe interface plays a role in the formation of the dark domain walls and that the changing contrast may be related to strain relaxation at the STO interface.



(a) Type 1: 300×300 nm^2 **(b)** Type 2: 300×300 nm^2

(c) Mixture: 300×300 nm^2 **(d)** Mixture: 100×100 nm^2

Figure 4.11: Effects of temperature on domain boundaries in monolayer FeSe.

When the film thickness approaches the bulk limit, all strain is presumably relaxed and the influence of the STO substrate should be negligible. Indeed, the bright domain walls (Figure 4.12 (a)−(b)) have disappeared and the STO terraces are no longer recognizable (Figure 4.12 (c)−(e)).

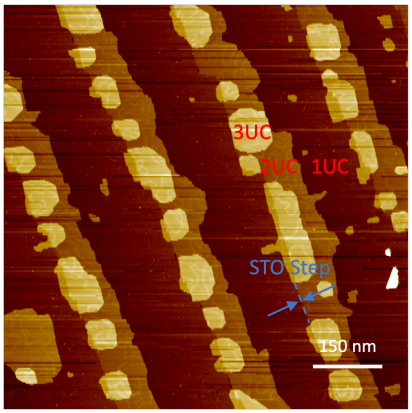
While as grown thick films tend to be quite rough, their morphology is markedly improved with post annealing, see Figure 4.13b. Figure 4.13c shows examples of screw dislocations that can lead to the formation of beautiful growth spirals. The screw location is at the center of the spiral. However, screw dislocations can also be found on Se-etched STO, as shown in Figure 4.13a. The screw dislocation in the FeSe film is not necessary related the substrate.

Thick FeSe films that are grown under Se rich condition and subsequently post annealed still exhibit a meandering step morphology, as shown in Figure 4.13c. Tiny 1−2 nm tall clusters decorate the step edges of the FeSe film, and are marked by red circles. These clusters pin the step edges at specific locations and prevent the formation of straight edges. These clusters could perhaps be eliminated upon prolonged high temperature annealing.

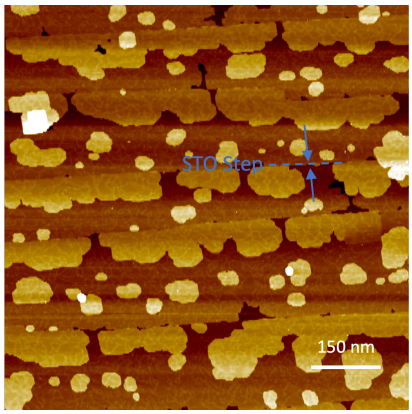
4.4 Strain Relaxation

The in-plane lattice parameter of the β-FeSe is 3.77 Å, which is about 3.5% smaller than that of bulk STO (3.90 Å). Thus, the FeSe monolayer should be under tensile strain. After growing multiple FeSe layers, the strain could be gradually relaxed. The lattice parameters of the FeSe can be measured by STM. However, STM is not very accurate for determining lattice constants as the piezo electric elements often need to be recalibrated. XRD is best suited to investigate lattice relaxation, although one needs rather thick films.

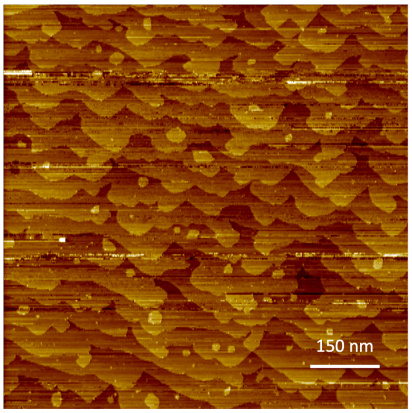
We grew two thick FeSe films under the same condition, one of which was post annealed. As will be shown, the film thickness corresponds to 177 ML FeSe. The unnnealed film is sample #246 and the post annealed film is sample #247. The



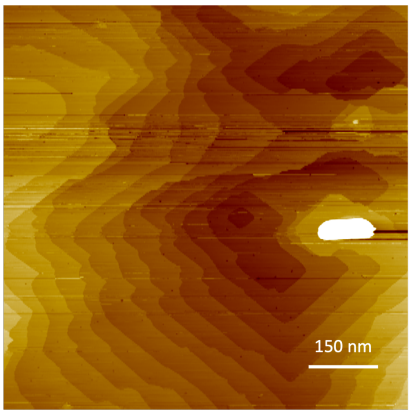
(a) 1.5 ML FeSe: 900×900 nm^2



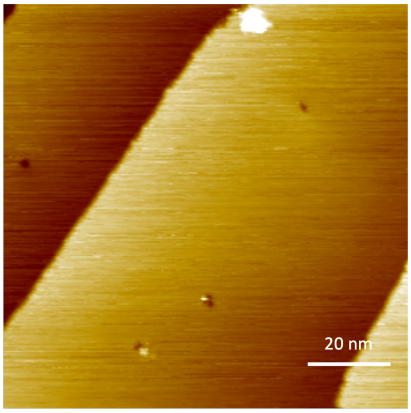
(b) 5 ML FeSe: 900×900 nm^2



(c) 60 ML FeSe: 900×900 nm^2

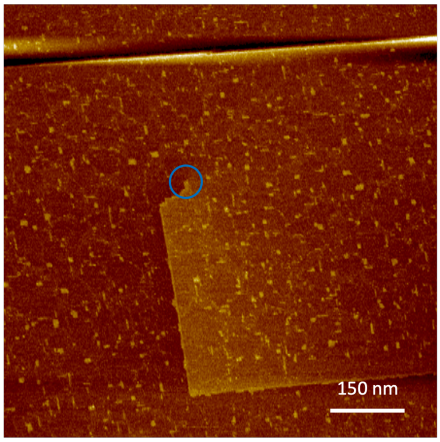


(d) 90 ML FeSe: 900×900 nm^2

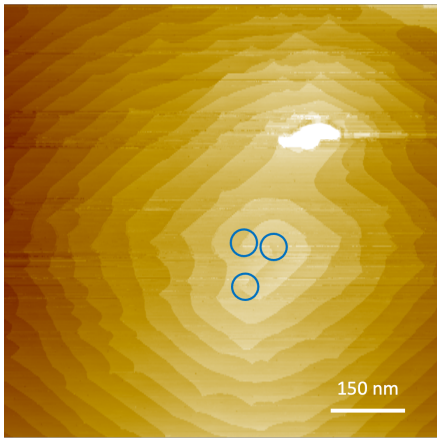


(e) 90 ML FeSe: 100×100 nm^2

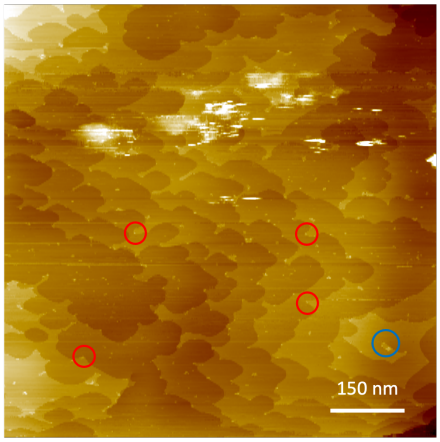
Figure 4.12: Strain relaxation of FeSe films on STO: The domain boundaries and STO terraces disappear as the film thickness approaches bulk limit. The blue arrows in these images indicates the locations of the STO terrace steps.



(a) Screw dislocation: Se-etched STO



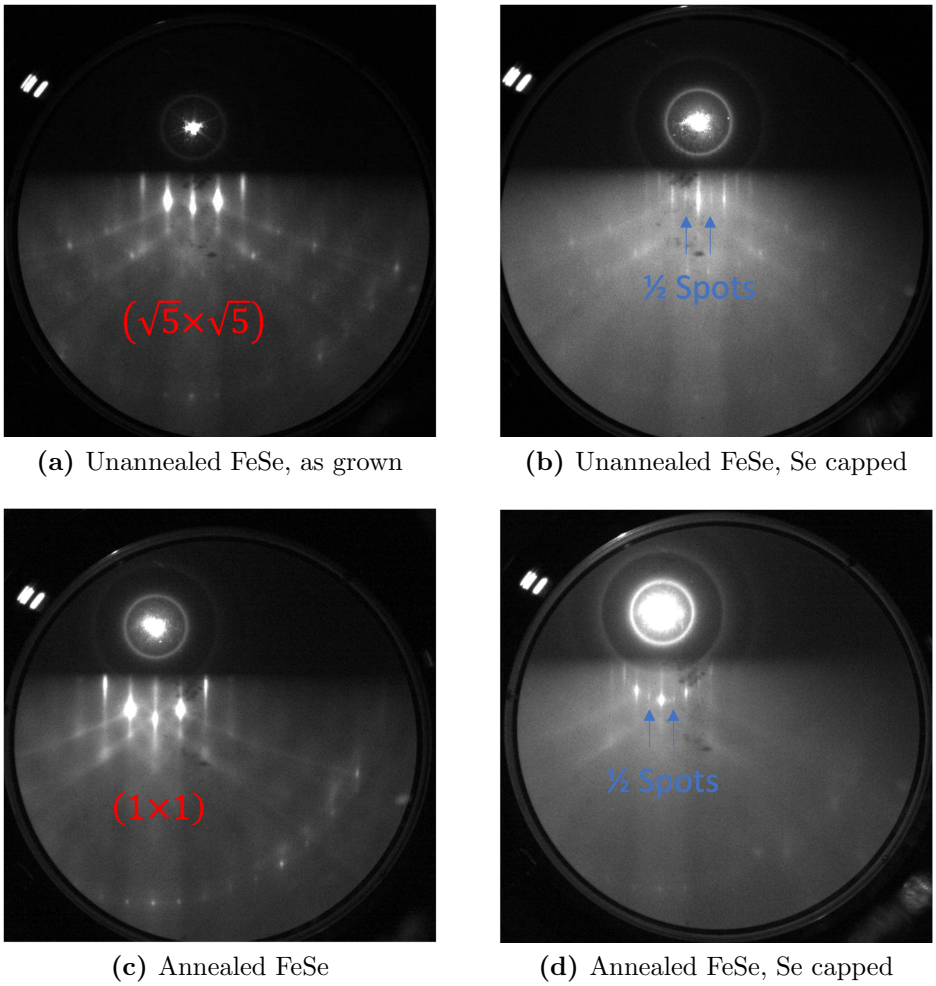
(b) Screw dislocation: 90 ML FeSe



(c) Defects pinning: 90 ML FeSe

Figure 4.13: Defects on Se-etched STO and on a 90 ML FeSe film: Blue circles indicates the locations of screw dislocations and red circles indicate defect pinning centers along the step edge.

films were grown on Se-etched STO at 350 °C for 14 hours, while keeping the Fe source at 1250 °C, and the Se source at 180 °C. The as-grown FeSe films display a weak $(\sqrt{5} \times \sqrt{5})$ superstructure, indicating that they are rich in Se, see Figure 4.14a. Sample #247 was subsequently post annealed at 350 °C. The $(\sqrt{5} \times \sqrt{5})$ superlattice spots were still visible after one hour of post annealing, but they disappeared after two hours, which is confirmed in Figure 4.14c. Both films were capped with Se before removal from vacuum for XRD experiments. During the capping procedure, one initially observes additional 1/2 order streaks in RHEED, indicating that the



(a) Unannealed FeSe, as grown

(b) Unannealed FeSe, Se capped

(c) Annealed FeSe

(d) Annealed FeSe, Se capped

Figure 4.14: RHEED patterns of 177 ML thick FeSe films: all the RHEED images were taken with the incident electron beam along the STO [100] direction.

Se exposure changes the surface periodicity, see Figure 4.14b and 4.14d. The 1/2 spots could perhaps be due to the formation of Se rich Fe_3Se_4, forming a $\sqrt{2} \times \sqrt{2}$ superstructure structure. The superstructure would be due to the ordering of Fe vacancies (Chen et al., 2014). As more Se accumulates, the RHEED pattern becomes increasingly blurred as the capping layer is amorphous. The preparation procedure of both samples is summarized in Table 4.1.

XRD 2θ-ω scans of both samples are shown in Figure 4.15. The peak positions of the post annealed and unannealed films are almost the same. The out-of-plane lattice constants c, calculated from the XRD data, are listed in Table 4.2. These are close to the lattice parameter of a β-FeSe single crystal 5.52−5.58 Å (Okamoto, 1991). Though the peak widths are slightly different, similar differences can be seen for the different STO substrates. This difference could be related to sample quality and/or alignment of the equipment. No clear splitting of peaks was found, which suggests that we obtained single phase FeSe. The good sample quality was also confirmed by X-Ray Reflectivity (XRR). The XRR measurement of the annealed FeSe film (#247) is shown in Figure 4.16. The oscillations indicate that the film is quite smooth, even

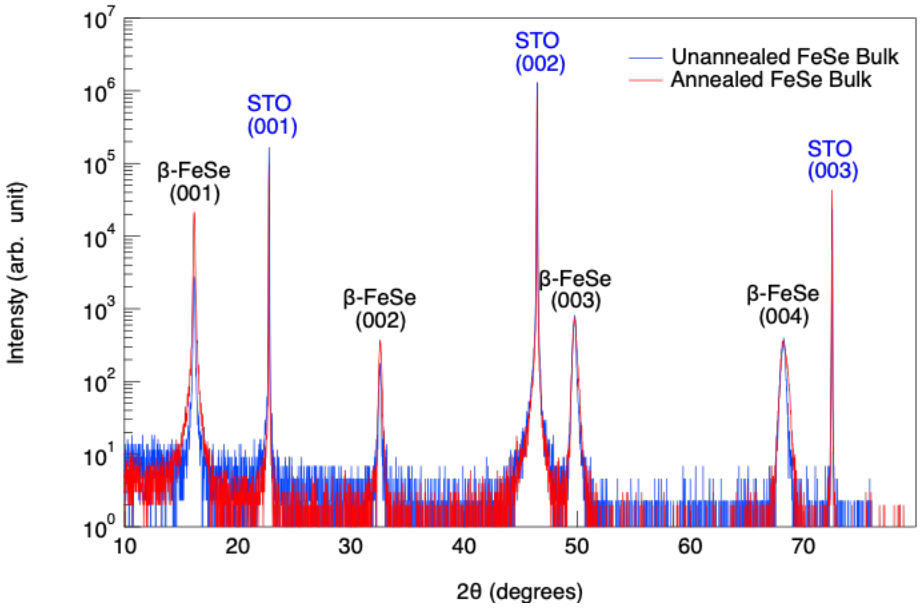


Figure 4.15: 2θ-ω scan of 177 ML thick FeSe films with and without post annealing

Table 4.2: Out-of-plane lattice parameter c of the 177 ML thick FeSe films with and without post annealing

Sample	XRD peak index	$2\Theta/^\circ$	c/Å
Unannealed FeSe bulk	(002)	32.61	5.487(8)
	(003)	49.83	5.486(5)
	(004)	68.27	5.491(4)
Annealed FeSe bulk	(002)	32.61	5.487(8)
	(003)	49.81	5.488(5)
	(004)	68.25	5.492(4)

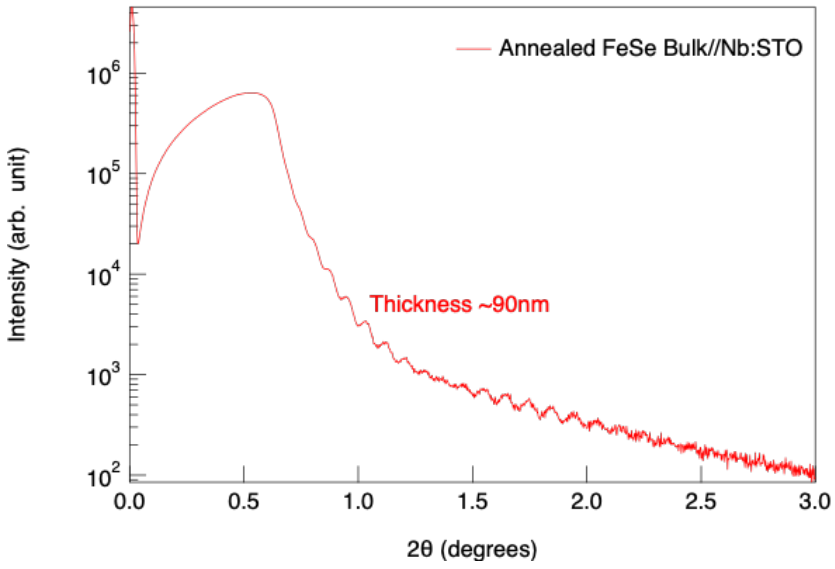


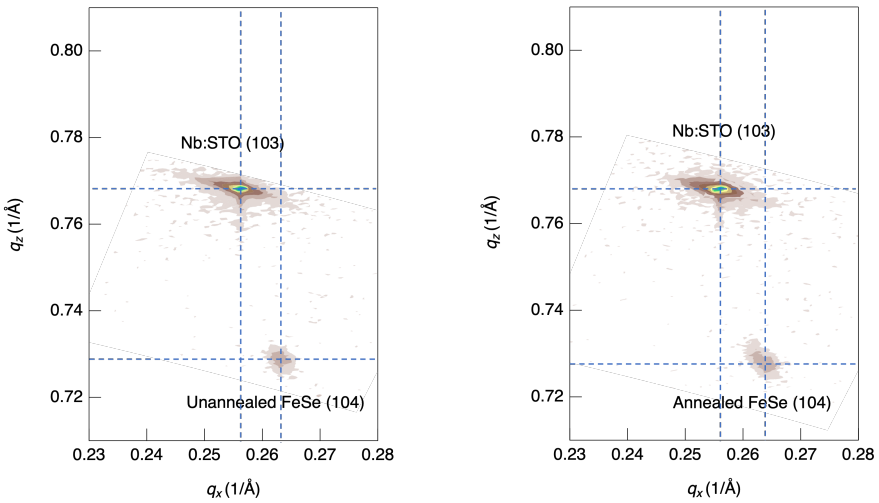
Figure 4.16: XRR data of the annealed 177 ML thick FeSe film

though the amorphous capping layer likely blurred these fringes. From the oscillation period, we infer a thickness of 164 ± 9 ML, which is close to our calibration from STM: It takes 4 minutes and 45 seconds to grow a complete one monolayer. The total growth time was 14 hours, which translates into 177 monolayers, assuming a constant growth rate.

In-plane lattice parameters were obtained from RSM measurements, see Figure 4.17 and Table 4.3. They are also quite close to the lattice constants of a β-FeSe single crystal: 3.77-3.83 Å (Okamoto, 1991). The out-of-plane results agreed with the data from 2θ-ω scan. In summary, our XRD measurements confirmed that the unannealed and post annealed FeSe films are single phase β-FeSe. The films are fully relaxed and of good crystalline quality. The $(\sqrt{5} \times \sqrt{5})$ vacancy ordering observed in RHEED and LEED did not noticeably affect the lattice parameter of the film. Therefore, it is plausible that Fe vacancies primarily accumulate near the surface and that the bulk of the film is closer to ideal stoichiometry.

4.5 Magnetic Properties

Magnetic properties measurements were also performed on samples #246 (unannealed) and #247 (post annealed). Both samples were cut into small rectangular shapes with dimension $3 \times 5 \times 0.5$ mm^3. They were subsequently mounted on the quartz sample holder. The applied magnetic field was normal to the sample plane. The $M(H)$ measurement is shown in 4.18a. Here, one must keep in mind that the magnetic signal of the thin film is usually overwhelmed by that of the substrate and sample holder. This is shown by measuring the bare STO substrate. Pure STO should be diamagnetic and its magnetic signal should be independent of temperature, but in practice, there is a paramagnetic upturn at low temperature due to the presence of Nb dopants. The STO signal is riding on a linear negative slope, which might be due to the changing sample position as a result of thermal expansion of the sample and sample holder.

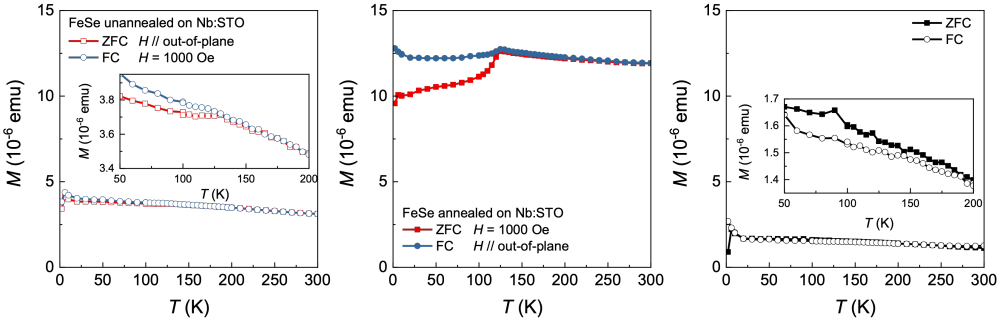


(a) Unannealed FeSe bulk **(b)** Annealed FeSe bulk

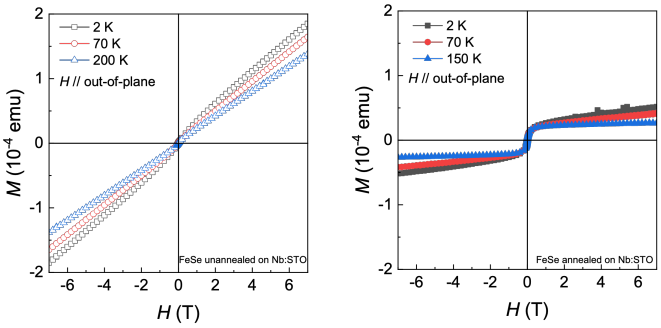
Figure 4.17: Reciprocal space map data of FeSe bulk sample.

Table 4.3: Lattice parameters of thick FeSe films obtained from RSM

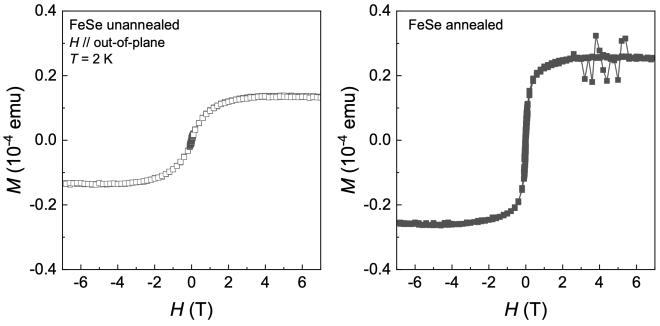
Sample	in-plane parameter a/Å	out-of-plane parameter c/Å
Unannealed FeSe bulk	3.801(9)	5.487(6)
Annealed FeSe bulk	3.791(10)	5.494(6)



(a) $M(T)$ data of sample #246 (unannealed) on the left. The middle panel are the $M(T)$ data for sample #247 (post annealed). The $M(T)$ data of pure STO are shown on the right. $H = 1000$ Oe.



(b) $M(H)$ curve of sample #246 (Left) and sample #247 (Right).



(c) $M(H)$ curve at 2 K after subtracting the linear background

Figure 4.18: Magnetic properties measurement on bulk FeSe.

The magnetization of the FeSe films reveals a kink around $T_c = 125$ K and a large separation between the field-cooled (FC) and zero-field cooled (ZFC) magnetization data below T_c. This behavior was not observed for pure STO and it is most prominent for the annealed FeSe film. This behavior is almost identical to that of bulk hexagonal Fe_7Se_8 below its spin reorientation temperature. The latter is associated with a rotation of the spins from the ab plane to the c axis as the temperature decreases (Li et al., 2016b). On the other hand, bulk Fe_4Se_5 has a kink feature around $T_c = 50$ K, which was not observed in the unannealed film (#246) (Yeh et al., 2020; Wu et al., 2015). Neither did we observe the paramagnetic to ferrimagnetic transition of Fe_3Se_4 ($T_c = 300$ K) (Yadav et al., 2024). $M(H)$ measurements are shown in Figure 4.18b, ferrimagnetic behavior was found for the post annealed sample #247. The magnetic response of sample #246 is dominated by a linear background susceptibility, similar to the one for pure STO. The background corrected $M(H)$ curve is plotted in 4.18c. From these data, one can obtain the spontaneous/saturation magnetization M_s, which is 1.3×10^{-5} emu (#246) and 2.6×10^{-5} emu (#247). If one assumes that the magnetic signal indeed originates from Fe_7Se_8 with an average moment of 2.56 μ_B per formula unit, one can obtain its volume fraction, and therefore the fraction of Fe vacancies in the films. Accordingly, we estimate that the nominal composition of the film is $Fe_{0.97}Se$. Notice, however, that we did not find evidence for the existence of Fe_7Se_8 in XRD. Alternatively, if we assume that the magnetic signal originates from tetragonal $Fe_{4+\delta}Se_5$, we estimate that $\delta = 0.2$ (Fe_4Se_5 is antiferromagnetic). In either case, the magnetic transition at $T_c = 125$ K would be associated with a change of magneto-crystalline anisotropy from the [001] direction below T_c to the in-plane direction above T_c, which could be resulted from tetragonal-to-orthorhombic structural transition (Chen et al., 2014).

4.6 Conclusions

We have explored the growth conditions for fabricating high quality bulk β-FeSe films on STO(001). The growth mode of the films is very sensitive to the susbtrate temperature, while the stoichiometry of the films depend on substrate temperature, Fe/Se flux ratio and post annealing protocol. Our results highlight the importance of post annealing in reducing the number of vacancies. The absence of superconductivity in this films suggest that additional annealing is required to reach near perfect 1:1 stoichiometry.

Chapter 5

Ultrathin FeSe Films on $SrTiO_3$

5.1 Morphology of Monolayer and Multilayer FeSe on STO.

Following the FeSe growth recipe mentioned in section 4.2, we grew monolayer (*i.e.*, one unit-cell thick) FeSe films under selenium rich conditions, with the Fe and Se sources kept at 1250 °C and 180 °C, respectively. Growth at lower temperature, for example at 375 °C, can result in 2D step-flow growth with uniform morphology, see Figure 5.1. Bright domain boundaries suggest Se rich conditions.

Long post annealing is crucial to obtain a superconducting FeSe film. Post annealing reduces the amount of excess Se and might also facilitate charge transfer

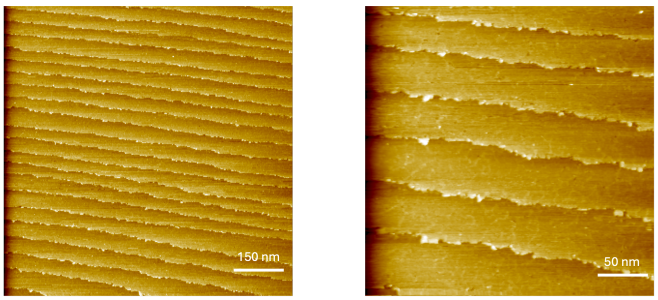
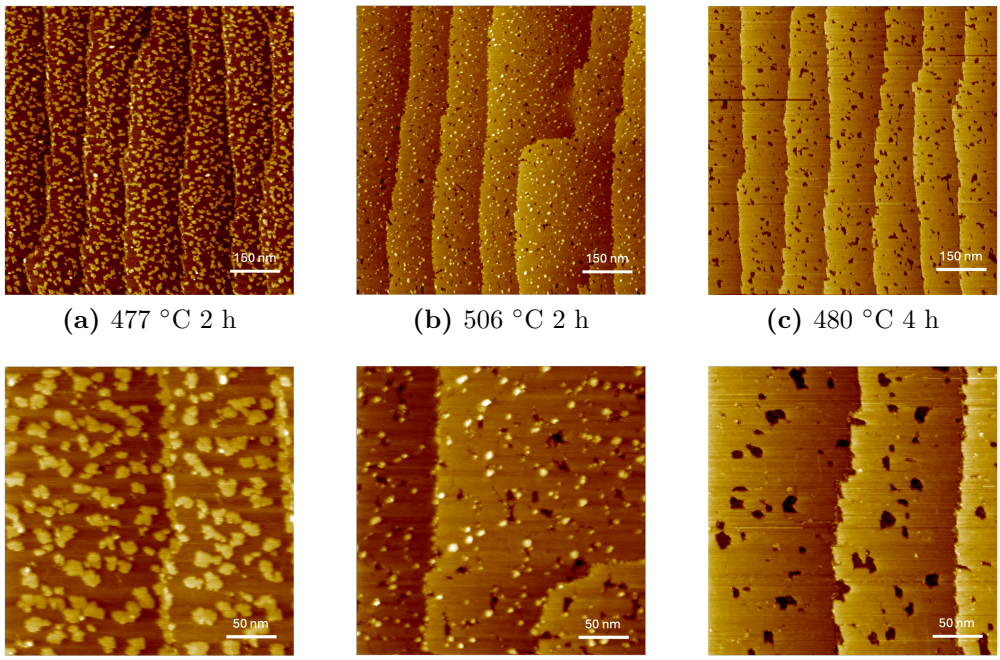


Figure 5.1: 2D step-flow growth of an FeSe monolayer on STO (Sample #155), resulting in a uniform step morphology. $T_{\text{sub}} = 375$ °C.

from the substrate (Li et al., 2014; Zhang et al., 2017; He et al., 2013). The presence of excess Se is due to the fact that the films have to be grown with a strongly oversaturated Se flux, as the sticking coefficient of Se is very small. To minimize Se excess, we increased the growth temperature to 450 °C. Under this condition, it took 4 minutes and 45 seconds to grow a single FeSe layer. The monolayer film was subsequently annealed for 1 to 6 hours at 480 °C, followed by an another very long anneal, typically 10 to 17 hours, at 375−400 °C. This procedure was deemed essential in order to create high temperature superconductivity. However, high temperature annealing (480 °C) also reduces the coverage of FeSe film, meaning that second layer FeSe islands gradually disappear while voids become visible in the first layer. One could grow an FeSe film with a coverage in excess of 1 ML and obtain perfect monolayer coverage by high temperature post annealing, which would be desirable for XPS and ARPES measurements. These measurements do not have much spatial resolution and thus it is highly desirable to have a uniform thickness across the whole sample, so that one can be sure that the XPS and ARPES spectra are truly representative of a single monolayer film. An example of high-temperature annealing sequence is given in Figure 5.2.

During the long low-temperature (375−400 °C) anneal, the areal densities of second layer islands and other bright features in the STM images gradually decrease. These other features possibly arise from small clusters of excess Se on top of the monolayer film; their height fluctuates a bit but is less than the expected step height for the second layer islands (Figure 5.3). The STM image of the FeSe monolayer barely changes at this temperature, indicating that the monolayer is stable. Figures 5.4a and 5.4b are topographic STM images after a 15 hour post anneal at 370 °C.

The high temperature annealing protocol is deemed necessary to make sure that the FeSe monolayer is electron doped with doping levels that are high enough to induce superconductivity. This will be shown with ARPES in the next section. Post annealing serves to remove excess Se (or reduce the Fe deficiency) of the film, thereby raising the Fermi energy. It probably improves the crystallinity as well.



(a) 477 °C 2 h **(b)** 506 °C 2 h **(c)** 480 °C 4 h

(d) 477 °C 2 h **(e)** 506 °C 2 h **(f)** 480 °C 4 h

Figure 5.2: Effects of high-temperature annealing on monolayer FeSe (#132): The monolayer FeSe film was grown at 454 °C for 5 minutes and then annealed following the sequences from (a) to (c). The scale of the STM images, annealing temperature and annealing time for each annealing sequence are indicated below each image.

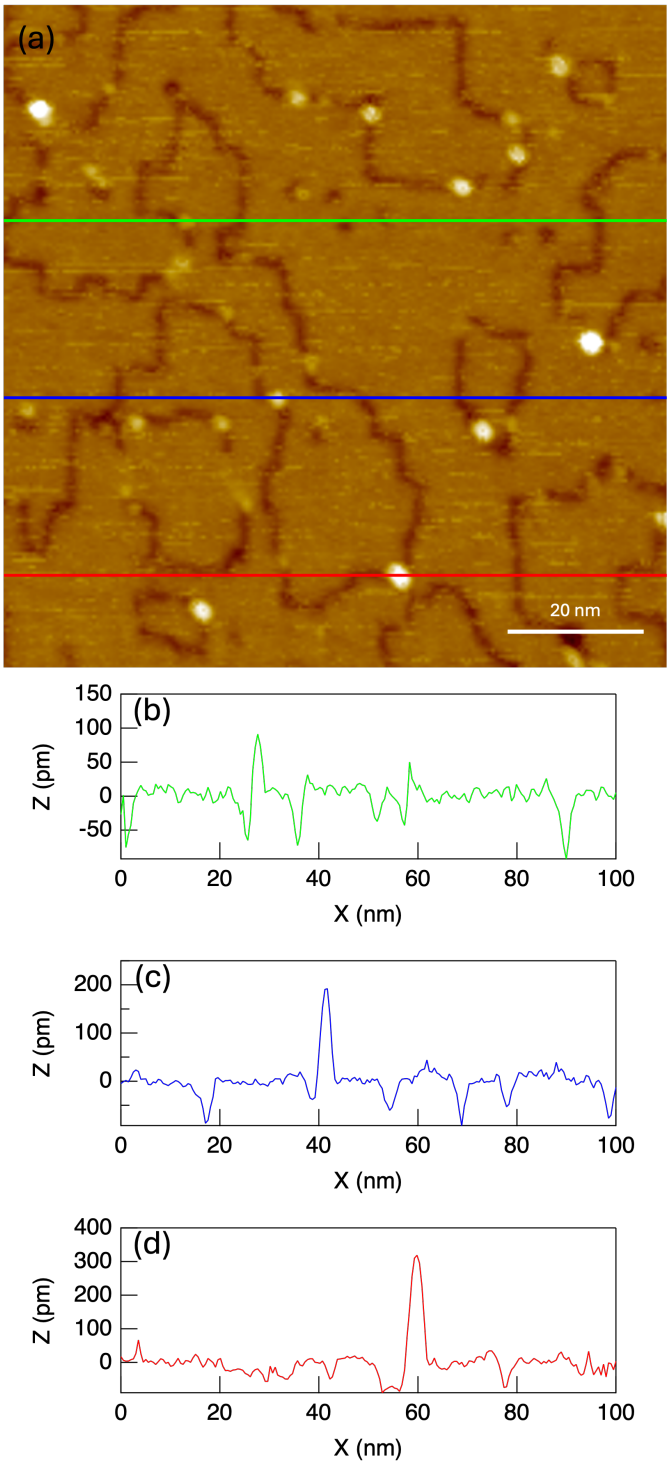
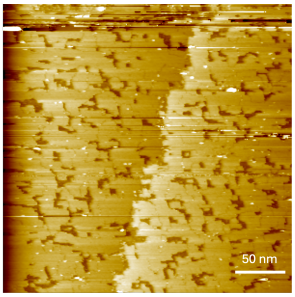
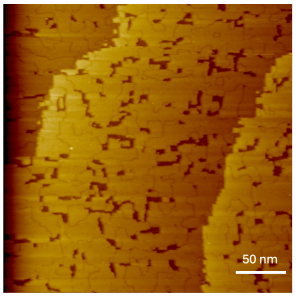


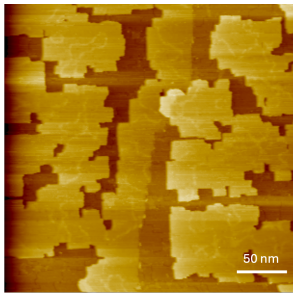
Figure 5.3: STM images showing some bright particles on top of the FeSe film: (a) 100×100 nm^2 topographic STM image of monolayer FeSe. Scan parameters: $U_{\text{bias}} = 2.5$ V, $I_{\text{sp}} = 500$ pA. (b)−(d) line profile data from image (a), measured along the corresponding green, blue and red lines in image (a).



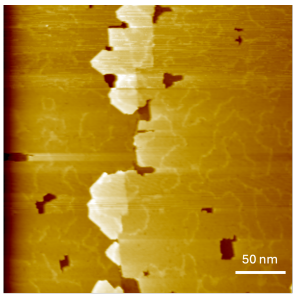
(a) After 480 °C 1 h annealing: $\theta = 0.91$ ML, $t = 4.75$ mins



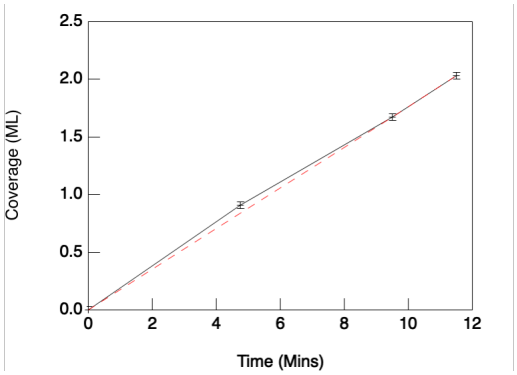
(b) After 370 °C 15 h annealing: $\theta = 0.91$ ML, $t = 4.75$ mins



(c) Overdose 1: $\theta = 1.67$ ML, $t = 9.5$ mins



(d) Overdose 2: $\theta = 2.03$ ML, $t = 11.5$ mins



(e) FeSe coverage (θ) vs. deposition time (t)

Figure 5.4: Growth rate inconsistency between the first and second FeSe layer (#157) on STO

The post annealing temperatures are too low for removing Fe. As the second layer islands gradually disappear upon post annealing without leaving any trace of excess Fe clusters on the surface, it is reasonable to conclude that the Fe is incorporated into the first layer, thus making it Fe rich. This suggests that the increased Fe content and emergence of superconductivity are related.

The second FeSe was grown 360 °C on top of the 480 °C post annealed monolayer, producing 2D step-flow growth mode, as mentioned in 4.2. Interestingly, it took 6 minutes and 45 seconds to finish the second layer, which is substantially longer than the the 4 minutes and 45 seconds needed to complete the first layer, see Figure 5.4. There may be several reasons to account for this discrepancy. First of all, the Se sticking coefficient on STO might be greater than that on the FeSe monolayer, which is reasonable because the FeSe monolayer is relatively inert, i.e., less 'sticky'. In that case, the first layer would be more Se rich (more Fe deficient) than the second layer. The longer growth time for the second layer would then be due to the increased Fe density in the second layer. Upon prolonged post annealing, much of the second layer Fe will be incorporated into the first layer, as discussed above. Indeed, Hu and Liu found that there was 10%−20% extra Fe in the superconducting monolayer FeSe film grown on STO (Hu et al., 2018; Liu and Zou, 2020).

We dismiss the idea that the increase growth time could be related to a strain relation in the second layer, as the atomic densities of the first and second layer would differ by at most 7%, which is too little to account for the difference in growth time. Post annealing condition of the monolayer and double layer FeSe films on Se-etched STO ware listed in Table 5.1.

Because it is difficult to separate the effects of carrier doping via Fe enrichment and other mechanisms such as charge transfer from the substrate, we also deposited extra Fe on the as-grown FeSe monolayer without any post annealing. If the excess Fe is incorporated into the film, it would change the stoichiometry of the FeSe layer. We deposited an excess amount of 10% and 15% atomic percent at the growth

Table 5.1: Post annealing condition of the monolayer and double FeSe films on Se-etched STO

Sample Label	1st layer	post anneal	2nd layer
1 ML #132	452−455 °C 5 mins	475−479 °C 2 h 503−510 °C 2 h 477−482 °C 4 h	
1 ML #155	371−377 °C 4.75 mins		
2 ML #157	452−459 °C 4.75 mins	472−481 °C 1 h 366−371 °C 15 h	359−367 °C 6.75 mins

temperature of the film, *i.e.*, 450 °C. The resulting surface morphology is shown in Figure 5.5.

The concentration of bright particles in the as grown films is large. Their heights fluctuate but are lower than that of a single-layer step height. Under Se rich conditions, we attributed them to Se clusters. Se atoms are easily 'grasped' and 'released' from the STM tip, which made the surface difficult to scan. Therefore, we could only obtain a rough estimate of the concentration of these bright particles, which is about 12% ± 5%. We could not obtain reliable numbers for the density of voids in the first layer. After depositing 10% extra Fe, the bright particle concentration shrunk to 4% ± 1% and the concentration of voids was 8% ± 1%. The height of the bright particles transformed into the step height expected for the second FeSe layer. This suggests that the excess Fe atoms reacted with the clusters of excess Se on the surface to form second layer FeSe islands. Finally, with 15% extra Fe, the concentration of bright islands and dark holes were 3% ± 1% and 4% ± 1%, respectively. From these results, the extra Fe would combine with the excess Selenium either fill the holes in the 1st layer or form 2nd layer FeSe. Comparing the 10% and 15% extra Fe deposits, we find no clear difference in the area fraction of the second layer FeSe islands, but there is a clear 4% difference in the area fraction of the holes. This shows that excess Fe is incorporated into the first layer. Notice that the domain boundaries remain bright (Figure 5.5 (g)), which is consistent with our previous observation that the

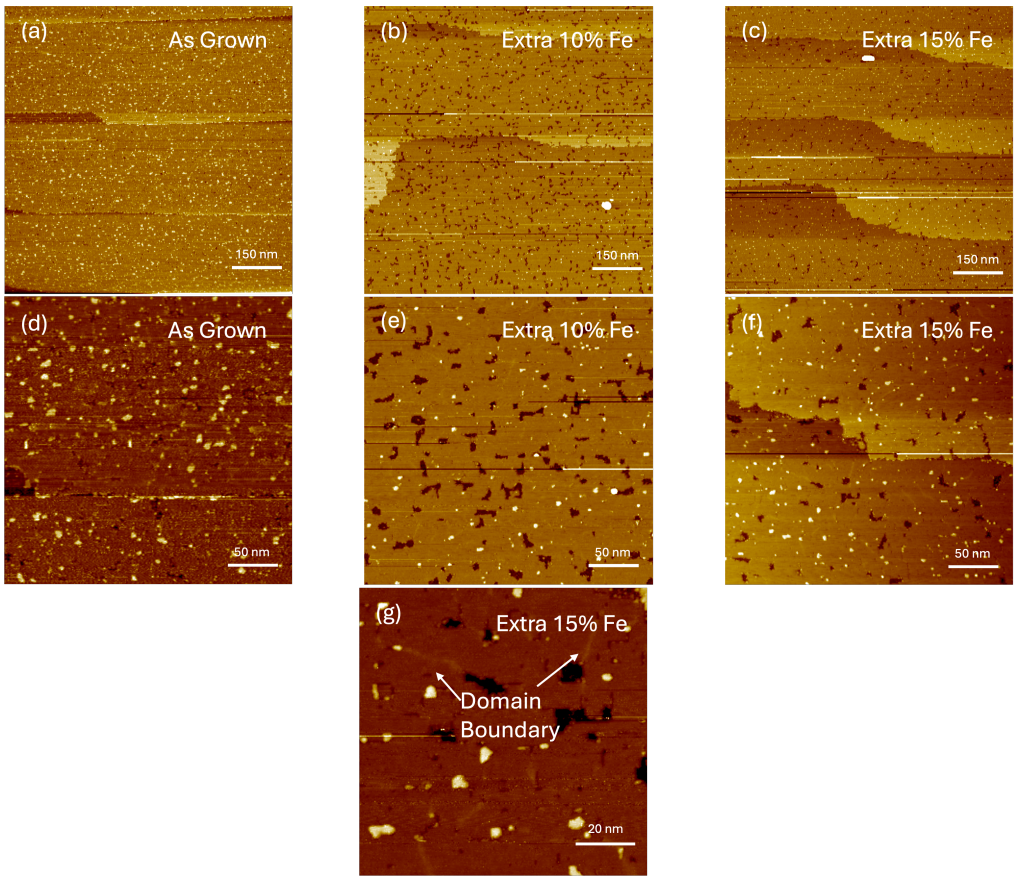


Figure 5.5: Extra Fe deposition on monolayer FeSe film without post annealing: STM morphology scan (a)−(f) at $U_{\text{bias}} = 2.5$ V, $I_{\text{sp}} = 300$ pA; (g) at $U_{\text{bias}} = 1.5$ V, $I_{\text{sp}} = 300$ pA.

appearance of dark domain boundaries requires post annealing. We should keep in mind that there always is a finite temperature gradient across the sample, and one can not guarantee that the concentrations inferred from those STM images are all the same. Stoichiometric analysis thus requires many more STM images and data averaging. We therefore resort to XPS to obtain the average stoichiometry over a large area.

5.2 Electron Doping

Post annealing is expected to increase the concentration of the Fe^{2+} ions and electron concentration in the FeSe monolayer. The latter is essential for obtaining high-temperature superconductivity. To verify whether our post annealing protocol increases the Fermi energy by the correct amount, we performed ARPES measurements. The FeSe monolayer was prepared following the recipe in section 5.1. The as-grown film was subsequently annealed at about 480 °C for 6 hours. The sample was then transferred from the MBE growth chamber to the ARPES system using a vacuum suitcase. After sample transfer, the film was first annealed at 350 °C for 30 minutes (anneal 'A') before taking the ARPES data. After the ARPES measurements were completed, we continued to anneal the same film at 400 °C for 10 hours to see if the carrier concentration could be further increased (anneal 'B'). In both cases, we measured the band structure along three different line cuts in the Brillouin zone (Figure 5.6: Left). The ARPES spectra reveal the presence of an electron pocket centered at the M-point of the Brillouin zone, which is shown in Figure 5.7. The corresponding Fermi contour in Figure 5.6: (Right) was acquired following anneal 'B'.

The ARPES spectra measured after anneal 'A' and 'B' barely differ. The valence band maximimum at the Γ point is well below the Fermi level. The electron pocket at M bottoms out at about 70 meV below the Fermi level (Figure 5.7).

The top of the valence band at Γ and the bottom of the conduction band at M can be determined more precisely from the momentum distribution curves (MDC) in Figure 5.8. The size of the Fermi surface at M was determined from the distance between the two peaks in the MDC at the Fermi level, 0.37 ± 0.05 Å (anneal A) and 0.39 ± 0.10 Å (anneal B), respectively. The bottom of the electron pocket (EP) was also marked in the MDC and is located at 76 ± 4 meV (anneal 'A') and 84 ± 6 meV (anneal 'B') below the Fermi level, respectively. The results were comparable to that of He et al. (50-60 meV below the Fermi level) (He et al., 2013). We conclude that the film is close to being optimally doped after the first anneal 'A' and that there are no significant changes upon prolonged post annealing.

5.3 Superconducting Gap

The superconductivity of our thin layer FeSe films was checked with STS, using the low-temperature STM in Prof. Wonhee Ko's laboratory. The monolayer FeSe film was grown in our MBE chamber, following the same recipe as before. The as-grown sample was annealed at 480 °C for 1 hour and at 380 °C for an additional 16 hours. Selenium was subsequently deposited at room temperature so as to form a protective

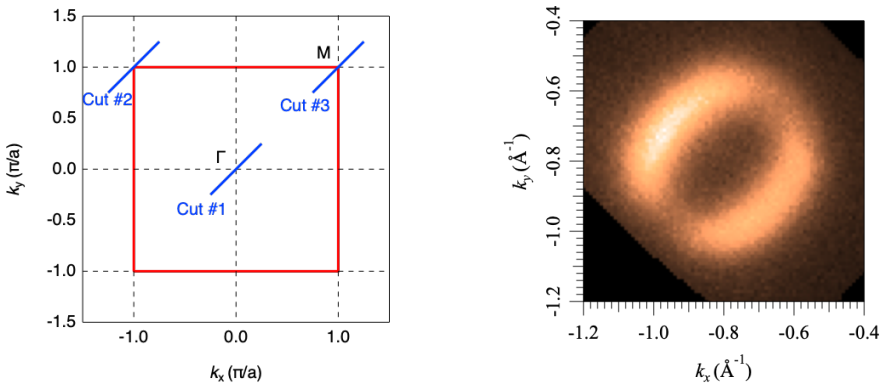
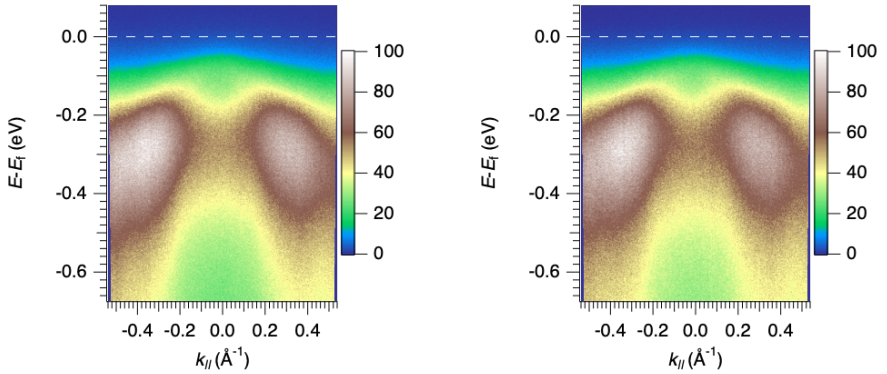
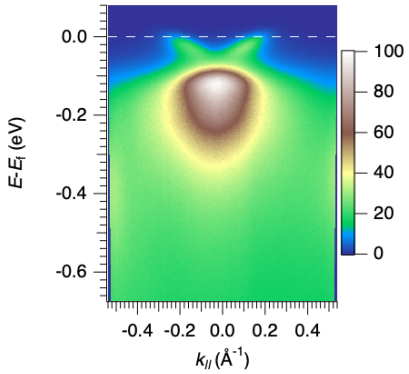


Figure 5.6: ARPES measurement on monolayer FeSe. (Left): Brillouin zone and orientation of the momentum cuts. (Right): Fermi contour near the M-point, following anneal 'B'. The spectral intensities were integrated over an energy window of ±10 meV.

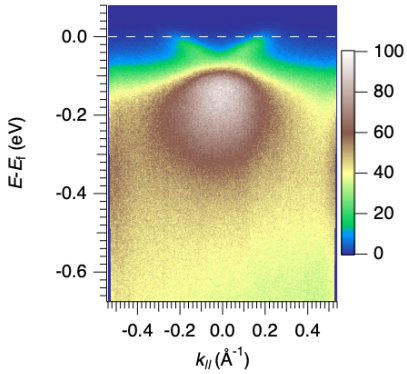


(a) annealing A cut #1

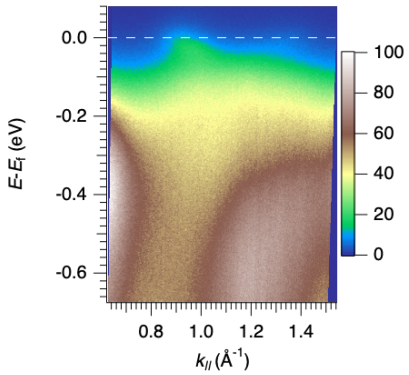
(b) annealing B cut #1



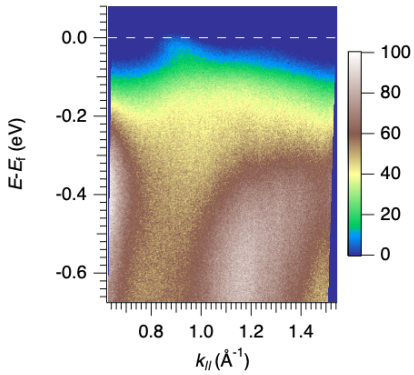
(c) annealing A cut #2



(d) annealing B cut #2

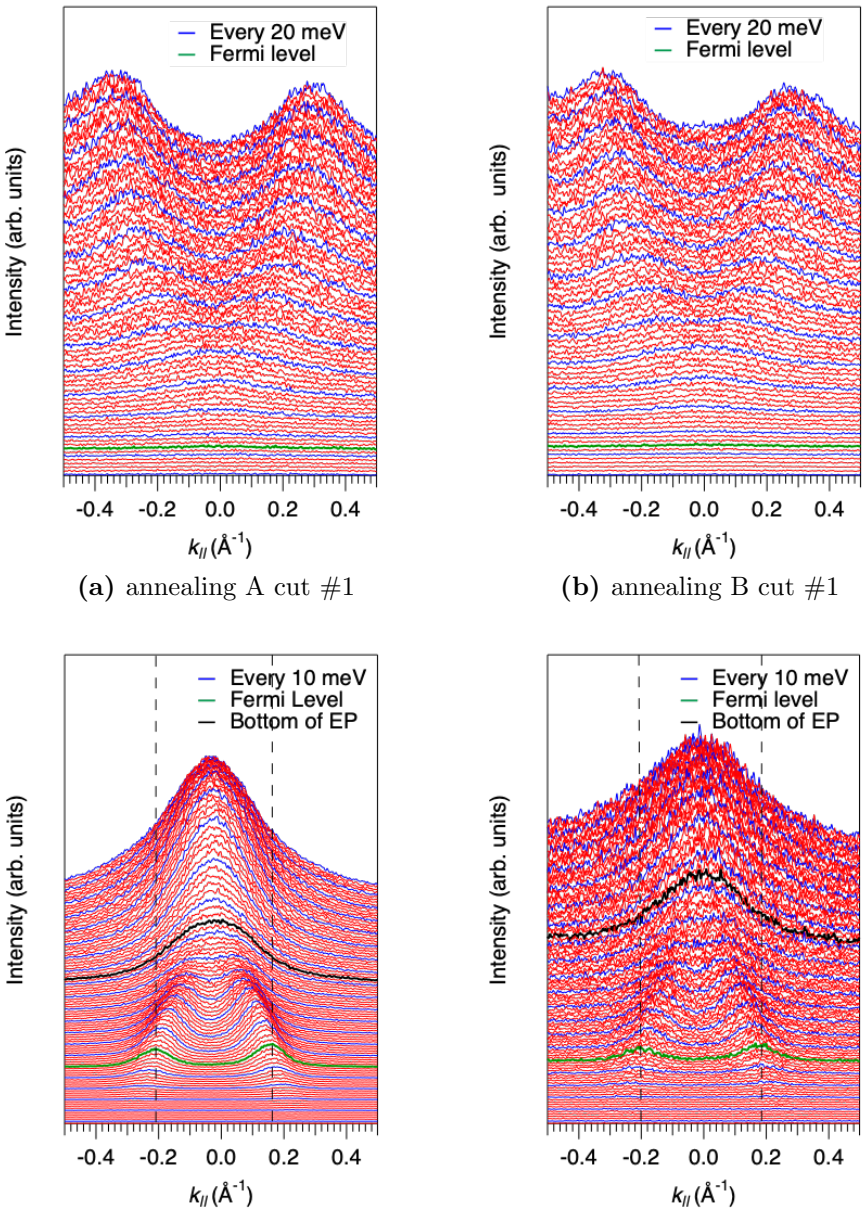


(e) annealing A cut #3



(f) annealing B cut #3

Figure 5.7: Comparison of the band structure of monolayer FeSe after one or two annealing cycles.



(a) annealing A cut #1

(b) annealing B cut #1

(c) annealing A cut #2

(d) annealing B cut #2

Figure 5.8: Comparison of the momentum distribution curve along cut #1 and #2

capping layer for sample transport through air. After the transfer, the film was briefly sputtered with Ar^+ ions (800 V, 10 mA, 30 s) to remove the atmospheric contaminants from the capping layer. This was followed by several post annealing cycles (30 minutes below 280 °C, 4 hours at 380−400 °C, 1 hour at 420 °C, and 1 hour at 450−460 °C), until the superconducting gap became visible in STS (Figure 5.9).

The STS data were obtained at 4.5 K with the help of a Lock-in amplifier. The obtained $\frac{dI}{dV}$ spectrum is proportional to the local density of states. The gap size Δ on the FeSe monolayer was about 16−17 meV, which corresponds to a $T_c \sim 68-73$ K (assuming that the $\Delta(T)$ relationship of bulk FeSe is a reliable predictor). We did not observe the double coherence peaks at ±9 meV, but detected the peaks at ±20 meV with a smaller value (Wang et al., 2012). We attribute this difference to the incomplete removal of the capping layer atoms or to variations in the preparation conditions of the STO substrate. We also found that the capping layer was not uniform and thus the quality of the surface might have degraded somewhat. A possible remedy might be to cap the film at liquid nitrogen temperature to prevent the Se from balling up. There also appear to be local variations in the size of the gap, indicating that the superconductivity is inhomogeneous, which is consistent with previous reports (Zhang et al., 2020). It is therefore highly desirable to conduct future STS experiments *in situ*, *i.e.*, without exposing the sample to atmosphere.

Some small areas of the sample were covered with a 2 ML film. The corresponding spectra indicate semiconducting behavior. (Figure 5.10 Right).

5.4 Conclusions

We successfully fabricated monolayer and double layer FeSe films on STO(001). The as-grown films are selenium rich, which is indicated by the formation of Fe vacancies inside the film and the presence of small Se clusters on top of the film. Post annealing was required to obtain an electron-doped, atomically smooth FeSe monolayer film. To

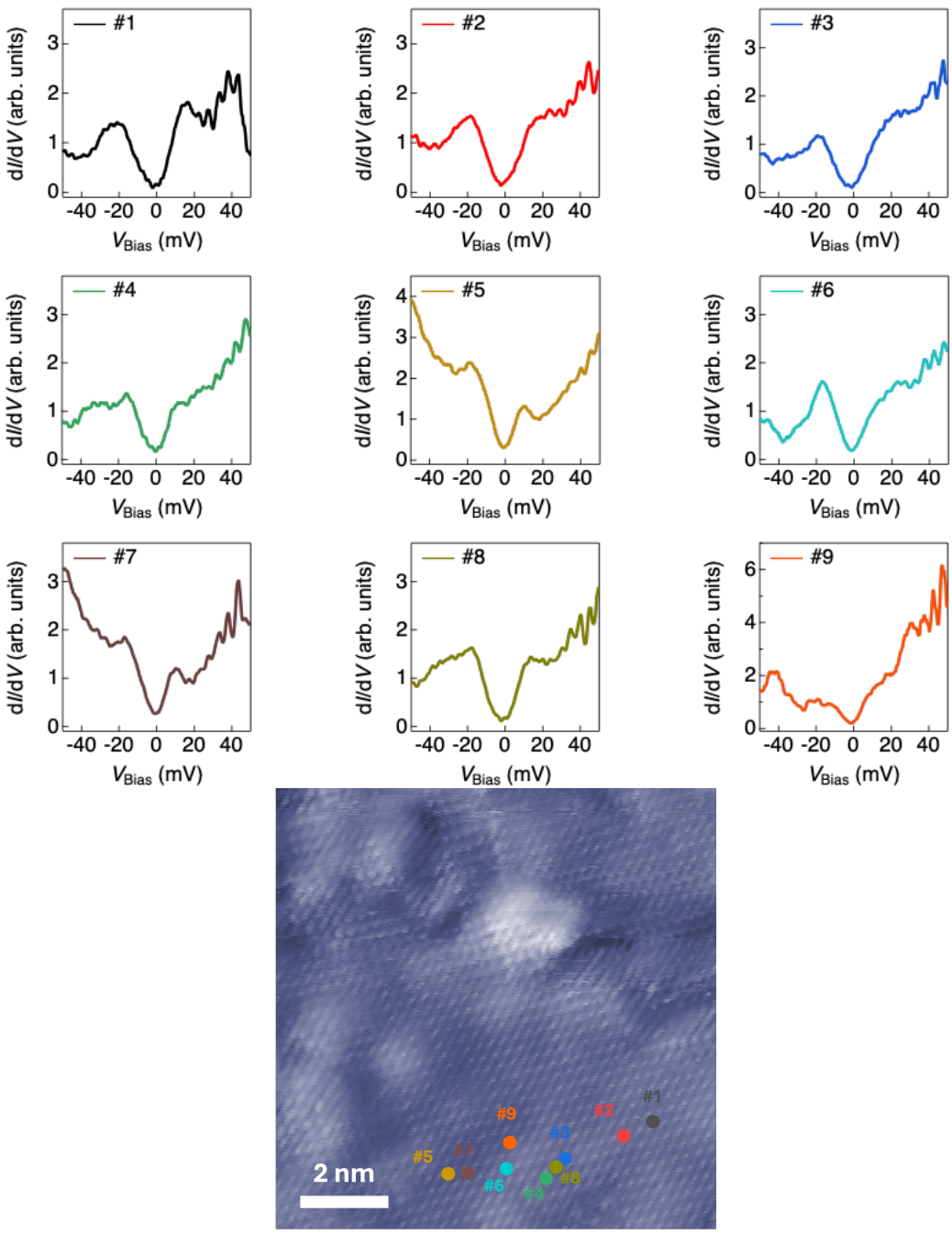


Figure 5.9: Scanning tunneling spectroscopy of monolayer FeSe: $V_{\text{amp}} = 1.0$ mV, $f = 973$ Hz for the STS (Top); $V_{\text{Bias}} = 50$ mV, $I_{\text{SP}} = 100$ pA for the topographic image (Bottom).

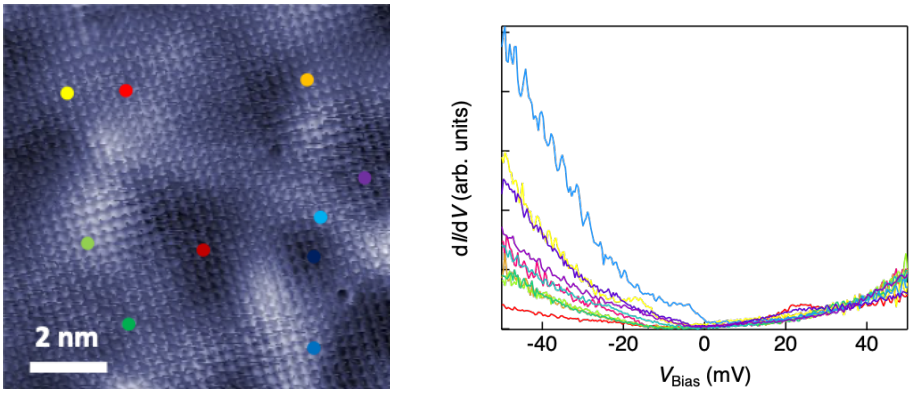


Figure 5.10: Scanning tunneling spectroscopy of the second layer FeSe: $V_{\text{bias}} = 50$ mV, $I_{\text{sp}} = 100$ pA for morphology image (Left); $V_{\text{AC}} = 1.0$ mV, $f = 973$ Hz for the STS (Right). The location of the colored STS point spectra are indicated by the corresponding colored dots in the topographic image (Right).

remove excess Se (and to increase the volume density of Fe), we studied the following post annealing protocol: (1) short high temperature post anneal; and (2) additional long low-temperature post anneal. A high quality film was obtained following step (2). ARPES measurements, however, indicate that a short high-temperature anneal produces a sufficiently high carrier concentration in the electron pocket centered at the M-point of the Brillouin zone, needed for superconductivity. The latter was confirmed using *ex-situ* STS measurements. The superconducting gap of the FeSe monolayer is about 16−17 meV, while the second FeSe layer appears to be semiconducting.

Chapter 6

Core Level and Auger Spectroscopy of FeSe on STO

6.1 Survey Spectrum of FeSe on $SrTiO_3$

The survey spectrum of FeSe on $SrTiO_3$ is very complicated. An example of a 2ML-thick FeSe film on STO is shown in Figure 6.1. For a very thin film, the core level and Auger spectra of the STO substrate are clearly visible. These originate from Sr, Ti, and O and are accompanied by various satellite peaks due to *e.g.*, plasmon excitation in the substrate and overlayer. The STO spectra are accompanied by the core level and Auger spectra of Fe and Se. It certainly is not a trivial task to assign all the features of the survey spectrum. Moreover, inelastic scattering produces a very complicated background, which makes it difficult to reliably determine the stoichiometry of the film from the core level intensities. Here we briefly discuss the most relevant features for this thesis. A first inspection of the survey spectrum should focus on the presence of contaminants on the sample, which is usually manifested by the presence of the carbon Auger peak appearing at $E_B = 1223$ eV. The absence of this peak indicates that there is no carbon contamination and that the sample is clean. Notice that the C $1s$ core level near $E_B = 285$ eV would be difficult to

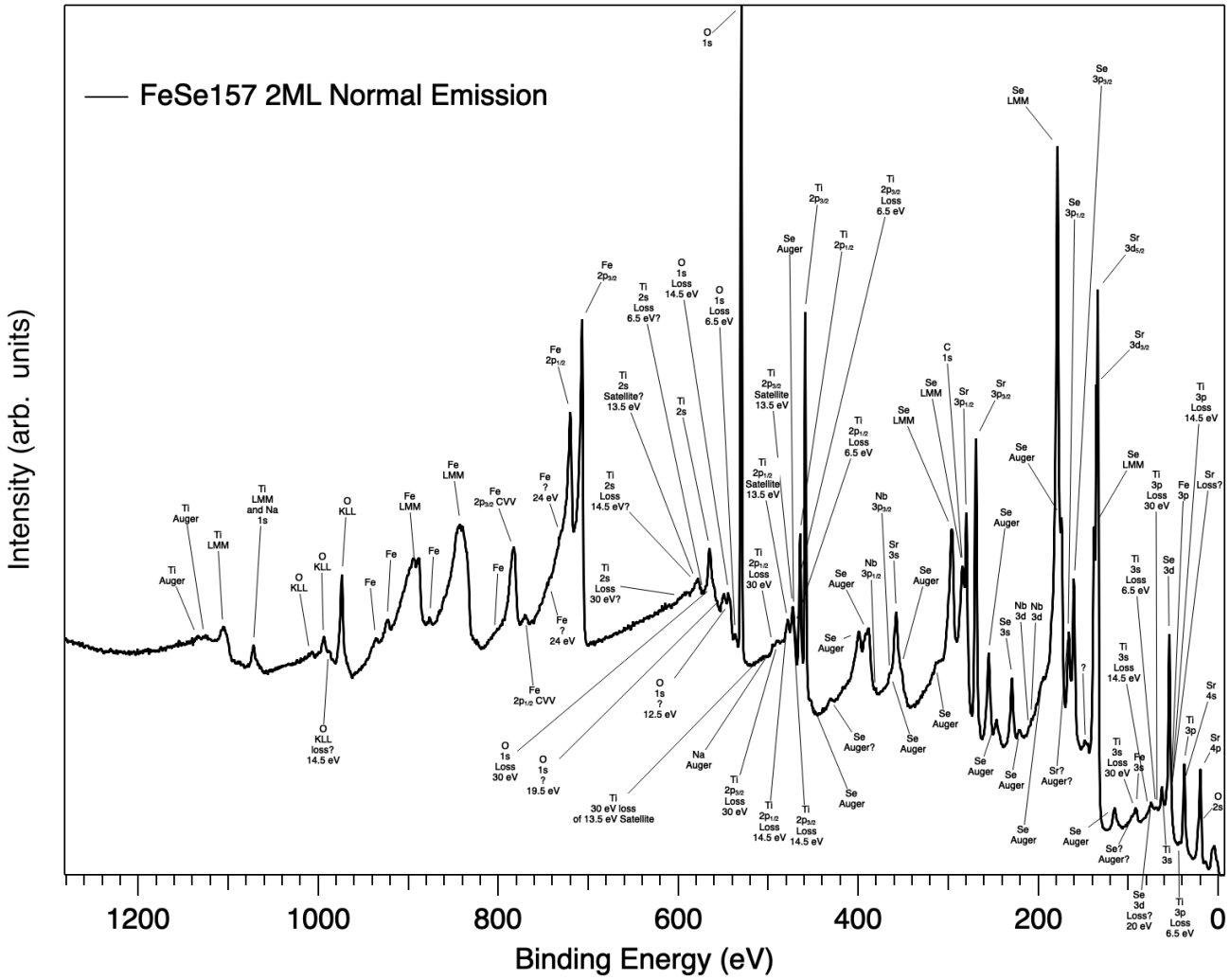


Figure 6.1: XPS survey spectrum of a 2ML-thick FeSe film on STO.

interpret since it overlaps with the Se LMM Auger spectrum. Oxygen can also be a contaminant but this requires a more detailed analysis of the oxygen $1s$ core level spectrum since oxygen is also the main element of the STO substrate. This procedure was discussed in Chapter 3. The core levels of 'dirty' oxygen (for instance physisorbed water, chemisorbed oxygen or -OH on the FeSe film), would coexist with oxygen bonded to Sr and Ti. Moreover, the presence of oxygen vacancies in the STO could produce a complex lineshape. Hence, understanding of the O $1s$ core level requires the deconvolution of the various component via core level fitting, which can be far from trivial. The two most intense core level spectra, the Ti $2p$ and Sr $3d$ spectra, were studied to elucidate the number of oxygen vacancies and to confirm the TiO_x/SrO termination of the STO substrate. Here, the analysis is complicated due to the presence of an energy-loss satellite near the Ti $2p$ made core level spectrum.

The Fe $2p$ core level and the corresponding CVV Aguer spectrum were studied to understand the electronic properties of the FeSe film, particularly the dynamics of core hole screening and to elucidate the significance of electron correlations in this compound via Auger spectroscopy. This will be discussed in detail in the next section. The Fe $2p$ core level spectrum does not show the presence of a chemically shifted component due to e.g. Fe_2O_3 (Fe^{3+}), again indicating that the film is clean.

In order to determine the stoichiometry of FeSe, we need to compare the core level intensities of Fe and Se. One usually selects the most intense peaks. The Se $3d$ and Fe $2p$ core levels are relatively far apart in binding energy, meaning that the core level intensities have to be corrected for the transmission function of the analyzer and for the difference in the inelastic mean free path. To avoid this complication, we settled on the Fe $3p$ and Se $3d$ spectra, even though they partially overlap.

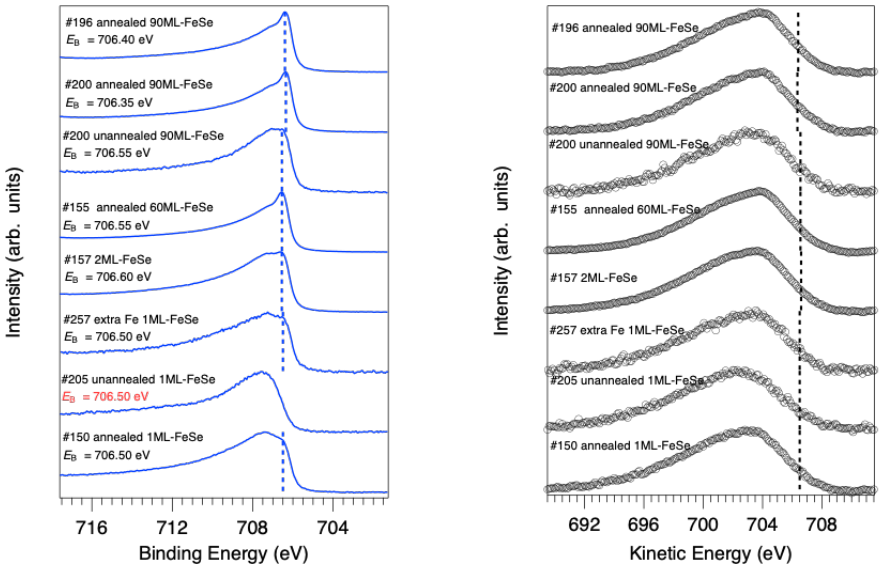
To complete this discussion, we mention the presence of small Nb and Na peaks. They are intentional and unintentional dopants of the STO substrate. Nb could possibly play a role in doping the FeSe thin film, which will be discussed later. The concentration of Na seems low enough to not be of any concern.

6.2 Fe 2p Core Level and CVV Auger Spectrum

We have studied the Fe 2p core level spectra and CVV Auger spectra for a series of FeSe samples with film thicknesses of 1 ML, 2 ML, 60 ML, and 90 ML, prepared under different growth conditions (extra Fe deposition), and post annealing treatments (w/o post annealing). The growth conditions for these samples are listed in Chapters 4 and 5. We remind the reader that sample #200 (90 ML) displayed $(\sqrt{5} \times \sqrt{5})$ and (1×1) RHEED patterns for the unannealed (Se rich) and post annealed films (Intermediate), respectively. Sample #196 (90 ML post annealed) displayed coexisting (1×1) and a 45° rotated (1×1) domain (Fe rich). We will show that there are subtle differences in the Fe 2p core level, CVV Auger, and XPS valence band spectra.

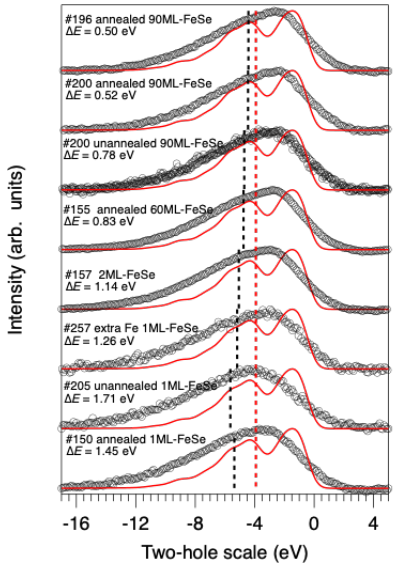
Figure 6.2a compares the Fe 2p core level spectra of the various samples. The Fe 2p spectra show at least two core level components, except for sample #205 (unannealed 1ML-FeSe). These two components are separated by about 1 eV. Post annealing enhances the relative ratio of low binding energy component no matter how thin or thick the films are. It is most pronounced for the post annealed thick film and least pronounced in the unannealed monolayer film. The low binding energy component is restored after adding some extra Fe onto the unannealed monolayer film. In principle, there are no inequivalent Fe sites in our single phase monolayer film. In addition, a possible mixture of Fe^{2+} and Fe^{3+} charge states would produce a core level splitting of about 3 eV, much larger than the observed splitting (Yeh et al., 2020). We therefore attribute the presence of the two peaks to a final state effect whereby the peak at low binding energy is attributed to a 'well screened' final state, and the one at higher binding energy to a'poorly screened final state' (Kotani and Toyozawa, 1974; Fujimori et al., 1988). A quantitative analysis of the various contributions to the core level spectrum is complicated due to the complicated back ground signal. A detailed analysis of the Fe 2p spectrum is currently in progress.

Interestingly, a similar double peak feature was found in NiO, CuO and in high T_c cuprates. In the case of NiO, the Ni 2p core level spectrum exhibits a shoulder on



(a) Fe $2p$ core level spectra

(b) Fe $2p$ CVV Auger spectra



(c) Fe $2p$ CVV Auger spectra plotted on the two-hole binding energy scale

Figure 6.2: (a) Fe $2p$ core level spectra; (b) CVV Auger spectra after subtracting a linear background. The spectra are normalized according to the maximum peak intensity. The dashed lines mark the Fe $2p$ core level binding energy obtained from (a). (c) Auger spectra plotted on two-hole binding energy scale. The SCDOS of the Fe $3d$ states, obtained from DFT (Berlijn and Kong, N D), is plotted in red. The dashed lines marked the centroid of the experimental data and that of the SCDOS. The difference ΔE is a measure of the hole-hole repulsion in the valence band of FeSe.

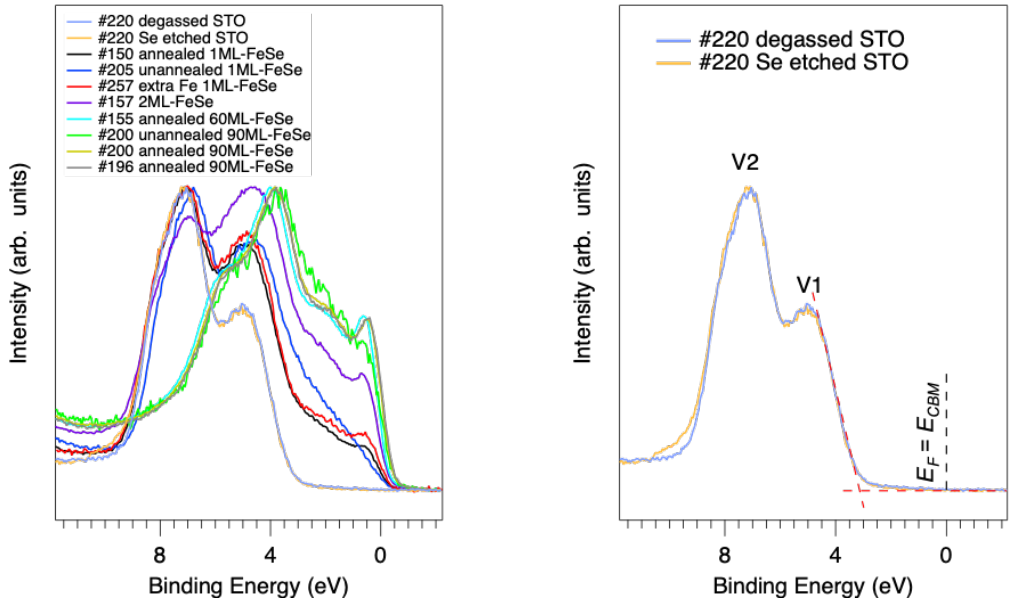
the high binding energy side of the main peak that is unrelated to the charge transfer satellites and multiplet features at higher binding energy. The intensity ratio between the two peaks was found to be very sensitive to the sample preparation conditions. For instance, deliberate introduction of oxygen vacancies via ion sputtering enhances the peak at high binding energy. Alternatively when growing NiO(100) films on MgO, the relative intensity of the low-binding energy component increases with film thickness (Van Veenendaal and Sawatzky, 1993; Alders et al., 1996). Van Veenendaal and Sawatzky proposed that the double peak feature is related to the nearest neighbor and next-nearest neighbor atomic configuration, which makes their ratio very sensitive to loss of coordination of the ionized atom due to *e.g.*, vacancies or surface effects. The upshot is that for oxides, the peak at high binding energy is associated with a non-local screening channel, while the peak at low binding energy is screened via charge transfer from a neighboring ligand orbital. For FeSe the situation should be different because FeSe is a (correlated) metal where the density of states near the Fermi levels is determined by the Fe $3d$ states. Nonetheless, the phenomenology is similar. Post annealed FeSe films have fewer Fe vacancies and the relative intensity of the low binding energy peak is strongest. The well screened final state is also most pronounced for post annealed thick films, as they are mostly bulk-like with few Fe vacancies.

Figure 6.2b shows the Fe $2p$ CVV Auger spectra after subtracting a linear background. The spectra are normalized by the peak maximum. As mentioned before, the background is complicated and the linear background subtraction represents an initial attempt for analyzing the data. The CVV Auger spectra are plotted on the 'two-hole binding energy scale', which is obtained by subtracting the binding energy of the well screened final state from the kinetic energy of Auger electrons. We calculated the first moment of the Auger spectrum and that of the self-convoluted partial density of states of the Fe $3d$ orbitals, obtained from the DFT calculation of bulk FeSe (Berlijn and Kong, N D). No significant differences were found in the DFT results of a free standing FeSe monolayer and the bulk (as expected for a layered van der

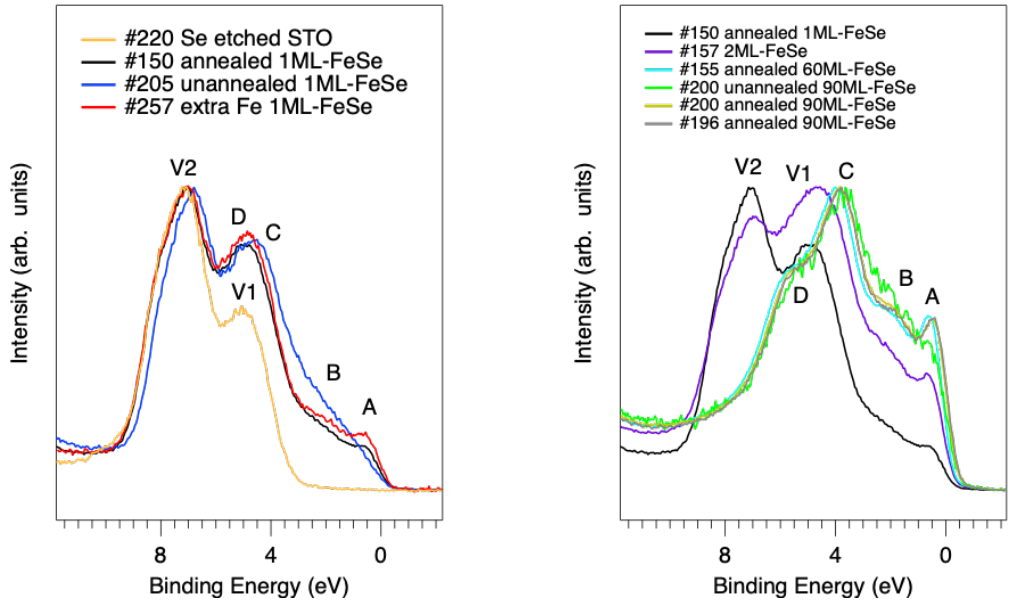
Waals compound), thus we use the Fe 3d partial DOS fron the bulk calculation. The first moments are indicated by the vertical dotted lines. As a common practice, the difference corresponds to the hole-hole repulsion energy in the final state of the Auger process. Evidently, these energies are of the order of 1 eV and smaller than those of the pnictides, even though the pnictides had been analyzed in greater detail via a detailed fitting procedure while our result is preliminary (Vilmercati et al., 2012). This result seems unexpected but the situation is far more complicated than that. Strictly speaking, the Cini-Sawatzky theory is only valid for closed band systems, whereas FeSe is a metal. Secondly, it assumes that the fully relaxed final state of the photoemission process is the initial state for the Auger decay, which does not seem valid for FeSe. Finally, the (metallic) energy loss tail on the high binding energy side should not be included in the calculation of the first moment of the Auger spectrum, as it is a consequence of the fact that FeSe is an open band system for which the Cini-Sawatzky is, strictly speaking, not valid. All these factors severely complicated the analysis of correlation effects in the FeSe films, which is still ongoing.

6.3 Valence Band Spectra and Core Level Shifts

Valence band spectra of various FeSe films on STO and bare STO substrates are shown in Figure 6.3. For ultrathin FeSe films, the STO contributions to the valence band spectrum are still quite intense. The STO spectrum contains two main features, V1 and V2, distributed around $E_B = 5$ and 7 eV (Figure 6.3b), respectively. Based on the calculated DOS, these features contains contributions from the O 2p states, hybridized with Sr 4d and Ti 3d states (Van Benthem et al., 2001). The spectra from degassed STO and Se-etched STO overlap almost perfectly, except for a shoulder on the high binding energy side of V2. This difference is probably due to the formation of the $\sqrt{13} \times \sqrt{13}$ surface reconstruction on Se-etched STO. In other words, the Sr:O ratio has changed, as we discussed in chapter 3. The concentration of oxygen vacancies in degassed STO should be very low. Given the fact that the valence band spectra of



(a) All **(b)** STO



(c) 1ML-FeSe **(d)** FeSe with different thickness

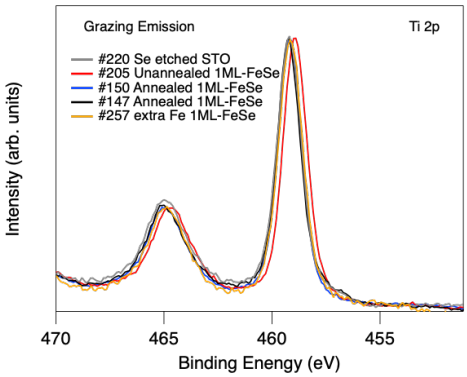
Figure 6.3: Valence band of various FeSe films and STO substrates.

the degassed and Se-etched STO samples are almost identical with no changes seen in the vicinity of V1, we conclude that the Se-etched sample also has a minimal vacancy concentration.

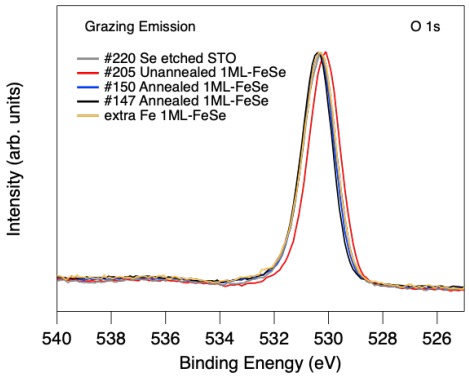
The valence band features of the FeSe monolayer can be recognized from those of thick (60 and 90 ML) FeSe films. They are labeled A, B, C, and D. Feature A around $E_B = 0.5$ eV and feature B around $E_B = 2$ eV correspond to the Fe $3d$ states. Feature C around $E_B = 4$ eV corresponds to hybridized Fe $3d$ and Se $4p$ orbitals, and feature D around $E_B = 6$ eV originates from the Se $4p$ levels (Mishra et al., 2015).

For the thin layer situation in Figure 6.3c, the valence band spectra contain both FeSe and STO related features. Features C and D are close to V1, which made it difficult to compare the differences around 4 to 6 eV without resorting to spectral fitting. V2 barely changes between the STO substrate and the 1 ML FeSe film, except for the fact that the unannealed 1ML-FeSe film shows a 0.25 eV energy shift towards low binding energy (see below). We conclude that the deposition of a 1 ML FeSe film does not change the location of the STO valence band features, meaning that there is no change in the band bending inside the STO substrate. This is corroborated by our core level spectra. The Ti $2p$ (Figure 6.4a) and O $1s$ (Figure 6.4b) core level spectra do not shift after growing a 1 ML FeSe film. The small shift for the unannealed film mentioned above needs to be verified as the workfunction of our spectrometer could change over time.

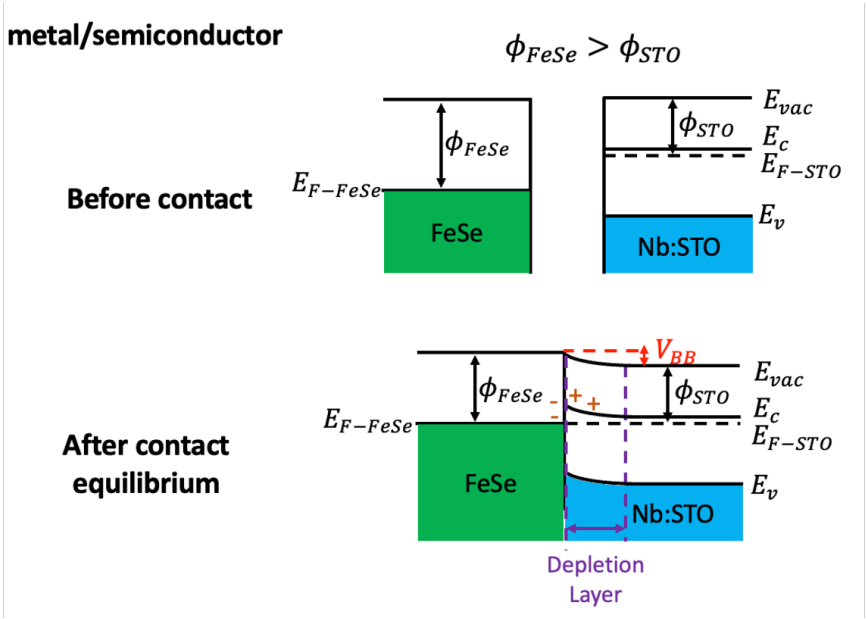
The valence band spectra of the unannealed and post annealed thin films reveal some interesting differences. Upon post annealing, feature B decreases in intensity while feature A near the Fermi level increases in intensity. The same is true when depositing extra Fe onto the unannealed film where feature A seems most pronounced. These changes upon annealing likely relate to the changes seen in the Fe $2p$ spectra. As the Fe vacancy concentration decreases upon post annealing, the density of Fe in the film increases and the Fermi level position rises relative to the bottom of the Fe $3d$ band. This is reflected in the increased intensity of feature A.



(a) Core level shift in Ti $2p$



(b) Core level shift in O $1s$



(c) Schematic of band bending

Figure 6.4: Core level shift and band bending

One would expect that when the n-type STO substrate forms an intimate contact with the FeSe metal film, n-type charge carriers would be transferred from the STO to the metal until the Fermi levels of the STO and FeSe are equilibrated. As a result, the valence band, conduction band, and core levels of the STO should bend upwards near the interface, as shown in Figure 6.4c.

Band bending at the STO $\sqrt{13}\times\sqrt{13}$ surface is minimal as the onset of the valence band is 3.2 eV below the Fermi level, meaning the the Fermi level is located at the bottom of the conduction band. The lack of a core level shift and zero shift of the STO valence band spectrum after growing an FeSe monolayer indicates that there is no charge transfer across the interface.

Yet, the content of the electron pocket near the M-point of the Brillouin zone is about 0.1 electron per Fe. Zhou *et al.* calculated that for typical Nb dopant concentrations of $N_{\mathrm{d}} = 1.1 \times 10^{20}$ cm^{-3}, one would expect a band bending in the STO of the order of 1−2 eV (Zhou and Millis, 2016). Our dopant level is very similar ($N_{\mathrm{d}} = 2 \times 10^{20}$ cm^{-3}), but we found no shift in the Ti $2p$ (Figure 6.4a), O $1s$ (Figure 6.4b) and STO valence band features before and after growing a 1 ML FeSe film (including the post processed films, *i.e.*, post annealing and/or extra Fe deposition). Considering the lack of band bending, we conclude that there is no charge transfer from the STO $\sqrt{13} \times \sqrt{13}$ substrate to the FeSe films.

6.4 Conclusions

The XPS spectra of our samples show that our films are free of contaminants, except for the presence of some Na impurities that likely originates from the fabrication process of the STO substrates. The information encoded in the core level and Auger spectra is compelling, but quantitative analysis, however complicated, would be highly desirable. Our data highlight the importance of Fe vacancies in determining the spectral lineshapes. In addition, they demonstrate the lack of charge transfer between

the STO substrate and FeSe film. The Fermi level rise in the post annealed films is therefore solely attributable to the increased Fe density in the film.

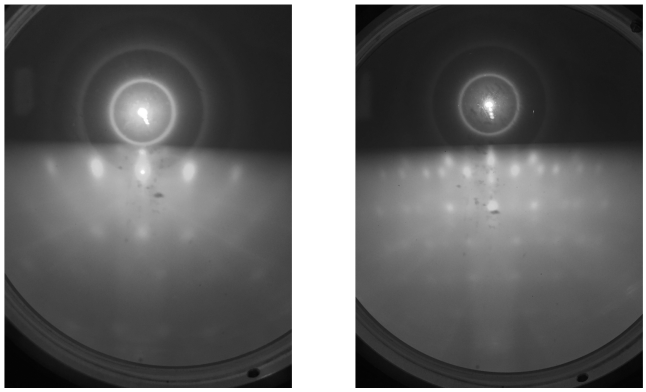
Chapter 7

FeTe on $SrTiO_3$

7.1 MBE synthesis, STM and XRD characterization

For the MBE synthesis of FeTe on STO, we followed the FeSe synthesis protocol discussed before. STO substrates were prepared via *in-situ* etching with Se to obtain atomically flat surfaces with the $(\sqrt{13} \times \sqrt{13})$ surface reconstruction. Interestingly, this process can be replicated using Te etching. The advantage of Te etching is that one does not have to worry about possible Se doping of the FeTe film. On the other hand, Se etching leaves no trace of Se in the XPS spectra of the $(\sqrt{13} \times \sqrt{13})$ surface while the quality of the resulting $(\sqrt{13} \times \sqrt{13})$ surface is better.

Once again, in order to obtain β-phase FeTe, we have to balance the Fe/Te flux ratio. Under Te deficient growth conditions, FeTe does not form a uniform monolayer, as is evident from the RHEED patterns in Figure 7.1: Low Te flux ($T_{\mathrm{Te}} = 260$ °C), results in the formation of transmission spots of bcc Fe, indicating that the film contains excess Fe in the form of metallic Fe clusters. Raising the source temperature T_{Te} to 300 °C produces a mixture of transmission spots belonging to bcc Fe and FeTe. At $T_{\mathrm{Te}} = 310$ °C, the RHEED pattern becomes more streaked, indicating the presence



(a) Te: 260 °C **(b)** Te: 300 °C

(c) Te: 310 °C **(d)** Te: 330 °C

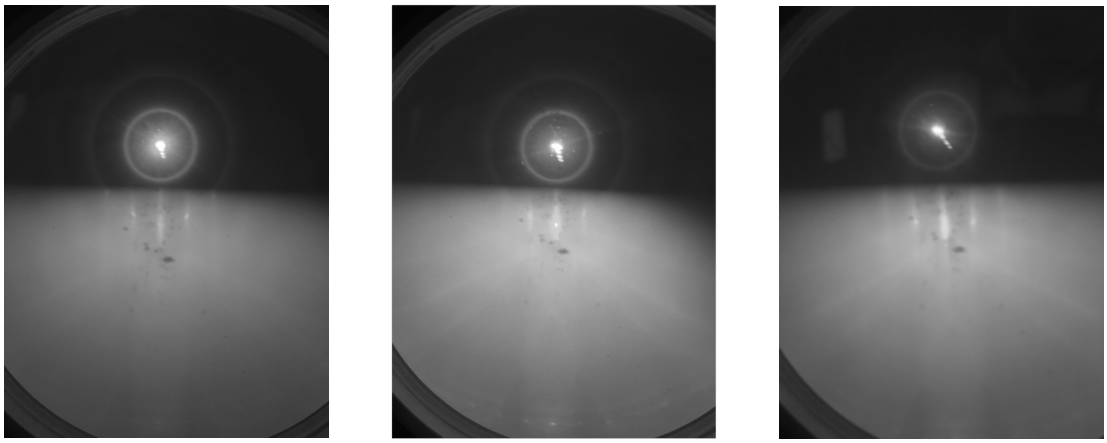
Figure 7.1: RHEED patterns of the FeTe films grown on Se-etched STO for different flux ratios. The source temperature of Fe, $T_{\mathrm{Fe}} = 1250$ °C. The substrate temperature $T_{\mathrm{sub}} = 280{-}290$ °C for all cases, except for panel (c) where $T_{\mathrm{sub}} = 320{-}324$ °C. All samples were post annealed at their respective growth temperature for about 5 to 10 minutes. The incident electron beam is along the STO[100] direction.

of a flat film with additional 3D islands of both FeTe and bcc Fe. Finally at T_{Te} = 330 °C, the RHEED pattern indicates the presence of a flat FeTe film.

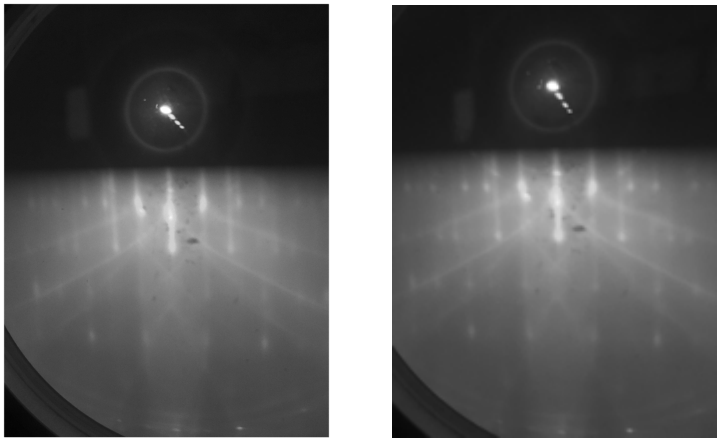
The Fe/Te composition ratio of the film can be fine-tuned by choosing the proper substrate and post annealing temperatures. Figure 7.2 shows the RHEED pattern of the as-grown FeTe monolayer film on STO, prepared using the following growth parameters: T_{Fe} = 1250 °C, T_{Te} = 340 °C and T_{sub} = 316−320 °C. The film was sequentially annealed at different temperatures for 10 minutes. The quality of the RHEED patterns do not show a significant improvement up to 390 °C. However, the thin film morphology does change, according to our STM images, which are shown in Figure 7.3. Fe transmission spots reappear at 390 °C, indicating a significant loss of Te content. At 320 °C (Figure 7.3 (a)−(c)), the majority of the film corresponds to the tetragonal FeTe monolayer (= 1 UC thick). The dark holes in this image expose the STO substrate and are about 0.63(3) nm deep. This depth matches the c-axis of tetragonal FeTe. In addition, the are some bright patches with a total height of about 0.99(5) nm, as measured from the STO substrate. Atomic resolution images of these patches reveal a honeycomb pattern with an in-plane lattice parameter of 1.22(5) nm. At 350 °C (Figure 7.3 (d)−(f)), the area fraction of the tetragonal monolayer decreases while that of the honeycomb structure increases. At 365 °C (Figure 7.3 (g)−(i)), the thickness of the first FeTe layer converted from 0.63(3) to 0.48(4) nm, indicating that the tetragonal phase is no longer stable. The heights of the mesas with honeycomb structure also decreased by almost same magnitude, about 0.15 nm, reaching a total thickness of 0.84(5) nm. Finally at 375 °C (Figure 7.3 (j)−(l)) the film was fully converted to the honeycomb structure with thickness of 0.81(3) nm. Some higher triangular shaped islands with 1.70(6) nm thickness were found as well.

Increasing the substrate temperature during the growth or extending the annealing time produces similar results. Both procedures result is Te deficiency, discontinuous film morphology and honeycomb structures in the STM, see Figure 7.4.

After fine tuning the growth parameters, we finally found the optimal condition to obtain high quality monolayer tetragonal FeTe on STO. The secret is to use



(a) $T_{\text{anneal}} = 316{-}320$ °C **(b)** $T_{\text{anneal}} = 340{-}350$ °C **(c)** $T_{\text{anneal}} = 365{-}375$ °C



(d) $T_{\text{anneal}} = 390{-}400$ °C **(e)** $T_{\text{anneal}} = 430{-}440$ °C

Figure 7.2: Influence of post annealing temperature on the quality of the FeTe thin film, according to RHEED: A monolayer FeTe was grown using $T_{\text{Fe}} = 1250$ °C, $T_{\text{Te}} = 340$ °C and $T_{\text{sub}} = 316{-}320$ °C. The film was post annealed for 10 minutes in several steps, each at slightly higher temperature. The incident electron beam is along the STO[100] direction.

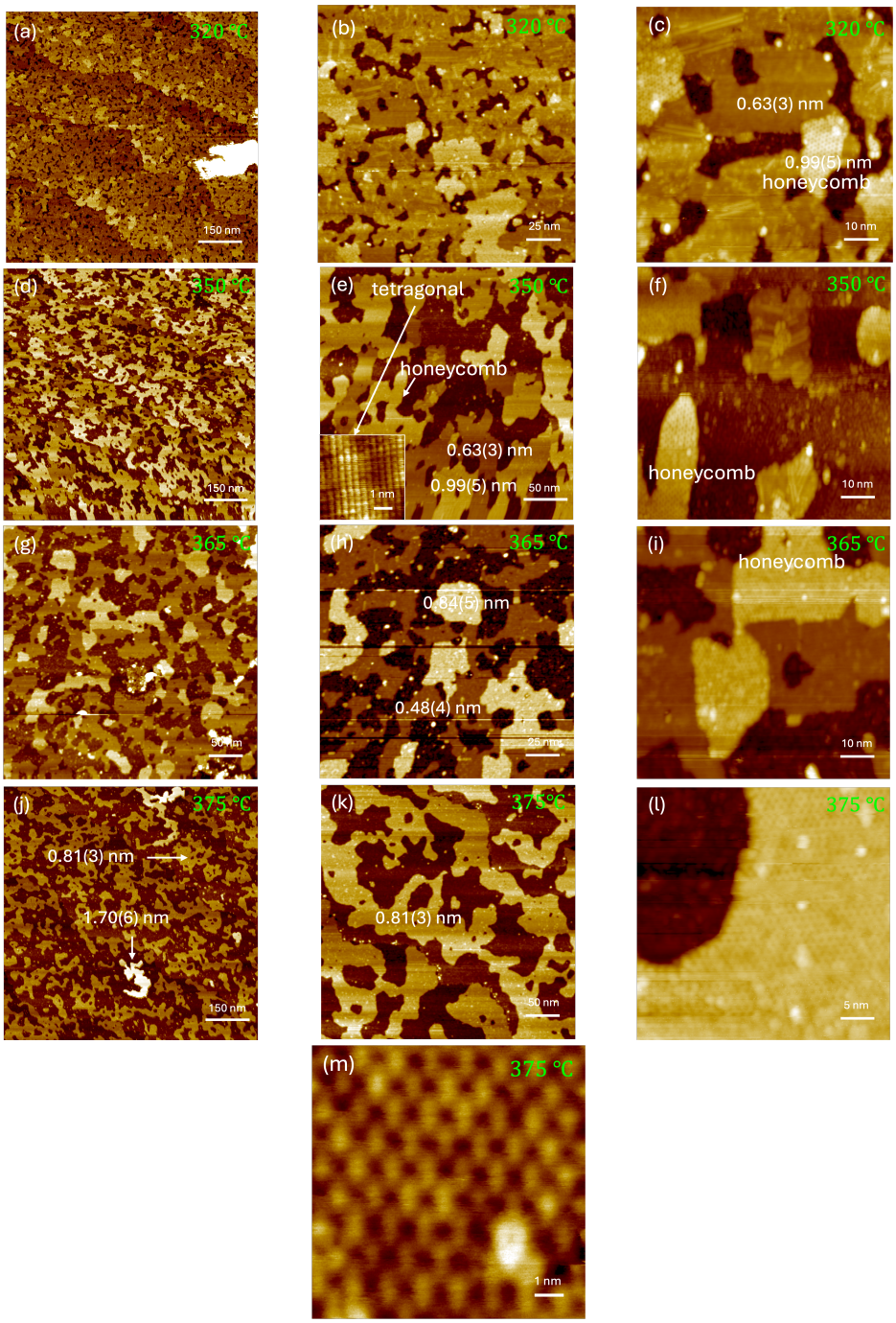


Figure 7.3: Evolution of the FeTe film morphology for different post annealing temperatures, monitored with STM. The atomic resolution images of the tetragonal phase and honeycomb structure in panels (e) and (m), respectively, were recorded at 1.5 V 300 pA. All other images were recorded at 3 V 100 pA. The annealing temperature is labeled by green color fonts. Even though the nominal coverage of the film is 1 UC, one observes terraces with different heights, as indicated by the white-font numbers.

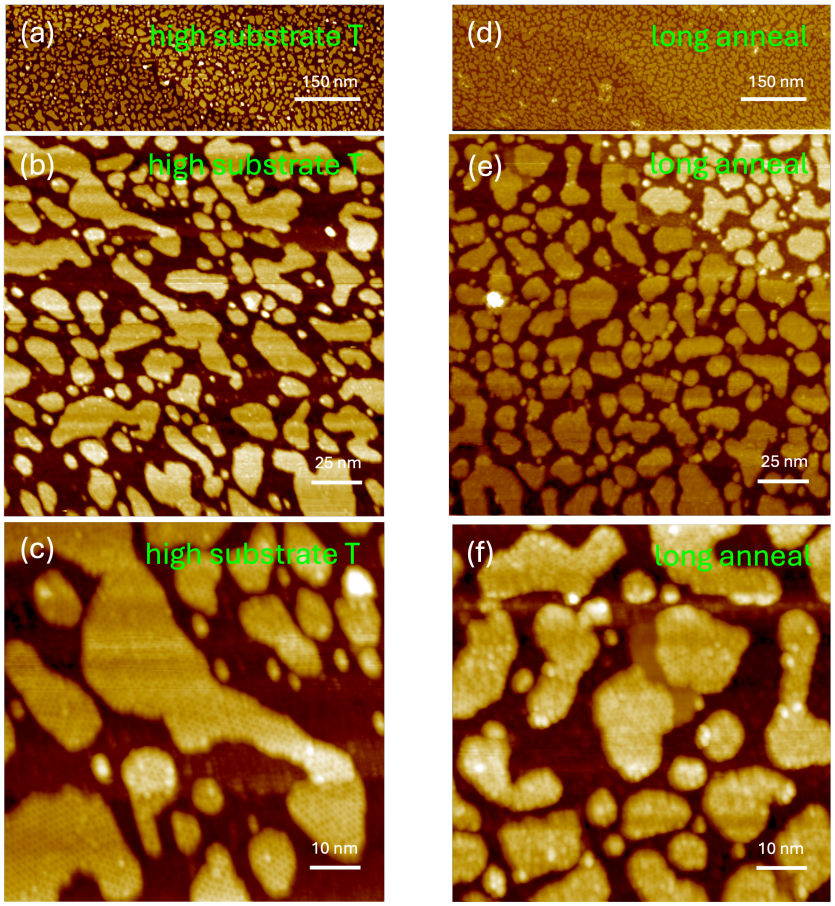


Figure 7.4: Influence of growth temperature and post annealing time on FeTe monolayers on STO, monitored with STM. The film in panels (a) through (c) was grown at T_{sub} = 350 °C, post annealed at 330 °C for 5 minutes and at 365 °C for 10 minutes. The film in panels (d) through (f) was grown at 320 °C, post annealed at 320 °C for 60 minutes. Both cases produced the honeycomb islands. Both samples were grown with T_{Fe} = 1250 °C, T_{Se} = 330 °C.

even lower growth temperatures. The STO substrate was treated by Te etching. The growth parameters are $T_{\mathrm{Fe}} = 1250$ °C, $T_{\mathrm{Te}} = 330$ °C, and $T_{\mathrm{sub}} = 280$ °C. Fe and Te were co-evaporated for 5 mins 45 s and the film was annealed at growth temperature for 5 minutes. Both RHEED and LEED patterns are very sharp with low background intensity, and reveal the sole presence of the tetragonal phase, see Figure 7.5. Second layer FeTe islands all have a rectangular shape with a thickness of about 0.6 nm, corresponding to the c-axis of the tetragonal phase. Atomic resolution imaging confirmed the presence of a uniform tetragonal film.

Prolonged usage of the Te effusion slowly leads to a lower Te flux as more Te atoms condense around the aperture of the cell. To compensate the loss of flux, we increased the Te source temperature from 330 °C up to 370 °C. This should not affect the coverage calibration above (5.75 minutes per layer) since the growth rate is limited by the Fe flux. We first studied the growth of FeTe multilayers on top of the FeSe monolayer on STO, which should proceed via van der Waals growth.

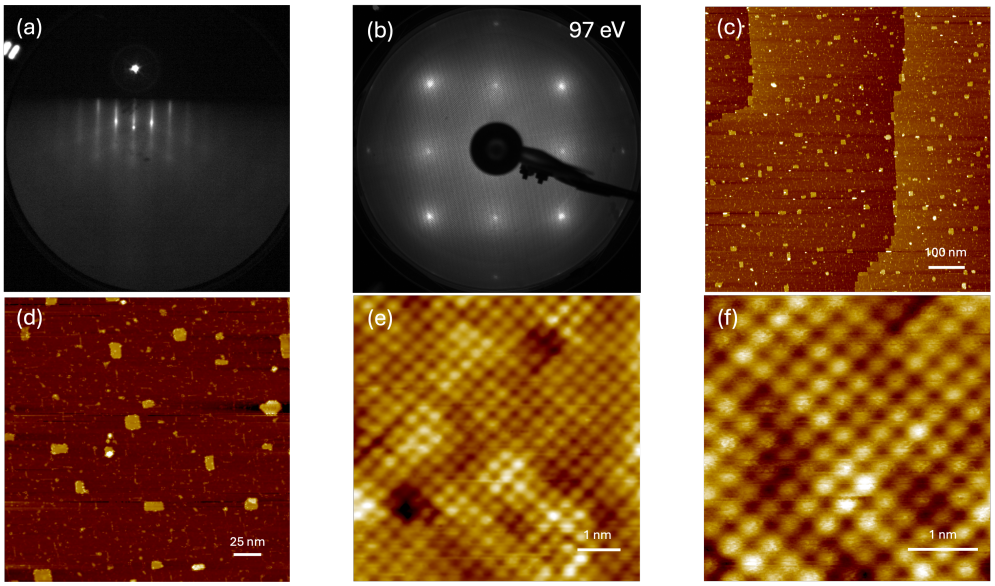


Figure 7.5: High quality tetragonal FeTe monolayer, grown on Te-etched STO: (a) RHEED pattern taken along STO [100] direction. (b) LEED pattern of the FeTe monolayer. (c) and (d) STM images at 2.0 V 200 pA; (e) and (f) STM images with atomic resolution at 20 mV, 200 pA. The STM data were measured at 77K.

The growth parameters were as follows: $T_{\mathrm{Fe}} = 1250$ °C, $T_{\mathrm{Te}} = 370$ °C, and $T_{\mathrm{sub}} = 280{-}290$ °C. (Direct FeTe deposition onto the Te-etched $(\sqrt{13} \times \sqrt{13})$ STO substrate will be discussed later).

Deposition of the first and second FeTe layer onto the FeSe monolayer produced an atomically flat films with sharp RHEED streaky patterns, as shown in Figure 7.6, panels (a) and (b).

A transmission pattern was observed after depositing 5 ML of FeTe. Additional deposition of pure Te for 20 mins at the same FeTe growth temperature (280−290 °C) did not make a clear difference in the RHEED pattern. Sharp RHEED streaks were recovered after heating the FeTe film to 480 °C for several minutes. Presumably, excess Te was removed during this step. One might argue that the FeTe film decomposed at 480 °C while the FeSe monolayer remains stable. In that case, the streaky pattern should be attributed to the exposure of the FeSe monolayer. However, the Fe atom cannot be removed at 480 °C and, consequently, one should expect to see evidence of bcc Fe crystallites in RHEED, which we did not. The STM image of this film revealed step heights that are consistent with the presence of a tetragonal FeTe film. It also revealed the presence of a 5 nm deep hole, where only a few monolayers of FeTe covered the 1ML-FeSe/STO.

Similar to the FeTe monolayer, increased growth temperature increases the Fe content of the film. Figure 7.7 shows The RHEED pattern of a thick FeTe grown at $T_{\mathrm{sub}} = 333{-}341$ °C on the 1 UC-thick FeSe monolayer. It exhibits sharp streaks with relatively low background intensity. The corresponding STM image in Figure 7.7 (c) reveals the presence of 1−3 nm height islands. The single UC step heights of the STO substrate are still recognizable, as indicated by the black arrows.

The growth parameters of the FeTe films grown on a 1 UC thick FeSe layer on Se-etched STO are listed in Table 7.1.

After opening the chamber and removing the condensation of Te around the aperture of the effusion cell, we grew a thick FeTe film on a Te-etched $(\sqrt{13} \times \sqrt{13})$ reconstructed STO substrate, using the following parameters: $T_{\mathrm{Fe}} = 1250$ °C, T_{Te}

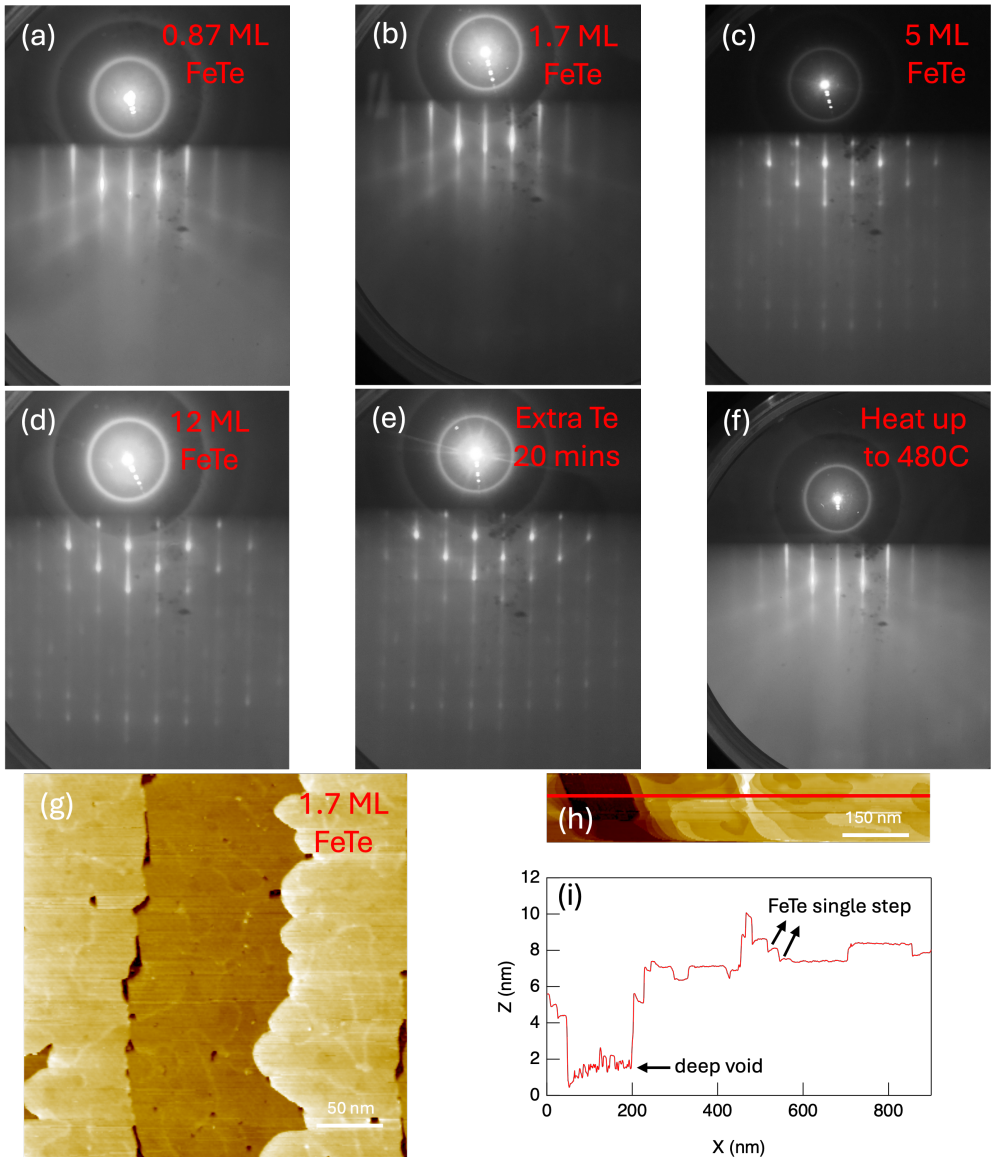


Figure 7.6: Thick FeTe film (#158) grown on a 1 UC-thick FeTe film under Te rich grow condition at a substrate temperature of 280−290 °C. (a)−(d) RHEED patterns of the FeTe film for different deposition times, corresponding to thicknesses of about 0.87 ML, 1.7 ML, 5 ML and 12 ML; (e) RHEED pattern after depositing additional Te at the same growth temperature; (f) FeTe film from panel (e), this time post annealed at 480 °C. The RHEED patterns were taken with the incident electron beam along the STO [100] direction. (g) and (h) STM images corresponding to panels (b) and (f); (i) Line profile along the red line in panel (h). The STM images were scanned at 2.5 V, 300 pA.

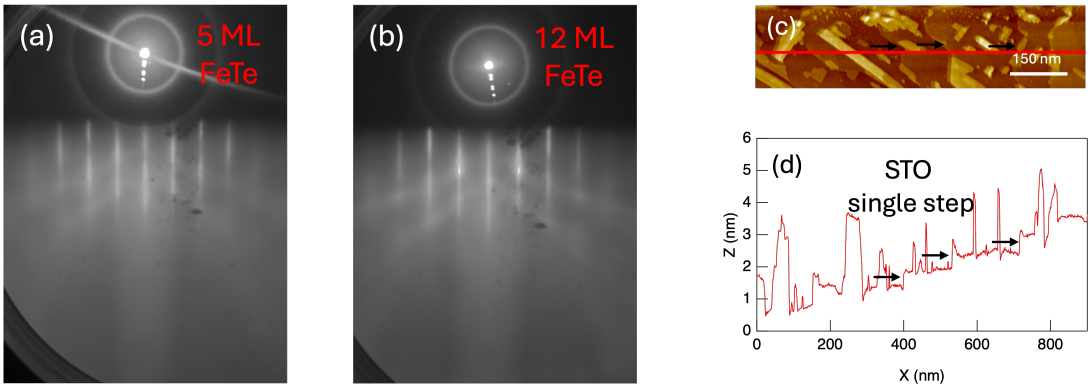


Figure 7.7: Thick FeTe film (#159) grown on a 1 UC thick FeSe film on STO, grown at 333−341 °C. (a) and (b): RHEED patterns after 30 minute (5 ML) and 70 minutes (12 ML) of deposition, respectively. Both RHEED pattern were taken with the incident beam along the [100] direction. (c) STM image corresponding to panel (b); (d) STM line profile along the red line in panel (c).

Table 7.1: Growth conditions of FeTe films on a 1 UC-thick FeSe layer on Se-etched STO

Sample label	T_{Te}	FeTe growth	Extra Te deposition	Post anneal
12 ML #158	370 °C	280−290 °C 70 mins	20 mins	480 °C several mins
12 ML #159	370 °C	333−341 °C 70 mins		

= 370 °C, T_{sub} = 280 °C. This resulted in a Te rich growth condition. The growth parameters are summarized in Table 7.2.

Additional RHEED streaks appeared after 30 minutes (about 5 ML). As the film grew thicker, transmission patterns became more clear, see Figure 7.8. Extra deposition of pure Te at 280 °C did not improve the film quality. A streaky pattern was recovered after annealing the film at 380 °C, but the pattern is rather poor and has a high background intensity. Blurred halos indicate that the film is becoming polycrystalline. Figure 7.9 reveals that a much better film quality is obtained after reducing the effusion cell temperature of Te to 330 °C. A streaky RHEED pattern, indicating a flat film morphology, remained clearly visible, even after 14 hours of deposition time (about 146 ML), see Figure 7.9.

This film was post annealed at the growth temperature (280 °C) for one hour. STM images revealed step heights of 0.6 nm, consistent with the c parameter of tetragonal FeTe. The atomic resolution image in Figure 7.9 (f) confirms the tetragonal

Table 7.2: Growth condition of the FeTe films on Te-etched STO

Sample label	T_{Te}	FeTe growth	Extra Te deposition	Post anneal	Te capping
1 ML #231	370 °C	280 °C 5 mins 45 s		280 °C 10 mins	
78 ML #231	370 °C	285 °C 7.5 h		280-287 °C 2 h; 336-354 °C 30 mins; 393-400 °C 10 mins	
146 ML #245	330 °C	280 °C 14 h		280 °C 1 h	RT 30 mins
1 ML #251	330 °C	280 °C 5 mins 45 s		280 °C 5 mins	
1 ML #253	330 °C	280 °C 5 mins 35 s	280 °C 5 mins	280 °C 5 mins	

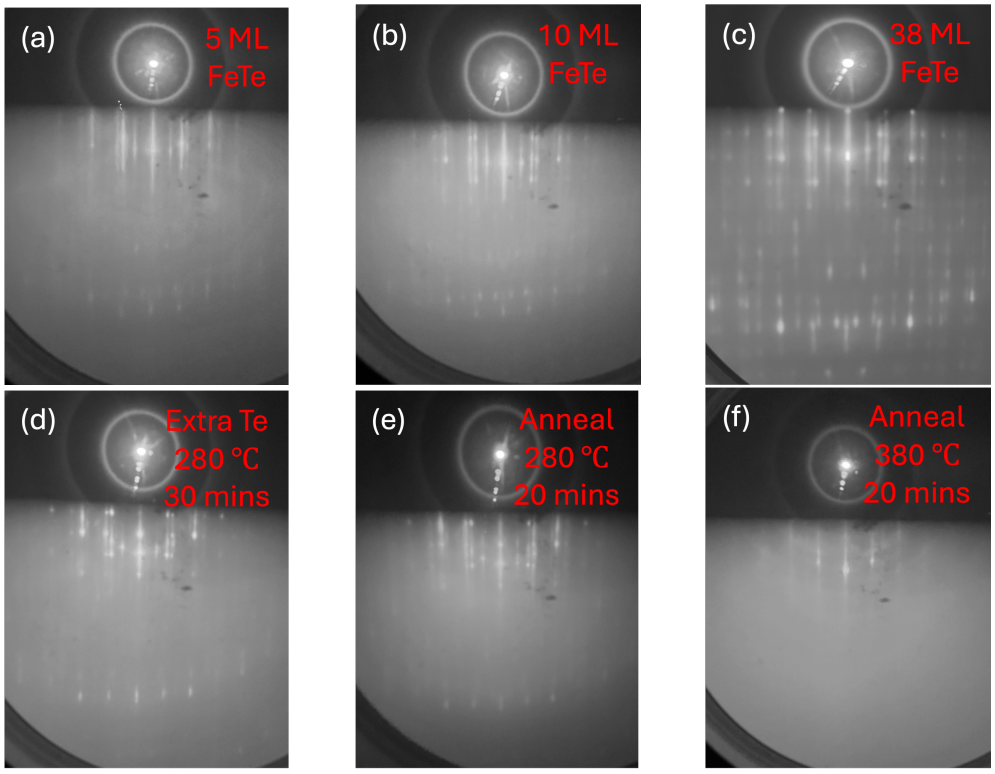


Figure 7.8: Thick 146 ML FeTe film (#245) grown on the $(\sqrt{13}\times\sqrt{13})$ reconstructed STO surface under Te rich growth condition (T_{Te} = 370 °C). RHEED patterns: (a)−(c) After growing FeTe for 30 minutes (5 ML), 60 minutes (10 ML), and 220 minutes (38 ML); (d) post annealed under a Te flux at 280 °C for 30 mins; (e) and (f) annealed in UHV at 280 °C and 380 °C for 20 minutes each. RHEED patterns were collected with the incident beam along the STO [100] direction.

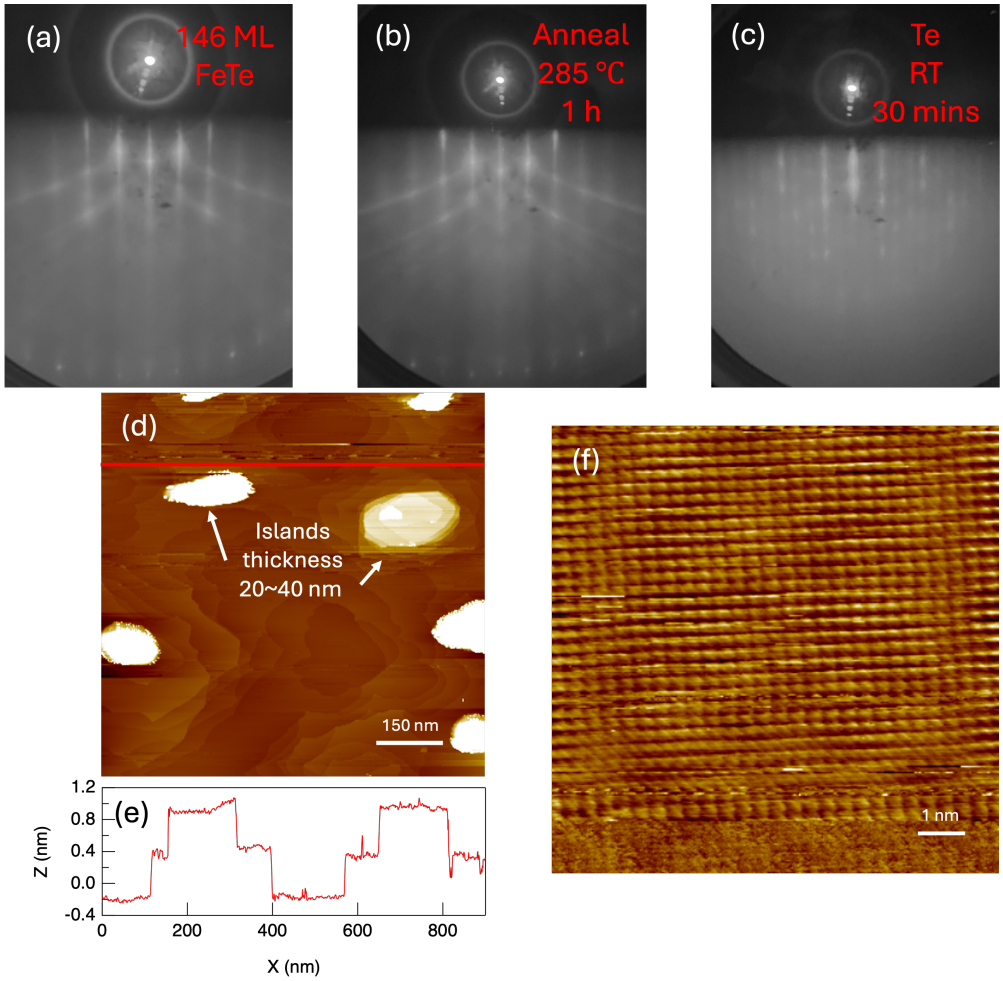


Figure 7.9: 146 ML thick FeTe film (#245) grown on the Te-etched ($\sqrt{13} \times \sqrt{13}$) reconstructed STO surface under optimal Fe:Te flux ratio (T_{Te} = 330 °C). RHEED patterns: (a) FeTe after 14 hours (146 ML) of deposition; (b) post annealed at 285 °C for 1 hour; (c) After Te capping at room temperature. All RHEED pattern were taken with the incident beam along the STO [100] direction. STM images corresponding to panel (b): (d) Large scale image, scanned at 2.5 V 300 pA; (e) STM line profile along the red line in panel (d); (f) atomic resolution image of the tetragonal FeTe lattice, scanned at 1.5 V, 300 pA.

lattice structure. We also observed some 20−40 nm tall islands, which was likely β-FeTe.

The out-of-plane lattice constant of the 146 ML thick FeTe film (#245) was measured with *ex-situ* XRD. To this end, we deposited a protective capping layer of pure Te at room temperature. The 2θ-ω scan is shown in Figure 7.10. The out-of-plane lattice parameter c was calculated from the XRD peak position and is given in Table 7.3, and is close to the lattice parameter of the β-FeTe single crystal 6.27−6.28 Å (Okamoto and Tanner, 1990).

We found some additional reflections that could be attributed to $FeTe_2$. This competing phase is likely produced by the capping layer, as indicated by the RHEED pattern in Figure 7.9 (c). Te films deposited at room temperature is expected to be amorphous or polycrystalline, but we find that the excess Te converts part of FeTe film to $FeTe_2$, even at room temperature. Notice that the (00l) reflections with odd l values are forbidden for $FeTe_2$ (space group $Pnnm$ (Persson, 2015)).

We also measured the XRR spectrum to confirm the thickness of the film. The result is shown in Figure 7.11, The thickness of the film was confirmed by calculating the oscillation period of the Kiessig fringes in XRR, and agreed with our STM calibration.

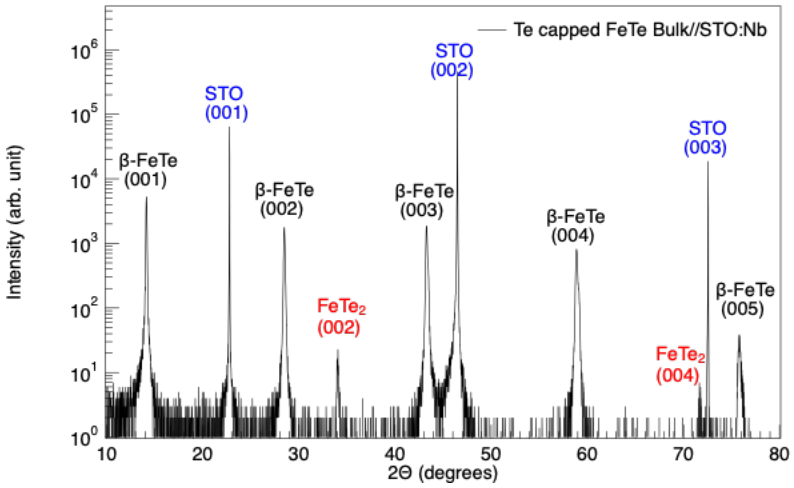


Figure 7.10: XRD 2θ-ω scan of a 146 ML thick FeTe film (#245) on Te-etched STO

Table 7.3: Out-of-plane lattice parameter of the 146 ML thick FeTe films (#245) on Te-etched STO

Composition	XRD peak index	2Θ/°	c/Å
β-FeTe	(001)	14.13	6.263(44)
	(002)	28.47	6.265(21)
	(003)	43.28	6.266(14)
	(004)	58.88	6.269(10)
	(005)	75.80	6.270(7)
$FeTe_2$	(002)	34.05	5.252(15)
	(004)	71.64	5.264(6)

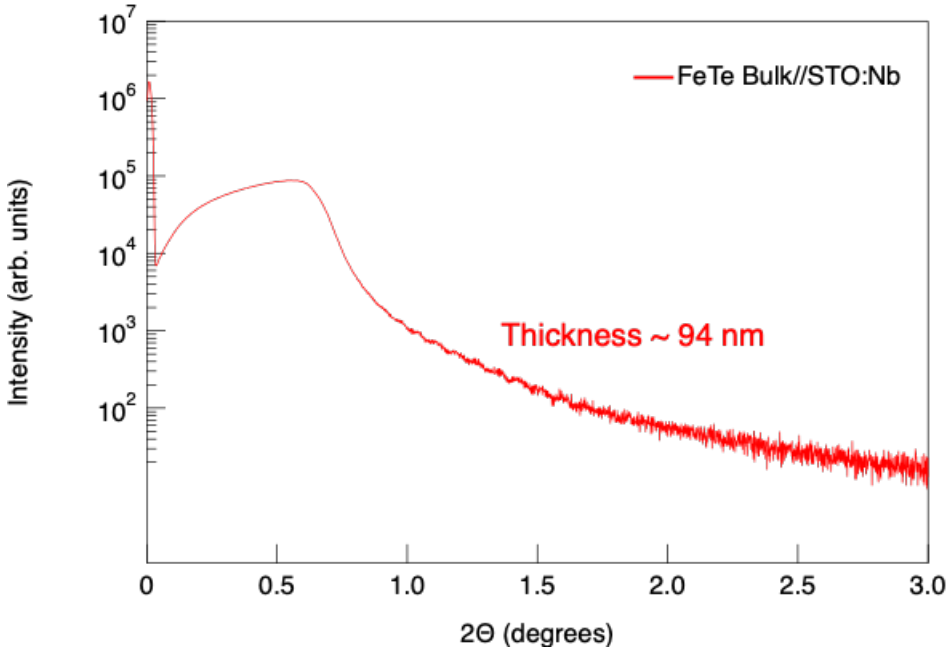


Figure 7.11: XRR data of the 146 ML thick FeTe bulk film (#245) on Te-etched STO

The in-plane lattice parameters of the FeTe film were obtained from RSM measurement, see Figure 7.12, Accordingly, we find that $a = 3.839(2)$ Å and $c = 6.269(3)$ Å. These lattice parameters are very close those of a bulk single crystal of β-FeTe: $a = 3.82$ Å, $c = 6.27{-}6.28$ Å (Okamoto and Tanner, 1990). We conclude that the 146 ML β-FeTe film on Te-etched STO is fully relaxed.

7.2 STS of Monolayer and Second-layer FeTe film

The scanning tunneling spectroscopy of FeTe film was checked at 79 K, using a lock-in amplifier. The FeTe monolayer exhibits metallic behavior (Figure 7.13). Some second layer FeTe patches were also found on the surface and displayed almost the same spectroscopy data as the monolayer film (Figure 7.14).

Atomically-resolved STM images revealed some local variations in contrast, as shown in Figure 7.15. Similar contrast variations have also been observed in monolayer FeSe on STO(001). The high brightness sites were attributed to Fe vacancies beneath the Se top layer or Se_{Fe} substitutional defects, while the dark sites

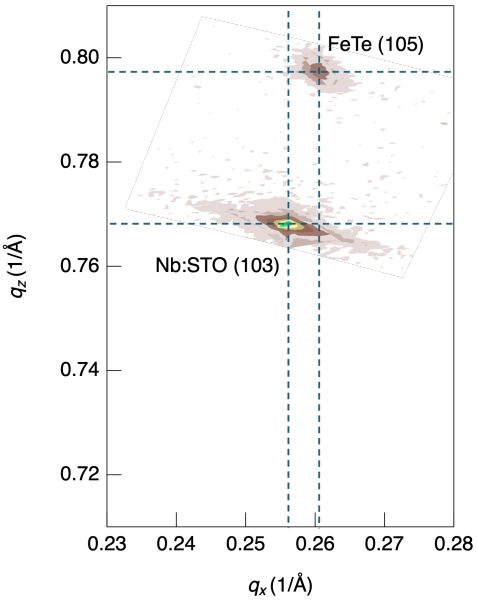
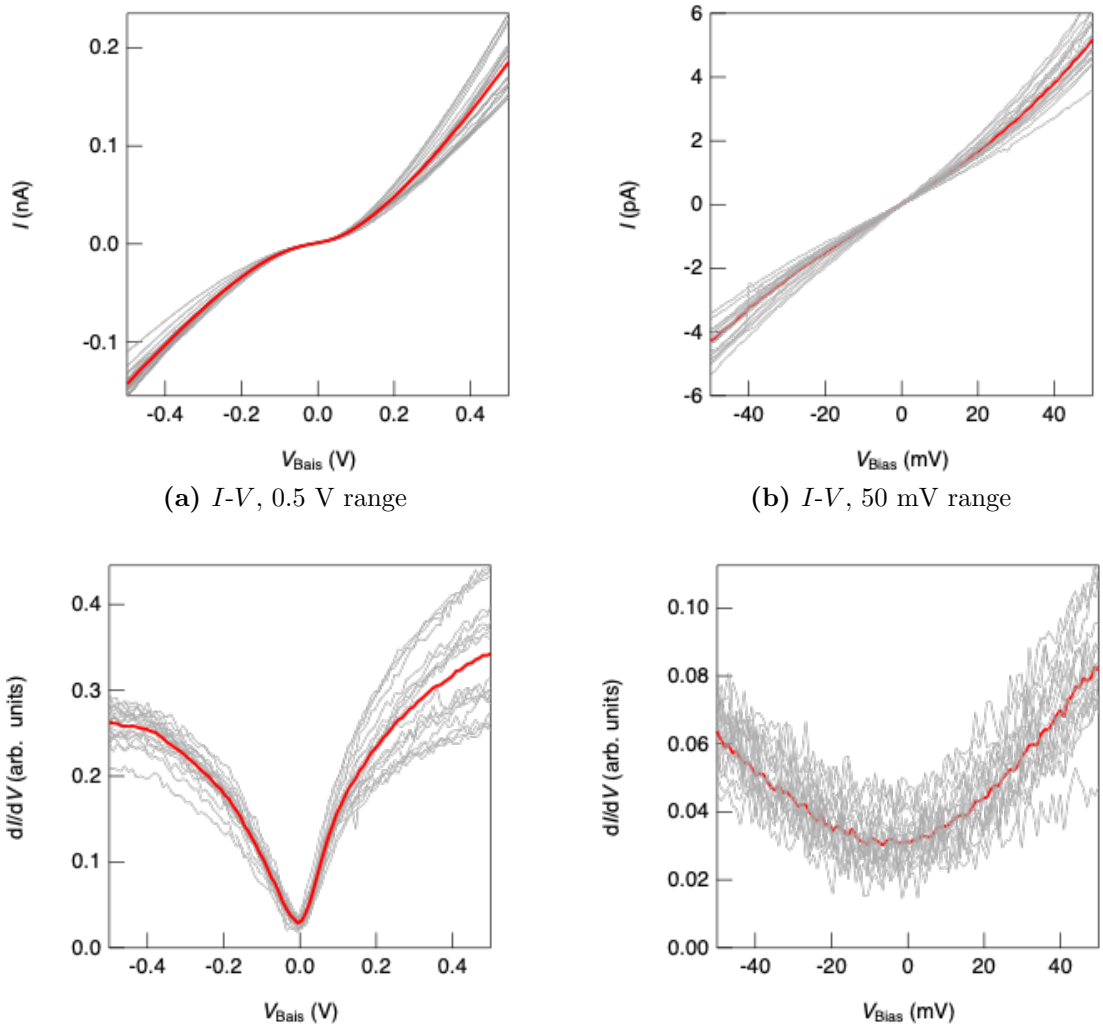


Figure 7.12: RSM data of the 146 ML thick FeTe film (#245) on Te-etched STO



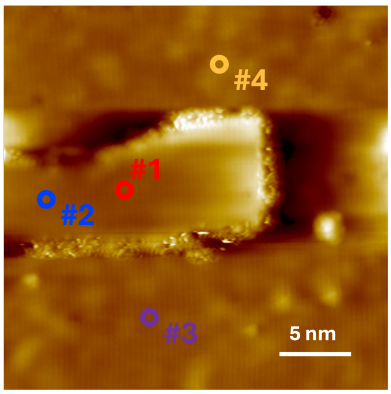
(a) I-V, 0.5 V range

(b) I-V, 50 mV range

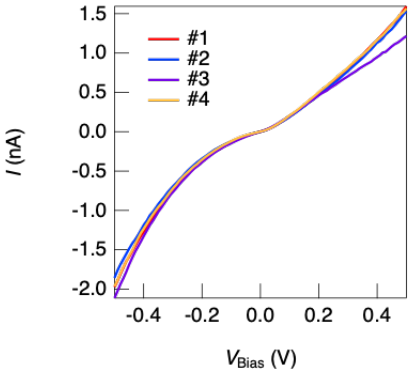
(c) $\mathrm{d}I/\mathrm{d}V$, 0.5 V range

(d) $\mathrm{d}I/\mathrm{d}V$, 50 mV range

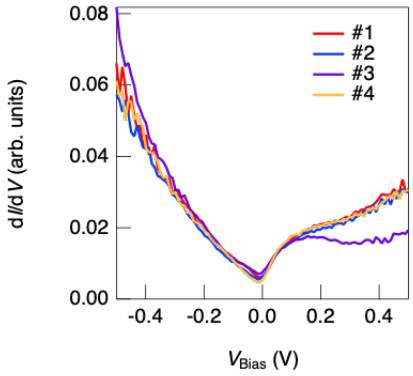
Figure 7.13: Scanning Tunneling Spectroscopy of an FeTe monolayer film on Te-etched STO. (a) and (b): I(V) point spectra (in grey) were repeatedly measured at the same location on the surface. The averaged I(V) spectrum is shown in red. (c) and (d): $\mathrm{d}I/\mathrm{d}V$ spectra measured with the lock-in detection system. The modulation frequency $f = 931$ Hz.



(a) STM morphology image: $V_{\text{bias}} = 100$ mV, $I_{\text{set}} = 200$ pA

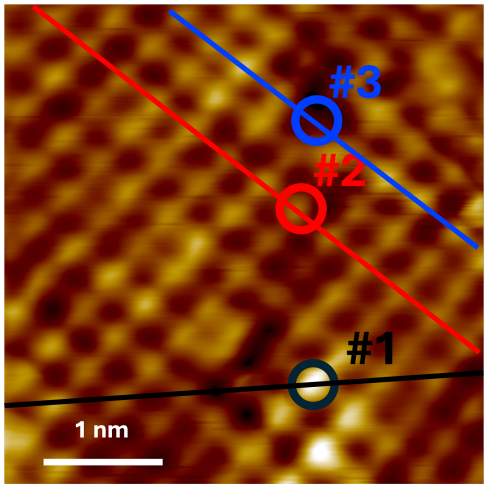


(b) I-V

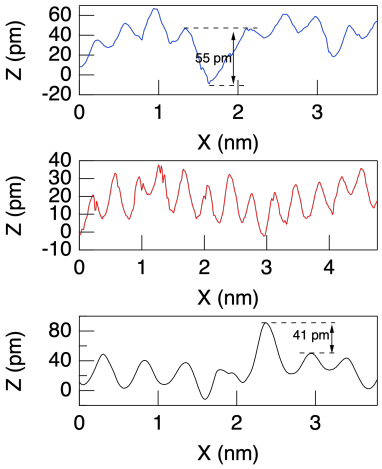


(c) $\mathrm{d}I/\mathrm{d}V$

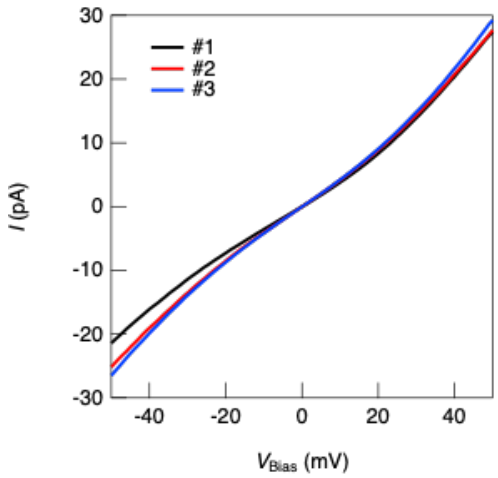
Figure 7.14: Comparison of the monolayer and second layer FeTe film on STO. The $\mathrm{d}I/\mathrm{d}V$ spectroscopy data were acquired with a lock-in amplifier. The modulation frequency $f = 931$ Hz.



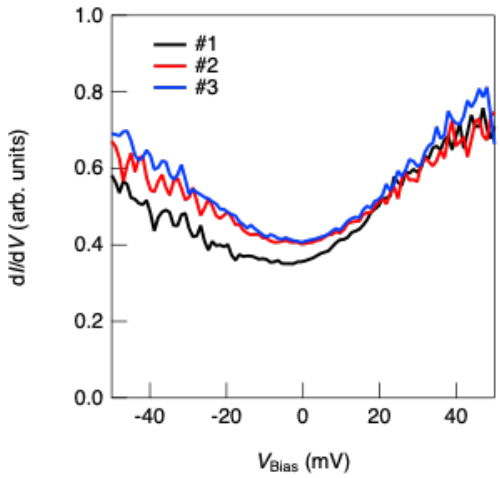
(a) STM morphology image: V_{bias} = 50 mV, I_{set} = 3000 pA



(b) Line-profile along the marked lines



(c) I-V



(d) dI/dV

Figure 7.15: Atomically-resolved contrast variations in a 1 UC thick FeTe layer on STO. (a): bright (#1), intermediate (#2), and dark atom sites (#3). (b) Color-coded line profiles along the directions indicated in panel (a). (c) corresponding I(V) spectra. (d) dI/dV spectra obtained by differentiating the $I(V)$ spectra in panel (c).

were attributed to Se vacancies (Liu et al., 2018; Zhang et al., 2020). Those defects are expected to produce localized defect states, but those were not observed within the -0.5 to 0.5 eV bias range. In fact, the STS point spectra are all very similar, see Figure 7.15 (d).

The high contrast regions enclosed by the white circles did not reveal a clear dependence on the tunneling bias 7.16, which suggests that the local contrast variation may not be related to lateral variations of the LDOS, but rather to small atomic height variations. The local height variations are of the order of 40−50 pm, as determined from the line-profile in Figure 7.15 (b). This is very similar to the case of $FeTe_{1-x}Se_x$, where the bigger Te site looks brighter than Se site, independent on bias. However, in our case we etched the STO substrate with Te and there is no detectable amount of Se in XPS. It is therefore likely that the contrast variations are related to a small non-periodic rippling of the atoms at the Fe/STO interface. For pure FeTe monolayers, the roughness is reported to be about 17 pm (Li et al., 2015).

7.3 XPS Survey Scan

The XPS survey scan of the 1 UC thick FeTe film on Te-etched STO is shown in Figure 7.17. For the most part, the spectrum is very similar to that of monolayer FeSe on STO, except that the Se core level and Auger spectra are replaced by the corresponding Te spectra. The Te MNN Auger spectrum around E_B = 1000−1100 eV coincides with the Ti LMM Auger spectrum, and its low-energy tail extends all the way to the C KVV Auger line at $E_B = 1233$ eV. This makes it hard to determine whether there is a tiny amount of carbon on the surface from the survey spectrum alone. There is no iron oxide satellite near the Fe $2p_{3/2}$ core level, which indicates that our FeTe film is clean. The Fe $2p$ core level and CVV Auger spectrum will be discussed later.

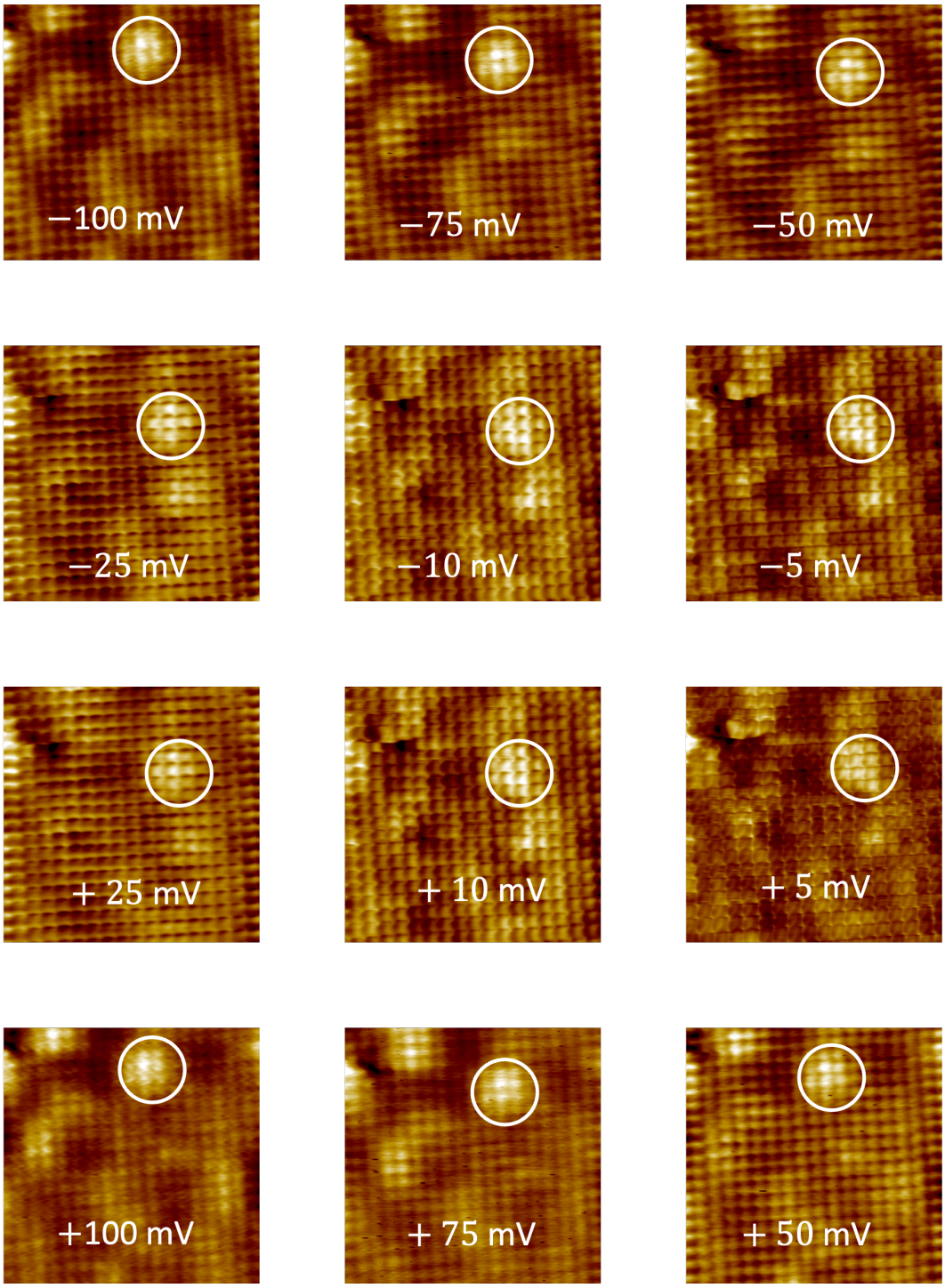


Figure 7.16: Bias-dependent atomically-resolved contrast variations. (a) White circles enclose the same 7×7 nm^2 region. I_{set} = 2500 pA.

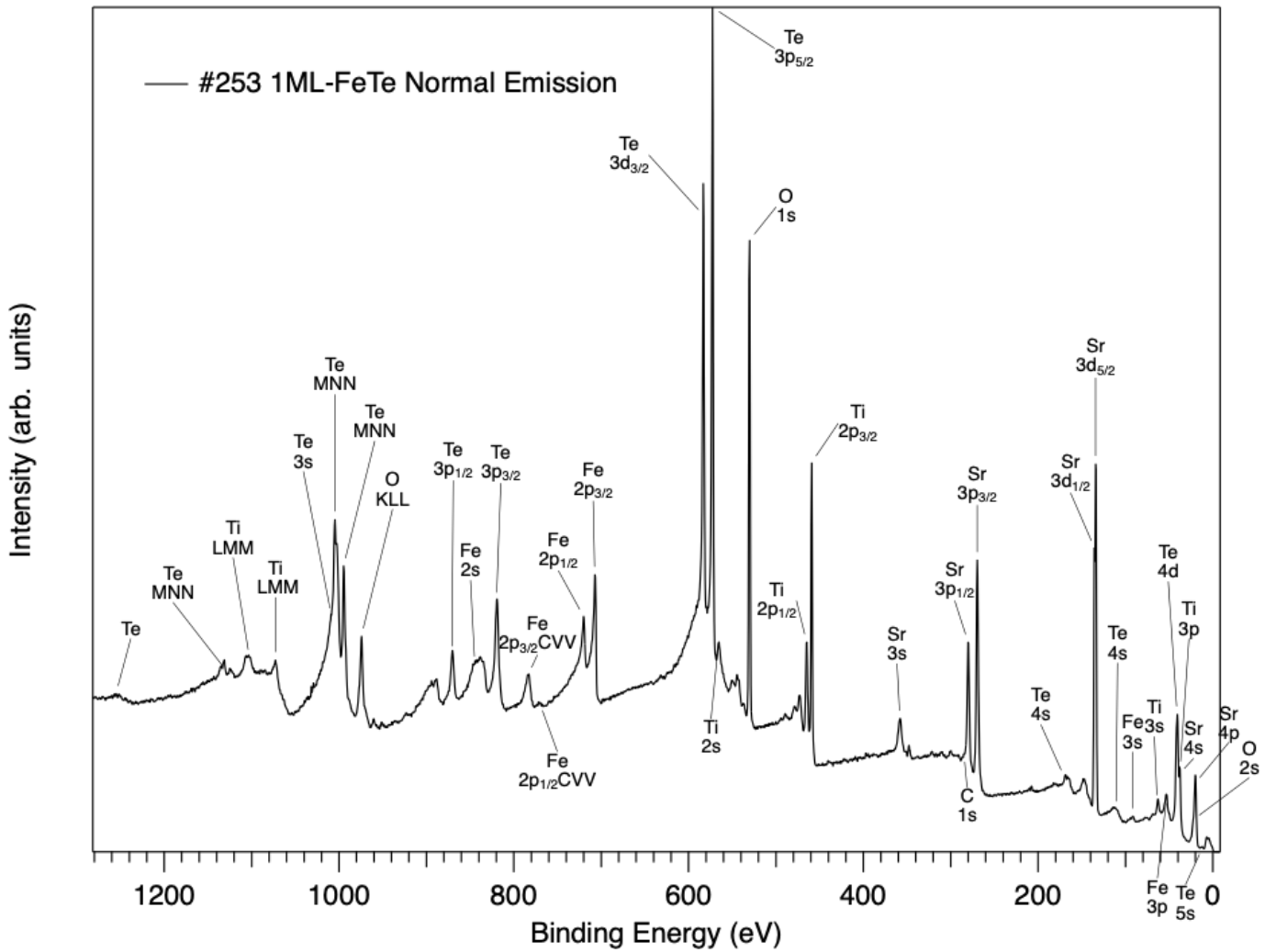


Figure 7.17: XPS survey spectrum of a 1 UC thick FeTe film on STO.

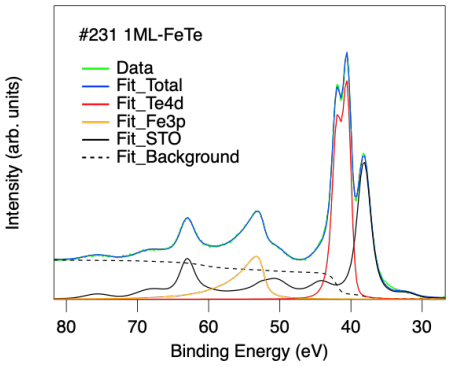
7.4 Stoichiometry

We investigated the stoichiometry of the FeTe films by analyzing Fe 3p and Te 4d core level spectra. The spectra of the 1 ML thick FeTe film on STO are very complicated due to the presence of overlapping signals from the Ti 3p, Sr 4s, and Ti 3s core levels, along with various energy-loss satellites that spread across the entire Fe 3p and Te 4d regions (Figure 7.18a).

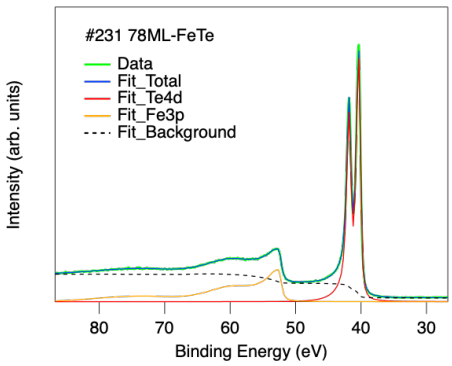
The spectra of the bulk-like multilayer films do not contain contributions from the STO substrate and are thus expected to be easier to analyze (Figure 7.18b). However, careful examination of those spectra also revealed considerable complexity. The analyses and fitting procedures described below were developed and implemented by Dr. Paolo Vilmercati.

To simplify the calculation of the stoichiometry, we focus on the Fe 3p and Te 4d core level spectra, which are very close in binding energy. This implies that the kinetic energies of the corresponding photoelectrons are almost the same. Accordingly, differences in the inelastic mean free path and transmission probabilities through the electron energy analyzer are negligible and will not affect the determination of the stoichiometry.

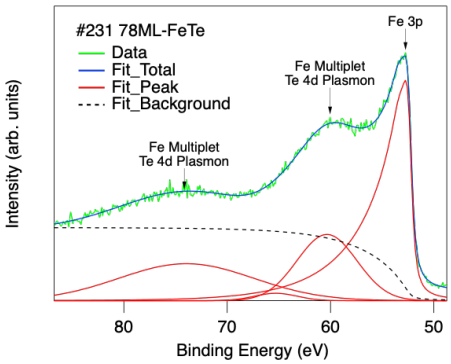
The Fe 3p spectra near 53 eV binding energy could be fitted using a spin-orbit split doublet with a Manhan line shape, complemented by at least three additional Gaussian peaks at higher binding energy (Figure 7.18c). Initially, we attributed these extra peaks to Fe multiplets; however, these multiplets features overlap with the plasmon loss satellites of the Te 4d core levels at about 41 eV binding energy. To estimate the excitation energies of these loss satellites, we investigated the loss satellites of Te 3d core level spectrum, which do not overlap with any other features in the photoelectron spectrum. They are shown in Figure 7.18d. Specifically, the figures shows the existence of several loss satellites on the high binding energy side of the Te 3d spectrum. A surface plasmon-loss satellite appears at $\Delta E = 14.75$ eV higher binding energy, as measured from the Te $3d_{5/2}$ core level. The bulk plasmon



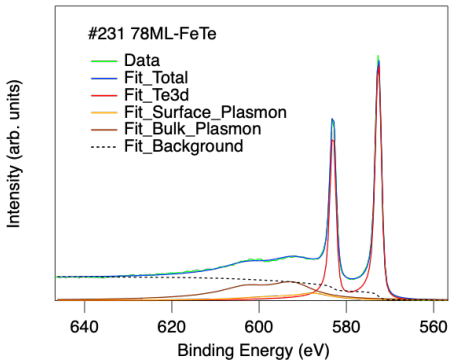
(a) #231 1ML-FeTe: Fe 3p, Te 4d and STO



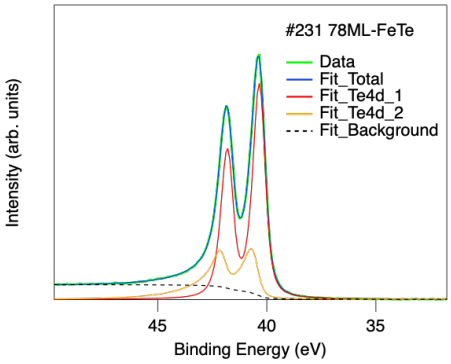
(b) #231 78ML-FeTe: Fe 3p and Te 4d



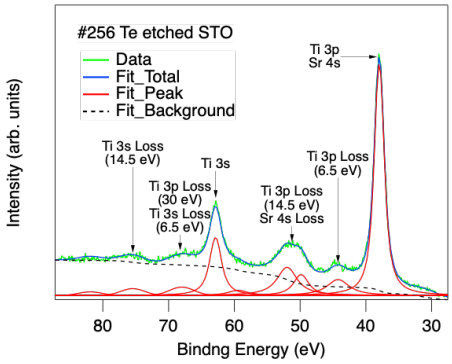
(c) #231 78ML-FeTe: Fe 3p



(d) #231 78ML-FeTe: Te 3d



(e) #231 78ML-FeTe: Te 4d



(f) #256 Te-etched STO

Figure 7.18: Stoichiometry determination of the FeTe films on STO from the XPS.

appears at $\Delta E = 19.32$ eV higher bonding energy. The intensity ratio between the Te $3d$ main core level and the plasmon-loss contribution was 1.48, which is substantial. Similar losses should be observed for the Te $4d$ spectrum where they overlap with the Fe $3p$ multiplet spectrum. In the following, we first assume that the Fe $3p$ core level spectrum does not include contributions from the plasmon-loss satellites. Then, we will correct the obtained stoichiometry for the presence of those satellites.

The grazing and normal emission spectra of Te $4d$ showed subtle differences, prompting us to fit these spectra using two doublets (7.18e). The intensity ratio between these two doublets was found to be 2.3, with minimal differences observed in grazing and normal emissions. The energy splitting between these doublets was determined to be 0.3 eV.

After fitting the Fe $3p$ and Te $4d$ core levels separately, we performed a simultaneous fitting of the entire spectrum using four parameters: the intensities of the extended Fe $3p$ and Te $4d$ core level spectra, and their associated backgrounds. The fitting results are presented in Figure 7.18b. The intensity ratio of the Fe $3p$ and Te $4d$ can be converted to a composition ratio, after accounting for the differences in photo-ionization cross-section. This produces a Fe:Te atom ratio of 1.57:1. Based on the STM and RHEED/LEED experiments, this ratio should be close to the ideal 1:1 ratio of β-FeTe.

The severe overestimation of the Fe content is due to the fact that the plasmon-loss intensities were erroneously attributed to Fe. If we assume that the plasmon excitation probabilities for the Te $3d$ and $4d$ core level are the same, then the plasmon-loss intensity associated with the Te $4d$ core level is 0.6 times the intensity of the main line. Taking the corresponding reduction of the Fe $3p$ intensity into consideration, the corrected stoichiometry becomes $Fe_{0.97}Te$, which is very close to the ideal stoichiometry. Alternatively, if we consider that the plasmon-loss probability is inversely proportional to the inelastic mean free path of the Te $3d$ and $4d$ photoelectrons, then one obtains $Fe_{1.1}Te$. Since we do not know precisely how the plasmon excitation probability varies with the kinetic energy, some ambiguity

remains. To improve the protocol for the determination of the stoichiometry, it would be best to measure the excitation probabilities of the satellites using an electron gun as the excitation source.

Next, we consider the stoichiometry of the FeTe monolayer film on STO. Before fitting the Fe 3p and Te 4d spectra of the 1 ML sample, we first analyzed and fitted the spectrum of Te-etched STO (Figure 7.18f). We then used the results from both the STO and bulk multilayer FeTe (#231, 78ML-FeTe) to fit the 1 ML spectrum. It is important to note that the 1 ML FeTe film was not grown on the exact same STO substrate, which necessitated the introduction of an additional energy shift and broadening parameters for the STO and Te 4d spectra. In our analysis, we found that the Te 4d and Fe 3p features in 1 ML FeTe differed from those observed in bulk FeTe. For Te 4d spectra, a single doublet was sufficient, whereas the Fe multiplet features and Te 4d plasmon contributions were significantly weaker. In fact, the intensity of the plasmon lossed should be greatly reduced in the monolayer limit. The background was obtained as the sum of the background generated by the STO, Fe 3p, and Te 4d core levels. The background intensity of the STO is reduced with respect to that of pure STO. This analysis resulted in a stoichiometry of $Fe_{0.96}Te$, which is close to the result of the FeTe multilayer films.

7.5 Fe 2p Core Level and CVV Auger Spectrum

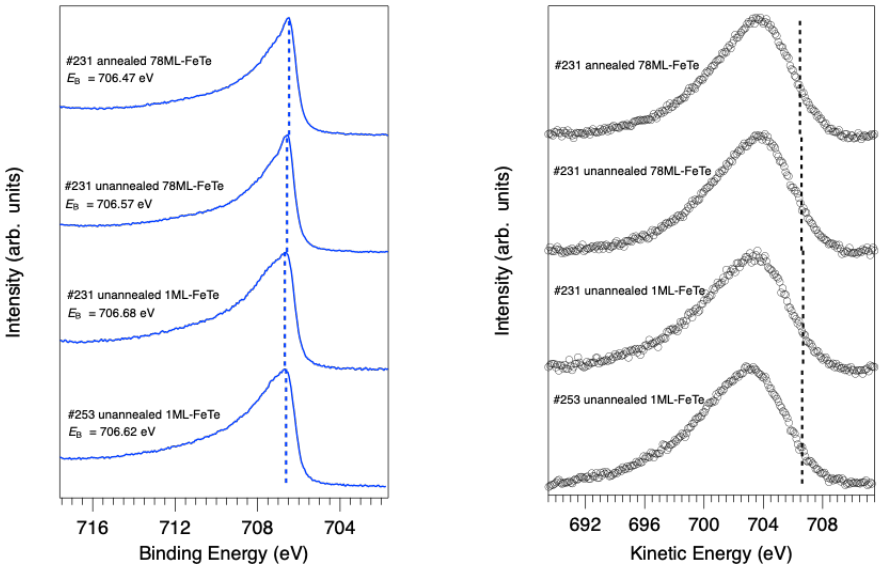
The Fe 2p core level and CVV Auger spectrum were measured and compared to those of FeSe. There is no clear difference between the spectra of the annealed and as-grown (unannealed) samples, which is probably due to the fact that our growth conditions do not lead to an appreciable density of Fe vacancies. This will need to be verified with a detailed stoichiometry analysis. Here, we only plot the data from the unannealed and post annealed 78 ML thick FeTe sample (#231). In addition, the reproducibility of our growth experiment is confirmed by the spectra of sample #253. Similar to the case of FeSe, the Fe 2p spectrum contains at least two components, although they are

not as distinct as in the case of FeSe. To elucidate the binding energies and relative intensities of the two components, one would need to fit the spectrum (Figure 7.19a). The relative intensity of the low-binding energy component in monolayer FeTe films seems a bit higher than that of the FeSe monolayer on STO (Figure 7.19a). Unlike the case of FeSe, post annealing does not change the spectrum in a significant way, suggesting that Fe vacancies may be far fewer in the as-grown FeTe films.

Similar to the case of FeSe, we plotted the Auger spectra on the two-hole binding energy scale by subtracting the core level binding energy of the well screened final state from the kinetic energy of the Auger electrons. This is shown in Figure 7.19c. The energy gap between the centroid of the CVV Auger spectra and SCDOS of the Fe $3d$ states, ΔE, is larger than that of FeSe. The ΔE's of the monolayer films are comparable, but the ΔE of the 78 ML FeTe film is almost twice as large as that of a 90 ML FeSe film. This tendency suggests the hole-hole repulsion in FeTe is stronger than that of FeSe, which is in line with expectations from the DFT+DMFT calculation (Yin et al., 2011). This preliminary conclusion does not take into account possible differences in screening dynamics. In addition, the centroid of the Auger spectrum needs to be corrected for the extrinsic and intrinsic contributions to the low-energy tail. More studies are needed here.

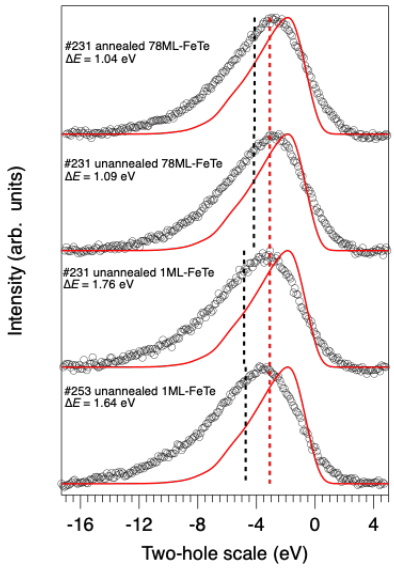
7.6 Valence Band Spectrum

The valence band spectra of the various FeTe films and STO substrates are shown in Figure 7.20a. The features labeled V1 and V2 in the STO valence band spectrum were discussed in Chapter 7. Likewise, the features labeled A, B, C and D from FeTe are also similar to those of FeSe in Chapter 7, except for the fact that the Se $4p$ contribution in FeSe now becomes the Te $5p$ contribution. Again, there is no evidence of band bending as the V2 feature doesn't shift after growing the FeTe monolayer film (see Figure 7.20a).



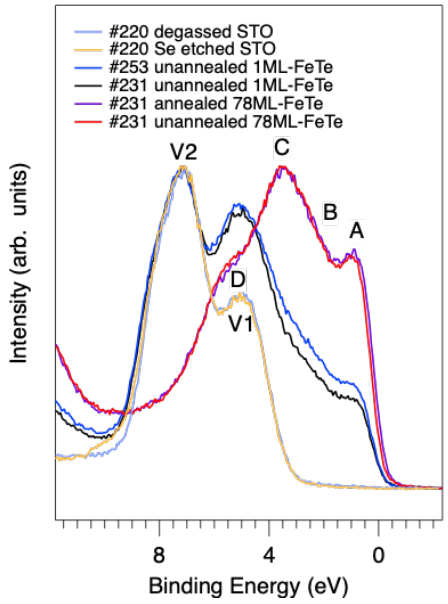
(a) Fe 2p core level spectra

(b) Fe 2p CVV Auger spectra

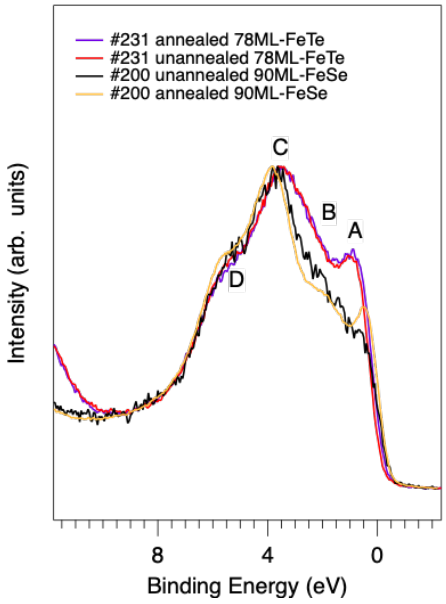


(c) Fe 2p CVV Auger spectra plotted on the two-hole binding energy scale

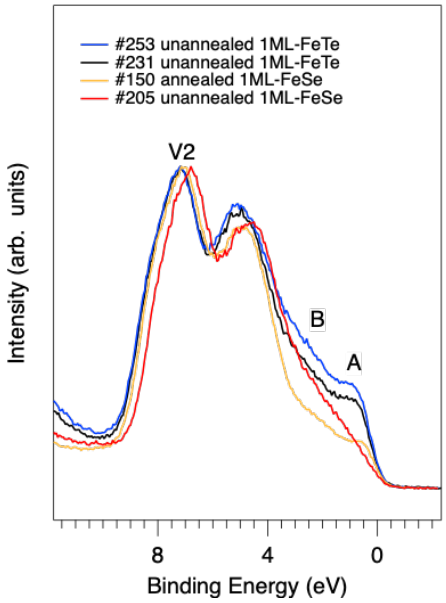
Figure 7.19: (a) Fe 2p core level and (b) CVV Auger spectrum, after subtracting a linear background. The dashed lines mark the Fe 2p core level binding energy obtained from (a). (c) CVV Auger spectra plotted on the two-hole binding scale. The SCDOS of the Fe 3d states, obtained from DFT (Berlijn and Kong, N D), is plotted in red. Dashed lines mark the first moments of the experimental Auger spectrum and the SCDOS.



(a) FeTe



(b) Comparsion of bulk FeTe and FeSe



(c) Comparsion of 1 ML FeTe and FeSe

Figure 7.20: Valence band of various FeTe films and STO substrates.

Figure 7.20b and Figure 7.20c, show a direct comparison between the FeSe and FeTe XPS valence band spectra of the 1 ML and bulk films (78 ML/90 ML), respectively. It seems that feature A is relatively more intense in the case of FeTe, even without post annealing. Overall, the XPS valence spectra of FeSe and FeTe are strikingly similar. To understand the differences in electronic properties of FeSe and FeTe, one would need to acquire high-resolution ARPES data and compare the details of their respective Fermi surfaces. Those ARPES data have been recorded and are currently being analyzed.

7.7 Magnetic Property Measurement

We explored the magnetic properties of the 146 ML thick FeTe film on STO (sample #245). The magnetic signal of the Nb doped STO substrate was measured independently to determine the magnetic background signal. We applied a 2000 Oe magnetic field parallel to the sample surface. As already discussed in section of the magnetic properties measurement on bulk FeSe, the linear negative slope of the magnetic singal of the STO (Figure 7.21), might be due to the changing sample position as a result of thermal expansion of the sample and sample holder, and the weak upturn at very low temperatures is likely due to paramagnetic impurities. In addition, the small peak at around 40 K is due to oxygen condensation on the sample, which is also a well-known artifact in SQUID magnetometry (Gregory, 1978). The magnetic moment of the thick FeTe film decreases almost linearly with temperature, but shows a weak cusp around 64 K. This cusp is attributed to an antiferromagnetic to paramagnetic transition in the FeTe film, see Figure 7.21 (Bao et al., 2009; Maheshwari et al., 2015).

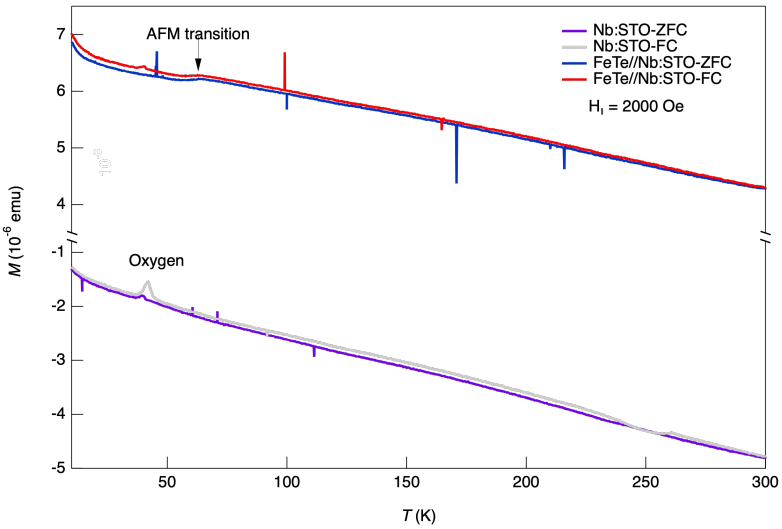


Figure 7.21: Magnetic property measurement on the 146 ML thick FeTe bulk film (#245) and of the Nb doped STO substrate.

7.8 Conclusions

High-quality monolayer and multilayer $\beta-$FeTe films were successfully grown on the STO substrate. An unknown honeycomb structure was found to coexist with the tetragonal monolayer, but further fine tuning of the growth parameters led to the formation of single phase $\beta-$FeTe, both in monolayer and multilayer form. The films are metallic at 77 K. Atomic resolution STM images reveal atomic scale contrast variations that are very similar to those seen in monolayer FeSe films on STO.

The Fe $2p$ core level spectra are also very similar to those of FeSe, showing a characteristic splitting between the poorly screened and well screened final states. However, the well-screened final state appears to have the larger spectral weight, even for the as-grown FeTe monolayer film. This suggests that Fe vacancies may not be as prevalent in the FeTe monolayer. The XPS valence band spectra are also very similar to those of FeSe, showing no evidence for FeTe induced bending shifts in the STO substrate.

An important difference between the FeSe and FeTe data is the presence of an antiferromagnetic transition in the magnetization data of the multilayer film at $T_c =$

64 K. This transition likely preempts the formation of the superconducting state seen in $\beta-$FeSe.

Chapter 8

Summary and Outlook

A critical experimental requirement for obtaining high-temperature superconductivity in 1 UC-thick FeSe films on STO appears to be the need to post anneal these MBE grown films. Yet, this aspect remained quite controversial as most researchers developed their own growth protocol. This called for a detailed analysis of the various materials aspects associated with the unusually high T_c. In this thesis, we investigated the effects of electron doping introduced by post annealing and additional post-growth Fe deposition, and compared the electronic properties of epitaxial FeSe and FeTe thin films to uncover the origin of the T_c in these materials.

We began with a thorough investigation of the STO substrate preparation, which included UHV annealing, acid etching, oxygen annealing, and Se/Te etching. These methods enabled us to achieve atomically flat surfaces with various reconstructions, which in turn are related to the different concentrations of oxygen vacancies. We adhered to an ultra-clean protocol, utilizing *in-situ* Se etching, which resulted in a $(\sqrt{13} \times \sqrt{13})$ surface reconstruction with minimal oxygen vacancies and flat band conditions. The low concentration of oxygen vacancies was confirmed by analyzing the Ti $2p$ and O $1s$ core level spectra from XPS. Data analysis of the Sr $3d$ core level spectrum confirmed the presence of surface SrO with a coverage that agrees well with the current structure model of the $(\sqrt{13}\times\sqrt{13})$ surface with double TiO_x termination.

We successfully fabricated high-quality monolayer, bilayer, and thick FeSe films on the Se-etched ($\sqrt{13} \times \sqrt{13}$) reconstructed STO(001) substrate. By varying the substrate temperature, source temperature, and annealing conditions, we were able to finely tune the stoichiometry of our FeSe films. The disappearance of domain boundaries as the films thickened indicated that our thicker films were fully relaxed, representing the properties of bulk FeSe, a conclusion that is also supported by X-ray diffraction (XRD) measurements. Interestingly, only monolayer FeSe exhibited two types of domain boundaries, highlighting the distinct nature of the interface. Magnetic property measurements of thick FeSe films indicated a deficiency in Fe content, resulting in the absence of superconductivity. In contrast, our post annealed FeSe monolayers exhibited a superconducting gap in STS, and sufficient electron doping was confirmed by ARPES. The STO valence band and core level spectra indicated that the Fermi level of the FeSe film is lined-up with the conduction band minimum of the STO substrate, and that there is no significant band bending in - and charge transfer from - the STO substrate. The enhancement of the Fe $3d$ DOS near the Fermi level upon post annealing or post-growth Fe deposition indicates that electron doping is mostly controlled by the stoichiometry of the film.

The two components observed in the Fe $2p$ core level are likely associated with two different screening channels. In particular, the contribution of the non-local screening channel associated with the high binding energy component of the spectrum is most prominent when the coordination of the Fe atoms is reduced in the presence of a surface or nearby Fe vacancies. The CVV Auger spectra are distinctly different from those of the Fe-based pnictide superconductors, which we tentatively attribute to the different correlation strength and screening dynamics in the FeSe films.

Additionally, we were able to grow FeTe films on Se-etched and Te-etched ($\sqrt{13} \times \sqrt{13}$) reconstructed STO(001) surfaces. By adjusting the growth conditions, we were able to optimize the growth parameters for obtaining single-phase β-FeTe. *Ex-situ* XRD measurements on Te-capped films revealed the presence of $FeTe_2$, which we attributed to the presence of excess Te near the FeTe/Te interface. Tunneling

spectroscopy data showed that both monolayer and bilayer FeTe films are metallic. The Fe $2p$ spectra of FeTe furthermore indicate that the well-screened final states carry more spectral weight as compared to the case of FeSe.

The main conclusion of this thesis is that the superconducting properties of the FeSe monolayer on STO are very sensitive to the Fe content of the film, and that the purported electron doping induced by post annealing should be primarily attributed to the increased Fe density. Secondly, the STM and XPS data of FeSe and FeTe monolayers reveal striking similarities between the two systems, which suggests that we should focus our attention to the comparison of the ARPES and CVV Auger spectra. The ARPES data of FeTe monolayer (not shown) are currently being analyzed. Also, detailed fittings of the Fe and Se core level spectra and the Fe CVV Auger spectra are currently underway. The fitting analyses are very complicated due the unusual background of the Fe $2p$ spectrum, overlapping Fe $3p$ and Se $4d$ core level spectra, and the theoretical complexity of the CVV Auger spectrum for open band systems. The latter is even more complicated than initially thought as we will need to include the dynamical aspects of core hole decay in the analysis.

ARPES and STS experiments on the monolayer FeSe with additional post-growth Fe deposition would further confirm the similarities observed with post annealing. Additionally, the reverse process of Se annealing to intentionally create Fe vacancies could also be implemented for comparison. Finally, it would be interesting to see if one can optimize the growth conditions, and/or develop effective doping protocols, to induce superconductivity in FeTe and FeS, as these compounds are all very similar. Doing so may enable us to further narrow down the reason behind the apparent uniqueness of the superconducting FeSe/STO interface.

Bibliography

Acharya, S., Pashov, D., Jamet, F., and van Schilfgaarde, M. (2021). Electronic origin of T_c in bulk and monolayer FeSe. *Symmetry*, 13(2):169. 17

Alders, D., Voogt, F., Hibma, T., and Sawatzky, G. (1996). Nonlocal screening effects in $2p$ X-ray photoemission spectroscopy of NiO(100). *Physical Review B*, 54(11):7716. 135

Aperis, A., Kotetes, P., Varelogiannis, G., and Oppeneer, P. M. (2011). Small-q phonon-mediated unconventional superconductivity in the iron pnictides. *Physical Review B—Condensed Matter and Materials Physics*, 83(9):092505. 14

Ashcroft, N. W. and Mermin, N. (1976). Solid state. *Physics (New York: Holt, Rinehart and Winston) Appendix C*. 2, 3, 4

Bachelet, R., Sánchez, F., Palomares, F., Ocal, C., and Fontcuberta, J. (2009). Atomically flat SrO-terminated $SrTiO_3$(001) substrate. *Applied Physics Letters*, 95(14). 86

Baek, J.-Y., Lee, S. Y., Seo, H., et al. (2020). Aluminum doping for optimization of ultrathin and high-k dielectric layer based on $SrTiO_3$. *Journal of Materials Science & Technology*, 42:28–37. 76

Baeumer, C., Xu, C., Gunkel, F., Raab, N., Heinen, R. A., Koehl, A., and Dittmann, R. (2015). Surface termination conversion during $SrTiO_3$ thin film growth revealed by X-ray photoelectron spectroscopy. *Scientific Reports*, 5(1):11829. 88

Bagus, P. S., Nelin, C. J., Zhao, X., Levchenko, S. V., Davis, E., Weng, X., Späth, F., Papp, C., Kuhlenbeck, H., and Freund, H.-J. (2019). Revisiting surface core-level shifts for ionic compounds. *Physical Review B*, 100(11):115419. 41, 86

Bang, J., Li, Z., Sun, Y., Samanta, A., Zhang, Y., Zhang, W., Wang, L., Chen, X., Ma, X., Xue, Q.-K., et al. (2013). Atomic and electronic structures of single-layer FeSe on $SrTiO_3$(001): the role of oxygen deficiency. *Physical Review B*, 87(22):220503. 101

Bang, Y. (2019). Phonon boost effect on the $S^{\pm}$-wave superconductor with incipient band. *Scientific Reports*, 9(1):3907. 15

Bao, W., Qiu, Y., Huang, Q., Green, M., Zajdel, P., Fitzsimmons, M., Zhernenkov, M., Chang, S., Fang, M., Qian, B., et al. (2009). Tunable ($\delta\pi$, $\delta\pi$)-type antiferromagnetic order in α-Fe (Te, Se) superconductors. *Phys. Rev. Lett.*, 102(24):247001. 16, 171

Bardeen, J. (1961). Tunnelling from a Many-Particle Point of View. *Physical Review Letters*, 6:57–59. 28

Barišić, N., Chan, M. K., Li, Y., Yu, G., Zhao, X., Dressel, M., Smontara, A., and Greven, M. (2013). Universal sheet resistance and revised phase diagram of the cuprate high-temperature superconductors. *Proceedings of the National Academy of Sciences*, 110(30):12235–12240. 5

Bednorz, J George and Müller, K Alex (1986). Possible high T_C superconductivity in the Ba-La-Cu-O system. *Zeitschrift für Physik B Condensed Matter*, 64(2):189–193. 5

Berlijn, T. and Kong, X. (N. D.). Unpublished. 134, 135, 169

Bulut, N. and Scalapino, D. (1996). $d_{x^2-y^2}$ symmetry and the pairing mechanism. *Physical Review B*, 54(21):14971. 14

Carter, D. B. W. C. B. (2009). *Transmission electron microscopy A textbook for materials science*. Springer New York, NY. 37

Chastain, J. and King Jr, R. C. (1992). Handbook of X-ray photoelectron spectroscopy. *Perkin-Elmer Corporation*, 40:221. 39, 41, 42

Chen, H., Ren, Y., Qiu, Y., Bao, W., Liu, R., Wu, G., Wu, T., Xie, Y., Wang, X., Huang, Q., et al. (2009). Coexistence of the spin-density wave and superconductivity in $Ba_{1-x}K_xFe_2As_2$. *Europhysics Letters*, 85(1):17006. 7

Chen, T.-K., Chang, C.-C., Chang, H.-H., Fang, A.-H., Wang, C.-H., Chao, W.-H., Tseng, C.-M., Lee, Y.-C., Wu, Y.-R., Wen, M.-H., et al. (2014). Fe-vacancy order and superconductivity in tetragonal β-$Fe_{1-x}Se$. *Proceedings of the National Academy of Sciences*, 111(1):63–68. 93, 94, 108, 113

Chen, W., Zeng, C., Kaxiras, E., and Zhang, Z. (2016). Dual role of Fe dopants in enhancing stability and charge transfer in $(Li_{0.8}Fe_{0.2})$OHFeSe superconductors. *Physical Review B*, 93(6):064517. 9

Choi, Y. W. and Choi, H. J. (2019). Role of electric fields on enhanced electron correlation in surface-doped FeSe. *Phys. Rev. Lett.*, 122(4):046401. 17

Chubukov, A. and Hirschfeld, P. J. (2015). Iron-based superconductors, seven years later. *Physics Today*, 68(6):46–52. 8

Cini, M. (1978). Comment on quasiatomic Auger spectra in narrow-band metals. *Physical Review B*, 17(6):2788. 46

Cooper, L. N., Bardeen, J., and Schrieffer, J. (1957). Theory of superconductivity. *Phys. Rev*, 108:1175. 3

Damascelli, A. (2004). Probing the electronic structure of complex systems by ARPES. *Physica Scripta*, 2004(T109):61. 51

Damascelli, A., Hussain, Z., and Shen, Z.-X. (2003). Angle-resolved photoemission studies of the cuprate superconductors. *Reviews of Modern Physics*, 75(2):473. 50

Deng, L., Lv, B., Wu, Z., Xue, Y., Zhang, W., Li, F., Wang, L., Ma, X., Xue, Q., and Chu, C. (2014). Meissner and mesoscopic superconducting states in 1–4 unit-cell FeSe films. *Physical Review B*, 90(21):214513. 9

Ding, H., Lv, Y.-F., Zhao, K., Wang, W.-L., Wang, L., Song, C.-L., Chen, X., Ma, X.-C., and Xue, Q.-K. (2016). High-temperature superconductivity in single-unit-cell FeSe films on anatase TiO_2(001). *Physical Review Letters*, 117(6):067001. 10

Doniach, S. and Sunjic, M. (1970). Many-electron singularity in X-ray photoemission and X-ray line spectra from metals. *Journal of Physics C: Solid State Physics*, 3(2):285. 42

Egelhoff Jr, W. (1987). Core-level binding-energy shifts at surfaces and in solids. *Surface Science Reports*, 6(6-8):253–415. 45, 46

Fan, Q., Zhang, W., Liu, X., Yan, Y., Ren, M., Peng, R., Xu, H., Xie, B., Hu, J., Zhang, T., et al. (2015). Plain *s*-wave superconductivity in single-layer FeSe on $SrTiO_3$ probed by scanning tunnelling microscopy. *Nature Physics*, 11(11):946–952. 16, 101

Fang, M., Pham, H., Qian, B., Liu, T., Vehstedt, E., Liu, Y., Spinu, L., and Mao, Z. (2008). Superconductivity close to magnetic instability in $Fe(Se_{1-x}Te_x)_{0.82}$. *Physical Review B—Condensed Matter and Materials Physics*, 78(22):224503. 16

Fujimori, A., Suga, S., Negishi, H., and Inoue, M. (1988). X-ray photoemission and Auger-electron spectroscopic study of the electronic structure of intercalation compounds M_xTiS_2 (M=Mn, Fe, Co, and Ni). *Physical Review B*, 38(6):3676. 133

Fukaya, Y., Zhou, G., Zheng, F., Zhang, P., Wang, L., Xue, Q.-K., and Shamoto, S.-i. (2018). Asymmetrically optimized structure in a high-T_C single unit-cell FeSe superconductor. *Journal of Physics: Condensed Matter*, 31(5):055701. 17

Ge, Z. (2018). Scanning Tunneling Microscopy Studies of Superconducting Single Layer Iron Selenide on Strontium Titanate. 99, 101

Ginzburg, V. (1950). Zh. VL Ginzburg and LD Landau. *Zh. Eksp. Teor. Fiz*, 20:1064. 2

Gor'kov, L. P. (1959). Microscopic derivation of the Ginzburg-Landau equations in the theory of superconductivity. *Sov. Phys. JETP*, 9(6):1364–1367. 4

Gregory, S. (1978). Magnetic susceptibility of oxygen adsorbed on graphite. *Physical Review Letters*, 40(11):723. 171

Han, Z.-Q., Shi, X., Peng, X.-L., Sun, Y.-J., and Wang, S.-C. (2017). High-quality $FeTe_{1-x}Se_x$ monolayer films on $SrTiO_3(001)$ substrates grown by molecular beam epitaxy. *Chinese Physics Letters*, 34(10):107401. 16

Harrington, G. F. and Santiso, J. (2021). Back-to-Basics tutorial: X-ray diffraction of thin films. *Journal of Electroceramics*, 47(4):141–163. 54

Hasegawa, S. (2012). Reflection high-energy electron diffraction. *Characterization of Materials*, 97:1925–1938. 34, 35, 36

He, S., He, J., Zhang, W., Zhao, L., Liu, D., Liu, X., Mou, D., Ou, Y.-B., Wang, Q.-Y., Li, Z., et al. (2013). Phase diagram and electronic indication of high-temperature superconductivity at 65 K in single-layer FeSe films. *Nature Materials*, 12(7):605–610. 9, 11, 116, 124

Hsu, F.-C., Luo, J.-Y., Yeh, K.-W., Chen, T.-K., Huang, T.-W., Wu, P. M., Lee, Y.-C., Huang, Y.-L., Chu, Y.-Y., Yan, D.-C., et al. (2008). Superconductivity in the PbO-type structure α-FeSe. *Proceedings of the National Academy of Sciences*, 105(38):14262–14264. 9, 91

Hu, Y., Xu, Y., Wang, Q., Zhao, L., He, S., Huang, J., Li, C., Liu, G., and Zhou, X. (2018). Identification of a large amount of excess Fe in superconducting single-layer FeSe/$SrTiO_3$ films. *Physical Review B*, 97(22):224512. 18, 120

Huang, D. and Hoffman, J. E. (2017). Monolayer FeSe on $SrTiO_3$. *Annual Review of Condensed Matter Physics*, 8(1):311–336. 14, 15, 16, 17, 92

Huang, Z., Pu, Y., Xu, H., Xu, D., Song, Q., Lou, X., Wen, C., Peng, R., and Feng, D. (2016). Electronic structure and superconductivity of single-layer FeSe on Nb: $SrTiO_3$/$LaAlO_3$ with varied tensile strain. *2D Materials*, 3(1):014005. 10

Hüfner, Stephan (2013). *Photoelectron spectroscopy: principles and applications*. Springer Science & Business Media. 39, 42, 43, 45

Jaworski, P. (2005). Wikipedia. diagram of the meissner effect. 2

Johnston, S., Abdel-Hafiez, M., Harnagea, L., Grinenko, V., Bombor, D., Krupskaya, Y., Hess, C., Wurmehl, S., Wolter, A., Büchner, B., et al. (2014). Specific heat of $Ca_{0.32}Na_{0.68}Fe_2As_2$ single crystals: Unconventional $s_{\pm}$ multiband superconductivity with intermediate repulsive interband coupling and sizable attractive intraband couplings. *Physical Review B*, 89(13):134507. 14

Johnston, S., Vernay, F., Moritz, B., Shen, Z.-X., Nagaosa, N., Zaanen, J., and Devereaux, T. (2010). Systematic study of electron-phonon coupling to oxygen modes across the cuprates. *Physical Review B—Condensed Matter and Materials Physics*, 82(6):064513. 14

Kamihara, Y., Hiramatsu, H., Hirano, M., Kawamura, R., Yanagi, H., Kamiya, T., and Hosono, H. (2006). Iron-based layered superconductor: LaOFeP. *Journal of the American Chemical Society*, 128(31):10012–10013. 6

Kamihara, Y., Watanabe, T., Hirano, M., and Hosono, H. (2008). Iron-based layered superconductor $La[O_{1-x}F_x]FeAs$ ($x = 0.05 - 0.12$) with $T_c = 26$ K. *Journal of the American Chemical Society*, 130(11):3296–3297. 7

Katsube, D., Shimizu, R., Sugimoto, Y., Hitosugi, T., and Abe, M. (2023). Identification of OH groups on $SrTiO_3(100)$-$(\sqrt{13} \times \sqrt{13})$-R33.7° reconstructed surface by non-contact atomic force microscopy and scanning tunneling microscopy. *Applied Physics Letters*, 122(7). 89

Kawasaki, M., Takahashi, K., Maeda, T., Tsuchiya, R., Shinohara, M., Ishiyama, O., Yonezawa, T., Yoshimoto, M., and Koinuma, H. (1994). Atomic Control of the $SrTiO_3$ Crystal Surface. *Science*, 266(5190):1540–1542. 67

Kienzle, D., Becerra-Toledo, A., and Marks, L. (2011). Vacant-Site Octahedral Tilings on $SrTiO_3(001)$, the $(\sqrt{13} \times \sqrt{13})$ R33.7° Surface, and Related Structures. *Physical Review Letters*, 106(17):176102. 89

Kim, D., Lim, H., Seo, M., Shin, H., Kim, K., Jang, S., Kim, K.-j., Kim, J., and Mun, B. S. (2024). An *in situ* study on the depth-resolved chemical states of undoped $SrTiO_3(001)$ surfaces during Ar^+ sputtering and annealing processes with XPS. *Journal of Materials Chemistry C*, 12(27):10110–10117. 86

Kim, J.-Y., Jin, M.-J., Hou, B., Kim, M. P., Um, D.-S., and Kim, C.-I. (2023). Reducing the oxygen vacancy concentration in $SrTiO_{3-\delta}$ thin films via an optimized O_2 plasma treatment for enhancing device properties. *Applied Surface Science*, 639:158271. 76, 82, 84

Kotani, A. and Toyozawa, Y. (1974). Photoelectron spectra of core electrons in metals with an incomplete shell. *Journal of the Physical Society of Japan*, 37(4):912–919. 133

Kotnala, R. and Shah, J. (2015). Ferrite materials: nano to spintronics regime. In *Handbook of magnetic materials*, volume 23, pages 291–379. Elsevier. 57

Kraft, A., Rupprecht, C., and Yam, Y.-C. (2017). Superconducting quantum interference device (squid). *UBC Phys.* 58

Lee, J., Schmitt, F., Moore, R., Johnston, S., Cui, Y.-T., Li, W., Yi, M., Liu, Z., Hashimoto, M., Zhang, Y., et al. (2014). Interfacial mode coupling as the origin of the enhancement of T_C in FeSe films on $SrTiO_3$. *Nature*, 515(7526):245–248. 9, 11, 13, 14, 60

Li, F., Ding, H., Tang, C., Peng, J., Zhang, Q., Zhang, W., Zhou, G., Zhang, D., Song, C.-L., He, K., et al. (2015). Interface-enhanced high-temperature superconductivity in single-unit-cell $FeTe_{1-x}Se_x$ films on $SrTiO_3$. *Physical Review B*, 91(22):220503. 16, 161

Li, F. and Sawatzky, G. A. (2018). Electron phonon coupling versus photoelectron energy loss at the origin of replica bands in photoemission of FeSe on $SrTiO_3$. *Physical Review Letters*, 120(23):237001. 15

Li, F., Zhang, Q., Tang, C., Liu, C., Shi, J., Nie, C., Zhou, G., Li, Z., Zhang, W., Song, C.-L., et al. (2016a). Atomically resolved $FeSe/SrTiO_3(001)$ interface structure by scanning transmission electron microscopy. *2D Materials*, 3(2):024002. 15, 17, 60

Li, G., Zhang, B., Baluyan, T., Rao, J., Wu, J., Novakova, A. A., Rudolf, P., Blake, G. R., de Groot, R. A., and Palstra, T. T. (2016b). Metal–insulator transition induced by spin reorientation in Fe_7Se_8 grain boundaries. *Inorganic Chemistry*, 55(24):12912–12922. 113

Li, Z., Peng, J.-P., Zhang, H.-M., Zhang, W.-H., Ding, H., Deng, P., Chang, K., Song, C.-L., Ji, S.-H., Wang, L., et al. (2014). Molecular beam epitaxy growth and post-growth annealing of FeSe films on $SrTiO_3$: a scanning tunneling microscopy study. *Journal of Physics: Condensed Matter*, 26(26):265002. 9, 11, 116

Liu, C., Mao, J., Ding, H., Wu, R., Tang, C., Li, F., He, K., Li, W., Song, C.-L., Ma, X.-C., et al. (2018). Extensive impurity-scattering study on the pairing symmetry of monolayer FeSe films on $SrTiO_3$. *Physical Review B*, 97(2):024502. 161

Liu, C. and Zou, K. (2020). Tuning stoichiometry and its impact on superconductivity of monolayer and multilayer FeSe on $SrTiO_3$. *Physical Review B*, 101(14):140502. 18, 97, 120

London, F. and London, H. (1935). The electromagnetic equations of the supraconductor. *Proceedings of the Royal Society of London. Series A-Mathematical and Physical Sciences*, 149(866):71–88. 2

Lu, X., Wang, N., Wu, H., Wu, Y., Zhao, D., Zeng, X., Luo, X., Wu, T., Bao, W., Zhang, G., et al. (2015). Coexistence of superconductivity and antiferromagnetism in $(Li_{0.8}Fe_{0.2})$OHFeSe. *Nature Materials*, 14(3):325–329. 9

Lundqvist, B. (1969). Characteristic structure in core electron spectra of metals due to the electron-plasmon coupling. *Physik der kondensierten Materie*, 9:236–248. 46

Mahan, G. D. (1975). Collective excitations in X-ray spectra of metals. *Physical Review B*, 11(12):4814. 43

Maheshwari, P., Jha, R., Gahtori, B., and Awana, V. (2015). Structural and magnetic properties of flux-free large FeTe single crystal. *Journal of Superconductivity and Novel Magnetism*, 28:2893–2897. 16, 171

McQueen, T. M., Huang, Q., Ksenofontov, V., Felser, C., Xu, Q., Zandbergen, H., Hor, Y. S., Allred, J., Williams, A. J., Qu, D., et al. (2009). Extreme sensitivity of superconductivity to stoichiometry in $Fe_{1+\delta}Se$. *Physical Review B—Condensed Matter and Materials Physics*, 79(1):014522. 93, 94

Medvedev, S., McQueen, T., Troyan, I., Palasyuk, T., Eremets, M., Cava, R., Naghavi, S., Casper, F., Ksenofontov, V., Wortmann, G., et al. (2009). Electronic and magnetic phase diagram of β-$Fe_{1.01}Se$ with superconductivity at 36.7 K under pressure. *Nature Materials*, 8(8):630–633. 9

Mishra, P., Lohani, H., Zargar, R., Awana, V., and Sekhar, B. (2015). Pseudogap behaviour in FeTe and FeSe probed by photoemission. In *AIP Conference Proceedings*, volume 1665. AIP Publishing. 138

Miyata, Y., Nakayama, K., Sugawara, K., Sato, T., and Takahashi, T. (2015). High-temperature superconductivity in potassium-coated multilayer FeSe thin films. *Nature Materials*, 14(8):775–779. 12

Motzkau, H. (2013). Wikipedia. Schematic doping phase diagram of cuprate high-temperature superconductors. 5

Mugiraneza, S. and Hallas, A. M. (2022). Tutorial: a beginner's guide to interpreting magnetic susceptibility data with the Curie-Weiss law. *Communications Physics*, 5(1):95. 57

Nandi, S., Kim, M., Kreyssig, A., Fernandes, R., Pratt, D., Thaler, A., Ni, N., Bud'ko, S. L., Canfield, P. C., Schmalian, J., et al. (2010). Anomalous suppression of the orthorhombic lattice distortion in superconducting $Ba(Fe_{1-x}Co_x)_2As_2$ single crystals. *Physical Review Letters*, 104(5):057006. 8

Ohsawa, T., Shimizu, R., Iwaya, K., Shiraki, S., and Hitosugi, T. (2016). Negligible Sr segregation on $SrTiO_3(001)$-$(\sqrt{13}\times\sqrt{13})$-R33.7° reconstructed surfaces. *Applied Physics Letters*, 108(16). 60, 76, 86

Okamoto, H. (1991). The FeSe (ironselenium) system. *Journal of phase equilibria*, 12(3):383–389. 93, 108, 110

Okamoto, H. and Tanner, L. (1990). The Fe-Te (iron-tellurium) system. *Bulletin of Alloy Phase Diagrams*, 11(4):371–376. 155, 157

Onari, S., Kontani, H., and Sato, M. (2010). Structure of neutron-scattering peaks in both s_{++}-wave and $s_{\pm}$-wave states of an iron pnictide superconductor. *Physical Review B—Condensed Matter and Materials Physics*, 81(6):060504. 9

Onnes, H. K. (1911a). Further experiments with liquid helium. In *Proceedings of the KNAW*, volume 13, pages 1910–1911. sn. 2

Onnes, K. (1911b). The resistance of pure mercury at helium temperatures. *Commun. Phys. Lab. Univ. Leiden, b*, 120. 2

Oura, K., Lifshits, V., Saranin, A., Zotov, A., and Katayama, M. (2003). *Surface science: an introduction*. Springer Berlin, Heidelberg. 21, 25

Pedersen, A. K., Ichinokura, S., Tanaka, T., Shimizu, R., Hitosugi, T., and Hirahara, T. (2020). Interfacial superconductivity in FeSe ultrathin films on $SrTiO_3$ probed by *in situ* independently driven four-point-probe measurements. *Physical Review Letters*, 124(22):227002. 9

Peng, R., Shen, X., Xie, X., Xu, H., Tan, S., Xia, M., Zhang, T., Cao, H., Gong, X., Hu, J., et al. (2014a). Measurement of an enhanced superconducting phase and a pronounced anisotropy of the energy gap of a strained FeSe single layer in FeSe/Nb: $SrTiO_3/KTaO_3$ heterostructures using photoemission spectroscopy. *Physical Review Letters*, 112(10):107001. 10

Peng, R., Xu, H., Tan, S., Cao, H., Xia, M., Shen, X., Huang, Z., Wen, C., Song, Q., Zhang, T., et al. (2014b). Tuning the band structure and superconductivity in single-layer FeSe by interface engineering. *Nature Communications*, 5(1):5044. 10, 15

Peng, R., Zou, K., Han, M., Albright, S. D., Hong, H., Lau, C., Xu, H., Zhu, Y., Walker, F., and Ahn, C. (2020). Picoscale structural insight into superconductivity of monolayer $FeSe/SrTiO_3$. *Science Advances*, 6(15):eaay4517. 15, 60

Persson, K. (2015). Materials Data on $FeTe_2$ (SG:58) by Materials Project. An optional note. 155

PJRay (2015). Wikipedia. Overview of superconducting critical temperatures for a variety of superconducting materials since the first discovery in 1911. 3

Plakida, N. M. (2012). *High-temperature superconductivity: experiment and theory*. Springer Science & Business Media. 6

Rademaker, L., Alvarez-Suchini, G., Nakatsukasa, K., Wang, Y., and Johnston, S. (2021). Enhanced superconductivity in FeSe/$SrTiO_3$ from the combination of forward scattering phonons and spin fluctuations. *Physical Review B*, 103(14):144504. 17

Rademaker, L., Wang, Y., Berlijn, T., and Johnston, S. (2016). Enhanced superconductivity due to forward scattering in FeSe thin films on $SrTiO_3$ substrates. *New Journal of Physics*, 18(2):022001. 14

Rebec, S., Jia, T., Zhang, C., Hashimoto, M., Lu, D.-H., Moore, R., and Shen, Z.-X. (2017). Coexistence of replica bands and superconductivity in FeSe monolayer films. *Physical Review Letters*, 118(6):067002. 10, 11, 12

Sandvik, A., Scalapino, D., and Bickers, N. (2004). Effect of an electron-phonon interaction on the one-electron spectral weight of a *d*-wave superconductor. *Physical Review B*, 69(9):094523. 14

Santi, G., Jarlborg, T., Peter, M., and Weger, M. (1996). *s*- and *d*-wave symmetries of the solutions of the Eliashberg equations. *Physica C: Superconductivity*, 259(3-4):253–264. 14

Sawatzky, G. (1977). Quasiatomic Auger spectra in narrow-band metals. *Physical Review Letters*, 39(8):504. 46

Scalapino, D. J. (2012). A common thread: The pairing interaction for unconventional superconductors. *Reviews of Modern Physics*, 84(4):1383–1417. 6

Shi, X., Han, Z., Peng, X., Richard, P., Qian, T., Wu, X., Qiu, M., Wang, S., Hu, J., Sun, Y., et al. (2017). Enhanced superconductivity accompanying a Lifshitz transition in electron-doped FeSe monolayer. *Nature Communications*, 8(1):14988. 12

Shigekawa, K., Nakayama, K., Kuno, M., Phan, G. N., Owada, K., Sugawara, K., Takahashi, T., and Sato, T. (2019). Dichotomy of superconductivity between monolayer FeS and FeSe. *Proceedings of the National Academy of Sciences*, 116(49):24470–24474. 15

Shimizu, R., Iwaya, K., Ohsawa, T., Shiraki, S., Hasegawa, T., Hashizume, T., and Hitosugi, T. (2012). Effect of oxygen deficiency on $SrTiO_3$(001) surface reconstructions. *Applied Physics Letters*, 100(26). 74

Shiogai, J., Ito, Y., Mitsuhashi, T., Nojima, T., and Tsukazaki, A. (2016). Electric-field-induced superconductivity in electrochemically etched ultrathin FeSe films on $SrTiO_3$ and MgO. *Nature Physics*, 12(1):42–46. 9

Si, W., Tanaka, T., Ichinokura, S., Hirahara, T., et al. (2022). Substrate-induced broken C_4 symmetry and gap variation in superconducting single-layer FeSe/$SrTiO_3$-($\sqrt{13} \times \sqrt{13}$). *Physical Review B*, 105(10):104502. 101

Sims, H., Leonard, D. N., Birenbaum, A. Y., Ge, Z., Berlijn, T., Li, L., Cooper, V. R., Chisholm, M. F., and Pantelides, S. T. (2019). Intrinsic interfacial van der Waals monolayers and their effect on the high-temperature superconductor FeSe/$SrTiO_3$. *Physical Review B*, 100(14):144103. 15, 60

Song, C.-L., Wang, Y.-L., Jiang, Y.-P., Li, Z., Wang, L., He, K., Chen, X., Ma, X.-C., and Xue, Q.-K. (2011). Molecular-beam epitaxy and robust superconductivity of stoichiometric FeSe crystalline films on bilayer graphene. *Physical Review B*, 84(2):020503. 9

Song, C.-L., Zhang, H.-M., Zhong, Y., Hu, X.-P., Ji, S.-H., Wang, L., He, K., Ma, X.-C., and Xue, Q.-K. (2016). Observation of double-dome superconductivity in potassium-doped FeSe thin films. *Physical Review Letters*, 116(15):157001. 12

Song, Y., Chen, Z., Zhang, Q., Xu, H., Lou, X., Chen, X., Xu, X., Zhu, X., Tao, R., Yu, T., et al. (2021). High temperature superconductivity at FeSe/$LaFeO_3$ interface. *Nature Communications*, 12(1):5926. 10, 15

Stewart, G. (2011). Superconductivity in iron compounds. *Reviews of Modern Physics*, 83(4):1589–1652. 7

Sun, J., Matsuura, K., Ye, G., Mizukami, Y., Shimozawa, M., Matsubayashi, K., Yamashita, M., Watashige, T., Kasahara, S., Matsuda, Y., et al. (2016). Dome-shaped magnetic order competing with high-temperature superconductivity at high pressures in FeSe. *Nature Communications*, 7(1):12146. 9

Sun, Y., Zhang, W., Xing, Y., Li, F., Zhao, Y., Xia, Z., Wang, L., Ma, X., Xue, Q.-K., and Wang, J. (2014). High temperature superconducting FeSe films on $SrTiO_3$ substrates. *Scientific Reports*, 4(1):6040. 9

Tan, S., Zhang, Y., Xia, M., Ye, Z., Chen, F., Xie, X., Peng, R., Xu, D., Fan, Q., Xu, H., et al. (2013). Interface-induced superconductivity and strain-dependent spin density waves in FeSe/$SrTiO_3$ thin films. *Nature Materials*, 12(7):634–640. 67

Tanaka, T., Akiyama, K., Ichinokura, S., Shimizu, R., Hitosugi, T., and Hirahara, T. (2020a). Superconducting dome revealed by surface structure dependence in single unit cell FeSe on $SrTiO_3$(001). *Physical Review B*, 101:205421. 60

Tanaka, T., Akiyama, K., Ichinokura, S., Shimizu, R., Hitosugi, T., and Hirahara, T. (2020b). Superconducting dome revealed by surface structure dependence in single unit cell FeSe on $SrTiO_3$(001). *Physical Review B*, 101(20):205421. 12, 13

Tanaka, T., Akiyama, K., Yoshino, R., and Hirahara, T. (2018). Superconductivity of single unit cell FeSe/$SrTiO_3$(001): Substrate-surface superstructure dependence. *Physical Review B*, 98(12):121410. 12

Tang, C., Liu, C., Zhou, G., Li, F., Ding, H., Li, Z., Zhang, D., Li, Z., Song, C., Ji, S., et al. (2016). Interface-enhanced electron-phonon coupling and high-temperature

superconductivity in potassium-coated ultrathin FeSe films on $SrTiO_3$. *Physical Review B*, 93(2):020507. 12

Tersoff, J. and Hamann, D. R. (1983). Theory and Application for the Scanning Tunneling Microscope. *Physical Review Letters*, 50:1998–2001. 29

Tersoff, J. and Hamann, D. R. (1985). Theory of the scanning tunneling microscope. *Physical Review B*, 31:805–813. 29

Tinkham, M. (2004). *Introduction to superconductivity*. Courier Corporation. 3, 58, 59

Tsuei, C. and Kirtley, J. (2000). Pairing symmetry in cuprate superconductors. *Reviews of Modern Physics*, 72(4):969. 6

Van Benthem, K., Elsässer, C., and French, R. (2001). Bulk electronic structure of $SrTiO_3$: Experiment and theory. *Journal of Applied Physics*, 90(12):6156–6164. 136

Van Veenendaal, M. and Sawatzky, G. (1993). Nonlocal screening effects in $2p$ X-ray photoemission spectroscopy core-level line shapes of transition metal compounds. *Physical Review Letters*, 70(16):2459. 135

Vanacore, G., Zagonel, L., and Barrett, N. (2010). Surface enhanced covalency and Madelung potentials in Nb doped $SrTiO_3$(100), (110) and (111) single crystals. *Surface Science*, 604(19-20):1674–1683. 86

Varelogiannis, G., Perali, A., Cappelluti, E., and Pietronero, L. (1996). Density-of-states-driven anisotropies induced by momentum decoupling in $Bi_2Sr_2CaCu_2O_8$. *Physical Review B*, 54(10):R6877. 14

Vilmercati, P., Cheney, C. P., Bondino, F., Magnano, E., Malvestuto, M., McGuire, M. A., Sefat, A., Sales, B. C., Mandrus, D., Singh, D. J., et al. (2012). Direct

probe of the variability of Coulomb correlation in iron pnictide superconductors. *Physical Review B*, 85(23):235133. 7, 8, 46, 47, 136

Wang, M., Ou, Y.-B., Li, F.-S., Zhang, W.-H., Tang, C.-J., Wang, L.-L., Xue, Q.-K., Ma, X.-C., et al. (2014). Molecular beam epitaxy of single unit-cell FeSe superconducting films on $SrTiO_3$(001). 60

Wang, Q.-Y., Li, Z., Zhang, W.-H., Zhang, Z.-C., Zhang, J.-S., Li, W., Ding, H., Ou, Y.-B., Deng, P., Chang, K., et al. (2012). Interface-induced high-temperature superconductivity in single unit-cell FeSe films on $SrTiO_3$. *Chinese Physics Letters*, 29(3):037402. 9, 10, 71, 127

Wang, Y., Linscheid, A., Berlijn, T., and Johnston, S. (2016). *Ab initio* study of cross-interface electron-phonon couplings in FeSe thin films on $SrTiO_3$ and $BaTiO_3$. *Physical Review B*, 93(13):134513. 14

Wiesendanger, R. (1994). *Scanning Probe Microscopy and Spectroscopy: Methods and Applications*. Cambridge University Press. 28, 29

Wu, M., Wu, P., Wen, Y., Wang, M., Lin, P., Lee, W., Chen, T., and Chang, C. (2015). An overview of the Fe-chalcogenide superconductors. *Journal of Physics D: Applied Physics*, 48(32):323001. 113

Xue, C.-L., Dou, L.-G., Xu, Y.-J., Yuan, Q.-Q., Li, Q.-Y., Jia, Z.-Y., Li, Z., Liu, R., and Li, S.-C. (2023). Iron Vacancy Tunable Superconductor-Insulator Transition in $SrTiO_3$(001) Monolayer. *Physical Review Letters*, 131(25):256002. 97

Yadav, S. J., Shaikh, I. A., Sahoo, S., and Shah, D. (2024). Investigating the structural and magnetic properties of Fe_3Se_4 nanoparticles and it's photocatalytic application. *Physica B: Condensed Matter*, 691:416358. 113

Yang, W., Sorini, A., Chen, C., Moritz, B., Lee, W.-S., Vernay, F., Olalde-Velasco, P., Denlinger, J., Delley, B., Chu, J.-H., et al. (2009). Evidence for weak electronic

correlations in iron pnictides. *Physical Review B—Condensed Matter and Materials Physics*, 80(1):014508. 7

Yao, G., Duan, M.-C., Liu, N., Wu, Y., Guan, D.-D., Wang, S., Zheng, H., Li, Y.-Y., Liu, C., and Jia, J.-F. (2019). Diamagnetic response of potassium-adsorbed multilayer FeSe film. *Physical Review Letters*, 123(25):257001. 12

Yasaka, M. et al. (2010). X-ray thin-film measurement techniques. *The Rigaku Journal*, 26(2):1–9. 55

Yeh, K.-W., Huang, T.-W., Huang, Y.-l., Chen, T.-K., Hsu, F.-C., Wu, P. M., Lee, Y.-C., Chu, Y.-Y., Chen, C.-L., Luo, J.-Y., et al. (2008). Tellurium substitution effect on superconductivity of the α-phase iron selenide. *Europhysics Letters*, 84(3):37002. 16

Yeh, K.-Y., Chen, Y.-R., Lo, T.-S., Wu, P. M., Wang, M.-J., Chang-Liao, K.-S., and Wu, M.-K. (2020). Fe-vacancy-ordered Fe_4Se_5: The insulating parent phase of FeSe superconductor. *Frontiers in Physics*, 8:567054. 97, 113, 133

Yin, Z., Haule, K., and Kotliar, G. (2011). Kinetic frustration and the nature of the magnetic and paramagnetic states in iron pnictides and iron chalcogenides. *Nature Materials*, 10(12):932–935. 17, 168

Zhang, H., Ge, Z., Weinert, M., and Li, L. (2020). Sign changing pairing in single layer FeSe/$SrTiO_3$ revealed by nonmagnetic impurity bound states. *Communications Physics*, 3(1):75. 127, 161

Zhang, H., Zhang, D., Lu, X., Liu, C., Zhou, G., Ma, X., Wang, L., Jiang, P., Xue, Q.-K., and Bao, X. (2017). Origin of charge transfer and enhanced electron–phonon coupling in single unit-cell FeSe films on $SrTiO_3$. *Nature Communications*, 8(1):214. 116

Zhang, P., Peng, X.-L., Qian, T., Richard, P., Shi, X., Ma, J.-Z., Fu, B., Guo, Y.-L., Han, Z., Wang, S., et al. (2016a). Observation of high-T_c superconductivity in rectangular FeSe/$SrTiO_3$ (110) monolayers. *Physical Review B*, 94(10):104510. 10

Zhang, S., Guan, J., Jia, X., Liu, B., Wang, W., Li, F., Wang, L., Ma, X., Xue, Q., Zhang, J., et al. (2016b). Role of $SrTiO_3$ phonon penetrating into thin FeSe films in the enhancement of superconductivity. *Physical Review B*, 94(8):081116. 14

Zhang, S., Guan, J., Wang, Y., Berlijn, T., Johnston, S., Jia, X., Liu, B., Zhu, Q., An, Q., Xue, S., et al. (2018). Lattice dynamics of ultrathin FeSe films on $SrTiO_3$. *Physical Review B*, 97(3):035408. 14

Zhang, W.-H., Sun, Y., Zhang, J.-S., Li, F.-S., Guo, M.-H., Zhao, Y.-F., Zhang, H.-M., Peng, J.-P., Xing, Y., Wang, H.-C., et al. (2014). Direct observation of high-temperature superconductivity in one-unit-cell FeSe films. *Chinese Physics Letters*, 31(1):017401. 9, 67

Zhang, Y., Lee, J., Moore, R., Li, W., Yi, M., Hashimoto, M., Lu, D., Devereaux, T., Lee, D.-H., and Shen, Z.-X. (2016c). Superconducting gap anisotropy in monolayer FeSe thin film. *Physical Review Letters*, 117(11):117001. 16

Zhou, X., He, S., Liu, G., Zhao, L., Yu, L., and Zhang, W. (2018). New developments in laser-based photoemission spectroscopy and its scientific applications: a key issues review. *Reports on Progress in Physics*, 81(6):062101. 51

Zhou, Y. and Millis, A. J. (2016). Charge transfer and electron-phonon coupling in monolayer FeSe on Nb-doped $SrTiO_3$. *Physical Review B*, 93(22):224506. 140

Zou, K., Mandal, S., Albright, S. D., Peng, R., Pu, Y., Kumah, D., Lau, C., Simon, G. H., Dagdeviren, O. E., He, X., Božović, I., Schwarz, U. D., Altman, E. I., Feng, D., Walker, F. J., Ismail-Beigi, S., and Ahn, C. H. (2016). Role of double TiO_2 layers at the interface of FeSe/$SrTiO_3$ superconductors. *Physical Review B*, 93:180506. 15, 60

Vita

Xiyou Peng was born on June 18, 1993, in Nanchang, Jiangxi, China. After graduating from the Attached Middle School of Jiangxi Normal University, he attended Peking University (PKU), where he earned a Bachelor's degree in Physics in 2015 after four years of study. In August 2015, Xiyou moved to the United States to join the Physics Department at the University of Tennessee (UT) as a graduate student. After one year, he became a member of Dr. Hanno Weitering's research group, focusing on experimental condensed matter physics. Initially, he worked on stabilizing the Mott insulator phase through straining, but later shifted his research to monolayer FeSe thin films. He anticipates receiving his Doctorate of Philosophy degree in Physics in December 2024.